University of Nottingham

School of Mechanical, Material, Manufacturing Engineering and Management

Fatigue of Dented Pipes

By

Renfan Luo, BSc., MSc.

Thesis submitted to the University of Nottingham
For the degree of Doctor of Philosophy
October 2002

Contents

Abstract

A dented pipe fails either through being punctured or by fatigue damage accumulation due to internal pressure fluctuation. Increasing the wall thickness may prevent these failures but is impractical. As a pipe is punctured, transmission services must be cut off and repair processes have to be made immediately. However, when a dent depth is not large enough to puncture the pipe, the pipe can safely continue in service for a long time until a fatigue crack initiation occurs. Therefore, the fatigue life assessment has attracted much attention in the pipe industries for economic and safety reasons.

The severe tensile residual stress concentration and the large plastic strain deformation in the dented region are the main causes of the pipe failure due to fatigue damage. Accurate calculation and prediction of the residual stress and variations resulting from internal pressure fluctuation can lead to safety assessments and prediction of the remaining life of the dented pipe. Due to the complex nature of the contact process, the deformed pipe geometry and the elastic-plasticity, analytical approaches are incapable of obtaining stress solutions. Therefore, FE modelling is employed in the present work. Experimental tests are employed to investigate the indenter force-dent depth behaviour which can be compared with the FE solutions to confirm and validate the FE models. The rigid perfect elastic-plastic limit load method and an energy-based method are also used to analytically calculate the limit load and the indenter force/deflection relationship of indented rings to predict damage.

Two dimensional FE modelling is performed to calculate the contact and residual stress and strain distributions on the outer, inner surfaces and through the wall thickness. These FE solutions show that high stress concentrations occur in the indented region, which give the potential for fatigue damage. As the 2D FE modelling requires only limited resources, the indenter size and indentation position can be changed to analyse their effects on stress and strain distributions in the indented region. This forms the foundation of later 3D FE modelling.

Stress sensitivity and the validation of shell models are investigated and confirmed through the 2D and 3D FE modelling and by comparing experimental test data with the FE solutions. Based on this work, the decision is made to use shell element modelling to perform the residual stress and stress range calculations in a 3D pipe.

Semi-empirical formulations are developed to predict stress and stress range values if the residual dent depth, the pipe and indenter geometries, material property, internal pressure and pressure range are known. These FE solutions and semi-empirical formulae can be used to calculate the stress range and mean stress.

Acknowledgements

The preparation of this Ph.D. thesis would not have been possible without the contributions, direct or indirect, made by certain individuals.

First and foremost, my deepest thanks and appreciation go to Professor Tom Hyde, my supervisor, whose experience and knowledge offered me the most solid foundations upon which to build my research work. I would like to thank him for his invaluable guidance, patience and support. Especially I would like to thank him for his trust in me to offer me the irreplaceable chance to start this Ph.D. research work without any hesitation after accepting my application.

I would also like to express my profound gratitude to Professor Adib Becker, my supervisor, for his excellent supervision in technique guidance, patience and support. I would like to thank him for believing in me of having the ability to do research work.

I would like to express my thanks to Dr Bin Fu at Advantica for his valuable advice and encouragement.

Acknowledgements go to Advantica and University of Nottingham for financial support of the research work through a Studentship.

Finally, my deep thanks go to my family, particular to my wife, Jinqu and my son, Danrui, for them to go through all the hard time and share all the good time with me.

Notation

α	Angular position of a circle beam
$\alpha_1, \alpha_2, \alpha_3, \alpha_4, \alpha_5$	Angles of plastic hinges.
$\alpha_{1max}, \alpha_{2max}$	Maximum rotational angles of plastic hinges
$\beta_1, \beta_2, \beta_3$	Three non-dimensional constants used in stress-strain empirical formulation (see Appendix 5.A)
δ	Deflection/ dent depth for the pipe/ring
δ_0	Non-dimensional dent depth (=δ/R).
δ_m	Measured dent depth after indentations
δ_{max}	Maximum deflection/ dent depth.
$\delta_{elastic}^{max}$	Maximum elastic deflection/ dent depth.
δ_p	Deflection/ dent depth caused purely by deformation.
δ_r	Residual dent depth.
$\Delta\delta$	Dent depth change due to a pressure fluctuation.
ε	Strain
$\varepsilon_{low}, \varepsilon_{up}$	Lower and upper yield strains
ε_y	Yield strain
ε_{uts}^{true}	True ultimate tensile strain
θ, θ_0	Angular positions of the support and the plastic hinge with symmetrical supports.
θ_1	Angular positions of the load.
$\theta_2, \theta_5, \theta_3, \theta_4$	Angular positions of the support for asymmetrical supports
σ	Stress
σ_0	A stress constant used in stress-strain empirical formulation (see Appendix 5.A)

σ_y, σ_f, σ_{UTS}	Yield, flow and ultimate tensile stresses
σ_h, σ_a, σ_e	Residual hoop, axial and von Mises stresses.
σ_r	Residual hoop stress
σ_{low}, σ_{up}	Lower and upper yield stresses
σ_{UTS}^{true}, σ_{UTS}^{eng}	True and engineering tensile ultimate stresses
$\Delta\sigma$	Hoop stress variation
$\Delta\sigma_h$, $\Delta\sigma_a$, $\Delta\sigma_e$	Ranges of residual hoop, axial and von Mises stresses caused by pressure changes.
E	Young's modulus
F	Indenter force or external load.
F_U	Upper bound limit load
F_{Limit}	Limit load of indented pipes
F^M	Non-dimensional coefficient contributed by bending moment
F^P	Non-dimensional coefficient contributed by internal pressure.
I	Sectional second moment of inertia
K	The equivalent stiffness of spring type support (MPa).
K_0	The vertical stiffness of a uniform spring (MPa).
K_1, K_2, K_3	The stiffness of single springs (N/mm).
K_σ	A non-dimensional constant used in a stress-strain empirical formulation (see Appendix 5.A)
K_{ep}, K_e, K_p	Gradients of indenter force versus dent depth curves predicted by equations (4.3), (4.11) and (4.12), respectively.
K_{total}	The total equivalent stiffness of pressurised pipe with spring type supports (MPa).
$K(\theta)$	Normalised initial flexibility of indenter force versus dent depth curves.
L	Axial length of a dented ring

L_i	Axial length of indenter.
$L(\theta)$	Non-dimensional function referring to magnitude of the limit load.
$Ls(\theta_1, \theta_2, \theta_5)$	Non-dimensional function.
M, M_A, M_B, M_E	Bending moments where subscripts A, B and E refer to section positions (see Fig 3.2).
M_0	Limit moment which is defined as $\sigma_y t^2/4$.
M_1, M_2, M_3	Bending moments used in imperfect rings.
N	Circumferential force at section A.
n	Material working hardening exponent
p_1, p_2	Internal pressures after pressure changes
Δp	Pressure range defined as $p-p_1$ or $p-p_2$
p	Internal pressure
p_m	Measured pressure level after indentations
r	Indenter radius
R	Mean radius of the pipe/ring
t	Wall thickness
U	Complementary strain energy
u_{xA}, u_{xC}	Displacements in the circumferential direction at sections A and C
u_{xB}, u_{yB}	Displacements in the x and y directions at position B
W_I	Internal energy dissipated
W_E	Work done by external force F
W_P	Work done by internal pressure

Chapter 1

Introduction

Pipelines are widely used for transmitting gases and liquids from their production sites to houses and industrial organisations. Many of these are buried underground, and if these pipelines should leak or rupture, there is a potential danger due to fires or explosions. Therefore, during the design of pipelines, a number of possible sources of failure need to be taken into account, e.g. indentation from diggers during construction or earth movement, corrosion, fatigue, etc. In addition to the failure due to indentations, pipes also may be damaged due to defects caused during forging processes, transportation and installations. Generally, the defects produced during the forging processes are called pre-existing flaws. These defects are normally easy to find and repair, therefore; severe damages due to these flaws can be avoided before accidents happen. However, it is very dangerous for pipes to have defects when the pipes are used in transmission services. In this case, if the transmission services are interrupted to repair the defect, it would result in substantial financial loss. If the defect is left unrepaired, the residual stress concentration in the defect region may gradually weaken the pipe due to the cyclic internal pressure changes. A microcrack may then be formed in the defected pipe. The pipe therefore may finally fail due to fatigue damage caused by internal pressure fluctuations and contribute to severe environment pollution and possible loss of life. Traditionally the flaws caused during the transmission services are called external defects which are the subject of investigation in this thesis.

Using advanced modern technology, it is relatively easy to locate the positions and estimate the severity of flaws in pipes, and subsequently assess the residual life of imperfect pipes.

The various approaches used to assess the residual life of an imperfect pipe are based on theoretical, numerical and experimental methods. Regardless of which method is used, it is difficult to accurately assess the residual life of imperfect pipes, although experimental results are generally regarded as more reliable than theoretical and numerical predictions. Fatemni and Yang [1] reviewed a number of fatigue theories. However, theoretical approaches based on crack initiations cannot accurately predict fatigue life. Therefore, present residual life prediction theories can be very conservative. It is extremely expensive to carry out laboratory tests with

real pipes under practical loading conditions. For these reasons, much research has concentrated on the improvement of methods used for determining the stress distributions in imperfect pipes.

In recent years, many assessment approaches based on theoretical, numerical and experimental methods have been proposed. Tam and Croll [2 - 4] proposed a theoretical analysis method called the equivalent load method, to analyse the stress concentration of dented pipes, based upon linear elastic cylindrical shell theory. Godoy [5, 6] proposed the use of a perturbation method to analyse the stress distributions of thin-walled plates and cylindrical shells with defects. However, elastic analyses neglect the locked-in residual stresses that contribute to fatigue life.

Flores and Godoy [7], Ohtani et al [8] investigated the stress distributions in imperfect spherical pressure vessels using finite element (FE) simulations. Fowler et al [9], Zarea et al [10] and Hart et al [11] investigated the residual fatigue life of dented pipes using FE modelling. Alexander [12] proposed a semi-empirical formulation to estimate stress concentration factors for a pipe with D/t = 68, with a range of residual depths.

Corder et al [13] investigated semi-empirical formulations, by using an experimental programme to explain the relationships between dent force and dent depth, dent depth and residual dent depth, puncture force and pressure or other geometric dimensions of pipe and dent, and burst pressure with other material or geometric parameters. Fowler et al [9], Kiefner et al [14], and Hagiwara et al [15] carried out a series of fatigue tests in order to estimate the residual fatigue life of dented pipes. Lancaster and Palmer [16, 17] carried out a series of tests to predict the burst pressure and strain distribution in dented pipes with a gouge.

Although most impact damage to pipelines is very localised [18-25], as indicated in Fig. 1.1 (a), in some cases, the damage can extend over a significant length of the pipe [10], as indicated in Fig. 1.1[b]. In the latter case, the behaviour (except at the ends of the damage) is essentially two-dimensional and can be analysed as a simple plane-strain ring, as indicated in Fig. 1.1(c).

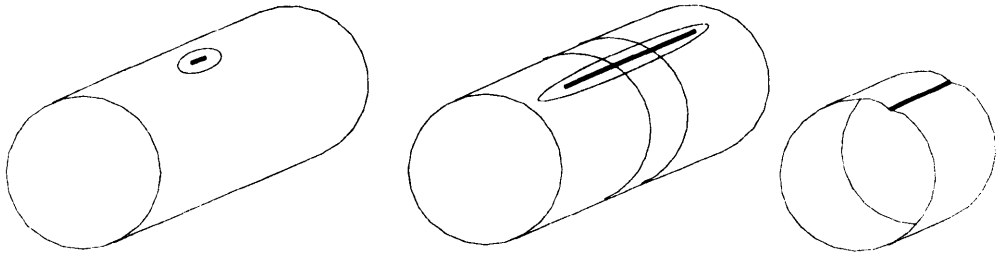

(a) Localised impact damage (b) Extensive impact damage (c) Two-dimensional approximation of extensive impact damage

Fig.1.1 Dented pipes

Indentation damage can occur with or without internal pressure and the deformations and residual stresses are affected by the magnitude of the internal pressure when the damage occurs. With suitable finite element software [26] the deformations and residual stresses due to impact can be obtained. However, these solutions may be time consuming and expensive. For rings, simple analysis methods can be used as an alternative. For example, Castiglano's theorem can be used to determine elastic deformations and the upper and lower bound methods can be used to determine limit loads when the rings are free of internal pressure. A comparison of the analytical and finite element solutions with experimental data showed that the analytical limit load method is simple to use and gives accurate predictions. However, investigations showed that if internal pressure is large enough, the limit load methods give inaccurate predictions. An alternative energy-based approach was therefore used to explain why the approach used when there is no pressure is inaccurate for the case of pressurised pipes, and the relationship between indentation force and dent depth was predicted when internal pressure is significant. The accuracy of the analytical method for pressurised rings with large, non-linear deformation is assessed by comparing predictions with the corresponding results of finite element analyses.

However, although the accuracy of analytical methods used in this thesis was reasonably confirmed by comparing the analytical solutions with the experimental data and the finite element analyses, residual stresses and stress changes caused when the internal pressure fluctuates cannot be assessed analytically. Finite element analyses were used in predicting the local stress concentration in indented pipelines. However, based on present developed experimental techniques, accurate assessment of residual stresses in pipes is not possible. Like analytical solutions obtained for indented rings, the accuracy of the finite element analyses for

indented pipes was validated by comparing the finite element force versus deflection curves with those obtained from experimental tests. Five 6082-T6 aluminum alloy tubes with a diameter of 86.4mm and a wall thickness of 1.2mm, were indented by a rigid indenter in experimental tests for pressure levels of 0, 2, 3, 4 and 5MPa. The indenter force versus deflection curves were automatically recorded on an Instron 1195 Automated Material Test System. These data were used for comparison with results obtained from the finite element analyses performed using the same conditions.

In reality, in order to assess the fatigue life of indented pipes after an accident, performing a valid finite element analysis is not a simple job even for an expert analyst. Comprehensive finite element analyses were therefore performed to develop an empirical formulation to predict the residual stresses in indented pipes. A semi-empirical formulation predicting the stress changes due to the internal pressure fluctuations was also developed on the basis of finite element analyses and analytical solutions of stresses in an imperfect pressurised ring. Using these results the fatigue life of any indented pipes with the same conditions used in this thesis would be expected to be accurately assessed.

In chapter 2, previous achievements of research on indented pipes and related subjects were reviewed. It can be seen that previously used approaches to investigate indented pipes are focused on experiments, FE analysis and linear elastic solutions. Some empirical formulations to predict the limit loads of the internal pressure and the relationships between indenter force and dent depth were developed. Analytical solutions of limit loads and indenter force-deflection relationships have not been reported. The experiments were mainly used to investigate fatigue life of indented pipes with an existing defect. Shell element models were generally applied to perform a FE analysis to predict residual stresses.

Chapter 3 discusses details of the elastic-plastic method used to analytically investigate the limit loads of indenter forces of indented unpressurised rings with symmetrical loading and boundary conditions. Subsequent analytical solutions of the limit loads of indented rings were obtained and compared with results obtained from experiments and FE analyses. A very good correlation of these results was obtained.

For pressurised indented rings with symmetrical loading and boundary conditions, analytical curves for the elastic-plastic solution of the indenter force versus dent depth were obtained and validated with the FE analyses and experimental results in chapter 4. Analytical solutions of the

limit loads and the indenter force versus dent depth curves of indented rings with asymmetrical loading and asymmetrical boundary conditions were investigated and obtained in chapters 5 and 6, respectively. These two analytical solutions were also confirmed and validated by comparison with results obtained from the experimental tests and the FE analyses. Chapter 7 focuses on investigations of the indenter force versus dent depth behaviours of the indented rings with spring-like supports which are closer to reality because the pipes are supported by soils. In this chapter the analytical solutions are obtained and compared with the corresponding FE analyses.

Chapter 8 starts to investigate the residual stresses and stress variations induced by the internal pressure fluctuations for indented rings using the FE analysis. In order to investigate the effects of the internal pressure, geometrical dimensions, supports and residual dent depths on the residual stresses and stress variations, subsequent parametrical analyses were performed. A semi-empirical formulation predicting the stress variations was developed after investigating the analytical solution of an imperfect pipe model.

In following chapters, three-dimensional indented pipes were investigated for different purposes using experiments and FE analyses. Chapter 9 investigates the stress sensitivity to the element sizes using the FE analysis and chapter 10 investigates the indenter force versus dent depth behaviors using aluminum alloy tubes to perform a series of tests and using the FE analysis. Comparisons of the results obtained from the shell element and 3D brick element models were carried out and a very good correlation of the validation of these models was obtained. Therefore, the shell element models were used to investigate residual stresses and stress variations in chapters 11 and 12 to reduce computer analysis times. The residual stresses in the pipes with a constant internal pressure were investigated in chapter 11 using the shell element models, and empirical formulations to predict the residual stresses were also developed using the FE results and curve fitting. Chapter 12 discusses the stress variations in the pipes using the shell element models when the internal pressure fluctuates after the indentation. Accurate semi-empirical formulations to predict the stress variations were also obtained. In chapter 13 all the work in this thesis was summarized and possible future work was proposed. The fatigue life of indented pipes therefore can be assessed using S-N curves and the obtained stress results here.

Missing pages are unavailable

Chapter 2

Literature Review

2.1 Main Factors Causing Pipe Failure

The threat of external damage has long been recognised in the design of onshore and offshore pipes. Most design codes take account of such damage by including measures that reduce the likelihood of failure in high risk areas. The most widely used approach is to limit the pipe design factor (ratio of hoop stress to specified minimum yield stress) in these areas. As Corder et al [13] reported, pipe damage occurs mainly from the pre-existing defects in the surface such as gouges, pores or inclusions formed when the pipes are forged.

Pipe failure is likely to be caused by an external indentation. For instance, a large stone may hit the surface of the pipe when landslip takes place; or pipes may be indented by teeth of excavators or tractors in public operation fields. The influences of pre-existing indentations on pipe safety and fatigue life have been studied for many years. Corder et al [13] proposed some semi-empirical formulae to explain quantitatively the influence of indenter size on the fatigue life of the pipes, limit burst pressure, etc. Bai et al [27] calculated the fracture strength of indented pipes with cracks. Hart et al [11] analysed the influence of the indentation on vibrations in a section pipe in Alaska by using infinite element technology.

Another cause of pipe failure is environmental chemical corrosion. The propagation of stress corrosion cracks in pipe steels at neutral pH was studied by Wilmott and Sutherby [28] under realistic environmental conditions. The impact of the hoop stress on the growth of shallow surface cracks in an X60 pipe steel was investigated at 40%, 70% and 100% of the minimum yield strength of the material. Crack growth rate is shown to be independent of the applied stress in the range studied for shallow cracks.

It is reported in the literature (see, for example Eiber et al, [29]) that failure of the pipe due to mechanical damage defects is generally due to a number of possible causes such as low-cycle fatigue of the highly strained material, and localised strain aging of the cold-worked steel that leads to failure as a result of hydrogen cracking.

2.2 Basic Codes For Pipe Safety Design

In early 1965, the Institution of Gas Engineers published its first recommendations concerning the installation of steel pipes for high-pressure gas transmission, issued as

Communication 674. It originally aimed to protect members of the public and the personnel of the pipe constructors and operators from possible hazards, so far as is reasonably practicable, as well as to ensure that the security of the gas supply is adequately maintained. The basic requirements for safety design were described, or simply presented with formulae. The new version issued is Communication 1530 in 1993. API (American Petroleum Institute) [31] published a pipe design code, called Specification for Line Pipe, in which the indentations are strictly included as follows:

(i) The pipe shall contain no indentations greater than 1/4 in. (6.35mm), measured as the gap between the lowest point of the indentation and a prolongation of the original contour of the pipe.

(ii) The length of the indentation in any direction shall not exceed one half of the diameter of the pipe.

(iii) All cold-formed indentations deeper than 1/8 in. (3.18mm) with a sharp bottom gouge shall be considered a defect.

(iv) The gouge may be removed by grinding.

Kannappan [30] presented a formula for the minimum wall thickness and allowable working pressure of the pipe from Design Codes as follows:

$$t_m = \frac{PD}{2(SE_q + PY)} + A = t + A \tag{2.1}$$

where

t_m = minimum required wall thickness, in inches

t = pressure design thickness, in inches

P = internal pressure, in Psig

D = outer diameter of the pipe, in inches

S = allowable stress at design temperature (known as hot stress), in Psig

A = allowance, additional thickness to provide for material removed in threading, corrosion, or erosion allowance. A manufacturing tolerance (MT) should also be considered.

Y = coefficient that takes material properties and design temperature into account.

For $t \geq d/6$ and temperature below 900^0F, Y = 0.4 may be assumed. The coefficient Y can be written as follows:

$$Y = d/(d + D) \tag{2.2}$$

where d is the inside diameter = D - 2t

A quality factor E_q is defined as follows:

$$E_q = E_c E_s E_j \tag{2.3}$$

where E_c is the casting quality factor, E_j is the joint quality factor, and E_s is structural quality factor.

Allowable working pressure is determined by:

$$P = \frac{2SE_q t}{D - 2Yt} \tag{2.4}$$

2.3 Limit Load Analysis

Because of the complexity of the structure, limit load analysis for a pipe with plain indentations or combined gouges and indentations is very difficult. A review has been presented by Miller [32], in which a number of semi-empirical formulae were highlighted. Here, for simplicity, only a number of formulations for pipes with surface defects are reviewed.

(i) Lower Bound Formula

$$\frac{PR}{\sigma_f t} = 1 - \frac{a}{t} + \frac{a/t}{\left(1 + 1.61c^2 / Ra\right)^{1/2}} \tag{2.5}$$

where

2c= defect length

a= defect depth

b= ligament thickness

R= cylinder radius

t= cylinder thickness

σ_f= flow stress which is defined as

$$\sigma_f = \frac{1}{2}\left(\sigma_y + \sigma_{UTC}\right) \tag{2.6}$$

or

$$\sigma_f = 1.15\sigma_y \tag{2.7}$$

(ii) Upper bound Formula

$$\frac{PR}{\sigma_f t} = \frac{\eta}{1 - (1 - \eta)/M(\rho)} \tag{2.8}$$

where

$$\rho = c/(Rt)^{1/2} \tag{2.9}$$

$$\eta = b/t \tag{2.10}$$

M(ρ) is a factor taken from the through-crack result, which is defined as

$$M(\rho) = \left(1 + 1.61\rho^2\right)^{1/2} \tag{2.11}$$

or

$$M(\rho) = \left(1 + 1.05\rho^2\right)^{1/2} \tag{2.12}$$

(iii) Miller's Formula

$$\frac{PR}{\sigma_y t} = 1 - \frac{a}{t} + \frac{a/t}{\left(1 + 1.61c^2/Ra\right)^{1/2}} \tag{2.13}$$

(iv) Kiefner Formula

$$\frac{PR}{\sigma_f t} = \frac{\eta}{1 - (1-\eta)/\left(1 + 1.05\rho^2\right)^{1/2}} \tag{2.14}$$

2.4 Experimental Work

To predict and improve the safety and reliability of pipes and better understand the damage mechanisms, research based on experimental techniques involving indented pipes has been performed by many researchers. Ong et al [24] investigated the strain distribution in the indented region. Lancaster and Palmer [16, 17] investigated the bursting pressure of pipes with a gouge in an indentation. EPRG (European Pipe Research Group) has carried out an extensive experimental programme to fully analyse the deformation of indented pipes, in which the main achievements were reviewed by Corder et al [13]. Based on measuring experimental data, some useful empirical formulae have been established, from which burst pressures and puncture forces may be predicted.

2.4.1 Empirical Formulations for Fatigue Life

From EPRG experiments, a new fatigue life formula has been given by Corder et al [13] as follows:

$$N_c = 100[(UTS - 50)/(2\sigma_A K_s)]^{4.292} \tag{2.15}$$

where

$$K_s = 2.871\sqrt{t(H/2S)} \tag{2.16}$$

$$2\sigma_A = UTS\left[B\left(4 + B^2\right)^{\frac{1}{2}} - B^2\right] \tag{2.17}$$

$$B = (\sigma_a / 1.3\sigma_{SMYS})[1 - (\sigma_a / 1.3\sigma_{SMYS})(1 + S)/(1 - S)] \tag{2.18}$$

where

N_c= number of cycles to failure

$2\sigma_A$ = equivalent cyclic stress at S=0, in MPa

S= minimum stress/maximum stress in fatigue cycle

UTS= $1.3\sigma_{SMYS}$

σ_{SMYS} = specified minimum yield strength, in MPa

σ_a = cyclic stress, in MPa

Fatigue tests for pipes with a gouge in an indentation were also carried out by Fowler et al [9], Kiefner et al [14], and Hagiwara et al [15]. Based upon test results, Hagiwara et al [15] proposed a power law equation for predicting fatigue life as follows:

$$N_f = C(d/D)^{\alpha}(t/T)^{\beta}(\Delta\sigma/E)^{\gamma} \tag{2.19}$$

where

C = defect half length

d = maximum dent depth during denting

T = gouge depth

D = pipe diameter

T = wall thickness of pipes

a,β,γ are material constants.

2.4.2 Burst Pressure Formulations

The burst pressure of pipes containing combined indentations and cracks was investigated by Bai et al [27]. Based upon previous research, they proposed a semi-empirical formula to predict the burst pressure of pipes containing a combined indentation and a longitudinal crack, as follows:

$$P = 2\sigma\frac{t}{D} \tag{2.20}$$

where t is the pipe wall thickness, D is pipe nominal outside diameter, and σ is critical stress at failure, which is given as follows:

$$\sigma = \frac{2\sigma_p}{\pi}\cos^{-1}\left(\exp\left(-\frac{\pi K_{mat}^2}{8Y^2 a\sigma_p^2}\right)\right) \tag{2.21}$$

$$K_{mat} = \left[1000\frac{E}{A}(C_v - 17.6)\right]^{\frac{1}{2}} \tag{2.22}$$

$$Y = \frac{F}{\sqrt{Q}}\left(1 - 1.8\frac{D_d}{D} + 5.1H\frac{D_d}{t}\right) \tag{2.23}$$

$$\sigma_p = \alpha\sigma_y\frac{t-a}{t-a/M_t} \tag{2.24}$$

K_{mat} = the material toughness parameter

a = crack depth

Y = pipe geometry shape function,

F, Q and a bending correction factor are given by Newman and Raju [33],

D_d = indentation depth

σ_y = yield strength stress

σ_p = collapse stress

M_t is a factor determined by

$$M_t = \sqrt{1 + 0.6275x^2 - 0.003375x^4} \quad \text{for } x \le 7.07 \tag{2.25}$$

$$M_t = 0.032x^2 + 3.3 \quad \text{for } x > 7.07 \tag{2.26}$$

$$x = L/\sqrt{Dt} \tag{2.27}$$

where L is defined as the length of local crack

2.4.3 Force and Deflection Formulations

Empirical formulae were reviewed by Bai et al [27] for the mean value of the indentation force F, as follows:

$$F = 0.011 P_r H^{0.42} \tag{2.28}$$

and for the mean value of the force based on a lower 95% confidence level:

$$F = 0.007 P_r H^{0.5} \tag{2.29}$$

where H is the indentation depth after springback (in mm) and P_r is given by:

$$P_r = \sqrt{\sigma_{SMYS} L t}(t + 0.7PD/\sigma_{UTS}) \tag{2.30}$$

where

F= indentation force, in kN

t= pipe wall thickness, in mm

σ_{SMYS} = specified minimum yield strength, in MPa

σ_{UTS} = ultimate tensile strength, in MPa

L= tooth length, in mm

D= pipe outside diameter, in mm

P= internal pressure, in MPa

2.4.4 Puncture Force Formulation

Lower bound:

$$F_p = 0.27\sigma_{UTS}(L + l)t \tag{2.31}$$

Mean value:

$$F_p = 0.23\sigma_{UTS}(L + l)t \tag{2.32}$$

Minimum value:

$$F_p = 0.16\sigma_{UTS}(L + l)t \tag{2.33}$$

where l is the width of the tooth (in mm).

The damage hoop stress limit formula with a gouge is given by

$$\sigma_h = \frac{2}{\pi}\bar{\sigma}\cos^{-1}\{\alpha\}$$

$$\alpha = e^{-\left[\frac{1.5\pi E}{\bar{\sigma}^2 Ad}\left(Y_1\left[1-\frac{1.8H}{2R}\right]+Y_2\left[10.2\frac{RH}{2Rt}\right]\right)^{-2} e^{\left(\frac{\ln C_v - 1.9}{0.57}\right)}\right]} \tag{2.34}$$

where

Y_1 and Y_2 are compliance functions given by

$$Y_1 = 1.12 - 0.23\left(\frac{d}{t}\right) + 10.6\left(\frac{d}{t}\right)^2 - 21.7\left(\frac{d}{t}\right)^3 + 30.4\left(\frac{d}{t}\right)^4 \tag{2.35}$$

$$Y_2 = 1.12 - 1.39\left(\frac{d}{t}\right) + 7.32\left(\frac{d}{t}\right)^2 - 13.1\left(\frac{d}{t}\right)^3 + 14.0\left(\frac{d}{t}\right)^4 \tag{2.36}$$

$$\bar{\sigma} = 1.15\sigma_{SMYS}\left(1-\frac{d}{t}\right) \tag{2.37}$$

σ_h= hoop stress at failure (lbf/in^2)

E= Young's modulus (lbf/in^2)

A= fracture area of 2/3 Charpy test specimen(in^2)

d= gouge depth(in)

H= dent depth corrected for springback (in)

R= pipe radius(in)

C_v=2/3 Charpy energy (ftlbf)

2.4.5 Dent Depth-Residual Dent Depth Formulation

The relationship between the indentation depth and the residual indentation depth has been given by Corder et al [13] as follows:

$$H = 0.32H_D^{1.2} \tag{2.38}$$

where H_D is damage dent depth.

Modern pipe materials are ductile and should therefore fail by ductile initiation or plastic collapse. When a pipe defect fails by plastic collapse (failure governed by the flow stress) the semi-empirical relationships were reviewed by Corder et al [13] can be used and have been adopted extensively by pipe operators around the world, as follows:

$$\sigma_h = \sigma_{flow}(1-d/t)/(1-Md/t) \tag{2.39}$$

$$M = (1+0.26(2c/\sqrt{Rt})^2)^{\frac{1}{2}} \tag{2.40}$$

where

σ_h = hoop stress at failure

σ_{flow} = flow stress

d = defect depth

2c = defect length

R = pipe radius

T = pipe wall thickness

These semi-empirical formulae are not commonly accepted because of the large differences that exist between the experimental data and results obtained from these simplified semi-empirical formulae.

2.5 Basic Analytical Approaches

The analytical approaches used in the analysis of imperfect pipes or thin-wall shells can be divided into two basic types; linear elastic analysis and elasto-plastic analysis.

2.5.1 Analysis based on linear elastic mechanics

For the analysis of the fatigue life of indented pipes, without cracks, using elastic linear theories, stress concentration factors may be determined in the indented region. If the indented pipe has a pre-existing crack, the stress intensity factor may be calculated using linear elastic fracture mechanics theories. Engineers can apply both of these approaches to predict the residual fatigue life of indented pipes.

2.5.1.1 Linear stress analysis for indented pipes

There are two main approaches used for linear stress analysis; perturbation approach and an equivalent load method.

(a) Perturbation method

Perturbation analysis, in which the solution is expanded as a series of terms containing a damage parameter, was employed by Godoy [5, 6]. When using this technique to analyse the linear elastic stress distribution of an imperfect shell, the displacement vector is expressed in terms of a damage parameter τ as follows:

$$\upsilon = \sum_{i=0}^{n} a_i \tau^i \tag{2.41}$$

where a_i is perturbation coefficient and a_0 is the displacement vector for a perfect cylindrical shells.

(b) Equivalent load method

To theoretically estimate the stress concentration factor of damaged pipe, Tam and Croll [3-4] proposed that the equivalent load method could be used. They assumed that for an indented tubular member a typical defect is as shown in Fig.2.1, such that

$$\begin{aligned} w &= w_0 e^{-bx/r} \\ R_1 &= r - \frac{\pi+2}{4} w \\ R_2 &= r + \frac{\pi-2}{4} w \\ S &= \frac{\pi}{2} w \end{aligned} \tag{2.42}$$

where x represents the axial position in the pipe, b is a dent shape factor, r and w are the radius of the pipe and the dent depth at position x, respectively, R_1 and R_2 represent the two radii of the deformed pipe, and S is the width of the dent, as shown in Fig.2.1.

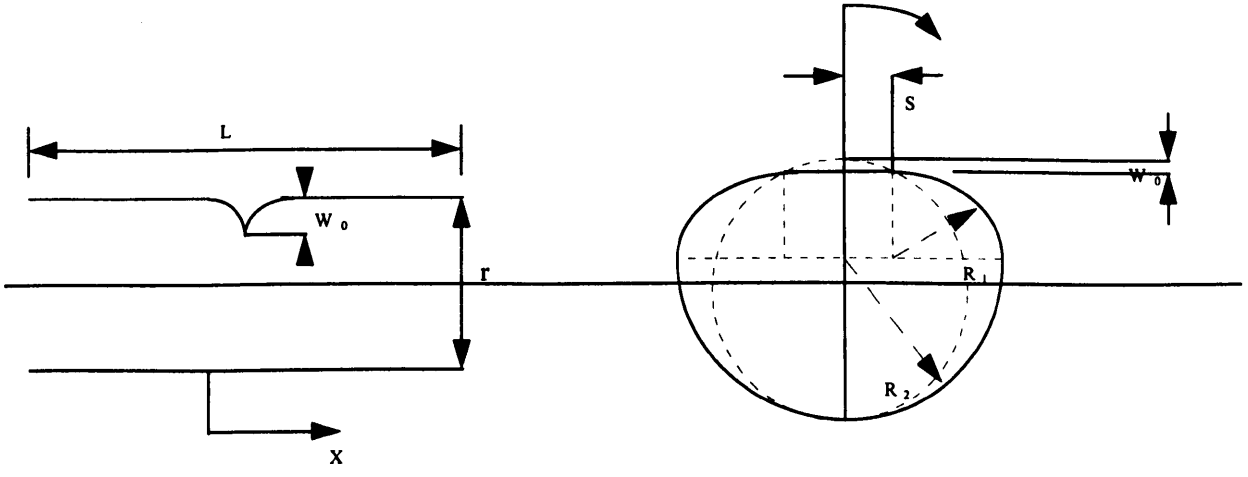

Fig. 2.1 Typical dent damage cylinder used for stress analysis in equivalent load method

The equivalent load method is based on the replacement of geometric deviations with an appropriately chosen normal pressure to be applied to the perfect (undamaged) shell. The damaged shell is taken to be subjected to the same in-plane stress resultants ($n_x^0, n_\theta^0, n_{x\theta}^0$) as

the perfect shell. The first order equivalent pressure, p_z^*, may be obtained through simple static equivalence as follows:

$$p_z^* = n_x^0 \chi_x^0 + n_\theta^0 \chi_\theta^0 + n_{x\theta}^0 \chi_{x\theta}^0 \tag{2.43}$$

where $(\chi_x^0, \chi_\theta^0, \chi_{x\theta}^0)$ are errors in axis, circumferential curvature and twist resulting from the local damage. When this equivalent pressure is applied to the perfect shell, an additional set of stress and moment resultants $(n_x^*, n_\theta^*, n_{x\theta}^*, m_x^*, m_\theta^*, m_{x\theta}^*)$ is produced. Adding these increments of stresses and moments to the perfect shell thus yields the first order correction for the damaged shell.

$$\begin{aligned} n_x' &= n_x^0 + n_x^* \\ n_\theta' &= n_\theta^0 + n_\theta^* \\ n_{x\theta}' &= n_{x\theta}^0 + n_{x\theta}^* \\ m_x' &= m_x^0 + m_x^* \\ m_{x\theta}' &= m_{x\theta}^0 + m_{x\theta}^* \end{aligned} \tag{2.44}$$

By analogy, a second order equivalent load is given by

$$p_z^{**} = n_x^* \chi_x^0 + n_\theta^* \chi_\theta^0 + n_{x\theta}^* \chi_{x\theta}^0 \tag{2.45}$$

The second order correction of in-plane stresses and moments (so-called membrane force or section moments) is written as

$$n_x^{**}, n_\theta^{**}, n_{x\theta}^{**}, m_x^{**}, m_\theta^{**}, m_{x\theta}^{**} \tag{2.46}$$

Therefore the second order approximation of in-plane stress and moments can be presented as

$$\begin{aligned} n_x' &= n_x^0 + n_x^* + n_x^{**} \\ n_\theta' &= n_\theta^0 + n_\theta^* + n_\theta^{**} \\ n_{x\theta}' &= n_{x\theta}^0 + n_{x\theta}^* + n_{x\theta}^{**} \\ m_x' &= m_x^0 + m_x^* + m_x^{**} \\ m_\theta' &= m_\theta^0 + m_\theta^* + m_\theta^{**} \\ m_{x\theta}' &= m_{x\theta}^0 + m_{x\theta}^* + m_{x\theta}^{**} \end{aligned} \tag{2.47}$$

By repeating the above process until convergence is reached, an appropriate solution for imperfect pipes can be obtained.

(c) linear elastic solution of dented cylinders

To systematically describe the indentation damage, Tam and Croll [2-4] applied a two-dimensional Fourier analysis, as follows:

$$w^0(x,\theta)=\sum_{i=0}^{*}\sum_{j=0}^{*} w_{ij}^0 \cos i\theta \cos j\frac{2\pi x}{l} \tag{2.48}$$

where $w^0(x,\theta)$ is the radial displacement component of the indentation, w_{ij}^0 is the amplitude of the Fourier harmonic (i, j) having i circumferential and j meridional waves, respectively, and l is the length over which the radial geometric errors have any significance.

At low deformation levels, the various changes in curvature, $(\chi_x^0,\chi_\theta^0,\chi_{x\theta}^0)$ may be approximated as follows:

$$\chi_x^0=\frac{\partial^2 w^0}{\partial x^2},\chi_\theta^0=\frac{1}{r^2}\frac{\partial^2 w^0}{\partial \theta^2},\chi_{x\theta}^0=\frac{1}{r}\frac{\partial^2 w^0}{\partial x\partial\theta} \tag{2.49}$$

Therefore the first order equivalent pressure is expressed as

$$\begin{aligned} p_z^* = &\sum_{i=0}^{\infty}\sum_{j=0}^{\infty} -\left[n_x^0(2\pi j/l)^2+n_\theta^0 i^2/r^2\right]w_{ij}^0 \cos i\theta\cos j\frac{2\pi x}{l} \\ &-2\sum_{i=0}^{\infty}\sum_{j=0}^{\infty}\left[n_{x\theta}^0 ij\frac{2\pi}{rl}\right]w_{ij}^0 \sin i\theta \sin j\frac{2\pi x}{l} \end{aligned} \tag{2.50}$$

When this equivalent pressure is applied to the perfect cylinder, a first order approximation of the incremental stress and moment resultants may be estimated. For clarity, the relevant simplified shell equilibrium equations can be written as follows:

$$\begin{bmatrix} \lambda^2+\frac{1}{2}(1+\mu) & \frac{1}{2}(1+\mu)i\lambda & -\mu\lambda \\ \frac{1}{2}(1+\mu)i\lambda & i^2+\frac{1}{2}(1-\mu)\lambda^2 & -i \\ -\mu\lambda & -i & \frac{1}{\alpha}\left(i^2+\lambda^2\right)^2+1 \end{bmatrix}\begin{bmatrix} u_{ij}^* \\ v_{ij}^* \\ w_{ij}^* \end{bmatrix}=\begin{bmatrix} 0 \\ 0 \\ -w_{ij}^0\left(n_x^0\lambda^2+n_\theta^0 i^2\right)K \end{bmatrix} \tag{2.51}$$

where

$$\alpha = 12(r/t)^2 \tag{2.52}$$

$$\lambda = 2\pi jr/l \tag{2.53}$$

$K\left(=Et/(1-\mu^2)\right)$ is the membrane stiffness

E is Young's modulus

t is cylinder wall thickness

$\left(u_{ij}^{*}, v_{ij}^{*}, w_{ij}^{*}\right)$ are harmonic amplitudes of the equivalent load induced incremental displacement components

$$u^{*}(x,\theta)=\sum_{i=0}^{\infty}\sum_{j=0}^{\infty}u_{ij}^{*}\cos i\theta\sin j\frac{2\pi x}{l}$$

$$v^{*}(x,\theta)=\sum_{i=0}^{\infty}\sum_{j=0}^{\infty}v_{ij}^{*}\sin i\theta\cos j\frac{2\pi x}{l} \tag{2.54}$$

$$w^{*}(x,\theta)=\sum_{i=0}^{\infty}\sum_{j=0}^{\infty}w_{ij}^{*}\cos i\theta\cos j\frac{2\pi x}{l}$$

To estimate the stress concentration factors on the surfaces of the cylinders, Tam and Croll [2-4] presented the following expressions, based on shell assumptions:

$$S_i=\frac{\sigma_i^{*}}{\sigma_x^{0}}=N_i^{0}+N_i^{'}\pm 6W_0M_i^{'}\left(\frac{r}{t}\right) \tag{2.55}$$

where

i=x, xθ, θ

$$N_i^{0}=\frac{n_i^{0}}{n_x^{0}}, N_i^{'}=\frac{n_i^{'}}{n_x^{0}}, M_i^{'}=\frac{m_i^{'}}{n_x^{0}w_0} \tag{2.56}$$

2.5.1.2 S-N fatigue life prediction

Cylindrical shells containing local damage have been shown to exhibit high stress concentrations at the most damaged positions. The two-dimensional nature of these stresses has complicated the fatigue assessment process. However, for simplicity, the maximum principal stress theory was used by Tam and Croll [4]. It implies that the number of cycles required to cause fatigue failure under combined stresses is the same as that due to the maximum principal stress acting alone. For this reason, the following fatigue evaluation is based upon the meridional stress component only. The S-N expression is given by

$$\log N=\log a-m\log\Delta\sigma \tag{2.57}$$

where m, a are material fatigue constants, and N and $\Delta\sigma$ represent the cyclic life and the stress range, respectively.

Under cyclic loading conditions, the design stress range for a perfect cylinder will induce a higher stress range in the damaged shell. This has the effect of lowering the number of cycles to failure. A measure of the fatigue strength reduction is based upon the fatigue cycle reduction factor, N_t, defined as

$$N_t = \frac{N_i}{N_p} = \left(\frac{\Delta\sigma_p}{\Delta\sigma_i}\right)^m = \left(\frac{1}{S_x}\right)^m \tag{2.58}$$

where subscripts i and p refer to imperfect and perfect cylinders, respectively, m is a material fatigue constant, and N_t is defined as the fatigue cycle reduction factor.

2.5.2 Analysis based on elastic-plastic fracture mechanics

For the elasto-plastic fracture mechanics analysis of structures, the stress intensity factor (SIF) must be calculated. For the analysis of cylindrical shells with cracks, Newman and Raju [33] calculated the stress intensity factors (SIF) for a cylinder with an elliptical crack on its inner surface, as follows:

$$K_I = \frac{PR}{t}\sqrt{\pi\frac{a}{Q}}F\left(\frac{a}{c},\frac{a}{t},\frac{R}{t},\phi\right) \tag{2.59}$$

where

$\frac{PR}{t}$ = means hoop stress due to the internal pressure

Q= shape factor for an elliptical crack $= 1 + 1.464(a/c)^{1.65}$

a= depth of surface crack

c= half-length of surface crack

t= cylinder wall thickness

R, R_o= inner and outer radii of cylinder

ϕ = parametric angle of elliptical crack

F= geometric shape function which is given by

$$F = 0.97\left[\begin{array}{l} 1.13 - 0.09\frac{a}{c} + \left(-0.54 + \frac{0.89}{0.2 + a/c}\right)\left(\frac{a}{t}\right)^2 + \\ \left(0.5 - \frac{1}{a/c} + 14(1 - a/c)^{24}\right)\left(\frac{a}{t}\right)^4 \end{array}\right] f_c g f_\phi \tag{2.60}$$

where

$$f_c = \left[\frac{R_o^2 + R^2}{R_o^2 - R^2} + 1 - 0.5\sqrt{\frac{a}{t}}\right]\frac{t}{R} \tag{2.61}$$

$$g = 1 + \left[0.1 + 0.35\left(\frac{a}{t}\right)^2\right](1 - \sin\phi)^2 \tag{2.62}$$

$$f_\phi = \left[\sin^2\phi + \left(\frac{a}{c}\right)^2 \cos^2\phi\right]^{\frac{1}{4}} \tag{2.63}$$

Koh and Na [34] calculated the stress intensity factor of a thick-walled cylinder with an autofrettaged residual stress and an external radial crack, as follows:

$$\begin{aligned} K_I &= K_{IP} + K_{IR} \\ K_{IP} &= \sigma_{OD}\sqrt{\pi a} f(a/t) \\ K_{IR} &= \sigma'_{OD}\sqrt{\pi a} f(a/t) \end{aligned} \tag{2.64}$$

where

K_{IP} and K_{IR} = stress intensity factors due to internal pressure and autofrettage residual stress

a= crack length

f= geometric shape function which is given by

$$f(a/t) = 1.12 + A_1\frac{a}{t} + A_2\left(\frac{a}{t}\right)^2 + A_3\left(\frac{a}{t}\right)^3 + A_4\left(\frac{a}{t}\right)^4 \tag{2.65}$$

σ_{OD} = the nominal tangential stress at the outer surface of cylinder subjected to pressure P

$$\sigma_{OD} = 2P\frac{R^2}{R_o^2 - R^2} \tag{2.66}$$

σ'_{OD} = autofrettage nominal residual stress at outer surface of smooth cylinder

$$\sigma'_{OD} = 2\sigma_{ys}\left\{\frac{\rho^2}{2R_o^2} + \frac{R^2}{R_o^2 - R^2}\left[\frac{\rho^2 - R_o^2}{2R_o^2} - \ln\frac{\rho}{R}\right]\right\} \tag{2.67}$$

ρ = boundary between elastic and plastic deformation during the autofrettage process

σ_{ys} = yield stress

2.6 Numerical analysis based on FE techniques

FE calculations of indented pipes have been the most commonly used approaches for fatigue life analysis. Linear elastic theory is inadequate for analysing pipes with locked-in residual stresses for an elasto-plastic material with work-hardening.

2.6.1 FE analysis using shell elements

Ohtani et al [8] proposed the use of curved quadrilateral shell elements to investigate the strain concentrations in an imperfect thin spherical shell. They found that a higher strain concentration was induced by the bending strain which is proportional to the amplitude of the imperfection. As expected, the peak value of the strain concentration occurs at the centre of the imperfection.

Ong et al [24] analysed the residual stress distributions in local indented pressurised pipes using experimental measurements and FE solutions using 8-node shell elements. Their work indicated that the maximum value of residual strain is at the flank of the indentation when the flaws are of a local nature rather than being long indentations. Otherwise, the peak value of residual strain is at the damage centre for a long indentation.

To estimate the residual life of indented damaged pipes, Zarea et al [10] proposed the use of static and dynamic FE models, using thin triangular shell elements for static analysis and quadrangular shell elements for dynamic analysis. Through this work, Zarea et al [10] established the relationships between dent depth and force, dent depth and residual dent depth, and calculated the residual stress distribution under cyclic pressure variation, in order to analyse the residual fatigue life. However, the paper by Zarea et al [10] did not give empirical analytical formulae derived from the FE calculations. Powell et al [11] also used the FE method to analyse the fatigue damage of indented pipes. However, unlike Zarea et al [10], they used 8-node shell elements to undertake all the computations. In the dynamic model, Zarea et al [10] simulated complete failure processes from void nucleation to the crack development.

2.6.2 FE analysis using three-dimensional (brick) solid elements

3-D solid brick elements have been used by many researchers to assess the integrity of pipes with a gouge in a dent. Solid brick elements are more accurate and more convenient than shell elements for modelling the gouges and cracks, but the computing costs are significantly higher. Because it is difficult to obtain analytical expressions for the stress intensity factor at the tips of cracks, many researchers have been successful in estimating SIF by using FE calculations using solid brick elements. Newman et al [33], Raju et al [35], Zheng et al [36], and Koh et al [34] obtained semi-empirical expressions for cylinders with different sizes of cracks using this method. Zarrabi [37] calculated the plastic collapse pressure for cylindrical vessels with defects using solid brick element models.

2.7 Fatigue theories for the analysis of the fatigue damage of pipes

A number of fatigue theories have been reviewed by Fatemi et al [1]. The most generally accepted approaches are the stress-life approaches, strain-life approaches and K-life approaches.

2.7.1 Stress-life approaches

For zero mean stress cycles, based on uniaxial tensile-compressive tests, Basquin proposed that the cyclic fatigue life relates to cyclic stress amplitude as follows (see, for example Suresh [38]):

$$\frac{\Delta\sigma}{2} = \sigma_a = \sigma_f'(2N_f)^b \tag{2.68}$$

where $\sigma_a (= (\sigma_{max} - \sigma_{min})/2)$ is cyclic stress amplitude, σ_f' is a fatigue strength coefficient (which , for most metals, can be represented to a good approximation, by the true fracture strength σ_f, corrected for necking, in a monotonic tension test) and b is called Basquin's exponent.

For a non-zero mean stress, the cyclic stress amplitude is generally defined in the same way as that for zero mean stress. However, in order to fit experimental results the cyclic stress amplitude used in equation (2.68) sometimes are modified, for example, Suresh [38] reviewed Gerber, Goodman, and Soderberg's models which are expressed as follows:

a. Soderberg expression:

$$\sigma_a = \left\{1 - \frac{\sigma_m}{\sigma_y}\right\}\sigma_{a0} \tag{2.69}$$

where σ_{a0} refers to the cyclic stress amplitude obtained with zero mean stress.

b. Modified Goodman expression:

$$\sigma_a = \left\{1 - \frac{\sigma_m}{\sigma_{UTS}}\right\}\sigma_{a0} \tag{2.70}$$

c. Gerber expression:

$$\sigma_a = \left\{1 - \left(\frac{\sigma_m}{\sigma_{UTS}}\right)^2\right\}\sigma_{a0} \tag{2.71}$$

where σ_y and σ_{UTS} are the material yield stress and ultimate tensile strength, respectively

While the Basquin relation is valid only for zero mean stress, Suresh [38] also reviewed Morrow relation which is a modification of Basquin relation and accounts for mean stress effects (for any σ_m), in the following form

$$\sigma_a = (\sigma'_f - \sigma_m)(2N_f)^b \tag{2.72}$$

For a multiaxial stress situation, Suresh [38] described the stress-life relationship in terms of an equivalent stress amplitude and an equivalent mean stress, defined as follows

$$\sigma_{a,e} = \frac{1}{\sqrt{2}}\sqrt{(\sigma_{1a} - \sigma_{2a})^2 + (\sigma_{1a} - \sigma_{3a})^2 + (\sigma_{2a} - \sigma_{3a})^2} \tag{2.73}$$

$$\sigma_{m,e} = \frac{1}{\sqrt{2}}\sqrt{(\sigma_{1m} - \sigma_{2m})^2 + (\sigma_{1m} - \sigma_{3m})^2 + (\sigma_{2m} - \sigma_{3m})^2} \tag{2.74}$$

where $(\sigma_{1a}, \sigma_{2a}, \sigma_{3a})$ and $(\sigma_{1m}, \sigma_{2m}, \sigma_{3m})$ are the amplitudes of the principal stresses and mean values of the principal stresses, respectively.

2.7.2 Strain-life approach

Suresh [38] reviewed the Coffin and Manson strain-life approach which was developed through their independently obtained experimental observations. The relationship is nearly satisfied:

$$\frac{\Delta\varepsilon_p}{2} = \varepsilon'_f (2N_f)^c \tag{2.75}$$

where $\Delta\varepsilon_p, \varepsilon'_f$ are the plastic strain amplitude and fatigue ductility coefficient, respectively, and c is the fatigue ductility exponent.

The total strain amplitude, in a constant strain amplitude situation, can be written as the sum of an elastic strain amplitude and a plastic strain amplitude, i.e.

$$\frac{\Delta\varepsilon}{2} = \frac{\Delta\varepsilon_e}{2} + \frac{\Delta\varepsilon_p}{2} \tag{2.76}$$

Using Basquin equation and linear elastic theory, gives:

$$\frac{\Delta\varepsilon_e}{2} = \frac{\sigma'_f}{E}(2N_f)^b \tag{2.77}$$

Combining the Coffin-Manson relationship and the above equation, results in:

$$\frac{\Delta\varepsilon}{2} = \frac{\sigma_f'}{E}(2N_f)^b + \varepsilon_f'(2N_f)^c \tag{2.78}$$

For multiaxial situations, as in the stress-based life approaches, the strain-life is expressed in terms of the amplitude of equivalent strain as follows:

$$\frac{\Delta\varepsilon_{eq}}{2} = \frac{\sigma_f'}{E}(2N_f)^b + \varepsilon_f'(2N_f)^c$$
$$\varepsilon_{eq} = \frac{\sqrt{(\varepsilon_1-\varepsilon_2)^2+(\varepsilon_1-\varepsilon_3)^2+(\varepsilon_2-\varepsilon_3)^2}}{\sqrt{2}(1+\upsilon)} \tag{2.79}$$

where for the fully plastic state, Poisson's ratio, υ=0.5, and for the elastic state, υ=0.33 for most metals and alloys, and $(\varepsilon_1,\varepsilon_2,\varepsilon_3)$ are the components of principal strains.

2.7.3 K factor-life approach

To estimate the fatigue life of cylinders with cracks, Paris and Erdogan [39] suggested a relationship between crack length and the number of cycles, as follows:

$$\frac{da}{dN} = C(\Delta K)^n \tag{2.80}$$

where

ΔK = Stress-intensity factor range

a = crack length

N= number of fatigue cycles

C= material constant

n= material constant (a value of 4 is given in [39])

The above equation has been shown to be in good agreement with experimental data when the SIF range is relatively small. However, if a larger range of ΔK is used, the fatigue life calculated by the Paris-Erdogan relationship does not give accurate correlation with test data. For this reason, Forman et al [40] proposed the modified formulation:

$$\frac{da}{dN} = \frac{C(\Delta K)^n}{(1-R)K_c - \Delta K} \tag{2.81}$$

where

R= load ratio

K_c= critical stress-intensity factor for fracture.

2.8 Summary

Summarising previous work, it is found that many empirical formulae to predict the limit loads of the internal pressure and external force have been developed. It is also found that the linear analysis methods, e.g. perturbation and equivalent load methods, which require a lot of numerical calculations, cannot accurately predict the non-linear behaviour of indented pipes. Responses of the residual stresses and stress variations of indented pipes to the material properties, the geometrical dimensions (of pipes and indenters), the internal pressure and the residual dent depth were not investigated and are unknown. No empirical formulae were developed to predict residual stresses and stress variations and no analytical solutions were obtained to predict the non-linear elastic-plastic behaviours of indented pipes. Therefore, this thesis will attempt to investigate those stresses using experiments, FE analysis and energy-based elastic-plastic methods.

Chapter 3

Elastic-Plastic Response of Unpressurised Indented Pipes

3.1 Introduction

Most impact damage to pipelines is very localised [1-4, 16, 17], as indicated in Fig. 1.1 (a). However, in some cases, the damage can extend over a significant length of the pipe [12], as indicated in Fig. 1.1(b). In the latter case, the behaviour (except at the ends of the damage) is essentially two-dimensional and can be analysed as a plane-strain ring, as indicated in Fig. 1.1(c).

Indentation damage can occur with or without internal pressure and the deformations and residual stresses are affected by the magnitude of the internal pressure when the damage occurs. With suitable FE software [26] the deformations and residual stresses due to impact can be obtained. However, these solutions may be time consuming and expensive. For rings, simple analysis methods can be used as an alternative. For example, Castiglano's theorem can be used to determine elastic deformations, and the upper bound methods can be used to determine limit loads. In this chapter, the accuracy of these methods will be assessed by comparing predictions obtained from analytical solutions with experimental data and with detailed FE analysis.

3.2 Experimental Work

3.2.1 Material

The material chosen for the experimental investigation is 6082-T6 aluminium alloy. The tensile stress-strain curve for the material is shown in Fig. 3.1; Young's modulus, Poisson's ratio, yield stress and ultimate tensile stress are 70 GPa, 0.3, 300 MPa and 351 MPa, respectively. Fig. 3.1 also shows the stress-strain curve for a practical gas pipeline material, namely X65 SAW, which has a Young's modulus, Poisson's ratio, yield stress and ultimate tensile stress of 223GPa, 0.3, 448MPa and 675MPa, respectively. These material properties were also used in some of the FE analyses.

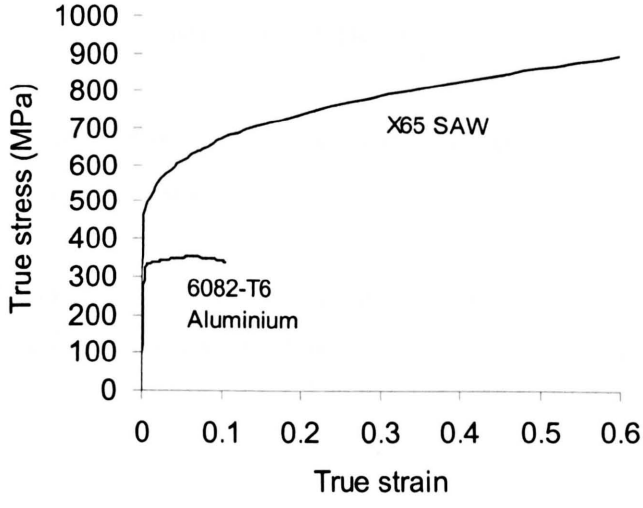

Fig. 3.1 True stress-strain curves of 6082-T6 aluminium alloy and X65 SAW pipe steel.

3.2.2 Geometry and Loading

For the experimental tests, 6082-T6 aluminium alloy rings were set on a V-block support cast with plaster to form the arc supporting bed as shown in Fig.3.2. The support conditions were essentially an arc support which was very close to a three point support situation. The support angle, θ, is shown in Fig. 3.2. The rings were radially loaded at point A (see Fig.3.3) by a Bright Drawn Mild Steel indenter with an end radius of 2 mm and an axial length of 50mm.

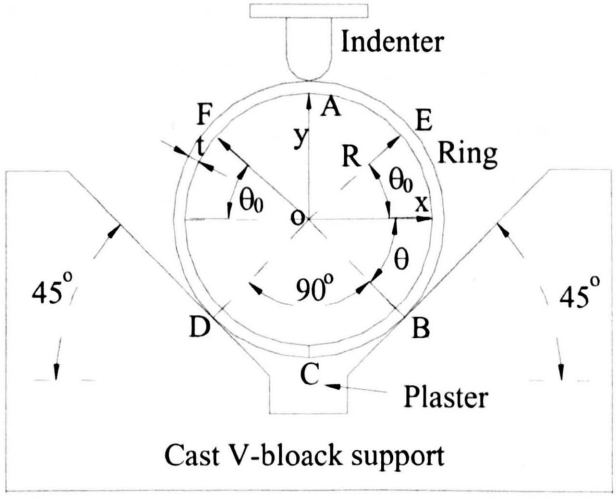

Fig. 3.3 Dented ring set on a v-block support for experimental tests

The tests were conducted on an Instron 1195 machine with 1 kN and 50 kN load cells, and the data (force and displacement) were recorded automatically; the load point displacement rate was set to 2mm/min.

Tests were performed on eight rings with dimensions, peak loads and initial gradients of force versus displacement curves given in Table 3.1.

Table 3.1 Geometries and experimental results of dented rings

Test No	Support Angle θ	**Geometry of 6082-T6 aluminium alloy rings used in tests** Outer diameter D; Wall thickness t; Axial length L					
		D (mm)	t (mm)	D/t	L (mm)	Limit load N/mm	Initial gradient $N/(mm)^2$
TE1	45°	88.8	1.2	72.0	40	14.6	2.33
TE2	45°	88.8	1.2	72.0	40	14.0	2.31
TE3	45°	88.8	1.2	72.0	40	13.5	2.25
TE4	45°	125	3	41.6	50	66.0	11.36
TE5	45°	125	3	41.6	50	61.0	10.28
TE6	45°	92.4	3	30.8	50	86.0	23.07
TE7	45°	92.4	3	30.8	50	88.7	24.09
TE8	45°	120	5	24	50	204	61.42

The peak loads (or limit loads) were obtained from the force (per unit length of the pipe) versus dent depth curves of the experimental data; initial gradients were obtained from the initial linear parts of the force versus dent depth curves obtained from experiments.

3.2.3 Results of the Ring Tests

A series of eight experimental indentation tests, of rings with a range of geometrical dimensions were performed; they were supported in a 90^0 V-block as shown in Fig.3.2. The indenter force versus depth curves obtained from the experiments are shown in Fig. 3.3.

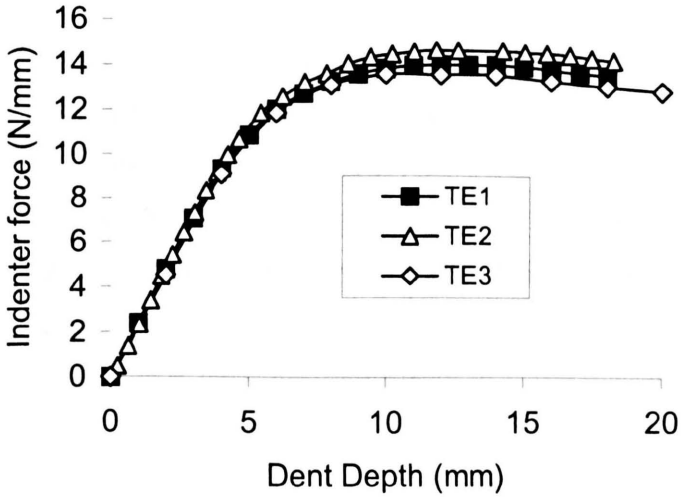

Fig.3.3 (a)

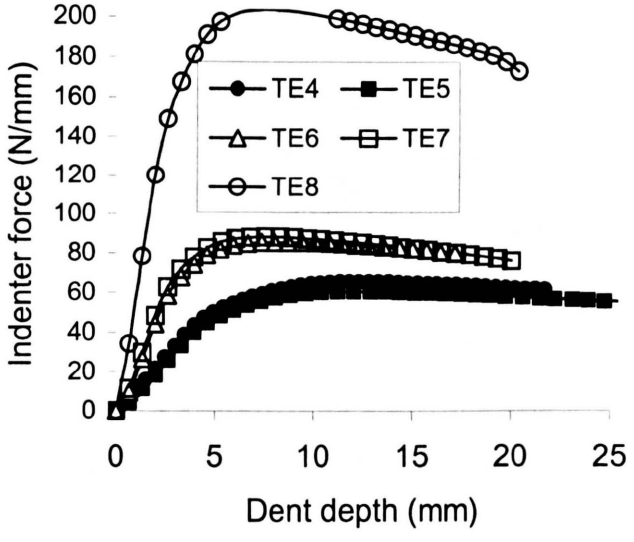

Fig. 3.3 (b)

Fig. 3.3 Indenter force versus depth curves obtained from experiments performed on the 6082-T6 aluminium alloy rings.

3.3. FE Analysis

3.3.1 Material

Six materials were used in the FE analyses. Results were obtained for the aluminium alloy (6082-T6) for comparison with the experimental results. Since practical pipelines are usually made from a variety of steels, FE analyses were performed using material data for one of these steels, namely X65 SAW. Four idealised materials (i.e. Ideal-A, B, C and D) with elastic, perfectly plastic material properties were also used to investigate the influence of material properties on the collapse load. Of the latter four idealised materials, three (Ideal-B, C and D) were chosen to have a Young's modulus of 223 GPa and yield stresses of 300 MPa, 448 MPa and 600MPa, respectively and the fourth, Ideal-A, has a Young's modulus of 70GPa and yield stress of 300MPa, i.e., the same yield stress as material Ideal-B but a different Young's modulus. The basic properties of these six materials are given in Table 3.2. In the FE analyses, all materials were assumed to obey an isotropic rule.

Table 3.2 Material properties used in FE analyses.

Material	E	σ_Y	σ_{UTS}	Poisson's ratio
6082-T6 alloy	70 GPa	300 MPa	351 MPa	0.3
X65 SAW	223 GPa	448 MPa	675 MPa	0.3
Ideal-A	70GPa	300 MPa	-	0.3
Ideal-B	223 GPa	300 MPa	-	0.3
Ideal-C	223 GPa	448 MPa	-	0.3
Ideal-D	223 GPa	600 MPa	-	0.3

3.3.2 FE Meshes, Boundary Conditions and Loading

The ABAQUS [26] FE software was used for the analyses. Due to symmetry, only one half of the rings were modelled. All models consisted of 675 8-noded, plane-strain, reduced integration elements, as shown in Fig. 3.4. Mesh convergence was checked for some of the cases by using four times as many elements and it was found that peak loads were the same to within 0.5% (compared with the 675 element results, see FE7 to FE10 in Table 3.3) in all cases. The nodes on the rings at sections A and C (Fig.3.4(a)) were restrained (i.e. $u_{xA}=u_{xC}=0$) in the circumferential direction for all analyses. In some of analyses the rings were fully restrained (i.e.$u_{xB}=u_{yB}=0$) at the outer diameter at position B, which is referred as boundary condition 1 or BC1 (see Fig.3.4(c)). In some of the analyses, the rings were restrained only in the vertical direction (i.e.$u_{yB}=0$) at the outer diameter at position B, which is referred as boundary condition 2

or BC2 (see Fig.3.4(d)). The load was applied in the radially inwards direction at the outer diameter position at point A. In total 62 analyses were performed, these are defined in Tables 3.3 to 3.8.

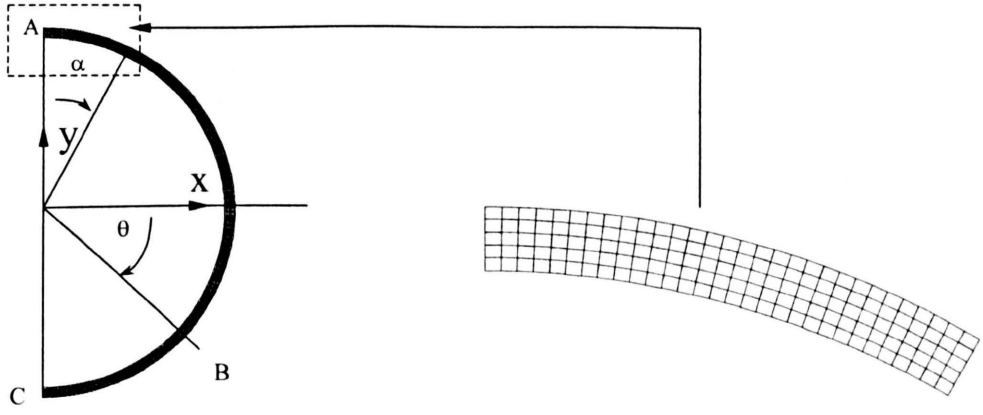

(a) FE meshes of half a ring (b) Locally amplified meshes

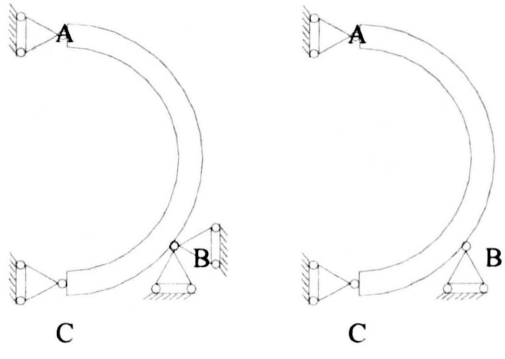

(c) Boundary condition 1 (BC1) (d) Boundary condition 2 (BC2)

Fig. 3.4 FE meshes and boundary conditions for the indented ring analyses.

Table 3.3 Geometrical dimensions, boundary conditions and FE results for 6082-T6 aluminium alloy rings

FE No.	**Ring Dimension** Outer diameter D (mm) Thickness t (mm)			Supported Angle θ	Boundary Condition	Limit Load N/mm	Initial Gradient N/(mm)^2	Number of Elements
	D	t	D/t					
FE1	88.8	1.2	72	45°	BC1	14.2	2.22	675
FE2	88.8	1.2	72	45°	BC2	12.3	1.53	675
FE3	125	3.0	41.6	45°	BC1	69.4	12.39	675
FE4	125	3.0	41.6	45°	BC2	62.0	9.69	675
FE5	92.4	3.0	30.8	45°	BC1	99.7	32.80	675
FE6	92.4	3.0	30.8	45°	BC2	90.0	23.85	675
FE7	120	5.0	24	45°	BC1	223	67.97	675
FE8	120	5.0	24	45°	BC2	203	56.79	675
FE9	120	5.0	24	45°	BC1	222	69.71	2700
FE10	120	5.0	24	45°	BC2	203	55.40	2700

Table 3.4 Geometrical dimensions, boundary conditions and FE results for X65 SAW pipeline steel rings.

FE No.	**Ring Dimension** Outer diameter D (mm) Thickness t (mm)			Supported Angle θ	Boundary Condition	Limit Load N/mm	Initial Gradient N/(mm)^2	Number of Elements
	D	t	D/t					
FE11	88.8	1.2	72	45°	BC1	24.2	7.34	675
FE12	128	3.0	42.6	45°	BC1	115	38.76	675
FE13	92.4	3.0	30.8	45°	BC1	169	107.28	675
FE14	88.8	1.2	72	0°	BC1	36.4	**	675
FE15	128	3.0	42.6	0°	BC1	180	**	675
FE16	92.4	3.0	30.8	0°	BC1	267	**	675
FE17	88.8	1.2	72	90°	BC1	17.3	**	675
FE18	128	3.0	42.6	90°	BC1	81.7	**	675
FE19	92.4	3.0	30.8	90°	BC1	119	**	675

** Not used

Table 3.5 Geometrical dimensions, boundary conditions and FE results for idealised elastic perfectly plastic material Ideal-A (σ_y=300MPa and E=70GPa).

FE No.	**Ring Dimension** Outer diameter D (mm) Thickness t (mm)			Support Angle θ	Boundary Condition	Limit Load N/mm	Initial Gradient N/(mm)^2	Number of Elements
	D	t	D/t					
FE20	88.8	1.2	72	-60°	BC1	54.0	206.56	675
FE21	88.8	1.2	72	-45°	BC1	36.5	68.68	675
FE22	88.8	1.2	72	-22.5°	BC1	24.0	19.64	675
FE23	88.8	1.2	72	0°	BC1	18.2	7.85	675
FE24	88.8	1.2	72	22.5°	BC1	14.9	4.08	675
FE25	88.8	1.2	72	45°	BC1	12.6	2.20	675
FE26	88.8	1.2	72	70°	BC1	10.3	1.22	675
FE27	88.8	1.2	72	90°	BC1	9.3	0.86	675
FE28	128	3.0	42.6	-45°	BC1	184	366.67	675
FE29	128	3.0	42.6	-22.5°	BC1	123	114.27	675
FE30	128	3.0	42.6	0°	BC1	92.0	47.15	675
FE31	128	3.0	42.6	22.5°	BC1	74.0	23.17	675
FE32	128	3.0	42.6	45°	BC1	61.3	12.18	675
FE33	128	3.0	42.6	70°	BC1	48.8	6.50	675
FE34	128	3.0	42.6	90°	BC1	43.4	4.71	675
FE35	92.4	3.0	30.8	-45°	BC1	263	824.04	675
FE36	92.4	3.0	30.8	-22.5°	BC1	185	313.45	675
FE37	92.4	3.0	30.8	0°	BC1	138	125.77	675
FE38	92.4	3.0	30.8	22.5°	BC1	110	62.86	675
FE39	92.4	3.0	30.8	45°	BC1	90.0	32.48	675
FE40	92.4	3.0	30.8	70°	BC1	72.0	17.69	675
FE41	92.4	3.0	30.8	90°	BC1	63.0	12.57	675
FE42	88.8	1.2	72	45°	BC2	11.3	**	675
FE43	128	3.0	42.6	45°	BC2	55	**	675
FE44	92.4	3.0	30.8	45°	BC2	81.5	**	675

** Not used

Table 3.6 Geometrical dimensions, boundary conditions and FE results for idealised elastic perfectly plastic material Ideal-B (σ_y=300MPa and E=223GPa).

FE No.	**Ring Dimension** Outer diameter D(mm) Thickness t (mm)			Supported Angle θ	Boundary Condition	Limit Load N/mm	Initial Gradient N/(mm)^2	Number of Elements
	D	t	D/t					
FE45	88.8	1.2	72	45°	BC1	15.2	7.54	675
FE46	128	3.0	42.6	45°	BC1	69.7	38.63	675
FE47	92.4	3.0	30.8	45°	BC1	101	107.16	675
FE48	88.8	1.2	72	45°	BC2	13.6	**	675
FE49	128	3.0	42.6	45°	BC2	63.6	**	675
FE50	92.4	3.0	30.8	45°	BC2	92.3	**	675

** Not used

Table 3.7 Geometrical dimensions, boundary conditions and FE results for idealised elastic perfectly plastic material Ideal-C (σ_y=448MPa and E=223GPa).

FE No.	**Ring Dimension** Mean Radius R (mm) Thickness t (mm)			Supported Angle θ	Boundary Condition	Limit Load N/mm	Initial Gradient N/(mm)^2	Number of Elements
	R	t	D/t					
FE51	88.8	1.2	72	45°	BC1	21.7	7.54	675
FE52	128	3.0	42.6	45°	BC1	101	38.63	675
FE53	92.4	3.0	30.8	45°	BC1	146	107.16	675
FE54	88.8	1.2	72	45°	BC2	19.2	**	675
FE55	128	3.0	42.6	45°	BC2	91.1	**	675
FE56	92.4	3.0	30.8	45°	BC2	133	**	675

** Not used

Table 3.8 Geometrical dimensions, boundary conditions and FE results for idealised elastic perfectly plastic material Ideal-D (σ_y=600MPa and E=223GPa).

FE No.	**Ring Dimension** Outer diameter D (mm) Thickness t (mm)			Supported Angle θ	Boundary Condition	Limit Load N/mm	Initial Gradient N/(mm)^2	Number of Elements
	R	t	D/t					
FE57	88.8	1.2	72	45°	BC1	28.0	7.54	675
FE58	128	3.0	42.6	45°	BC1	131	38.63	675
FE59	92.4	3.0	30.8	45°	BC1	191	107.16	675
FE60	88.8	1.2	72	45°	BC2	24.6	**	675
FE61	128	3.0	42.6	45°	BC2	118	**	675
FE62	92.4	3.0	30.8	45°	BC2	173	**	675

** Not used

The loads were applied using a rigid indenter with a 2mm radius and rigid surface contact elements. Large deformation, elastic-plastic analyses were performed using the standard arc-length (Riks) algorithm facility within the ABAQUS [26] program.

3.3.3 FE Results

3.3.3.1 Idealised Elastic Perfectly Plastic Materials

Four idealised elastic perfectly plastic materials (Ideal-A, B, C and D) were chosen to investigate the effects of the Young's modulus and yield stress on the limit loads, using FE analysis, for three geometries (D/t=72, 42.6, 30.8). The results were also used to investigate the effects of the support angular positions on peak loads, which can be obtained from the maximum

points of the force versus dent depth curves from the FE analyses. The results obtained from each of the FE analyses are shown in Tables 3.5 to 3.8. Typical indenter force versus depth curves, obtained from FE32, 46, 52 and 58 for D/t=42.6, are shown in Fig.3.5.

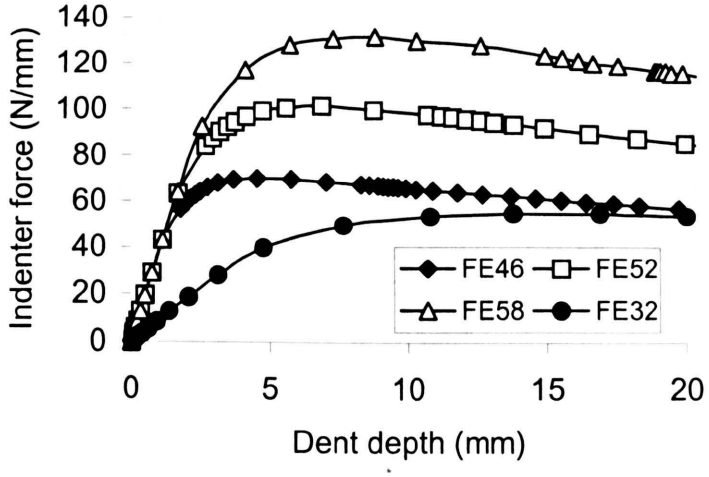

Fig.3.5 Typical indenter force versus depth curves obtained from idealised materials: Ideal-A, B, C and D for a ring with a diameter of 128 mm and a wall thickness of 3mm.

Fig.3.6 shows the initial gradients for D/t ratios of 72, 42.6 and 30.8 which have been multiplied by 10^4 and then been normalised by dividing them by their Young's moduli of 70GPa and 223GPa. It can be seen that normalised initial gradients for these materials are consistent.

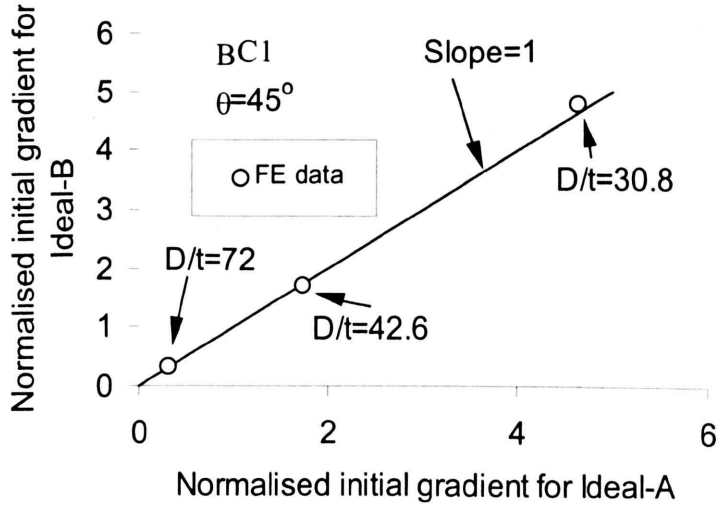

Fig.3.6 Normalised initial gradients for idealised materials of Ideal-A and B

For the Ideal-A material, the initial gradients, G, shown in Table 3.5 obtained from the FE analyses can be conveniently normalised by dividing by Et^3/R^3. The subsequent normalised initial flexibility $(1/G), K(\theta)$, is shown in Fig. 3.7 from which it can be seen that the initial gradients, G, of the force versus dent depth curves decrease with increasing of support angles.

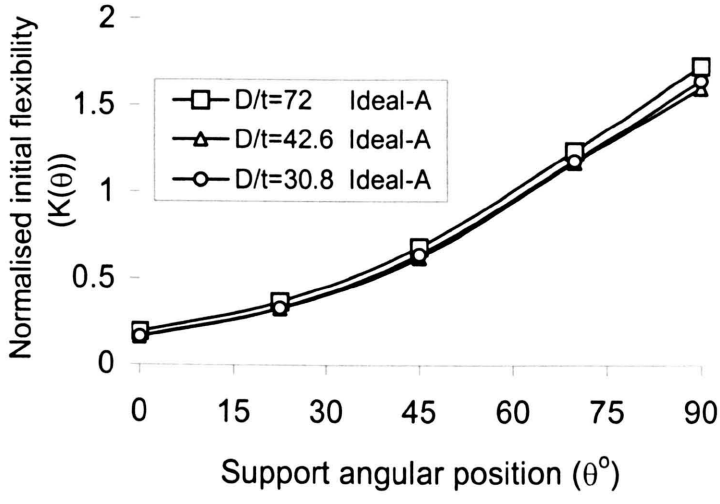

Fig.3.7 Normalised initial flexibility of indenter force versus dent depth curves for different angular support positions and different ratios of D/t of 72, 42.6 and 30.8 for idealised material Ideal-A

The peak loads for FE25, FE32, FE39, FE45 to FE47, FE51 to FE53 and FE57 to FE59 shown in Tables 3.5 to 3.8 were obtained with boundary condition 1 and the angular support position of 45°. The peak loads were normalised by dividing by the associated yield stresses; a comparison of some of these results is shown in Fig.3.8. It can be seen that these normalised peak loads are in good agreement with each other (differences are less than 5%).

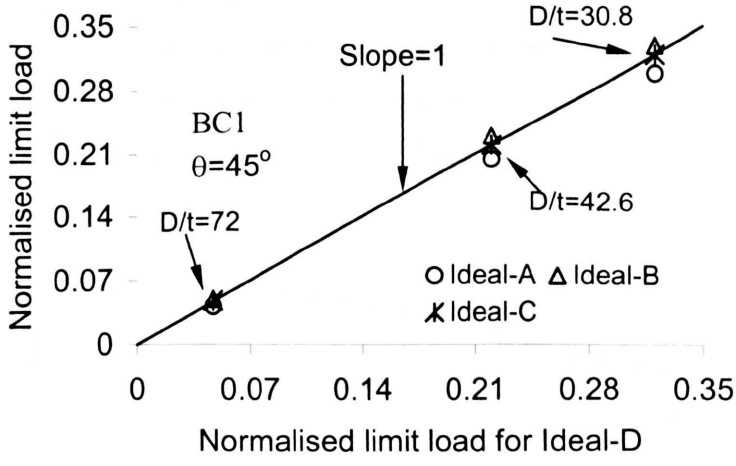

Fig.3.8 Normalised peak loads for idealised materials of Ideal-A, B, C and D

The peak load for material Ideal-A with different angular support positions are given in Table 3.5 and these are shown in Fig. 3.9 (see FE20 to FE41), from which it can be seen that the peak loads decrease as the support angle is increased.

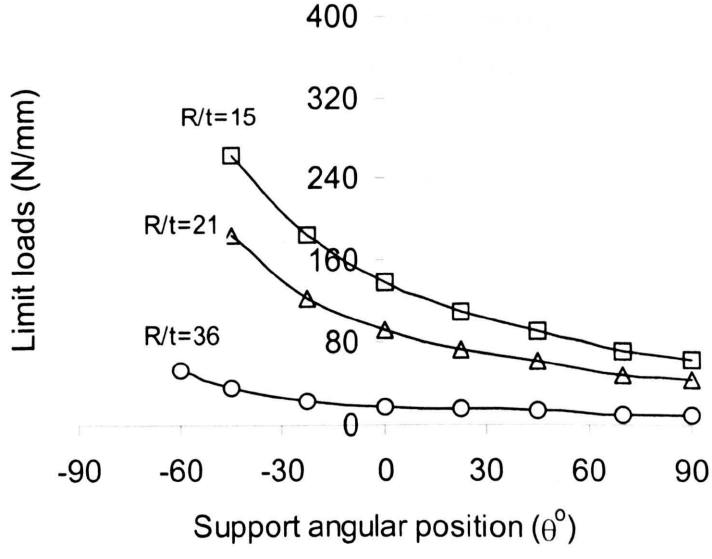

Fig.3.9 Peak loads for different angular support positions and different D/t ratios.

3.3.3.2 6082-T6 Aluminium Alloy

Typical indenter force versus depth curves, obtained from the FE1, FE3 and FE5 analyses performed on the aluminium alloy models, are shown in Fig.3.10. The initial gradients and peak loads obtained from FE1 to FE10 are given in Table 3.3.

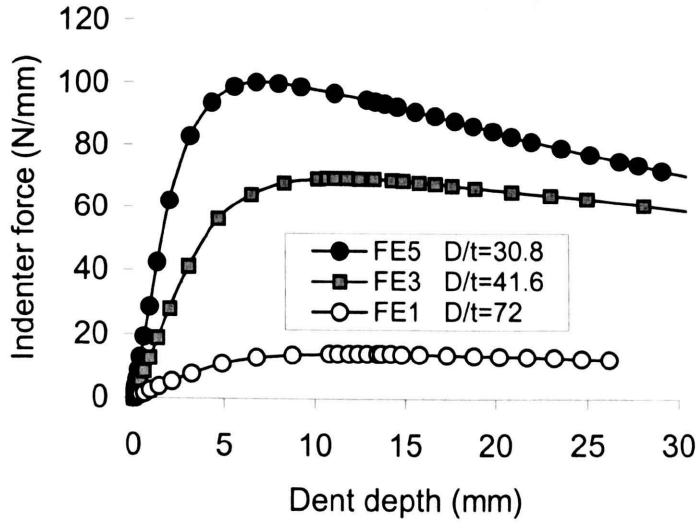

Fig. 3.10 Typical indenter force versus depth curves obtained from FE analyses for 6082-T6 aluminium alloy rings

From Table 3.3 it can be seen that the indenter forces obtained when all movements at point B and D are constrained (boundary condition 1) are higher than those obtained by constraining only the vertical movements at points B and D (boundary condition 2). FE7 to FE10 indicate that peak loads obtained from the FE models with 675 reduced integration, 8-nodes, quadratic, plane-strain elements are very close to those obtained with 2700 elements.

The initial gradients (see FE1 to FE8) obtained for boundary conditions 1 and 2, are plotted against each other in Fig. 3.11. It can be seen that the initial gradients obtained using boundary condition 1 are, in general, about 24% higher than those obtained by using boundary condition 2.

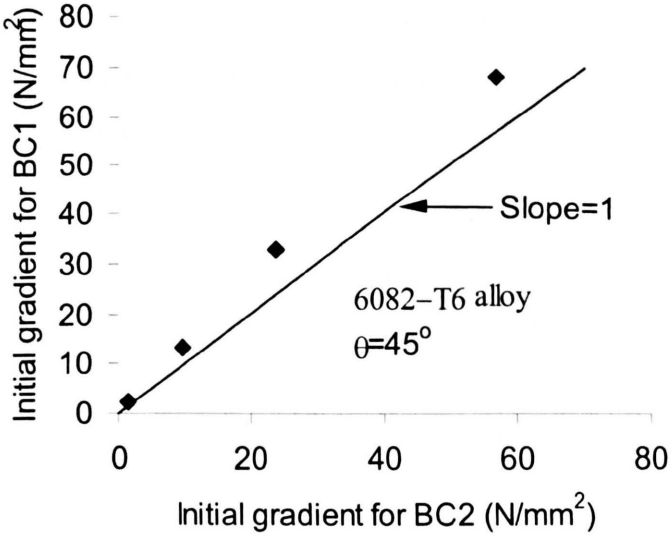

Fig. 3.11 Comparisons of initial gradients obtained by using boundary conditions 1 and 2 for 6082-T6 aluminium alloy rings.

3.3.3.3 X65 SAW Steel

Typical indenter force versus dent depth curves obtained from the FE11 to FE13 FE analyses, performed on the X65 SAW steel models, are shown in Fig. 3.12. The peak loads are given in Table 3.4.

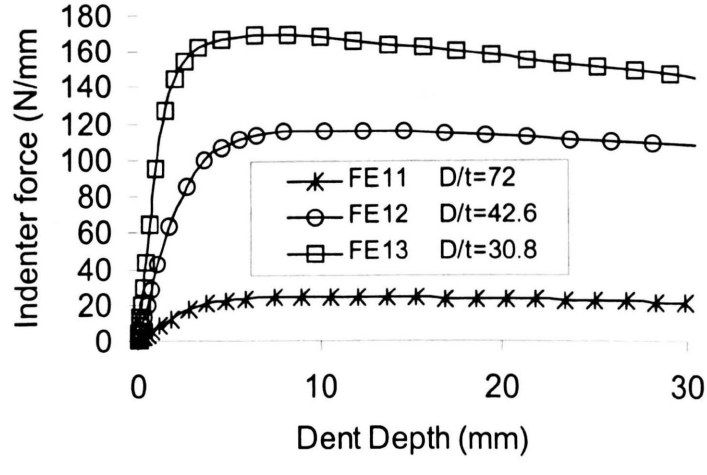

Fig. 3.12 Typical indenter force versus depth curves obtained from FE analyses for X65 SAW steel rings

The normalised initial gradients for the FE1, FE3, FE5 and FE11 to FE13 FE analyses, given in Tables 3.3 and 3.4 for the 6082-T6 aluminium alloy and the X65 SAW steel are shown in Fig. 3.13. In this figure all of the gradients are amplified by 10^4. It can be seen from this figure that there is good agreement.

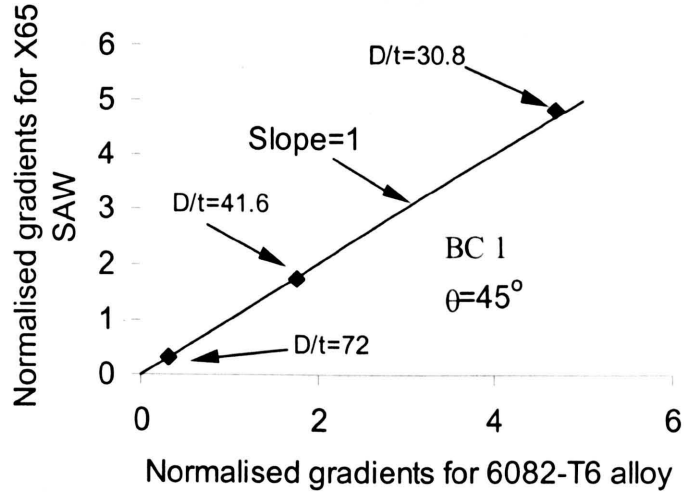

Fig. 3.13 Normalised initial gradients for 6082-T6 aluminium alloy and X65 SAW

The peak loads obtained from the FE1, FE3, FE5, FE11, FE12 and FE13 analyses have been normalised with respect to the appropriate yield, flow and ultimate tensile stresses. The representative flow stress, σ_f, is defined as the average of the yield and ultimate stresses, i.e. $\sigma_f = (\sigma_y + \sigma_{UTS})/2$. The normalised peak loads for the X65 SAW material are plotted against the corresponding results obtained for the 6082-T6 aluminium alloy material in Fig.3.14. It can be seen that the best correlation is obtained using the representative flow stress.

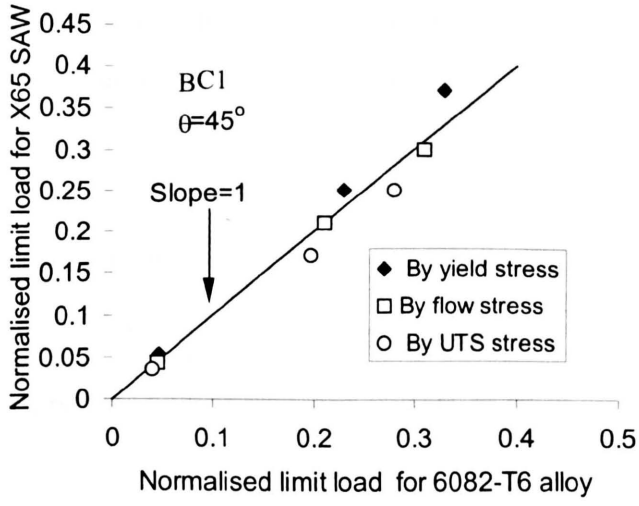

Fig.3.14 A comparison of normalised peak limit loads for 6082-T6 aluminium alloy and X65 SAW

3.4 Analytical Methods

3.4.1 Elastic Strain Energy Solution

For the elastic response of the ring, Castiglano's theorem [41] can be used, i.e.

$$\delta = \frac{\partial U}{\partial F} \tag{3.1}$$

where δ is the displacement due to and in the direction of the load F and U is the complementary strain energy in the structure.

Considering the ring as a thin curved beam, the strain energy can be determined from the bending moment, M, distribution.

$$U = \frac{1}{2EI}\int M^2 ds \tag{3.2}.$$

Taking the angle α to be measured from point A (see Fig.3.4 (a)), the bending moment at angular position, α, is given by

$$M(\alpha) = M_A - N_A R(1-\cos\alpha) - \frac{F}{2} R \sin\alpha \tag{3.3}$$

where M_A and N_A are the unknown moment and circumferential force at section A. It is assumed that the beam is built in at position B, as indicated in Fig.3.2 and there is no internal pressure, hence

$$U = \frac{12}{Et^3}\int_0^{\frac{\pi}{2}+\theta} RM(\alpha)^2 d\alpha \tag{3.4}$$

Therefore using equation (3.1) gives

$$\delta = \frac{12R^3}{Et^3}\left(A + \frac{B+C}{D}\right)F = \frac{R^3}{Et^3}K(\theta)F \tag{3.5}$$

where A, B, C and D are functions only of the support angle, θ, i.e.,

$$\left.\begin{aligned} A &= \frac{1}{4}\left(\frac{\pi}{2}+\theta+\frac{1}{2}\sin 2\theta\right) \\ B &= (1+\sin\theta)\left[\frac{3}{2}\sin 2\theta + 3\cos\theta - \left(\frac{\pi}{2}+\theta\right)\left(\cos^2\theta+\sin\theta+1\right)\right] \\ C &= \cos\theta\left(\frac{1}{2}+\frac{1}{2}\sin^2\theta+\sin\theta\right)\left[\left(\frac{\pi}{2}+\theta\right)\cos\theta - 2\sin\theta - 2\right] \\ D &= 2\left(\left(\frac{\pi}{2}+\theta\right)^2 - 2\cos^2\theta - \frac{1}{2}\left(\frac{\pi}{2}+\theta\right)\sin 2\theta\right) \end{aligned}\right\} \tag{3.6}$$

Normalised initial flexibility, $K(\theta)$, of the force-displacement curves obtained from the FE method for the material Ideal-A are compared with those obtained using equation (3.5) in Fig.3.15. It can be seen that the normalised initial flexibility obtained using equation (3.5) and obtained from the FE analyses are very close in all cases. This figure clearly shows that equation. (3.5) is capable of accurately predicting the initial gradients.

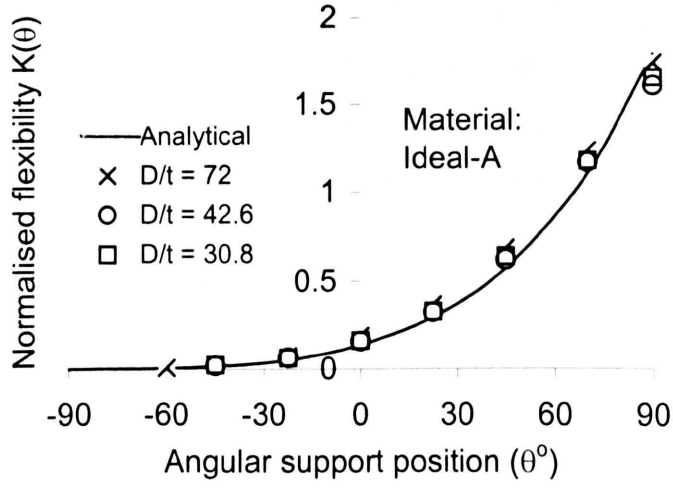

Fig.3.15. Normalised initial flexibility obtained from the FE and analytical solutions for different support angular positions.

3.4.2 Limit Loads

Upper bound theorems exist for determining limit loads [42, 43]. The upper bound method is based upon the use of a kinematically admissible velocity field in which, if all boundary conditions are satisfied, the loads determined by equating the rate at which the external forces do work to the rate of internal energy dissipation will be either higher than or equal to the actual limit load.

To calculate the limit load for the dented ring shown in Fig.3.2, the indenter force is assumed to be a concentrated force (denoted by F). It is assumed that there are five plastic hinges at A, B, D, E and F, which can form an admissible velocity field and that arcs of the ring between the hinges are rigid (see p.98). Based on the compatibility of the assumed kinematic velocity field, the relationship of the angular rotations at those five plastic hinges and the displacement of hinge A, for small deformation, is given by

$$\delta = \frac{\cos\theta_0 - \cos\theta + \sin(\theta_0 + \theta)}{1 - \sin\theta_0} R\alpha_1 \tag{3.7}$$

$$\alpha_2 = \frac{1 + \sin\theta}{1 - \sin\theta_0}\alpha_1 \tag{3.8}$$

$$\alpha_3 = \alpha_2 - \alpha_1 \tag{3.9}$$

where θ_0 (see Fig.3.2) is the angular position of the plastic hinges of E and F, and α_2 is the relative rotation of arcs AE and EB or of arcs AF and FD. The displacement and rotation of hinge A are δ and $2\alpha_3$, respectively, and α_1 is the rotational angle of hinges B and D. The upper bound can be optimised by allowing θ_0 to be a variable. The value of θ_0 which minimises the upper bound load is the optimised value of θ_0. The limit moment M_0 at the hinges is given by

$$M_0 = \frac{1}{4}\sigma_y t^2 \tag{3.10}.$$

The internal energy dissipated, W_I, and the work, W_E, done by the external force F, are given by

$$W_I = 2(M_0\alpha_1 + M_0\alpha_2 + M_0\alpha_3) = 4M_0\alpha_2 = 4M_0\frac{1 + \sin\theta}{1 - \sin\theta_0}\alpha_1 \tag{3.11}$$

and

$$W_E = F\delta \tag{3.12}.$$

By employing the virtual work principle and minimising the external force F with respect to θ_0, the optimised upper bound is given by

$$F_U = L(\theta)\frac{4M_0}{R} \tag{3.13}$$

where $L(\theta)$ is given by

$$L(\theta) = \frac{(1+\sin\theta)}{(2\sin(\frac{\pi}{4}+\frac{1}{2}\theta)-\cos\theta)} \tag{3.14}.$$

The non-dimensional function, $L(\theta)$, relates the magnitude of the limit load to the position, θ, of the support; the variation of $L(\theta)$ with θ is shown in Fig.3.16, which illustrates that the upper-bound limit load of the dented ring decreases with increasing support angle, θ. The FE results for idealised material Ideal-A, normalised by dividing the peak loads by $t^2\sigma_y/R$, are also included in Fig. 3.16, for comparison with the upper-bound prediction.

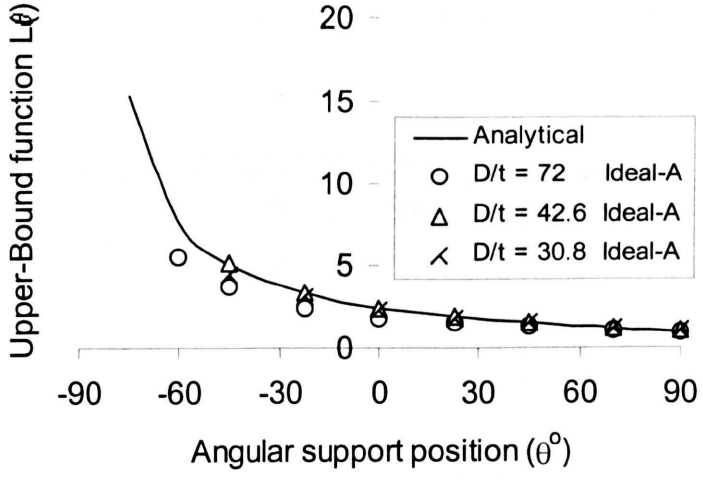

Fig.3.16 Values of non-dimensional limit load function, $L(\theta)$, for different support angular positions for material Ideal-A.

3.5 Comparisons of Experimental, FE and Analytical Solutions

A comparison of the solutions obtained from experiments, FE and analytical solutions is performed in order to validate the FE modelling analyses and the analytical solutions derived in this chapter.

3.5.1. Initial gradient

The initial gradient results given in Tables 3.1 and 3.3 for the 6082-T6 aluminium alloy, with different D/t ratios, are shown in Table 3.8. It is seen that for the large D/t ratio, the initial gradients obtained from the experiments are in good agreement with those obtained from FE analyses with boundary condition 1, but are smaller than those obtained from the analytical solution described in this chapter. However, for small D/t ratios, the initial gradients obtained from the experiments are closer to those from the FE analyses with boundary condition 2 and are much smaller than those obtained from the analytical solution, i.e. Eq.(3.5). However, the initial gradients obtained from the FE analyses with boundary condition 1 are also quite close to those obtained from the analytical solution. These differences occur because in the analytical solution the vertical movements at C are prevented but in the FE analyses and experiments point C is allowed to move vertically.

Table 3.8 Initial gradients from experiments, FE analyses and analytical solutions for the 6082-T6 aluminium alloy

D/t	Experimental Results		FE (BC1) Solution		FE (BC2) Solution		Analytical Solution
72	TE1	2.33	FE1	2.22	FE2	1.53	2.52
	TE2	2.31					
	TE3	2.25					
41.6	TE4	11.36	FE3	12.39	FE4	9.69	14.58
	TE5	10.28					
30.8	TE6	23.07	FE5	32.80	FE6	23.85	37.06
	TE7	24.09					
24	TE8	61.42	FE7	67.97	FE8	56.79	80.60

The close agreement between the FE and analytical elastic predictions, indicated in Fig.3.15, for material Ideal-A, shows that similar conclusions on the relative magnitudes of initial deflections would be obtained with all of the other material models.

3.5.2. Limit loads

3.5.2.1 6082-T6 Aluminium Alloy

The force versus displacement curves obtained from each of the FE and analytical solutions performed on the aluminium alloy models are shown in Fig. 3.17; the analytical limit loads were calculated by using the representative flow stress. Also shown in these figures are the corresponding experimental results. The limit loads obtained from the FE and analytical analyses are given in Table 3.9, which shows that the analytical limit loads, obtained using the yield stress in the predictions, are generally very close to those obtained from the experiments. These data indicate that the analytical, FE and experimental results are consistent and that using representative flow stress gives closer correlation of analytical solutions to those obtained using the FE results with boundary condition 1.

Table 3.9 FE and analytical solution for limit loads in 6082-T6 aluminium alloy rings by using yield, flow and ultimate tensile stresses in the analytical formulation (σ_y= yield stress; σ_f= representative flow stress; σ_{uts}= ultimate stress); θ=45°

D/t	Experimental N/mm		FE (BC1) N/mm		FE (BC2) N/mm		Analytical Using σ_y	Analytical Using σ_f	Analytical using σ_{UTS}
72	TE1	14.6	FE1	14.2	FE2	12.3	14.2	16.0	17.2
	TE2	14.0							
	TE3	13.5							
41.6	TE4	66.0	FE3	69.4	FE4	62.0	66.2	71.8	77.5
	TE5	61.0							
30.8	TE6	86.0	FE5	99.7	FE6	90.0	90.6	98.0	105.7
	TE7	88.7							
24	TE8	204	FE7	223	FE8	203	195.1	211.7	228.3

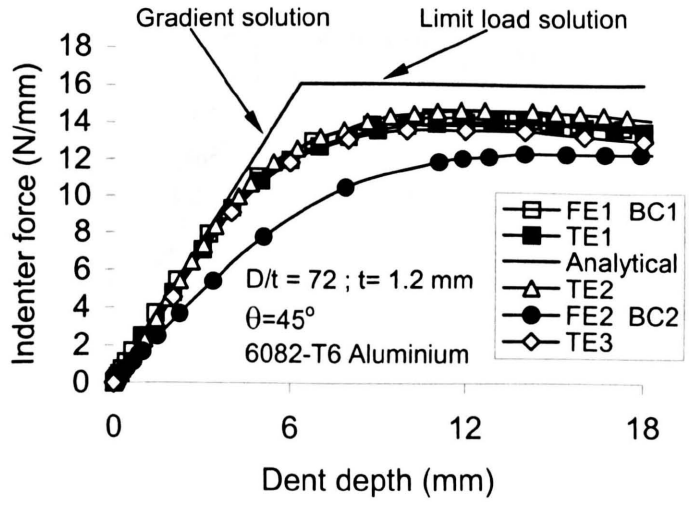

Fig 3.17 (a) D/t=72

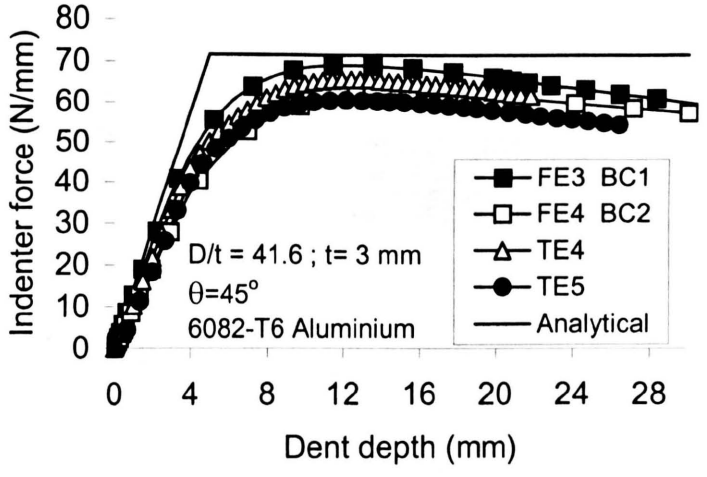

Fig 3.17 (b) D/t=41.6

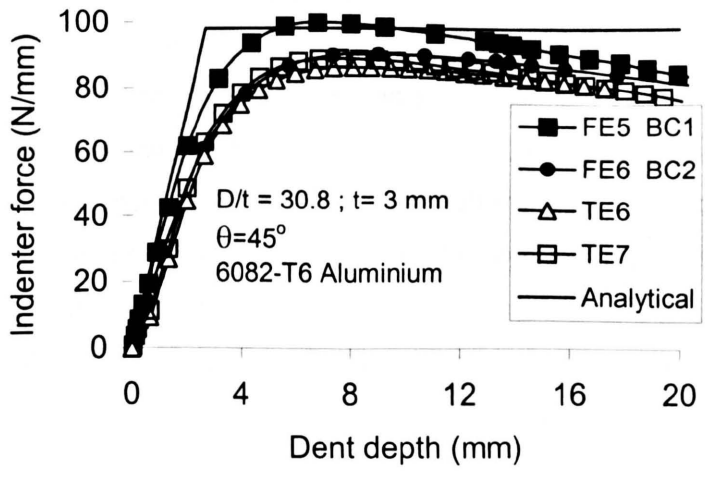

Fig 3.17 (c) D/t=30.8

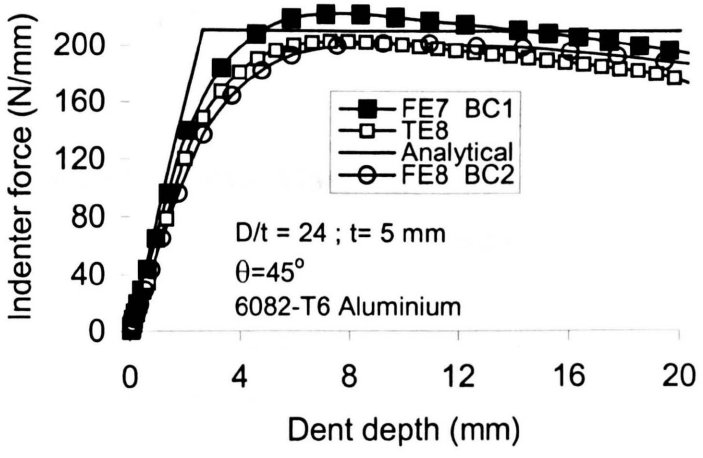

Fig 3.17 (d) D/t=24

Fig.3.17 Indenter force versus dent depth curves obtained from the analytical formulation, the FE modelling analyses and the experimental tests for 6082-T6 aluminium alloy rings; BC1 and BC2 refer to boundary conditions 1 and 2, respectively.

A comparison of the solutions of the analytical, FE and experimental results indicates that for large D/t ratios, the limit load results obtained from the experimental tests and the FE analyses,

with boundary condition 2, are in good agreement but they are significantly smaller than those obtained using the analytical solutions. The results obtained from the FE analyses, with boundary condition 2, were found to be smaller than those obtained from the experimental tests for D/t =72. For smaller D/t ratios ranging from 24 to 41.6, it was found that the solutions obtained from the FE analyses, the analytical formulations and the experimental tests are reasonably close. For the smaller D/t ratios, it can also be seen that the indenter forces obtained from the FE analyses, with boundary condition 1, are higher than those obtained from the experimental tests. In these cases, better agreement between the FE and the experimental results is obtained when the FE analyses are performed with boundary condition 2.

All of the above analyses show that the analytical formulation for predicting the limit load is capable of giving reasonably accurate predictions of the limit loads for smaller D/t ratios, with the support as shown in Fig.3.2. However, the analytical formulation for predicting the limit load overestimates the limit loads for larger D/t ratios, i.e. D/t=72. The differences between the analytical, FE modelling and experimental test results are considered to be mainly due to the differences in the boundary conditions and the assumption of rigid arcs between AE, EB etc in the analytical solution.

3.5.2.2 Elastic Perfectly Plastic Materials

The results obtained from each of the FE analyses using the elastic perfectly plastic material models and the theoretical analyses, were normalised by dividing them by the yield stress. The results are given in Table 3.10 which illustrates that the material properties influenced the value of the predictions, by between 1.4% to 14%.

Table 3.10 Normalised peak loads obtained from the analytical and FE analyses performed for elastic perfectly plastic materials with boundary conditions 1 and 2 (BC1 and BC2).

$\theta = 45^{o}$		Materials: Ideal-B, C and D (E=223GPa)						Ideal-A (E=70GPa)		Analytical
Yield stress		300MPa B		448MPa C		600MPa D		300MPa A		
D/t	T (mm)	FE BC1	FE BC2	FE BC1	FE BC2	FE BC1	FE BC2	FE BC1	FE BC2	
30.8	3	0.337	0.307	0.326	0.297	0.318	0.288	0.302	0.272	0.3
42.6	3	0.232	0.212	0.225	0.203	0.218	0.197	0.205	0.183	0.215
72	1.2	0.051	0.045	0.048	0.043	0.047	0.041	0.043	0.038	0.049

From a comparison of the FE predictions, for boundary condition 1, with the analytical predictions, it can be seen that the peak loads obtained from the FE analyses with a Young's modulus of 223GPa are higher than those obtained using the analytical method. This comparison also shows that the yield stress used in the FE analyses has an effect on the normalised peak load predictions. The FE results with a lower Young's modulus (70GPa) indicate that the peak loads obtained from the FE analyses, with boundary condition 1, for large D/t ratios are smaller than those obtained using the analytical method. The results also clearly show that Young's modulus influences the peak loads obtained from the FE analyses.

The results in Table 3.10 also show that for rings made from materials Ideal-B, C and D, with smaller D/t ratios, the peak loads obtained using boundary condition 2 are relatively close to predictions obtained using the analytical method. For the higher D/t ratio, i.e. D/t=72, the use of boundary condition 1 gives better agreement with the predictions of peak loads obtained using the analytical method. A comparison of results for material Ideal-A and boundary condition 1, with analytical predictions, indicates better agreement of the predictions of peak loads than that obtained using boundary condition 2. The same conclusion was made in section 3.5.2.1 for the 6082-T6 aluminium alloy material. The results show that for the highest D/t ratio, i.e. D/t=72, using boundary condition 1, the correlations with the analytical results are generally better than when boundary conditions 2 is used. The results also show that for materials with higher E values and smaller D/t ratios, the correlation is better using boundary conditions 2 than boundary conditions 1. For the lower E value, Ideal-A material, using boundary conditions 1 gives better correlation of peak loads than is obtained using boundary conditions 2.

The effects of D/t on the correlation of the analytical limit load and the FE prediction of peak load, can also be obtained from Table 3.10. It can be seen that for the idealised material Ideal-B, the FE peak loads and the analytical limit load are closer for a D/t ratio of 72 rather than for that of 30.8. However, for idealised material Ideal-A, the limit loads obtained from the analytical method are closer to the FE peak loads for a D/t ratio of 30.8 rather than for that of 72.

The effects of angular positions of the support on limit loads (see Table 3.5) are shown in Fig.3.16 which indicates that FE modelling can predict the limit loads better at large rather than small angular positions. However, small angular support positions (i.e. $\theta \leq -45^0$) are likely to be rare in practical applications.

3.5.2.3 X65 SAW Steel

The indenter force versus displacement curves obtained from each of the FE analyses, using boundary conditions 1, and the analytical solutions for the X65 SAW steel models, are shown in Fig. 3.18; the analytical limit loads were calculated using the representative flow stress. The peak loads are shown in Table 3.11.

Table 3.11 FE and analytical peak load comparisons for X65 SAW steel rings using the yield, flow and ultimate tensile stresses in the analytical formulation (σ_f= representative flow stress; σ_y= yield stress; σ_{UTS}= ultimate tensile stress)

θ	D/t=30.8 ; t= 3 mm				D/t=42.6 ; t= 3 mm				D/t=72 ; t = 1.2 mm			
	FE	Analytical by using			FE	Analytical by using			FE	Analytical by using		
		σ_y	σ_f	σ_{uts}		σ_y	σ_f	σ_{uts}		σ_y	σ_f	σ_{uts}
90°	119	90	113	135	81.7	64.5	90.9	97	17.3	15	18.5	22
45°	169	135	169.2	203	115	96.5	121	145	24.2	22	27.6	33
0°	267	218	273	328	180	156	195	235	36.4	35.5	44.6	53.6

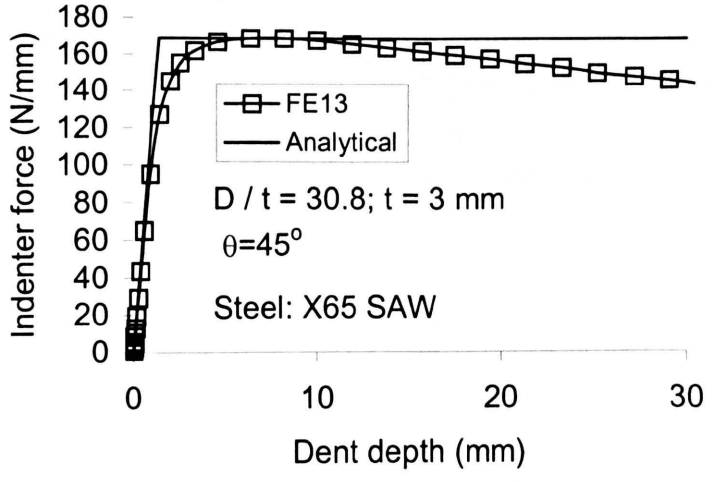

Fig. 3.18 (a) D/t=30.8

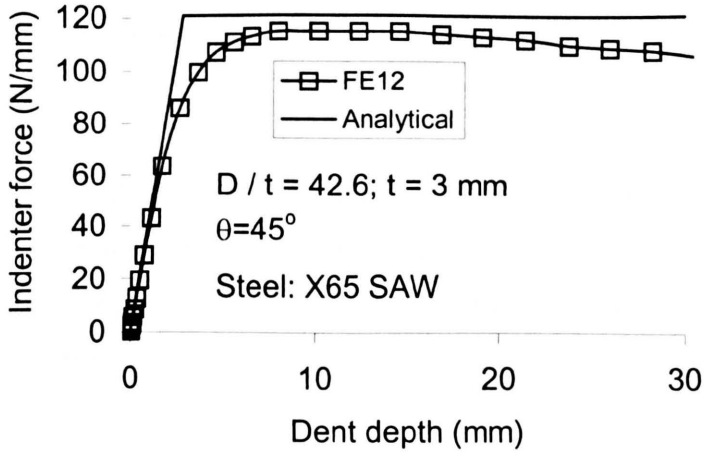

Fig. 3.18 (b) D/t=42.6

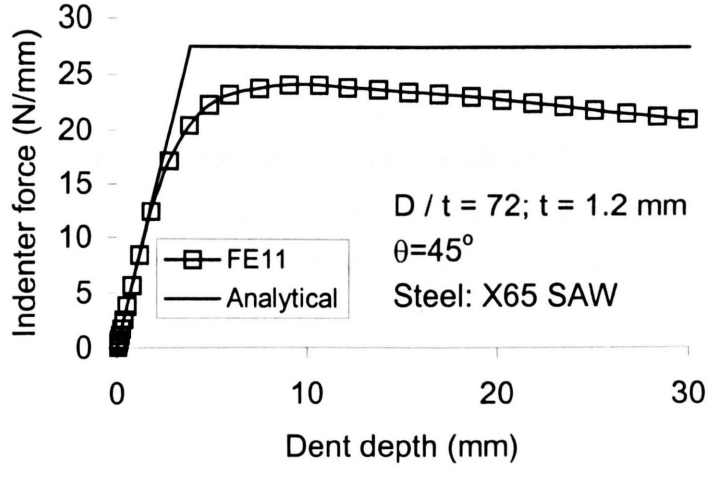

Fig. 3.18 (c) D/t=72

Fig. 3.18 The indenter force versus depth curves from analytical, FE and experimental tests using X65 SAW steel models with the support angular position of 45°

It can be seen that similar conclusions can be derived from the steel data as were derived from the aluminium data. For higher D/t ratios, i.e. D/t=72, using the yield stress in the analytical solution gives closer correlation with predictions of peak loads obtained from the FE analyses. For the lowest D/t ratio, i.e. D/t=30.8, the peak FE load is very close to that obtained using the representative flow stress in the analytical formulation. This is because the analytical limit load

solutions are based on small deformation theory whereas the FE and the experimental data include large deformation and large strain effects.

3.6 Conclusions

All of the above analyses illustrate that due to the effects of the non-linear large deformations and large strains in dented rings, material properties and geometries can influence the accuracy of the predictions of the peak loads obtained using the analytical solutions, i.e. Eq.3.13. However, using the flow or yield stress in the analytical solutions can give reasonably accurate peak load predictions. For smaller D/t ratios, peak loads can be accurately predicted using the analytical solutions.

Due to the differences of the boundary conditions in the FE, experimental and analytical solutions, the initial gradients obtained from the analytical solution are higher than those obtained from the FE and the experimental test results. However, for larger D/t ratios, i.e. D/t=72, the analytical solutions can give very good agreement for the predictions of initial gradients.

The FE and the experimental results indicate that using boundary condition 1 results in more accurate predictions of the initial gradients and limit loads of dented rings on a saddle-type support with larger D/t ratios, i.e. D/t=72. However, using boundary condition 2 is capable of predicting the peak loads and initial gradients for smaller D/t ratios, i.e. D/t=30.8.

3.7 Summary

The elastic-plastic responses of pipes with long indentations were investigated in this chapter using experimental tests, FE analyses and simple analytical methods (initial gradients and limit loads). Six different materials, four different geometries and two different boundary conditions were used to investigate their effects on the elastic-plastic responses. All of results presented in this chapter indicate that by using the average of yield and ultimate stresses as the representative flow stress in the limit load method, it is possible to obtain reasonably accurate predictions for the peak loads.

Chapter 4

Prediction of Indentation Force-Deflection Behaviour of Pressurised Pipes

4.1 Introduction

In chapter 3, the upper bound method has been used to determine the limit loads for unpressurised rings. A comparison of the analytical and FE solutions with experimental data showed that the analytical limit load method is simple to use and can give accurate predictions. It is shown in this chapter that if the internal pressure is large enough, the limit load methods previously used in chapter 3 for unpressurised pipes, give inaccurate predictions. This chapter explains why the approach used when there is no pressure is inaccurate for the case of pressurised pipes, and presents an alternative energy-based approach for predicting the relationship between indentation force and dent depth when internal pressure is significant. The accuracy of the analytical method for pressurised rings with large, non-linear deformation is assessed by comparing predictions with the corresponding results of FE analyses.

4.2 FE Analyses

4. 2.1 Material

Seven materials were used in the FE analyses. They are designated as idealised materials Ideal-A to E, 6082-T6 aluminium alloy and X65 SAW steel, which is a practical pipe material. The tensile stress-strain curves for 6082-T6 aluminium alloy and X65 SAW are shown in Fig. 3.1; Young's modulus, Poisson's ratio, yield stress and ultimate tensile stress for the materials are given in Table 4.1.

The five idealised materials (i.e. Ideal-A, B, C, D and E) with elastic, perfectly plastic material properties, were used to investigate the influence of Young's modulus and yield stress on the force-deflection curves. Of the idealised materials, Ideal-B, C and D, were chosen to have the same Young's modulus of 223 GPa and yield stresses of 300 MPa, 448 MPa and 600MPa, respectively. The other two idealised materials, Ideal-A and E, together with material Ideal-B, were chosen to have a yield stress of 300MPa and Young's moduli of 70GPa, 150GPa and

223GPa. The material properties for the seven materials are summarised in Table 4.1. In all of the FE analyses, the materials were assumed to obey an isotropic hardening rule.

Table 4.1 Material parameters used in FE analyses

Material	E (GPa)	σ_y (MPa)	σ_{UTS} (MPa)	Poisson's ratio
6082-T6 alloy	70	300	351	0.3
X65 SAW	223	448	675	0.3
Ideal-A	70	300	-	0.3
Ideal-B	223	300	-	0.3
Ideal-C	223	448	-	0.3
Ideal-D	223	600	-	0.3
Ideal-E	150	300	-	0.3

4.2.2 FE Meshes, Boundary Conditions and Loading

ABAQUS [26] FE software was used for the analyses of the rings; the dimensions, support and loading conditions are shown in Fig. 4.1. Due to symmetry, only one half of the rings were modelled (see Fig. 3.4). All models consisted of 3600 8-noded, plane-strain, reduced integration elements. The nodes on the rings at sections A and C (Fig. 3.4(a)) were restrained in the circumferential direction (i.e. $u_{xA}=u_{xC}=0$) for all of the analyses. Also, the rings were fully restrained (i.e.$u_{xB}=u_{yB}=0$) at the outer diameter at positions B and D, which are at an angle θ to the x-direction, see Fig. 4.1. The load was applied in the radially inwards direction at the outer diameter position at point A. In total 25 analyses were performed, as defined in Table 4.2.

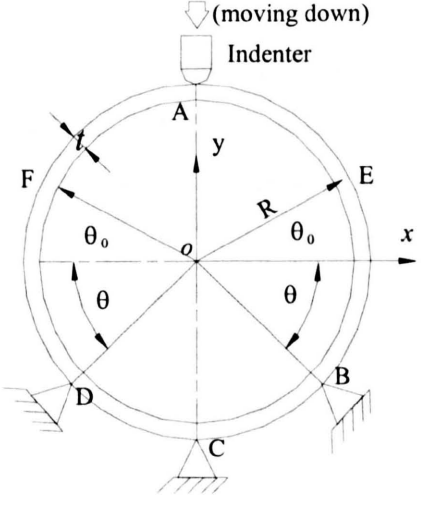

Fig.4.1 Indented ring geometry, loading and boundary conditions

Table 4.2 Materials, Geometries and Pressures used in the FE analyses

FE No.	Material	Diameter D (mm)	Wall thickness t (mm)	D/t	Support angle θ	Pressure p (MPa)	Initial gradient Per unit length K_{ep} (MPa)
FE1P	Ideal-A	128	3.0	42.6	0°	5	84.37
FE2P	Ideal-A	128	3.0	42.6	25°	5	45.76
FE3P	Ideal-A	128	3.0	42.6	45°	5	29.32
FE4P	Ideal-A	128	3.0	42.6	65°	5	20.71
FE5P	Ideal-A	128	3.0	42.6	90°	5	14.55
FE6P	Ideal-A	128	3.0	42.6	45°	0	12.96
FE7P	Ideal-A	128	3.0	42.6	45°	0.1	13.37
FE8P	Ideal-A	128	3.0	42.6	45°	0.5	14.96
FE9P	Ideal-A	128	3.0	42.6	45°	1	17.09
FE10P	Ideal-A	128	3.0	42.6	45°	2	19.25
FE11P	Ideal-A	128	3.0	42.6	45°	8	40.21
FE12P	Ideal-E	128	3.0	42.6	45°	5	46.95
FE13P	Ideal-B	128	3.0	42.6	45°	5	60.39
FE14P	Ideal-C	128	3.0	42.6	45°	7.47	69.13
FE15P	Ideal-D	128	3.0	42.6	45°	10	79.09
FE16P	Ideal-C	128	3.0	42.6	45°	5	60.39
FE17P	Ideal-D	128	3.0	42.6	45°	5	60.39
FE18P	Ideal-A	88.8	1.2	72	45°	2.82	12.05
FE19P	Ideal-A	92.4	3.0	30.8	45°	6.77	56.34
FE20P	6082-T6	88.8	1.2	72	45°	2.82	11.46
FE21P	6082-T6	128	3.0	42.6	45°	5	31.57
FE22P	6082-T6	92.4	3.0	30.8	45°	6.77	57.60
FE23P	X65 Saw	88.8	1.2	72	45°	2.82	17.21
FE24P	X65 Saw	128	3.0	42.6	45°	5	60.31
FE25P	X65 Saw	92.4	3.0	30.8	45°	6.77	136.90

4.2.3 FE Results

4.2.3.1 Typical Behaviour

The force-deflection predictions obtained from the FE analyses of a ring with zero, low and high pressures are shown in Fig. 4.2 for a ring with a D/t=42.6 (t=3mm), θ=45° and material Ideal-A. The general behaviour is typical of that obtained with other D/t ratios (30<D/t<70) and θ values (0°<θ<90°), see Figs. 4.3 to 4.7. As was shown previously in chapter 3, when the internal pressure is zero, the force deflection curve reaches a maximum value and then, with continued deformation, the load reduces. The initial (elastic) slope and maximum load can be accurately predicted, in this case, using the simple analytical techniques in chapter 3. It can be seen that the internal pressure has a significant effect on the initial slope and on the subsequent force versus deflection behaviour in the elastic-plastic region. Hence, the straightforward use of a limit load approach, to determine the maximum load and to predict the post-yield behaviour, is

obviously inadequate. The modifications introduced to the limit load approach to enable the post-yield behaviour to be reasonably accurately predicted, are described in Section 4.3.

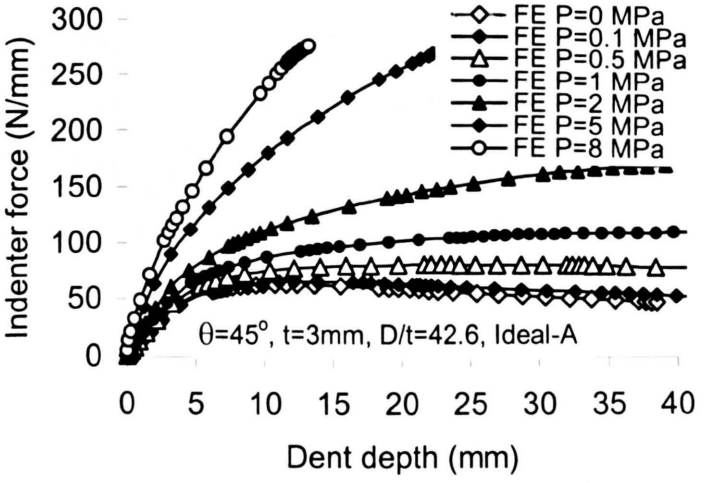

Fig. 4.2 Indenter force per unit length versus dent depth curves, for different internal pressures, i.e. p=0, 0.1, 0.5, 1, 2, 5 and 8MPa, and for idealised material Ideal-A,θ =45°, D/t=42.6 and t=3mm

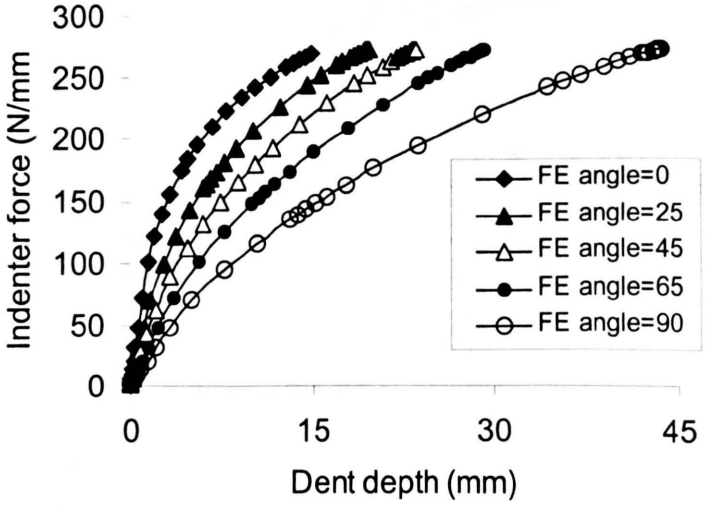

Fig. 4.3 Indenter force per unit length versus dent depth curves for different angular support positions, i.e. θ=0°, 25°, 45°, 65° and 90°, and for idealised material Ideal-A, p=5MPa, D/t=42.6 and t=3mm

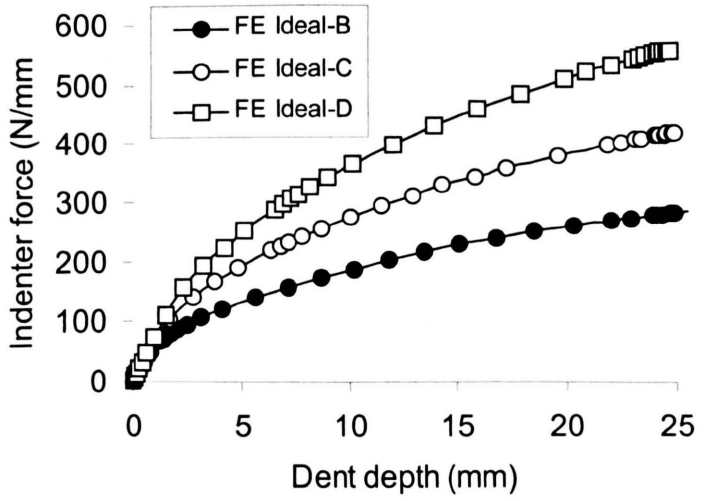

Fig. 4.4 Indenter force per unit length versus dent depth curves for different yield stresses of 300, 448 and 600MPa, and for a pressure, p, which produces a mean hoop stress of $0.34\sigma_y$ in the ring; D/t=42.6, t=3mm and $\theta=45^o$

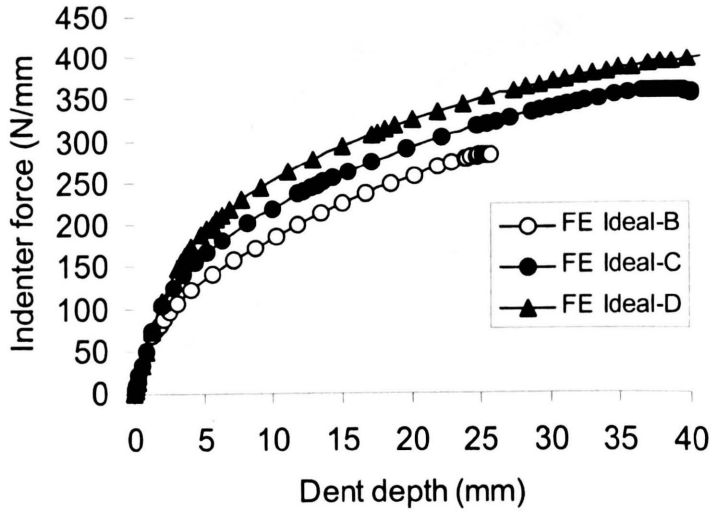

Fig. 4.5 Indenter force per unit length versus dent depth curves for different yield stresses of 300, 448 and 600MPa, for p=5MPa, D/t=42.6, t=3mm and $\theta=45^o$

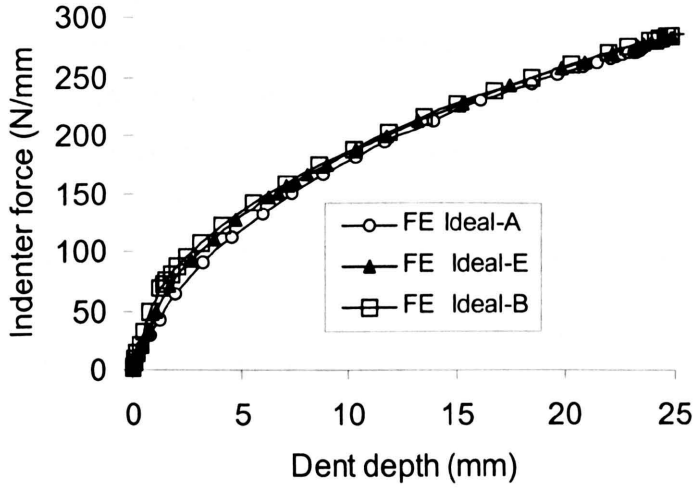

Fig. 4.6 Indenter force per unit length versus dent depth curves for different Young's moduli, i.e. E=70, 150 and 223Gpa, and for p=5MPa, θ=45°, D/t=42.6 and t=3mm

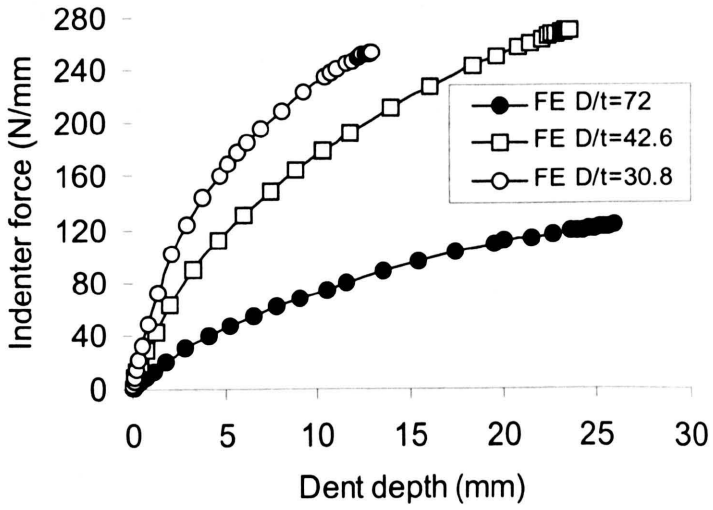

Fig. 4.7 Indenter force per unit length versus dent depth curves for different D/t ratios of 72, 42.6 and 30.8, with their corresponding thicknesses, i.e. t=1.2, 3 and 3mm, and for idealised material Ideal-A, a pressure which produces a mean hoop stress of $0.34\sigma_y$ in the ring, and θ=45°

4.2.3.2 Initial Force-displacement Gradient

The FE initial gradient results, were obtained from the force-deflection curves obtained from the FE analyses, FE1P to FE25P, and are shown in Table 4.2. The results indicate that the initial gradients per unit length, for pressurised rings, are functions of the internal pressure (p), Young's modulus (E), D/t ratio and angular support position (θ). The associated curves are shown in Figs.4.8 to 4.11, along with the results of analytical solutions which will be described in section 4.3.

From Figs 4.8 to 11, it can be seen that the initial gradients, obtained from the FE analyses, in pressurised rings vary linearly with the Young's modulus (E), as expected, and linearly with the internal pressure (p) and that they vary non-linearly with the angular support position (θ) and with the D/t ratio.

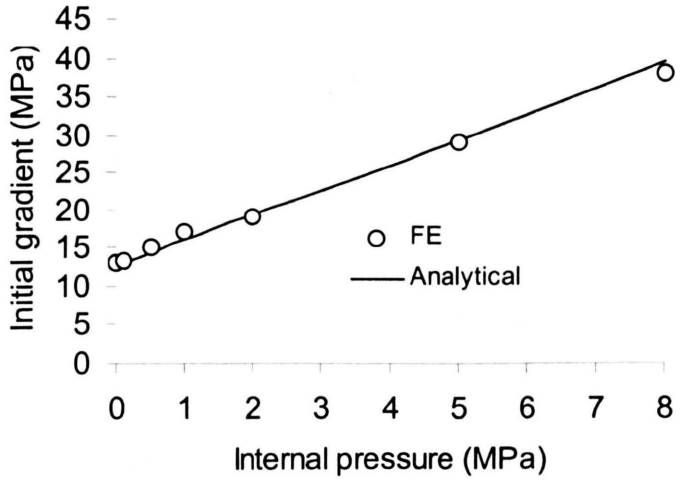

Fig. 4.8 Initial gradient per unit length versus pressure curves for material Ideal-A,θ =45°, D/t=42.6 and t=3mm

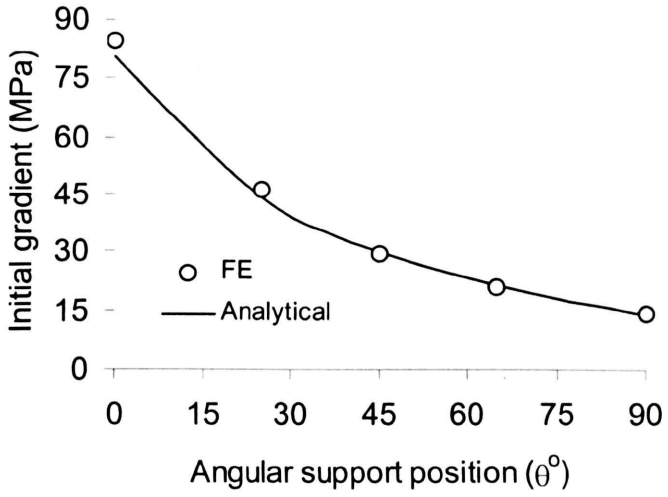

Fig. 4.9 Initial gradient per unit length versus angular support position curve for material Ideal-A, p=5MPa, θ =45°, D/t=42.6 and t=3mm

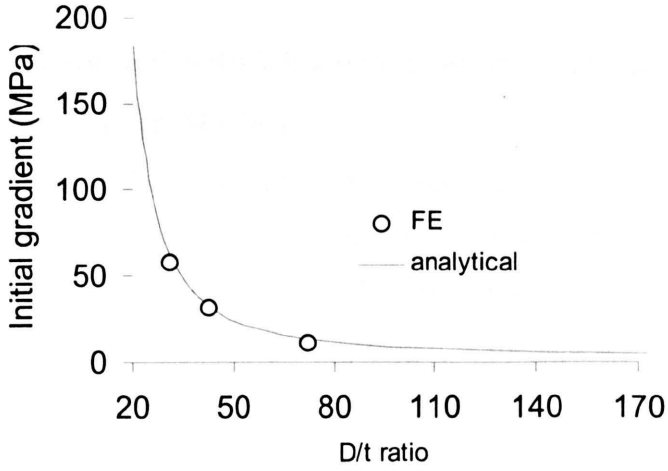

Fig. 4.10 Initial gradient per unit length versus D/t ratio curve for material Ideal-A, θ =45° and a pressure which produces a mean hoop stress of $0.34\sigma_y$.

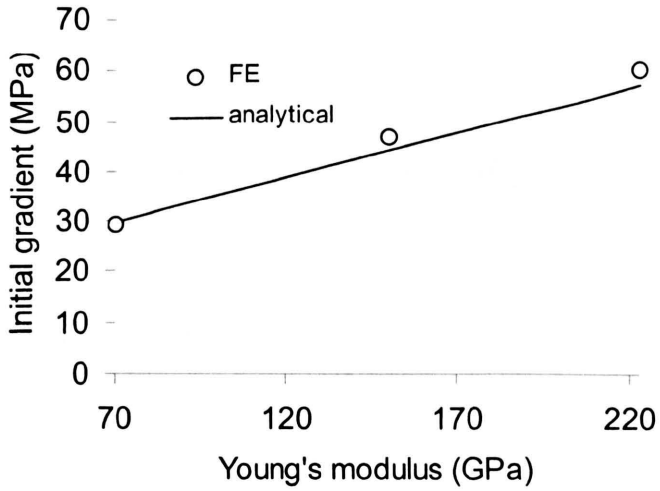

Fig. 4.11 Initial gradient per unit length versus Young's modulus curve for $\theta = 45^{o}$, D/t=42.6, t=3mm and p=5MPa.

4.2.3.3 Response Obtained with Idealised Elastic, Perfectly Plastic Material Behaviour Models

Five idealised elastic perfectly plastic materials (Ideal-A, B, C, D and E) were chosen to investigate the effects of the Young's modulus and yield stress on the typical force-deflection curves for three geometries (D/t=72, 42.6, 30.8). The results were also used to investigate the effects of the support angular positions and magnitudes of the internal pressure on the force-deflection curves. Typical force-deflection curves, obtained from FE1P to FE19P, are shown in Fig.4.2 to 4.7.

The general shape of the force-deflection curve depends on the magnitudes of the internal pressure. In general, the load carrying capacity increases with increasing pressure and the deformation caused by a given load reduces with increasing internal pressure (Fig.4.2). However, the deformation caused by a given load is increased as the support angle, θ, is increased (Fig.4.3). It can be seen from Figs. 4.4 and 4.5, that the force versus displacement response is significantly affected by the magnitude of the yield stress. However, apart from the early low deformation regions of the response, the magnitude of the Young's modulus has a relatively small effect on the force versus displacement response, see Fig 4.6. As the diameter,

D, increases, for a given thickness, t, the deformation for a particular load is increased, see Fig. 4.7.

4.2.3.4 6082-T6 aluminium alloy and X65 SAW

Typical indenter force per unit length versus depth curves obtained from the FE20P to FE25P FE analyses, performed with the 6082-T6 aluminium alloy and X65 SAW steel material models, are shown in Figs. 4.12 and 4.13, respectively. The general behaviour is similar to that obtained for the elastic perfectly plastic materials, see Fig. 4.7.

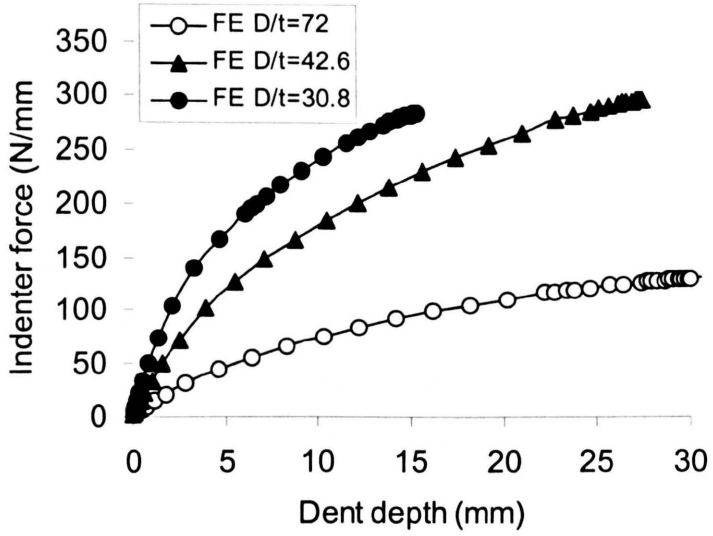

Fig. 4.12 Indenter force per unit length versus dent depth curves for different D/t ratios of 72, 42.6 and 30.8, with their corresponding thickness, i.e. t=1.2, 3 and 3mm, for 6082-T6 aluminium alloy, with a pressure which produces a mean hoop stress of $0.34\sigma_y$ in a ring with $\theta=45^o$

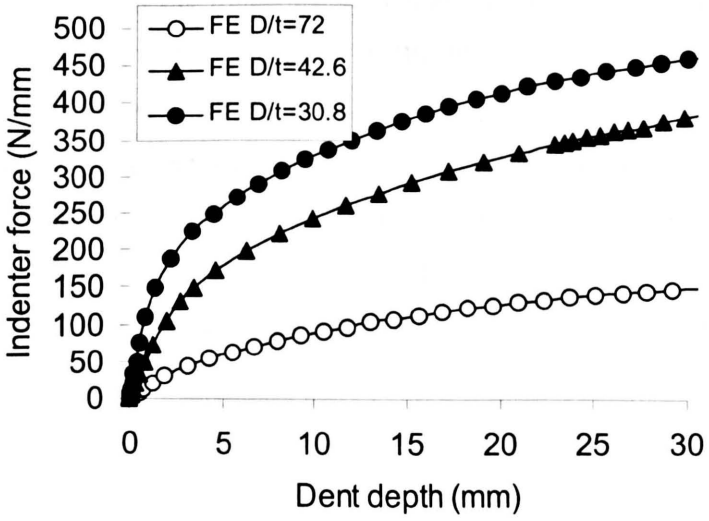

Fig. 4.13 Indenter force per unit length versus dent depth curves for different D/t ratios of 72, 42.6 and 30.8 with their corresponding thickness, i.e. t=1.2, 3 and 3mm, for X65 SAW, with a pressure which produces a mean hoop stress of $0.22\sigma_y$ in a ring with $\theta=45^\circ$

4.3 Analytical Solutions

4.3.1 Elastic Behaviour

In chapter 3, the small deformation relationship between force and deflection, for an unpresssurised ring, was obtained using Castiglano's theorem as follows:

$$F = \frac{Et^3}{12R^3}\left(\frac{D}{AD+B+C}\right)\delta \tag{4.1}$$

where A, B, C and D are functions of the support angle θ, as follows:

$$\left.\begin{aligned} A &= \frac{1}{4}\left(\frac{\pi}{2}+\theta+\frac{1}{2}\sin 2\theta\right) \\ B &= (1+\sin\theta)\left[\frac{3}{2}\sin 2\theta + 3\cos\theta - \left(\frac{\pi}{2}+\theta\right)\left(\cos^2\theta+\sin\theta+1\right)\right] \\ C &= \cos\theta\left(\frac{1}{2}+\frac{1}{2}\sin^2\theta+\sin\theta\right)\left[\left(\frac{\pi}{2}+\theta\right)\cos\theta - 2\sin\theta - 2\right] \\ D &= 2\left(\left(\frac{\pi}{2}+\theta\right)^2 - 2\cos^2\theta - \frac{1}{2}\left(\frac{\pi}{2}+\theta\right)\sin 2\theta\right) \end{aligned}\right\} \tag{4.2}.$$

Hence, the small deformation "stiffness", K_e, is given by

$$K_e = \frac{Et^3}{12R^3}\left(\frac{D}{AD+B+C}\right) \tag{4.3}$$

which is only related to the ring dimensions, the support position and Young's modulus.

Equation (4.3) indicates that the initial elastic deformation can be simulated using a spring with an elastic constant K_e; this concept is valid for any structure in the linear elastic deformation range. However, because the internal pressure causes initial deflections and stresses within the pipe, the initial " tangent stiffness matrix " [44] relating the indentation force to the indentation depth is dependent upon the internal pressure when the indentation force is applied, hence, there is a coupled effect between the pressure and force on the displacement caused by the combined load such that the force (F) versus displacement (δ) curve is dependent on the pressure p.

The displacements in the radial-directions, obtained from a FE analysis for a ring with θ=45°, D/t=42.6 and E=230GPa are plotted against the circumferential position, α, in Fig. 4.14. This indicates that the load induced curvature of the ring is large at angular positions in the vicinity of α=0°, ±72° and ±135° and is relatively small at other positions. Hence, the elastic deformation can be reasonably accurately represented by five elastic hinges, at α=0°, ±72° and ±135°, connected by rigid beams between these hinges. For indented rings with a support angle θ, the positions of the five elastic hinges may be assumed to be at α=0°, $\pm(\frac{1}{4}\pi+\frac{1}{2}\theta)$ and $\pm(\frac{1}{2}\pi+\theta)$, which are the positions predicted by limit load analysis for unpressurised rings in chapter 3. In such circumstances, the relationship between the angles of rotation at the elastic hinges (i.e. α_1, α_2, α_3) and the displacement δ can be obtained from a kinematic analysis of the system (see Appendix 1.A.1).

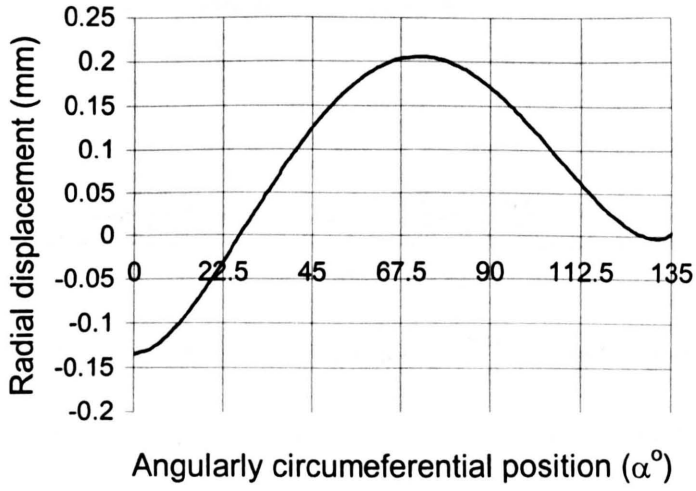

Fig. 4.14 Radial displacement versus circumferential position curves in the elastic deformation range for D/t=42.6, θ=45° and E=230GPa.

For small deformations, the energy stored in the five hinges will be $\frac{1}{2}K_e\delta^2$, where K_e is the stiffness of an equivalent linear spring, irrespective of whether the ring is pressurised or not, because the rotation of the hinges is simply governed by the kinematics of the system (see Appendix 1.A.2). The kinematic analysis is given in Appendix 1.A.1.

The work done by the external force, F, is given by $W_E = \int_0^\delta F d\delta$ and the work, W_P, done by internal pressure is given by

$$W_p = W_p^1 + W_p^2 \tag{4.4}$$

where W_P^1 and W_P^2 are the sum of the work done by internal pressure on the D-F and B-E arcs and on the F-A and A-E arcs of the ring in Fig. 4.1, respectively, and are given by

$$W_p^1 = 2\alpha_1 pR^2(1-\cos(\theta+\theta_0)) \tag{4.5}$$

and

$$W_p^2 = 2pR^2\int_0^{\alpha_1}\left\{-(1-\sin\theta)\left(\frac{d\alpha_2}{d\alpha_1}-1\right)+[\sin(\theta-\alpha_2)+\sin(\theta_0+\alpha_2)+\cos(\theta+\theta_0+\alpha_2)-\cos\alpha_2]\right\}d\alpha_1 \tag{4.6}$$

Hence, it follows that

$$\int_0^\delta F d\delta + W_P = \tfrac{1}{2}K_e\delta^2 \tag{4.7}$$

Differentiation of equation (4.7) with respect to δ gives

$$F = K_e\,\delta + pR\,F^P \tag{4.8}$$

where F^P is given by

$$F^P = 2\frac{(1-\sin\theta_0)\cos\left(\frac{\theta-\theta_0}{2}+\alpha_1\right)+2\sin\left(\frac{\pi}{4}-\frac{\theta_0}{2}-(\alpha_2-\alpha_1)\right)\cos\left(\frac{\pi}{4}+\frac{\theta_0}{2}\right)\left[2\cos\left(\frac{\theta+\theta_0}{2}+\frac{\alpha_2}{2}\right)\sin\frac{\alpha_2}{2}-\cos\left(\frac{\theta-\theta_0}{2}+\alpha_2\right)\right]}{\cos\left(\frac{\theta+\theta_0}{2}+\alpha_2\right)+\sin\left(\frac{\theta-\theta_0}{2}+\alpha_2\right)} \tag{4.9}.$$

The term $pR\,F^P$ in equation (4.8) can be rewritten as $\frac{pRF^P}{\delta}\delta$ and expressing $\frac{pRF^P}{\delta}$ as K_p, in the limit, as $\delta \to 0$, and putting $\delta_0 = \delta/R$, the small elastic deformation stiffness, K_P, associated with the internal pressure, is given by

$$K_p = p\lim_{\delta_0 \to 0}\frac{F^P}{\delta_0} \tag{4.10}.$$

From the kinematics of the system (see Appendix 1.A.1) and equation (4.9), the limiting solution, as $\delta \to 0$, of equation (4.10) is given by

$$K_p = 2p\frac{-(1-\sin\theta_0)^2\sin\frac{\theta-\theta_0}{2}+\cos\theta_0\cos\frac{\theta-\theta_0}{2}(\sin\theta+\sin\theta_0)+(1-\sin\theta_0)(1+\sin\theta)\left[\cos\frac{\theta+\theta_0}{2}+\sin\frac{\theta-\theta_0}{2}\right]}{\cos\theta_0-\cos\theta+\sin(\theta+\theta_0)\left[\cos\frac{\theta+\theta_0}{2}+\sin\frac{\theta-\theta_0}{2}\right]} \tag{4.11}$$

Substituting equation (4.10) into equation (4.8) gives

$$F = K_{ep}\delta = (K_e + K_p)\delta \tag{4.12}.$$

Hence, it can be seen that the initial gradient, K_{ep}, of the indenter force versus deflection curve, in the small deformation range, depends upon the Young's modulus, E, the geometrical ratio, D/t, the internal pressure, p, and the support position, θ. The theory predicts a linear relationship between K_{ep} and p or E, but a non-linear relationship between K_{ep} and D/t or θ.

The initial gradients obtained from the FE analyses FE1P to FE25P and those obtained from the above analytical method are plotted against each other in Fig.4.15, also plotted for comparison are analytical results obtained without the coupling effect, due to the pressure, being included.

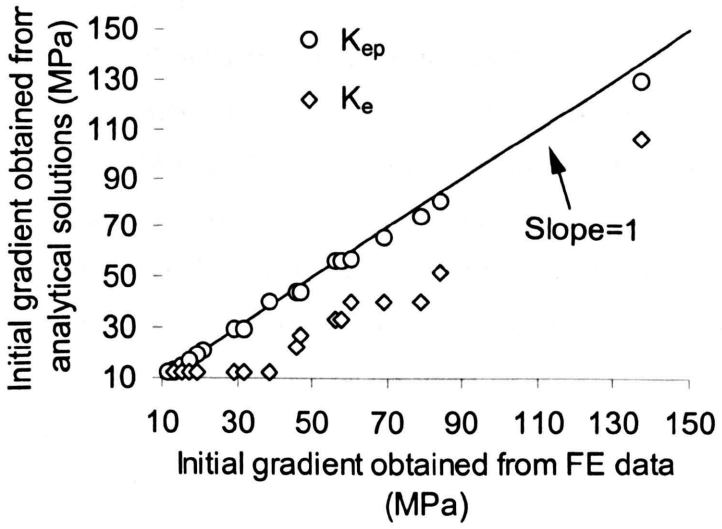

Fig.4.15 Comparison of the FE and the analytical solutions of the initial gradients per unit length of indenter force versus dent depth curves, for small deformations in pressurised pipes.

From Fig.4.15 it can be seen that the analytical initial gradient solutions for different materials, different geometrical dimensions, different angular support positions and different magnitudes of the internal pressure are very close to those obtained from FE analyses, provided that the effects of pressure are included. The analytical predictions of initial gradient are also compared with the FE results in Figs. 4.8 to 4.11. The correlation of the initial gradient solutions is very good and indicates that the theory is capable of predicting the initial gradients, for small deformations, provided the coupling effect between the pressure and force, on the deformation, is included.

Equations (4.10) and (4.12) reflect the effects of the internal pressure on the external indenter force or displacement, for small additional deformations induced by the indenter force. For a given indenter force F, the displacement δ, reduces with an increase of the internal pressure, p; or for a given displacement, δ, the external indenter force, F, increases as the internal pressure, p, is increased. This is in agreement with the FE solutions shown in Fig. 4.2. However, although equations (4.10) and (4.12) provide an approximate relationship between the indenter force and dent depth, for small deformations induced by the indenter force, such accurate results could not be obtained if the coupling effect was ignored.

4.3.2 Inelastic Behaviour

For unpressurised pipes with long indentations, it was found that the limit load method in chapter 3 is capable of accurately predicting peak loads by assuming five plastic hinges at positions A, E, B, D and F (see Fig.4.1). The kinematics of this five hinge system allows the vertical displacement, or dent depth to be related to the angular rotation of the hinges, see Appendix 1.A.1. Hence the work, W_E, done by the external indenter force, F, can be equated to the sum of the dissipation of energy at the hinges, W_I, during deformation. Since W_I can be determined, the external force at collapse may be obtained.

With the addition of internal pressure during the indentation process and the geometric changes which occur during the indentation process, the superposition of the elastic solution (based on small deformation theory) and a limit load solution (also based on small deformation theory), which gives accurate predictions for unpressurised rings in chapter 3, is inadequate. For the plastic behaviour of pressurised rings, energy is dissipated at the five hinges, as in the unpressurised situation, but as well as work being done by the applied force, F, there is work done by the internal pressure, p, associated with displacements which occur as F is increased. In this case, the 'coupling effect' as well as the finite deformation effect is important and the kinematic analysis relating the hinge rotations to the load-line displacement, must reflect this. The kinematic analysis including large deformation effects is given in Appendix 1.A.1. Since the relationship between the load-line displacement and hinge rotations is non-linear, an incremental approach is required. In this case, by equating the work done by the applied force, F, during an increment of displacement and the associated work done by the internal pressure, p, to the energy dissipated in the hinges by the corresponding increments of the rotation, the instantaneous force, F, associated with the increment of load-line displacement, can be determined. Hence, by adding this plastic solution to the elastic solution, section 4.3.1, an elastic-plastic force-deflection prediction can be obtained. The results of a kinematic analysis incorporating large deformation effects, together with expressions for the work done by the internal pressure and the energy dissipated at hinges, are outlined in the Appendices 1.A.3 to 1.A.4.

It should be noted that the kinematic analysis is only appliable until the three hinges at A, E and F are in line; the conditions under which this occurs are given in Appendix 1.A.1. The resulting maximum displacement, δ_{max}, and rotations α_{1max} and α_{2max} at hinges B and E, i.e. α_1 and α_2 when A, E and F are in line, are shown in Figs. 4.16(a) and 4.16(b). It can be seen that

when δ_{max} is achieved, the deformation is generally large and therefore predictions for higher values of δ would be of little practical interest, particularly for the higher values of θ. Predictions based on the analytical method are only valid for values of δ less than δ_{max} and hence all of the results presented graphically are terminated when this value of δ is reached.

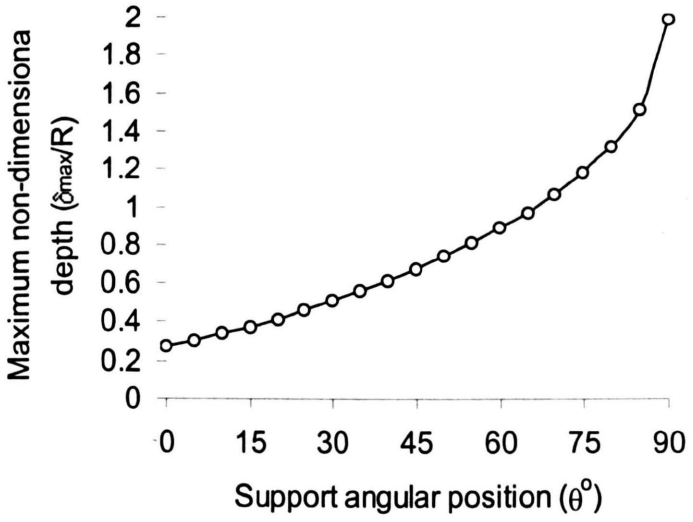

(a) Maximum non-dimensional dent depth

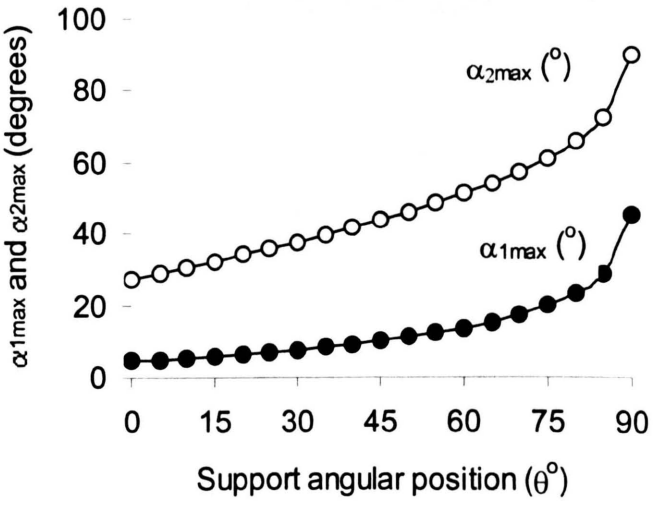

(b) Maximum rotational angles

Fig.4.16 Maximum non-dimensional dent depth and rotational angles, α_{1max} and α_{2max} (when A, E and F are in line), for the plastic hinges at positions D and F, for different support angular positions

Figs. 4.16 (a) and (b) clearly show that large angular support positions will allow large maximum displacements and maximum rotational angles in those analyses.

Since the deformation is non-linear, W_E is given by

$$W_E = \int_0^{\alpha_1} F \frac{d\delta}{d\alpha_1} d\alpha_1 \qquad (4.13).$$

From the conservation of energy principle and equations (1.a13), (1.a14) and (4.13), it can be shown that the external force, F, is given by

$$F = 4M_0 \frac{d\alpha_2}{d\delta} - \frac{dW_p}{d\delta} \qquad (4.14)$$

where $\frac{d\alpha_2}{d\delta}$ and $\frac{dW_P}{d\delta}$ are given by

$$\frac{d\alpha_2}{d\delta} = \frac{1}{R} \frac{\cos(\alpha_2-\alpha_1)-\sin(\theta_0+\alpha_2-\alpha_1)+\sin(\theta+\alpha_1)+\sin(\theta_0-\alpha_1)}{\cos(\theta_0-\alpha_2)+\sin(\theta+\theta_0+\alpha_2)-\cos(\theta+\alpha_2)-\sin\alpha_2} \qquad (4.15)$$

and

$$\frac{dW_p}{d\delta} = -2pR \frac{(1-\sin\theta_0)\cos\left(\frac{\theta-\theta_0}{2}+\alpha_1\right)+2\sin\left(\frac{\pi}{4}-\frac{\theta_0}{2}-(\alpha_2-\alpha_1)\right)\cos\left(\frac{\pi}{4}+\frac{\theta_0}{2}\right)\left[2\cos\left(\frac{\theta+\theta_0}{2}+\frac{\alpha_2}{2}\right)\sin\frac{\alpha_2}{2}-\cos\left(\frac{\theta-\theta_0}{2}+\alpha_2\right)\right]}{\cos\left(\frac{\theta+\theta_0}{2}+\alpha_2\right)+\sin\left(\frac{\theta-\theta_0}{2}+\alpha_2\right)}$$

(4.16).

For convenience, two non-dimensional coefficients, F^P and F^M, are defined, where F^P is given by equation (4.9) and

$$F^M = \frac{\cos(\alpha_2-\alpha_1)-\sin(\theta_0+\alpha_2-\alpha_1)+\sin(\theta+\alpha_1)+\sin(\theta_0-\alpha_1)}{\cos(\theta_0-\alpha_2)+\sin(\theta+\theta_0+\alpha_2)-\cos(\theta+\alpha_2)-\sin\alpha_2} \qquad (4.17).$$

Therefore, the external force, F, can be expressed as

$$F = \frac{4M_0}{R} F^M + pR F^P \qquad (4.18)$$

For $\theta=0°$, 25°, 45°, 65° and 90°, F^M and F^P are plotted against the indenter displacement (dent depth) in Fig.4.17 (a) and (b). It can be seen that at small dent depths, F^M is dominant but F^P becomes more significant for the larger dent depths.

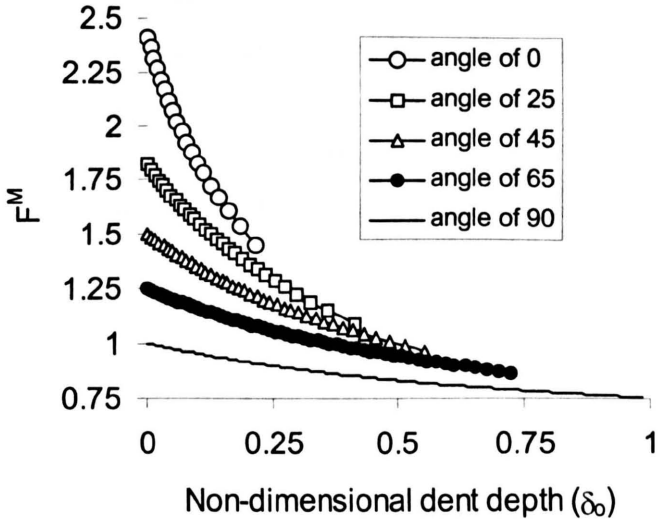

(a) Non-dimensional coefficient, F^M

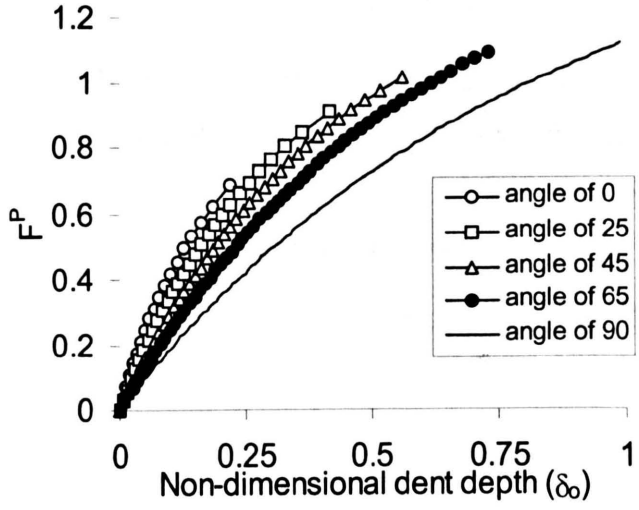

(b) Non-dimensional coefficient, F^P

Fig. 4.17 Non-dimensional coefficients for support angular positions of 0°, 25°, 45°, 65° and 90°.

A schematic indenter force per unit length versus displacement predicted by equation (4.18) is shown in Fig. 4.18, as curve OAC. It can be seen that the initial elastic region is poorly described, i.e., the figure implies a steep change in force for no change in deflection in the early deformation part of the curve. To overcome this problem, the elastic behaviour predicted by

equation (4.12) has been superimposed in Fig.4.18, as line OD. Hence the predicted behaviour is taken to be that of curve OBC. However, it should be noted that equation (4.8) is capable of predicting the elastic behaviour with a 'coupling effect' between the indenter force and the internal pressure, as shown by line OF. Therefore, an alternative prediction, given by curve OEC, could be obtained. However, in general, the difference between curves OB and OE is very small.

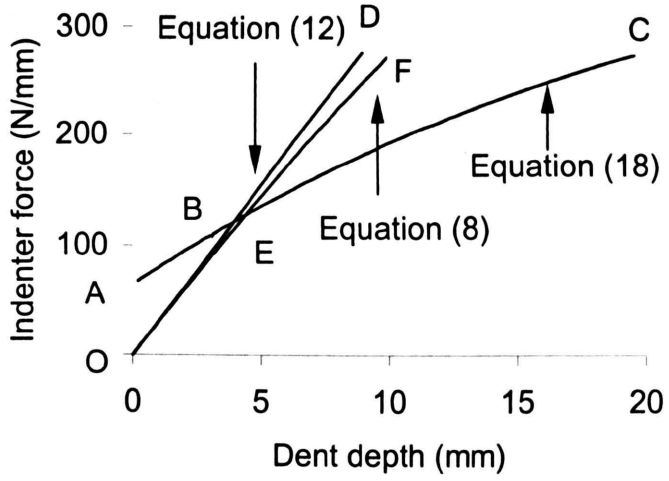

Fig. 4.18 Schematic indenter force versus depth curves, obtained using equations (4.8), (4.12) and (4.18), for E=70GPa, D/t=46.2, t=3mm, θ=45°, p=5 MPa and σ_y=300 MPa

4.4 Comparisons of FE and Analytical Solutions

A comparison of the solutions obtained from the FE analyses and analytical solutions was performed in order to assess the accuracy of the analytical solutions described in this chapter.

4.4.1. Idealised Elastic, Perfectly Plastic Materials

4.4.1.1 Comparison with Different Support Positions

The force-deflection curves obtained from FE analyses FE1P to FE5P and the corresponding analytical solutions, for the idealised material model (Ideal-A), for support angular positions of 0°, 25°, 45°, 65° and 90°, are shown in Fig. 4.19. These curves indicate that the analytical and FE results are consistent and that for smaller angular positions, in particular, very close correlation of the analytical and FE solutions can be obtained. It should be noted that very good correlation of analytical and the FE solutions were obtained for small dent depths, i.e. in the elastic region, as

well as in the elastic-plastic region unlike the situation that would result if the 'coupling effect' was excluded from the analytical model.

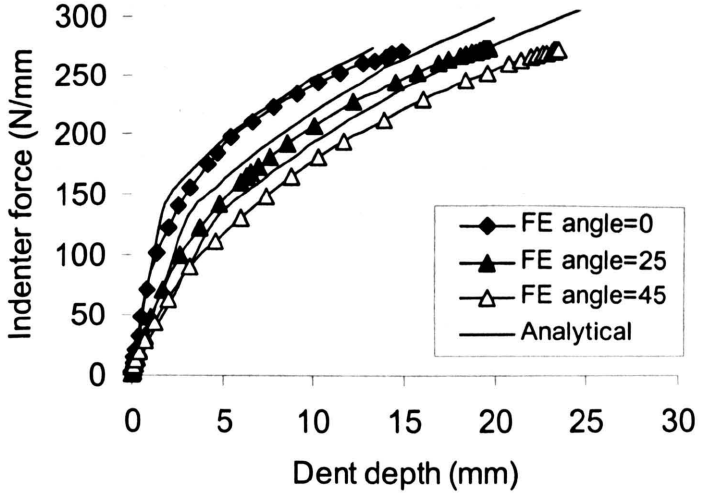

(a) Support angles of 0°, 25° and 45°

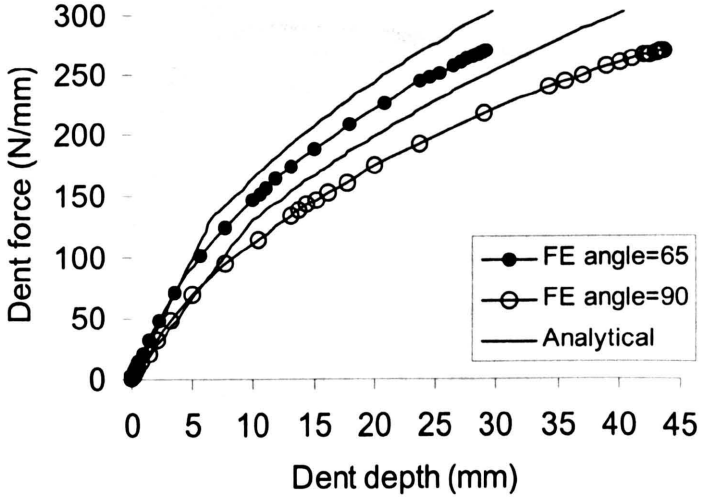

(b) Support angles of 65° and 90°

Fig. 4.19 Indenter force per unit length versus dent depth curves obtained from the FE and analytical solutions for different support angles, for material Ideal-A, p=5MPa, D/t=42.6 and t=3mm

4.4.1.2 Comparison with Different Internal Pressures

The force-deflection curves obtained from the FE analyses FE6P to FE11P and FE3P and the corresponding analytical solutions for the (Ideal-A) idealised material model, for different internal pressures, are shown in Fig. 4.20. These curves indicate that the analytical and FE results are reasonably consistent. They indicate that for the higher pressures, the analytical solutions are slightly higher than the FE solutions when the dent depths are large, and that for the lower pressures, the analytical solutions are slightly lower than the FE solutions. Also at the lower pressures, the curves exhibit a maximum in the force for both the FE and analytical results. It is shown that generally, when pressure is low the analytical solutions are underestimated while when pressure is high the analytical solutions are conservative.

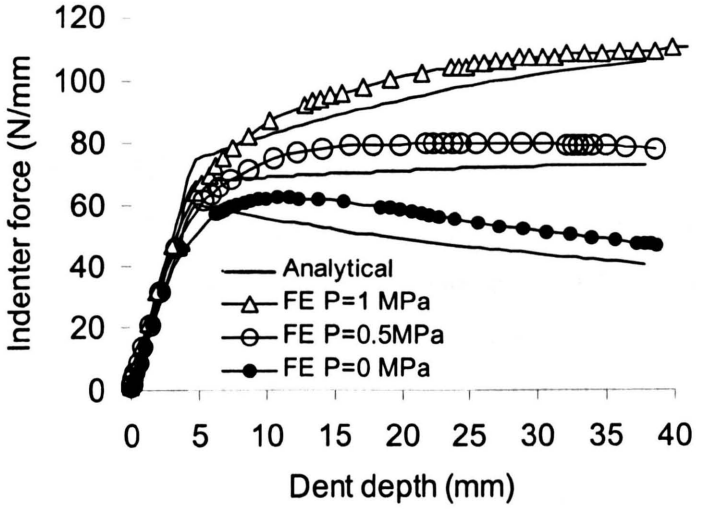

(a) p=0, 0.5 and 1MPa

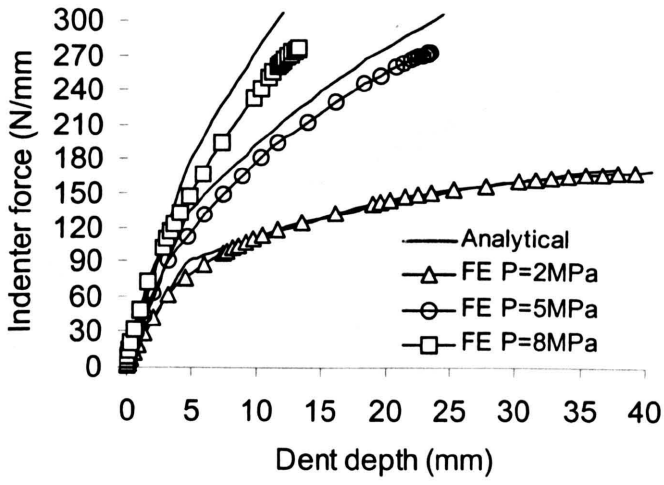

(b) p=2, 5 and 8 MPa

Fig. 4.20 Indenter force per unit length versus dent depth curves obtained from the FE and analytical solutions for different pressure levels, for idealised material Ideal-A, $\theta=45^{\circ}$, D/t=42.6 and t=3mm

4.4.1.3 Comparison with Different Young's Moduli

The force-deflection curves obtained from the FE analyses FE3P, FE12P and FE13P and the corresponding analytical solutions for the idealised material models (Ideal-A, E and B) with Young's moduli of 70GPa, 150GPa and 223GPa, are shown in Fig. 4.21. These curves indicate that the analytical and FE results are in close agreement. They also indicate that the Young's moduli affect the indenter force solutions, see equations (4.3) and (4.12). For the higher values of Young's moduli, the FE solutions are higher. However, it can be seen that the analytical solutions, when the dent depths are large, are not strongly dependent on the Young's moduli, but there is an effect in and near the elastic range. For dent depths greater than about 4mm, all analytical curves are practically identical.

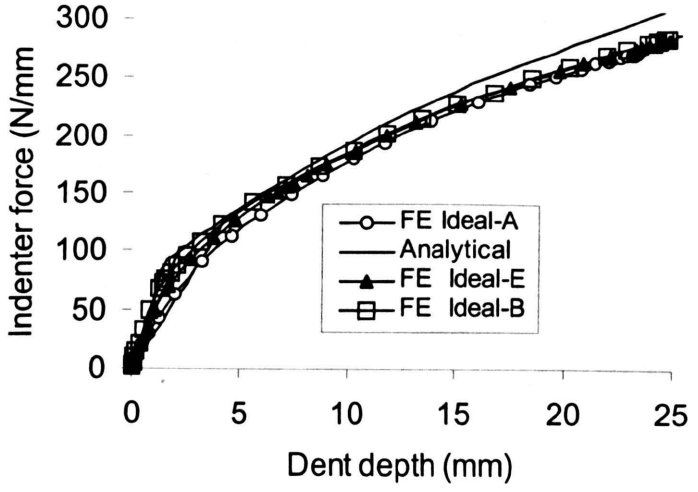

(a) Full curves

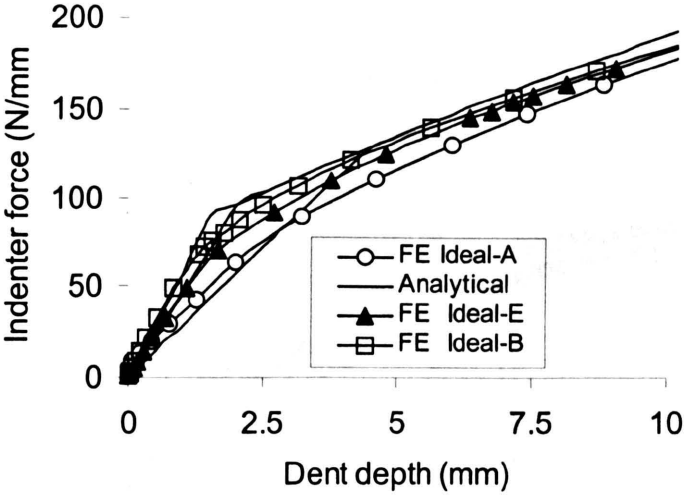

(b) Initial gradients

Fig. 4.21 Indenter force per unit length versus dent depth curves obtained from the FE and analytical solutions for different Young's moduli of 70, 150 and 223GPa, with p=5MPa, θ=45°, D/t=42.6 and t=3mm

4.4.1.4 Comparison with Different Yield Stresses

The force-deflection curves obtained from the FE analyses FE13P to FE17P and the corresponding analytical solutions performed on the idealised material models (Ideal-B, C and D)

with yield stresses of 300MPa, 448MPa and 600MPa, are shown in Fig. 4.22. These curves indicate that the analytical and FE results are in close agreement.

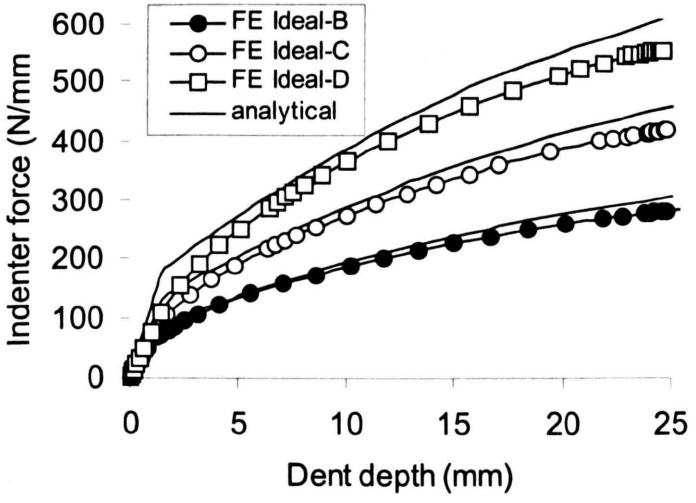

(a) Pressure to cause a hoop stress of 0.34 σ_y

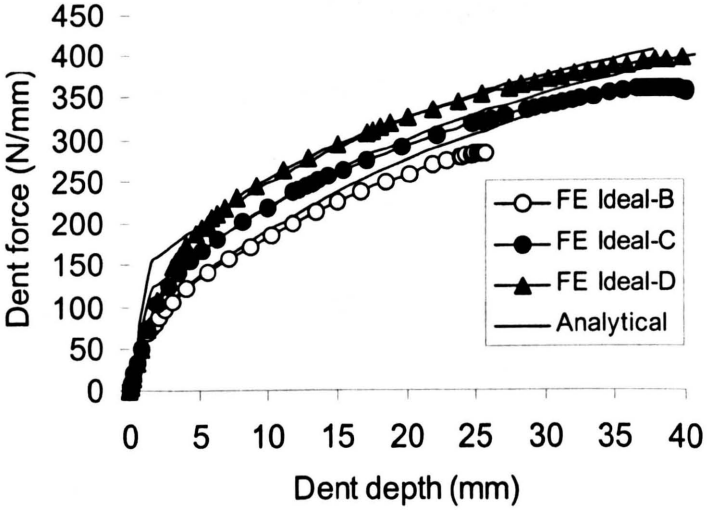

(b) p=5 MPa

Fig. 4.22 Indenter force per unit length versus dent depth curves obtained from the FE and analytical solutions for different yield stresses of 300, 448and 600MPa, θ=45°, D/t=42.6 and t=3mm

4.4.1.5 Comparison with Different D/t Ratios

The force-deflection curves obtained from the FE analyses FE3P, FE18P and F19P and the corresponding analytical solutions for the (Ideal-A) idealised material model, with D/t ratios of 72, 42.6 and 30.8, are shown in Fig. 4.23. These curves indicate that the analytical and FE results are in good agreement. They also indicate that the analytical predictions are higher than the FE solutions for all D/t ratios investigated.

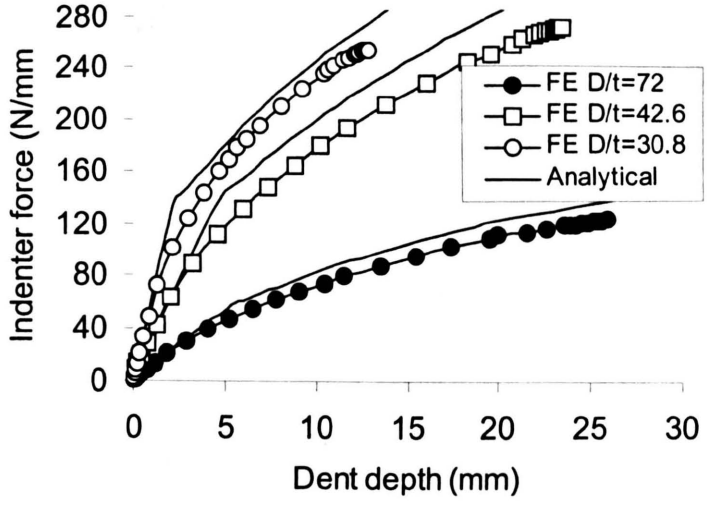

Fig. 4.23 Indenter force per unit length versus dent depth curves obtained from the FE and analytical solutions for different D/t ratios of 72, 42.6and 30.8,with material Ideal-A, a pressure which produces a mean hoop stress of 0.34 times σ_y and θ=45°

4.4.2. 6082-T6 Aluminium Alloy and X65 SAW Steel

The force-deflection curves obtained from the FE analyses FE20P to F22P for 6082-T6 aluminium alloy models and FE23P to FE25P for X65 SAW models, are shown in Fig. 4.24 and 4.25, respectively. The analytical solutions also shown, were obtained using a representative flow stress, σ_f, equal to average of the yield stress and the UTS, i.e. $(\sigma_y+\sigma_{UTS})/2$. These curves indicate that the analytical and FE results are in good agreement. The agreement is generally better than that obtained with the idealised, elastic perfectly plastic models.

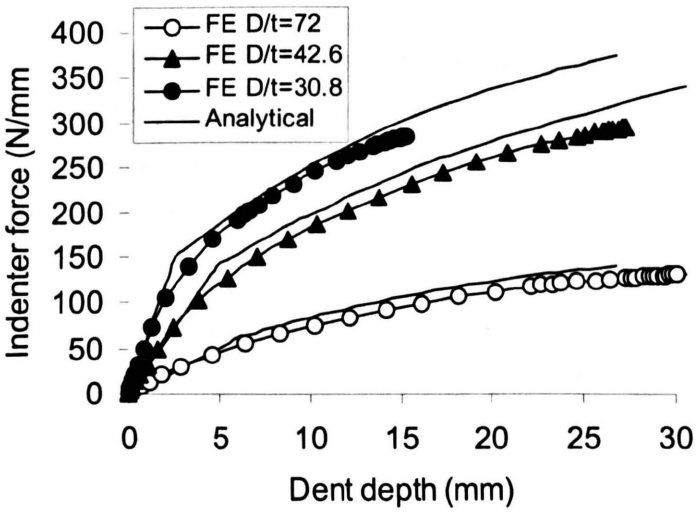

Fig. 4.24 Indenter force per unit length versus dent depth curves obtained from the FE and analytical solutions for different D/t ratios of 72, 42.6and 30.8, for the 6082-T6 aluminium alloy, a pressure which produces a mean hoop stress of 0.34 times σ_y and θ=45°

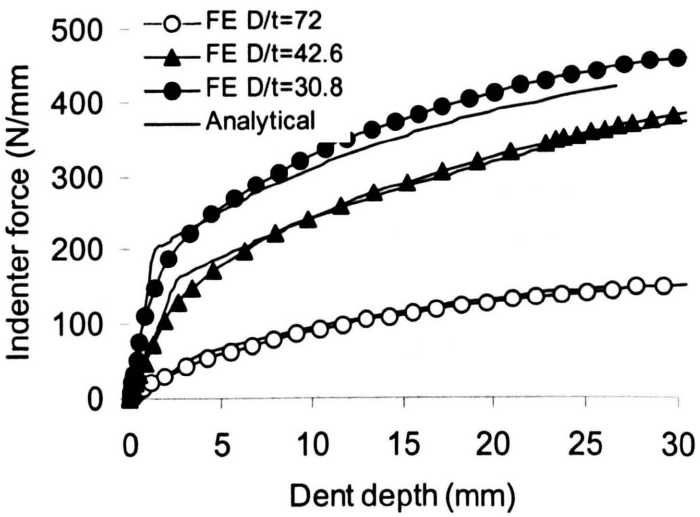

Fig. 4.25 Indenter force per unit length versus dent depth curves obtained from the FE and analytical solutions for different D/t ratios of 72, 42.6and 30.8, for the X65 SAW, a pressure which produces a mean hoop stress of 0.22 times σ_y and θ=45°

4.5 Conclusions

An approximate analytical approach, which incorporates the large deformation effects and the coupling effect between internal pressure and indenter force on the force versus indenter depth response, has been developed for pressurised rings. For axially long indentations, the analytical model can be applied to pipes as well as to rings.

The validity of the analytical model has been assessed by comparing predictions based on it with corresponding results from FE analyses. The FE and analytical predictions correlate well in both the elastic and elastic-plastic regions for a wide range of D/t ratios, pressures, angular support positions, Young's moduli and yield stress (see Figs. 4.19 to 4.23).

The analytical model can be incorporated in a computer program to run quickly on a small desk-top computer, thus obviating the need for expensive and time-consuming FE calculations. Hence the program can be conveniently used to perform parametric analyses of the effects of various input parameters (D/t, p, θ, E and σ_y).

The results obtained for 6082-T6 aluminium alloy and for X65 SAW steel indicate that using a representative flow stress, σ_f ($=(\sigma_y+\sigma_{UTS})/2$), as a representative yield stress in the analytical model, produces accurate results when compared with the FE results obtained using the actual stress-strain curves.

4.6 Summary

The force-deflection behaviour of pressurised pipes, due to radial indentation loading, was investigated using FE and analytical methods. Seven different materials, three different geometries, seven different pressure levels and five different support conditions were used to investigate their effects on the force-deflection behaviour. The comparisons of the FE and analytical solutions indicate that an energy-based, analytical approach can accurately predict the force-deflection behaviour in both the elastic and elastic-plastic states.

Chapter 5

Elastic-Plastic Response of Unpressurised Pipes Subjected to Long Offset Indentations

5.1 Introduction

In chapters 3 and 4 efforts have been made to investigate the limit load and force-deflection predictions of dented rings, with symmetrical supports, subject to symmetrical radial indenter loading using experimental tests, analytical methods and FE analyses. In this chapter the effects of asymmetric support and loading conditions on the indenter limit load are investigated using experimental tests, FE analyses and analytical methods.

For underground pipelines, the surrounding soil produces support for the pipelines and reaction forces to resist the pipeline deformation or the movements caused by indentation loads. Exact simulation of the support conditions of the soil is difficult, since they are very variable. A complete investigation of the support produced by the surrounding soil when an indentation load is applied would require many experimental tests to be performed and corresponding FE and/or analytical analyses to be performed. In this chapter a general analytical formulation, which covers the effects of the support and indentation positions on the limit loads of indented rings, is described.

The indentation type investigated in this chapter is shown in Fig. 5.1. If the offset indentation angle, θ_1, is zero, the indentation is radial with asymmetric support conditions. Symmetric indentation conditions, in which equal right and left support angles ($\theta_2=\theta_5$) and zero offset indentation angle ($\theta_1=0^o$) exist, were covered in chapters 3 and 4.

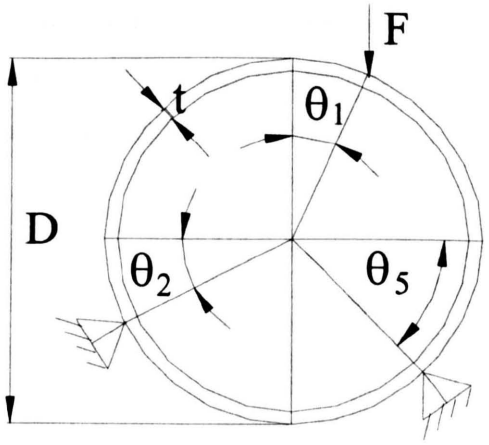

Fig.5.1 Indentation loading and support conditions.

5.2 Experimental Work and Validation of the FE Analyses

5.2.1 Material

The material chosen for the experimental investigation is 6082-T6 aluminium alloy. The tensile stress-strain curve for the material is shown in Fig. 3.1; the Young's modulus, Poisson's ratio, yield stress and ultimate tensile stress are given in Table 5.1. Fig. 3.1 also shows the stress-strain curve for a practical gas pipeline material, namely X65 SAW. The material properties for 6082-T6 aluminium alloy, X65 SAW steel and an idealised elastic-plastic material (Ideal-A) are given in Table 5.1.

Table 5.1: Material parameters used in experiment tests

Material	E (GPa)	σ_y (MPa)	σ_{UTS} (MPa)	Poisson's ratio
6082-T6 alloy	70	300	351	0.3
X65 SAW	223	448	675	0.3
Ideal-A	70	300	-	0.3

5.2.2 Geometry and Loading

In order to perform the experimental tests, the 6082-T6 aluminium alloy rings were placed on a V-block, plaster, which was cast into the gap between the rings and the V-block, used to form an arc supporting bed, as shown in Fig.5.2. The rings were also clamped to the V-block at position F. These support conditions provide an arc support. The support angles, θ_2 and θ_5 (55°

and 35°, respectively) are shown in Fig. 5.2. Radial indentation, i.e., θ_1=0°, was used. The rings were radially loaded at point A (see Fig.5.2) by a Bright Drawn Mild Steel indenter with an end radius of 2 mm and an axial length of 50mm.

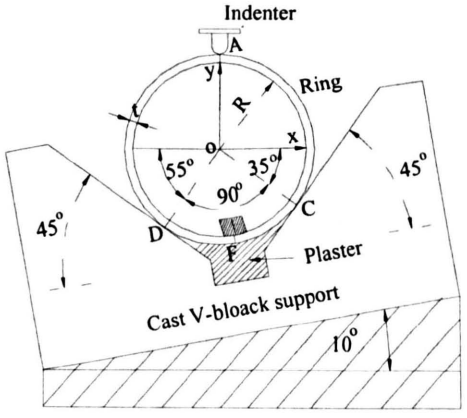

Fig. 5.2 Dented ring test conditions.

The tests were conducted on an Instron 1195 uniaxial test machine with 1 kN and 50 kN load cells. The load point displacement rate was set to 2mm/min and the data (force and displacement) were recorded automatically. Tests were performed on four rings with the dimensions given in Table 5.2. Also given in Table 5.2 are the peak indenter loads obtained during the tests. The peak loads, or limit loads, were obtained from the maximum load point of the indenter force (per unit length of the pipe) versus dent depth curves, as shown in Fig. 5.3.

Table 5.2: Geometries and experimental peak load results for 6082-T6 aluminium alloy dented ring tests

Test No	D (mm)	t (mm)	D/t	L (mm)	Peak load / unit length N/mm
TE1	120	1.5	80.0	50	14.9
TE2	125	3	41.6	50	64.0
TE3	120	5	24	50	203
TE4	120	5	24	50	200.3

5.2.3 Ring Test Results

The indenter force versus depth curves obtained from the four experiments are shown in Fig.5.3. The repeatability of the results is seen to be good from the results obtained for tests TE3 and TE4, which have the same dimensions and test conditions. As the thickness is reduced and

hence the D/t value is increased, the peak load drops very significantly and the initial slopes are also reduced.

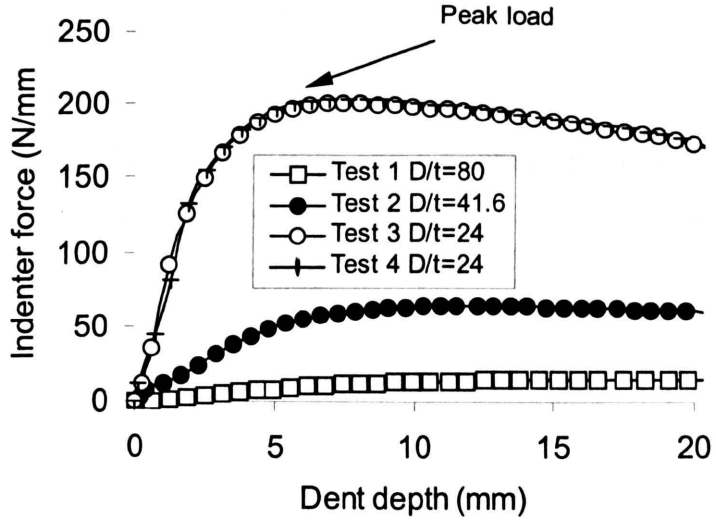

Fig. 5.3 Indenter force versus dent depth curves for 6082-T6 aluminium alloy rings, obtained from experiments with an offset angle, $\theta_1 = 0°$, a right support angle $\theta_2 = 55°$, and a left support angle $\theta_5 = 35°$.

5.2.4 FE Meshes, Boundary Conditions and Loading

The ABAQUS [26] FE software was used for the analyses. All models consisted of 3600 8-noded, plane-strain, reduced integration elements, as shown in Fig. 5.4. The rings were fully restrained at the outer diameter at positions C and D. The indentation load was applied in the vertically downward direction at the outer diameter position at point A.

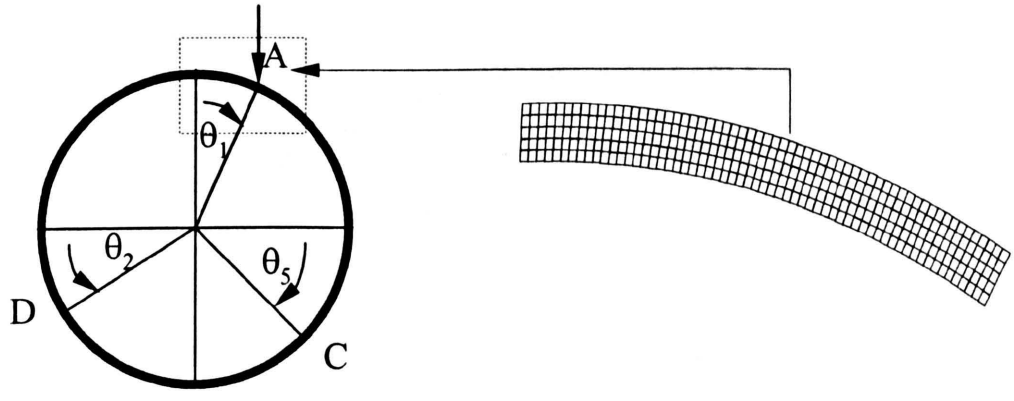

(a) Mesh of a ring (b) Locally amplified mesh

Fig. 5.4 Mesh used for the dented ring tests.

The loads were applied using a rigid indenter with a 2mm radius and rigid surface contact elements and assuming that no slipping occurs between the indenter and the rings. The large deformation, elastic-plastic analyses were performed using the standard RIKS algorithm facility within ABAQUS [26].

5.2.5 Comparison of FE Results with the Experimental Data

The FE predictions are compared with the experimental results in Table 5.3 and Fig. 5.5. It can be seen that the FE predictions are slightly higher than the experimental results, but in general, the predictions are in good agreement with the experimental data. The small discrepancy between the FE and experimental results is thought to be due to the fact that the support conditions, on the outer surface of the rings at C and D, used in the FE analyses, were fully fixed, whereas the displacements at the same positions in the experiments are only prevented from movements in the outer normal directions of the rings. Hence, the rings used in FE analyses are subjected to a slightly higher level of constraint than those used for the experiments. However, all of the differences between the FE solutions and the corresponding experimental results are within 13%. This degree of correlation was considered to be good enough and so the same mesh was used for all of the subsequent analyses reported in this chapter.

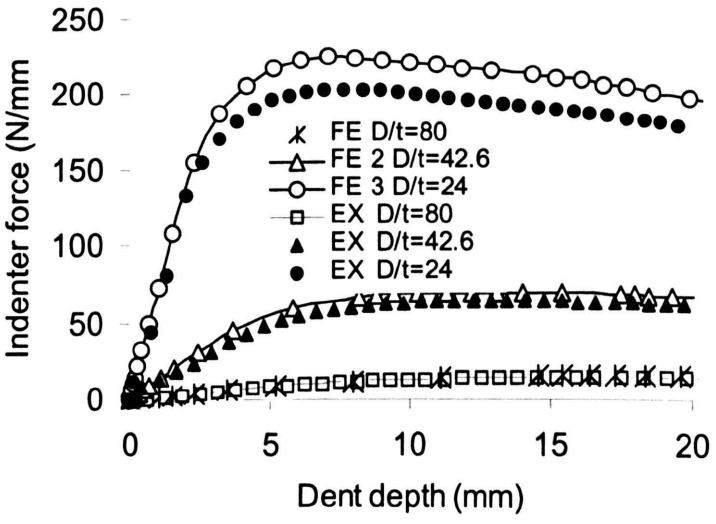

Fig.5.5 Comparison of FE predictions with experimental indenter force versus depth curves obtained from the 6082-T6 alloy ring tests with $\theta_1=0^\circ$, $\theta_2=55^\circ$ and $\theta_5=35^\circ$.

Table 5.3: D/t ratios, limit loads obtained from the experimental tests and FE.

D/t	Limit load (N/mm)		Limit load (N/mm)		Difference (%)
80	TE1	14.9	FE1	15.5	4
41.6	TE2	64.0	FE2	69.5	8.6
5	TE3	203.0	FE3	225	10.8
5	TE4	200.3			12.5

5.3 Results of General FE Analyses

5.3.1 Materials and Geometry

In addition to the FE analyses performed for comparison with the experimental test results for the aluminium alloy (6082-T6), FE analyses were obtained for two other materials. Since practical pipelines are usually made from a variety of steels, FE analyses were performed using material data for one of these steels, namely X65 SAW. An idealised material, Ideal-A, with elastic, perfectly plastic material properties was also used to investigate the influence of material properties on the elastic-plastic response. Ideal-A material has a Young's modulus of 70GPa and yield stress of 300MPa. The material properties are summarised in Table 5.1. In all of the FE analyses, the materials were assumed to obey an isotropic hardening rule. The ring dimensions used in the FE analyses are shown in Table 5.4.

Table 5.4: Ring dimensions used in the FE analyses

FE Model No.	D (mm)	t (mm)	D/t
1	120	1.5	80
2	120	5.0	24
3	128	3.0	42.6
4	88.8	1.2	72
5	92.4	3.0	30.8

5.3.2 Behaviour for Pipes Made from an Idealised Elastic Perfectly Plastic Material (Ideal-A)

The idealised elastic, perfectly plastic material, Ideal-A, was chosen to investigate the effects of the support and indenter offset angular position on the limit loads. A total of 111 FE analyses (FE4 to FE114) were performed for the Ideal-A material, see Appendix 2.A. for details of the FE analyses. The typical behaviour obtained from these analyses is as indicated in Fig. 5.5 which

was obtained for the aluminium alloy (FE and experiments). The peak (i.e. limit) loads obtained from analyses (FE4 to FE114) were normalised by dividing them by $\sigma_y t^2/2R$ and these are shown in Figs.5.6 to 5.9; the loading and boundary conditions used in the FE analyses are summarised in Appendix 2.A.

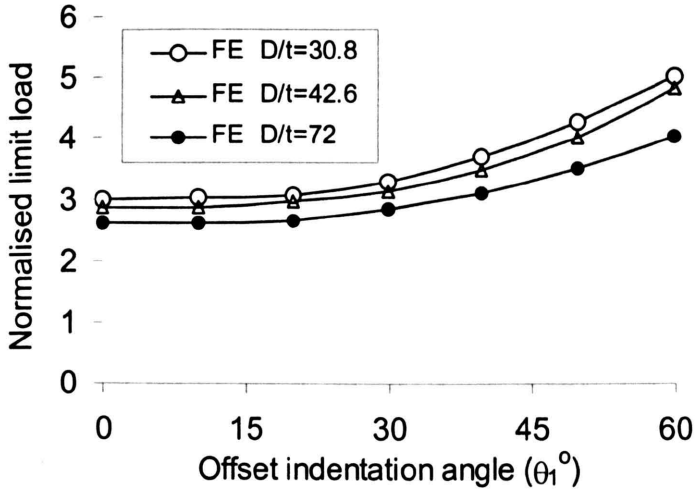

Fig. 5.6 The normalised peak load versus indenter offset angular position, with $\theta_2=\theta_5=45°$ and D/t =72, 42.6 and 30.8, for idealised material Ideal-A

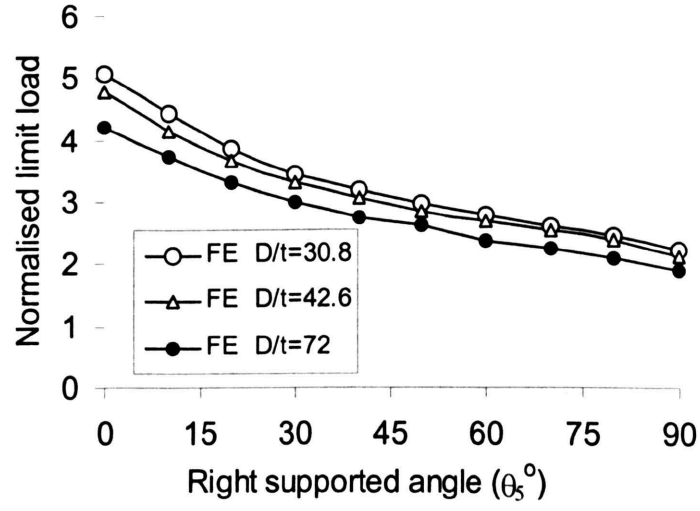

Fig. 5.7 The normalised peak load versus right support angular position, with $\theta_2=45°$, D/t =72, 42.6 and 30.8 and $\theta_1=20°$, for idealised material Ideal-A.

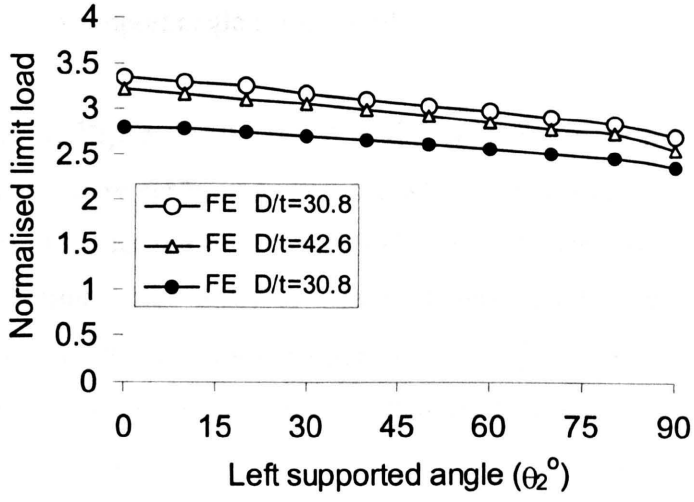

Fig. 5.8 The normalised peak load versus left support angular position, with θ_5= 45°, D/t=72, 42.6 and 30.8 and θ_1=20°, for idealised material Ideal-A

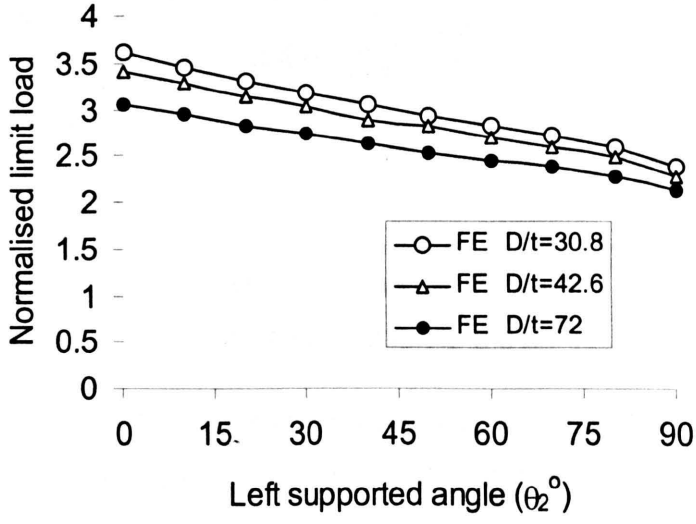

Fig. 5.9 The normalised peak load versus left support angular position, with θ_5=45°, D/t=72, 42.6 and 30.8 and θ_1= 0°, for idealised material Ideal-A

Fig. 5.6 shows that the peak load slightly increases as the indenter offset angle increases from 0° to 20°. The peak load increases more significantly as the offset angle increases from 20° to 60°. However, at these higher offset angles, it is more likely that slipping will occur between the

indenter and the ring. Also, it can be seen, from Figs.5.7 to 5.9, that the peak load decreases when either the right or left support angle is increased.

5.3.3 Behaviour of Pipes Made from X65 SAW Steel Material

A further 111 analyses were performed using the X65 SAW steel material data. The loading and boundary conditions used for the analyses (FE115 to FE225) are given in Appendix 2.A. The main reason for performing these analyses was to investigate the applicability of using a representative flow stress, σ_f, for predicting the peak loads. In this chapter, σ_f was taken to be the average of the yield stress and the ultimate tensile stress. As with the idealised material, Ideal-A, the peak loads obtained from X65 SAW steel were normalised by dividing them by $\sigma_f t^2/2R$; the results are shown in Figs. 5.10 to 5.13.

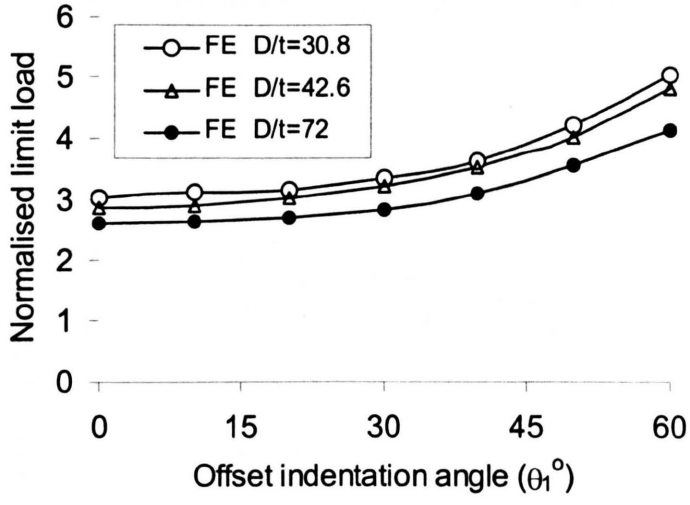

Fig. 5.10 The normalised peak load versus indenter offset angular position, with $\theta_2=\theta_5=45°$ and D/t=72, 42.6 and 30.8, for X65 SAW steel.

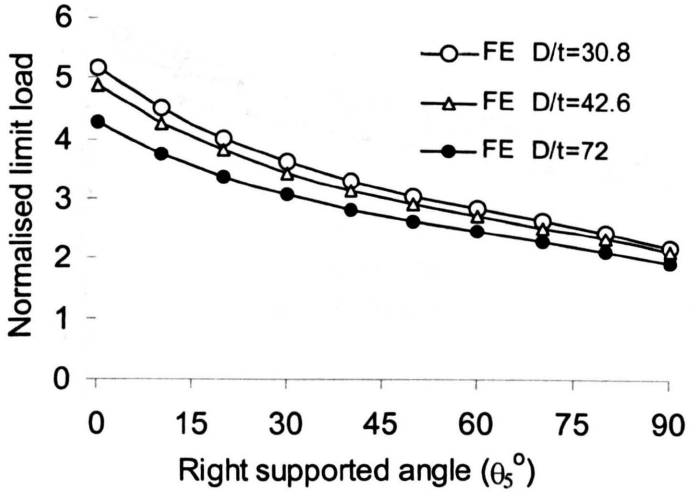

Fig. 5.11 The normalised peak load versus right support angular position, with θ_2=45°, D/t=72, 42.6 and 30.8 and θ_1=20°, for X65 SAW steel.

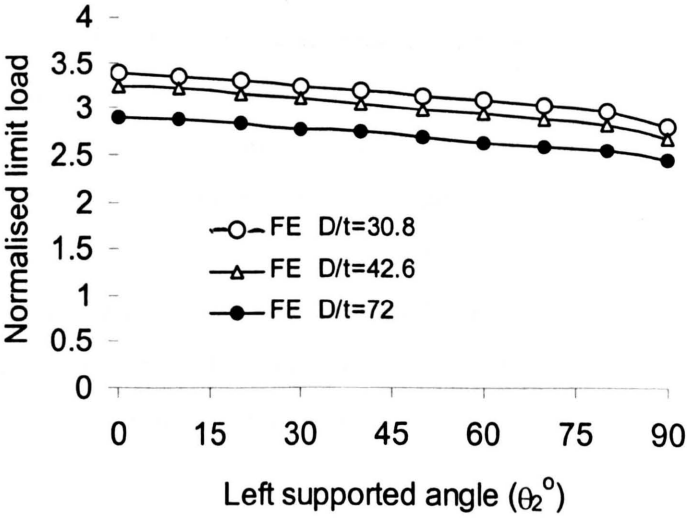

Fig. 5.12 The normalised peak load versus left supported angular position, with θ_5=45°, D/t=72, 42.6 and 30.8 and θ_1=20°, for X65 SAW steel.

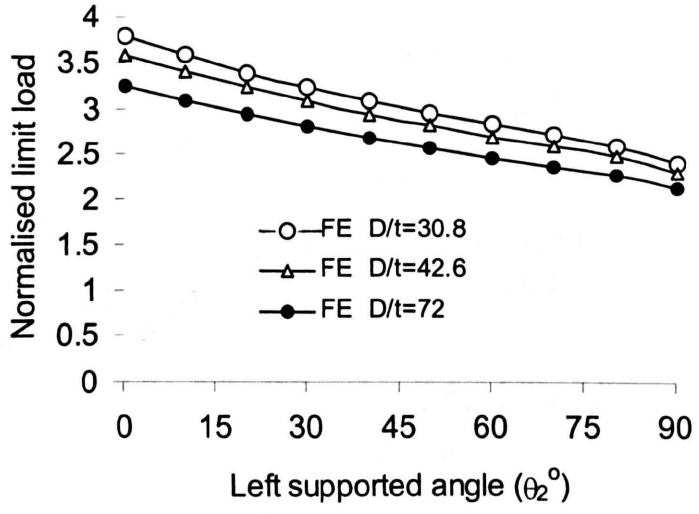

Fig. 5.13 The normalised peak load versus left support angular position, with θ_5=45°, D/t=72, 42.6 and 30.8 and θ_1=0°, for X65 SAW steel.

A comparison of Figs. 5.10 to 5.13, for the X65 SAW material, with the corresponding results for the Ideal-A material (Figs. 5.6 to 5.9) shows very close correlation. This is more clearly shown in Figs.5.14 (a) to (d) in which the normalised peak loads for the X65 SAW material are also plotted against the corresponding results obtained for the Ideal-A material, for different indenter offset and support angles. It can be seen, from Figs. 5.14 (a) to (d), that very close correlation of the results is obtained for Ideal-A and X65 SAW steel materials. This indicates that the representative flow stress chosen to normalise the data can be used to predict the peak loads, or limit loads, for hardening materials, from data for idealised elastic-plastic materials [see chapter 3]. This conclusion is important when considering the suitability of simple analytical methods for predicting the behaviour of steel pipes.

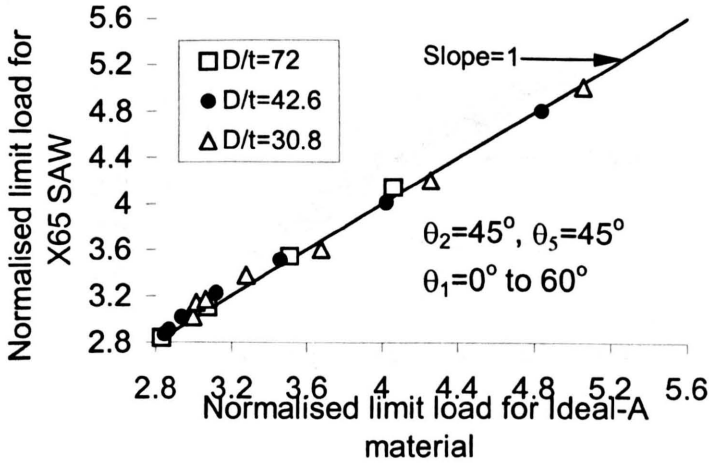

Fig. 5.14 (a)

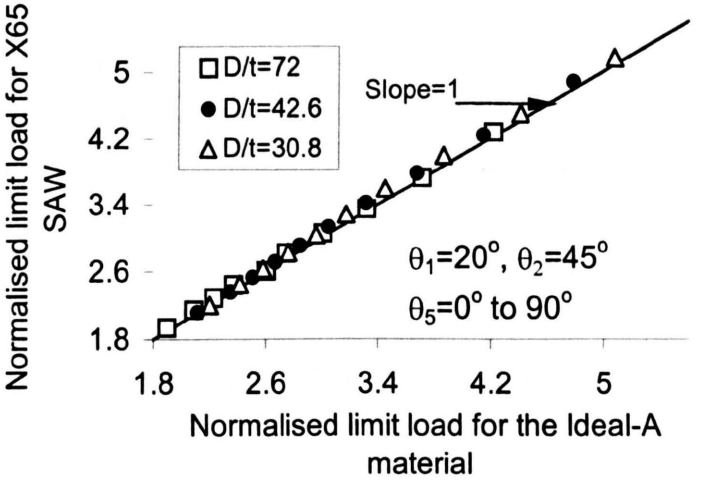

Fig. 5.14 (b)

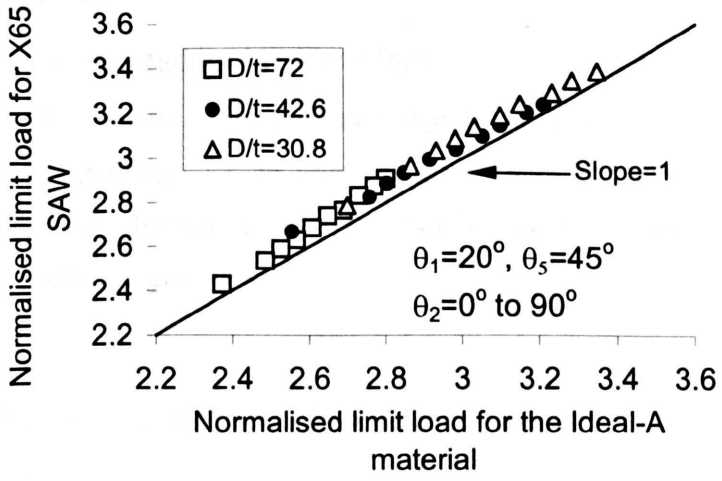

Fig. 5.14 (c)

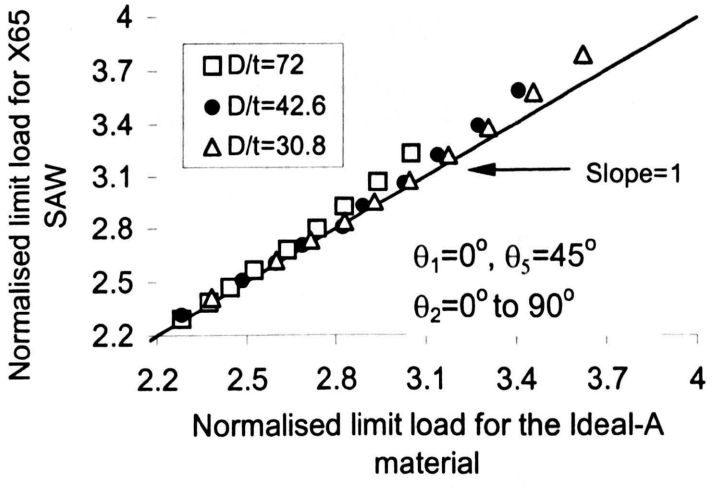

Fig.5.14 (d)

Fig.5.14 FE normalised peak loads for X65 SAW steel versus those for 6082-T6 aluminium alloy, for different indenter offset angular positions, different support angular positions and for different D/t ratios.

5.4 Analytical Methods

5.4.1 Initial Load-Displacement Gradient

As with the case of symmetrical loading and support conditions applied in chapter 3, the elastic force-deflection behaviour, for an unpresssurised ring, with asymmetrical loading and support conditions, can be obtained using Castiglano's theorem. The resulting relationship between force and deflection is given by

$$F = \frac{Et^3}{12R^3}\left(\frac{D}{AD+B+C}\right)\delta \tag{5.1}$$

where A, B, C and D are functions of the angles θ_2 and θ_5, i.e.

$$\left.\begin{aligned}
A &= \tfrac{1}{8}\left(\pi+\theta_2+\theta_5+\tfrac{1}{2}(\sin 2\theta_2+\sin 2\theta_5)\right)\\
B &= \left(1+\tfrac{1}{2}\sin\theta_2+\tfrac{1}{2}\sin\theta_5\right)(B1+B2+B3)\\
B1 &= \sin 2\theta_2+\sin 2\theta_5+\sin(\theta_2+\theta_5)+\left(3+\tfrac{1}{2}\sin\theta_2\sin\theta_5\right)(\cos\theta_2+\cos\theta_5)\\
B2 &= -\tfrac{1}{2}(\pi+\theta_2+\theta_5)\left(\cos^2\theta_2+\sin\theta_2+\cos^2\theta_5+\sin\theta_5+2\right)\\
B3 &= -\tfrac{1}{2}\cos\theta_2\sin^2\theta_5-\tfrac{1}{2}\sin^2\theta_2\cos\theta_5\\
C &= \tfrac{1}{4}\left(1+\tfrac{1}{2}\sin^2\theta_2+\sin\theta_2+\tfrac{1}{2}\sin^2\theta_5+\sin\theta_5\right)(C1+C2)\\
C1 &= (\pi+\theta_2+\theta_5)\left(\cos^2\theta_2+\cos^2\theta_5\right)\\
C2 &= -\sin 2\theta_2-\sin 2\theta_5-2\sin(\theta_2+\theta_5)-4\cos\theta_2-4\cos\theta_5\\
D &= \tfrac{1}{2}(\pi+\theta_2+\theta_5)^2-(\cos\theta_2+\cos\theta_5)^2-\tfrac{1}{4}(\pi+\theta_2+\theta_5)(\sin 2\theta_2+\sin 2\theta_5)
\end{aligned}\right\} \tag{5.2}$$

Hence, the initial slope, K, of the indenter force versus depth curves, for an unpressurised ring with asymmetrical loading and support condition, is given by

$$K = \frac{Et^3}{12R^3}\left(\frac{D}{AD+B+C}\right) \tag{5.3}$$

Fig. 5.15 shows a typical comparison between the initial gradients obtained from the FE and experimental tests with the analytical predictions. It can be seen that the agreement is excellent. This degree of accuracy is applicable to all of the materials, geometries, load positions and support positions investigated.

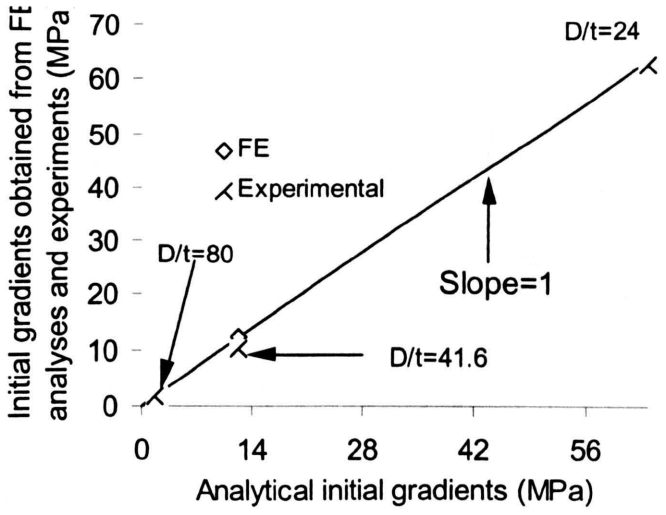

Fig. 5.15 A comparison of initial gradients of the indenter force versus dent depth curves obtained from the FE analyses, the experimental test data and the analytical methods for 6082-T6 aluminium alloy ring models with D/t=80, 41.6 and 24, $\theta_1=0°$, $\theta_2=55°$ and $\theta_5=35°$.

5.4.2 Upper Bound Limit Load Theory

As in the case of symmetrical support and loading conditions [see chapter 3], in order to determine the upper bound, it was assumed that the offset indenter ring has five plastic hinges, at positions A, B, C, D and E, as shown in Fig. 5.16 (a). The rotational angles of these five plastic hinges (A, B, C, D and E) are denoted as α_5, α_2, α_1, α_3 and α_4, respectively, as shown in Fig.5.16 (b). If the load point, position A, moves vertically downwards, as shown in Fig.5.16 (b), the relationships between angles of rotation and the loadline displacement can be determined and hence the upper bound analysis method, previously used for symmetrical support and loading [chapters 3 and 4], can again be used.

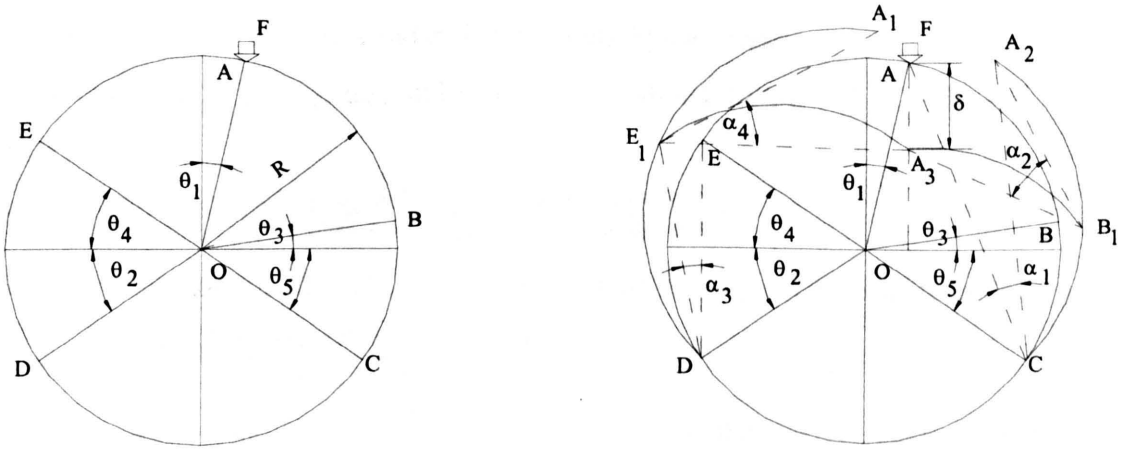

(a) Offset indented ring

(b) Deformation of offset indented ring

Fig. 5.16 Kinematically admissible velocity field for the upper bound analysis

The kinematic relationships can be represented by the following five equations:

$$d\alpha_2 = \frac{\cos\theta_1 + \sin\theta_5}{\cos\theta_1 - \sin\theta_3} d\alpha_1 \qquad 5.4(a)$$

$$d\alpha_4 = \frac{\cos\theta_1 + \sin\theta_2}{\cos\theta_1 - \sin\theta_4} d\alpha_3 \qquad 5.4(b)$$

$$d\alpha_5 = d\alpha_2 + d\alpha_4 - d\alpha_1 - d\alpha_3 \qquad 5.4(c)$$

$$d\delta = R\frac{\cos(\theta_4 - \theta_1) - \cos(\theta_2 - \theta_1) + \sin(\theta_2 + \theta_4)}{\cos\theta_1 - \sin\theta_4} d\alpha_3 \qquad 5.4(d)$$

$$d\delta = R\frac{\cos(\theta_3 + \theta_1) - \cos(\theta_5 + \theta_1) + \sin(\theta_5 + \theta_3)}{\cos\theta_1 - \sin\theta_3} d\alpha_1 \qquad 5.4(e).$$

From equations 5.4(d) and (e), it follows that

$$d\alpha_3 = \frac{\cos\theta_1 - \sin\theta_4}{\cos\theta_1 - \sin\theta_3} \frac{\cos(\theta_3 + \theta_1) - \cos(\theta_5 + \theta_1) + \sin(\theta_5 + \theta_3)}{\cos(\theta_4 - \theta_1) - \cos(\theta_2 - \theta_1) + \sin(\theta_2 + \theta_4)} d\alpha_1 \qquad (5.5).$$

Substituting equation (5.5) into 5.4(b) gives

$$d\alpha_4 = \frac{\cos\theta_1 + \sin\theta_2}{\cos\theta_1 - \sin\theta_3} \frac{\cos(\theta_3 + \theta_1) - \cos(\theta_5 + \theta_1) + \sin(\theta_5 + \theta_3)}{\cos(\theta_4 - \theta_1) - \cos(\theta_2 - \theta_1) + \sin(\theta_2 + \theta_4)} d\alpha_1 \qquad (5.6).$$

The internal energy dissipated, W_I, at the plastic hinges, is given by

$$W_I = M_0(d\alpha_1 + d\alpha_2 + d\alpha_3 + d\alpha_4 + d\alpha_5) \qquad (5.7)$$

where

$$M_0 = \frac{1}{4}\sigma_y t^2 \tag{5.8}$$

where t is the ring wall thickness and σ_y is the material yield stress.

Substituting for $d\alpha_2$, $d\alpha_3$, $d\alpha_4$ and $d\alpha_5$ from equations 5.4(a), (5.5), 5.4(b) and 5.4(c) into (5.7) gives

$$W_I = 2M_0\left[\frac{\cos\theta_1+\sin\theta_5}{\cos\theta_1-\sin\theta_3}+\frac{\cos\theta_1+\sin\theta_2}{\cos\theta_1-\sin\theta_3}\frac{\cos(\theta_3+\theta_1)-\cos(\theta_5+\theta_1)+\sin(\theta_5+\theta_3)}{\cos(\theta_4-\theta_1)-\cos(\theta_2-\theta_1)+\sin(\theta_2+\theta_4)}\right]d\alpha_1 \tag{5.9}.$$

Based on equations 5.4(d) and 5.4(e), the work done, W_E, by the external force, F, is given by

$$W_E = Fd\delta = RF\frac{\cos(\theta_3+\theta_1)-\cos(\theta_5+\theta_1)+\sin(\theta_5+\theta_3)}{\cos\theta_1-\sin\theta_3}d\alpha_1 \tag{5.10}.$$

Since the work done by the external force is equal to the internal energy dissipated, then equations (5.9) and (5.10) give

$$F = 2M_0\frac{1}{R}\left[\frac{\cos\theta_1+\sin\theta_5}{\cos(\theta_3+\theta_1)-\cos(\theta_5+\theta_1)+\sin(\theta_5+\theta_3)}+\frac{\cos\theta_1+\sin\theta_2}{\cos(\theta_4-\theta_1)-\cos(\theta_2-\theta_1)+\sin(\theta_2+\theta_4)}\right] \tag{5.11}.$$

Minimising the external force F with respect to θ_3 and θ_4, the optimised upper bound, F_U, is given by

$$F_U = 2M_0\frac{1}{R}Ls(\theta_1,\theta_2,\theta_5) \tag{5.12(a)}$$

where $Ls(\theta_1,\theta_2,\theta_5)$ is a non-dimensional function of θ_1, θ_2 and θ_3, given by

$$Ls(\theta_1,\theta_2,\theta_5) = \frac{\cos\theta_1+\sin\theta_2}{2\sin\left(\frac{\pi}{4}+\frac{\theta_2+\theta_1}{2}\right)-\cos(\theta_2+\theta_1)}+\frac{\cos\theta_1+\sin\theta_5}{2\sin\left(\frac{\pi}{4}+\frac{\theta_5-\theta_1}{2}\right)-\cos(\theta_5-\theta_1)} \tag{5.12(b)}.$$

5.5 Comparison of the Analytical Solutions with the FE and Experimental Results

5.5.1 6082-T6 Alloy Results

The indenter force versus dent depth curves, obtained from the FE analyses and experimental tests performed on the aluminium alloy models, are shown in Fig. 5.17. The analytical limit load solutions, also shown in Fig. 5.17, are calculated by using a representative flow stress which is the average of the yield stress and the ultimate tensile stress. The analytical, elastic solutions for the initial gradient, also shown in Fig. 5.17, are obtained using equation (5.1). The limit loads, obtained from the FE and analytical analyses, are also given in Table 5.5, which shows that the analytical limit loads, obtained using the representative flow stress in the predictions, are

generally in reasonably good agreement with those obtained from the experiments and the FE analyses. However, these data indicate that if a slightly lower representative flow stress was used for the analytical predictions, then generally closer correlation between the analytical solutions and those obtained from the FE analyses and experimental tests would be obtained.

Table 5.5: FE, experimental and analytical limit loads for 6082-T6 aluminium alloy rings using yield, flow and ultimate tensile stresses in the analytical formulations (σ_y= yield stress; σ_f= representative flow stress; σ_{uts}= ultimate tensile stress) for $\theta_1=0°$, $\theta_2=55°$ and $\theta_5=35°$

D/t	Experimental N/mm		FE N/mm	Analytical using σ_y	Analytical using σ_f	Analytical Using σ_{UTS}
80	TE1	14.69	15.5	17	18.4	19.8
41.6	TE2	64.03	69.5	66.6	72.3	77.9
24	TE3	203.25	225	196.3	213.	229.7
	TE4	200.29				

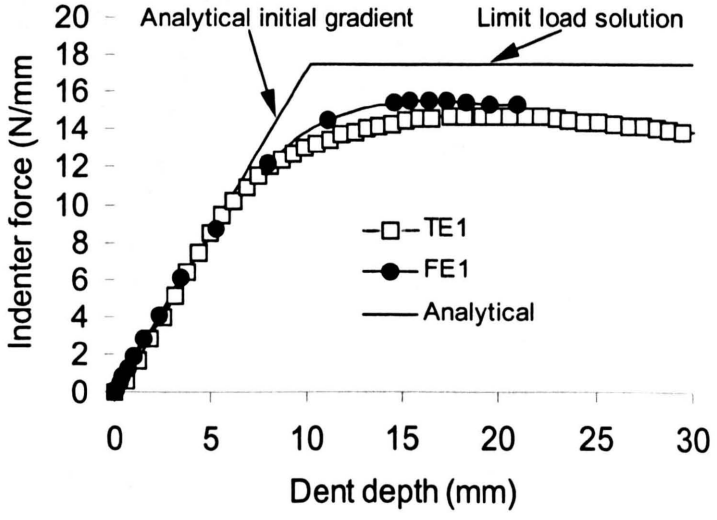

(a) D/t =80

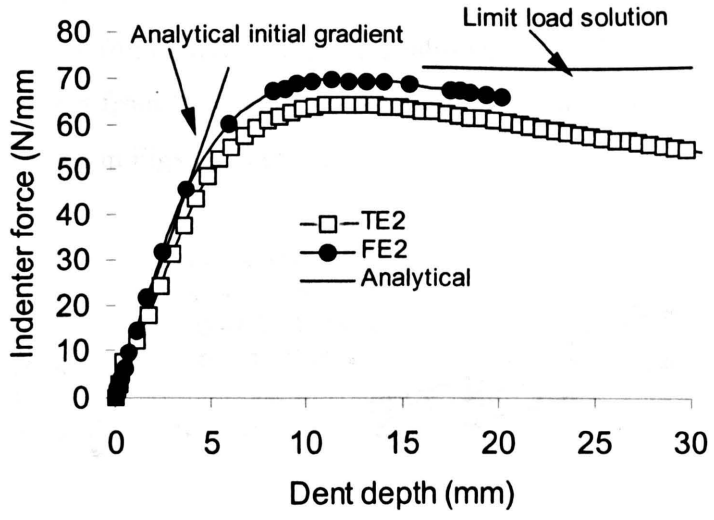

(b) D/t =41.6

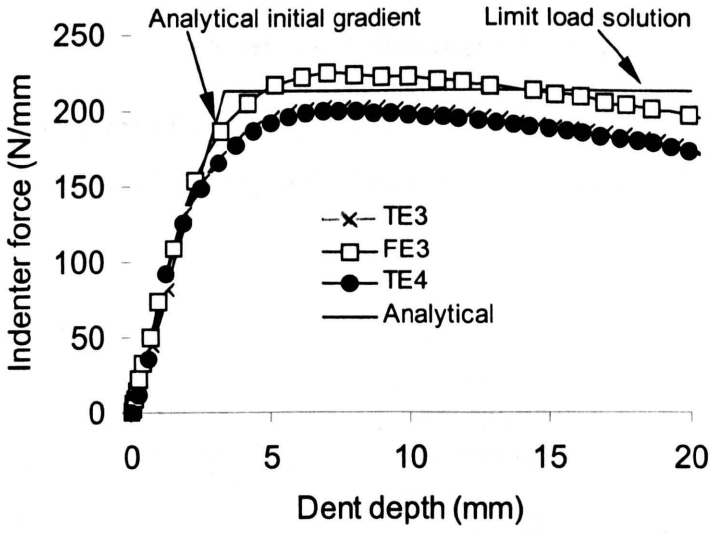

(c) D/t =30.8.

Fig. 5.17 Indenter force versus dent depth curves obtained from the FE analyses, experimental tests and the analytical methods, for the case with θ_1=0°, θ_2=55° and θ_5=35°, for the 6082-T6 aluminium alloy rings

5.5.2 Ideal-A Results

The peak loads obtained from each of the FE analyses, using the elastic perfectly plastic material model (Ideal-A) and from the theoretical analyses, are normalised by dividing them by $\sigma_y t^2/2R$; the results are shown in Figs. 5.18 to 5.21.

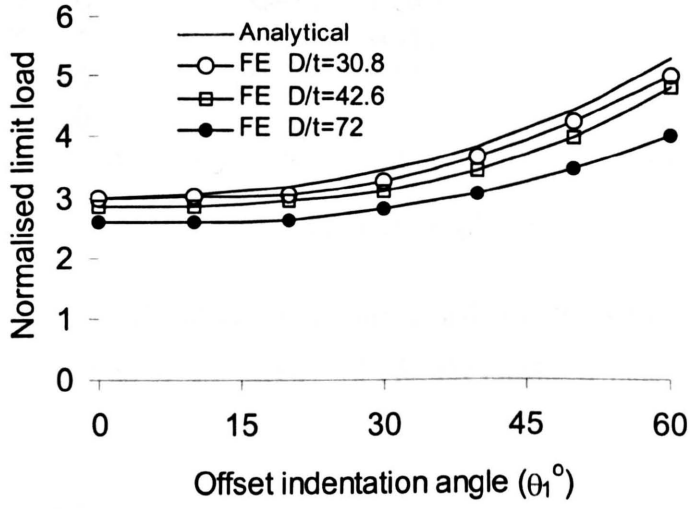

Fig.5.18 A comparison of the FE and analytical normalised limit loads for different offset angular positions, with $\theta_2=\theta_5=45°$, for the idealised material Ideal-A

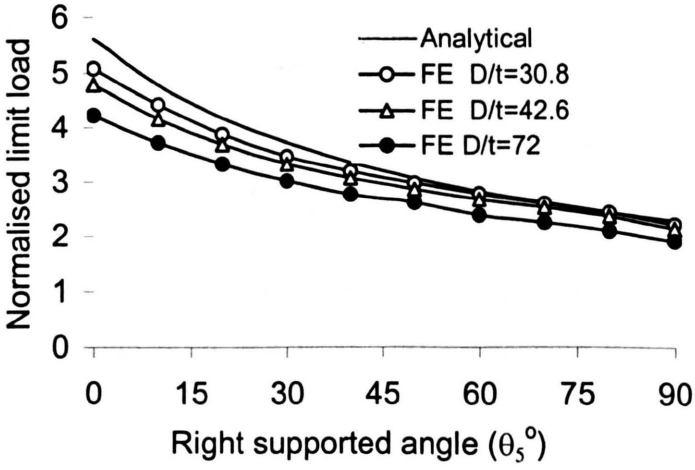

Fig.5.19 A comparison of the FE and analytical normalised limit loads for different right support angular positions, with $\theta_1=20°$ and $\theta_2=45°$, for the idealised material Ideal-A

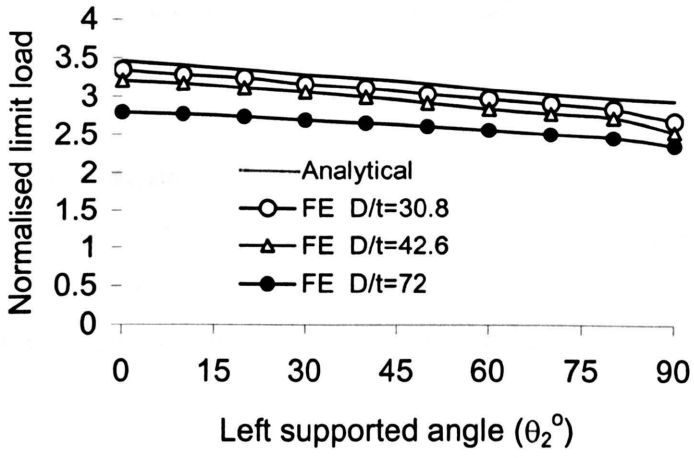

Fig.5.20 A comparison of the FE and analytical normalised limit loads for different left support angular positions, with $\theta_1=20^o$ and $\theta_5=45^o$, for the idealised material Ideal-A

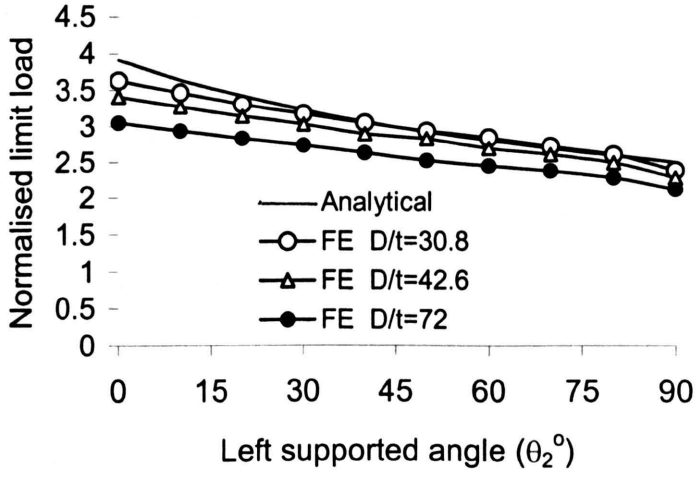

Fig.5.21 A comparison of the FE and analytical normalised limit loads for different left support angular positions, with $\theta_1=0^o$ and $\theta_5=45^o$, for the idealised material Ideal-A

Figs. 5.18 to 5.21 show that for the smaller D/t ratios, i.e. D/t=41.6 and 30.8, very close correlation of the FE and the analytical solutions can be obtained. However, for the larger D/t ratios, i.e. D/t=80, the FE solutions are significantly lower than the corresponding analytical solutions. This is because large non-linear deformation effects which occur for the large D/t ratio

rings, are included in the FE analyses but not in the analytical solutions. Therefore, for the peak load predictions of large D/t ratios, it is suggested that the yield stress should be used in the analytical method (see chapter 3).

5.5.3 X65 SAW Steel Results

The normalised limit loads obtained from each of the FE analyses for the X65 SAW steel models are compared with those obtained for the idealised material Ideal-A in Figs.5.14 (a) to (d). The close correlation of the results indicates that the normalised limit loads can be obtained either using the idealised material Ideal-A or using the X65 SAW steel models in the FE analyses. The normalised limit loads obtained from the FE analyses and the analytical methods for the idealised material Ideal-A are the same as those for the X65 SAW steel. Comparisons of the peak loads, obtained from the FE analyses, and the analytical solutions are shown in Figs. 5.22 to 5.25 for the X65 SAW steel material. It can be seen from Figs. 5.22 to 5.25 that a reasonably close correlation exists between the analytical solutions and the FE predictions of the peak loads for the X65 SAW steel material.

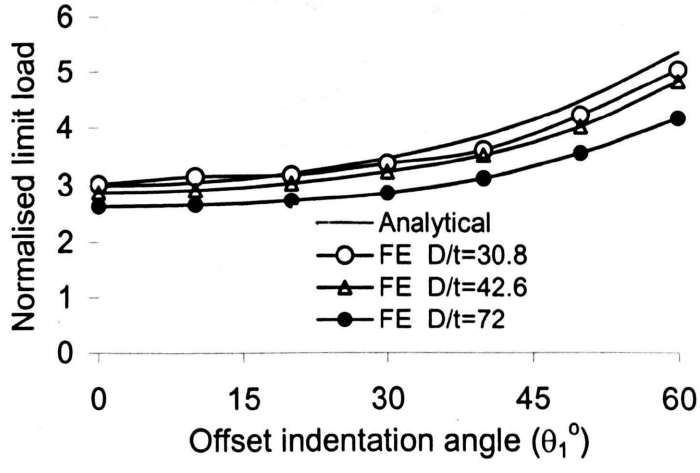

Fig.5.22 A comparison of the FE and analytical normalised limit loads for different offset angular positions, with $\theta_2=\theta_5=45^o$, for X65 SAW steel material

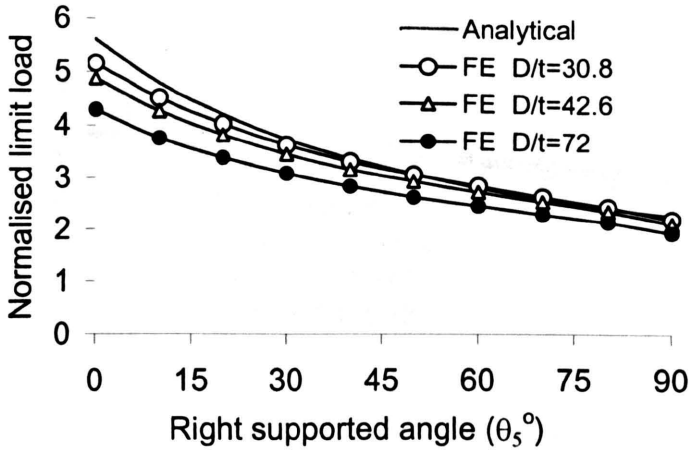

Fig.5.23 A comparison of the FE and analytical normalised limit loads for different right support angular positions, with θ_1=20° and θ_2=45°, for X65 SAW steel material

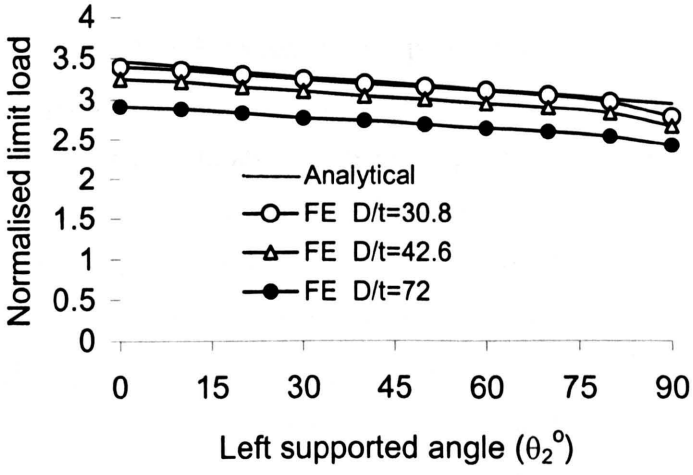

Fig.5.24 A comparison of the FE and analytical normalised limit loads for different left support angular positions, with θ_1=20° and θ_5=45°, for X65 SAW steel material

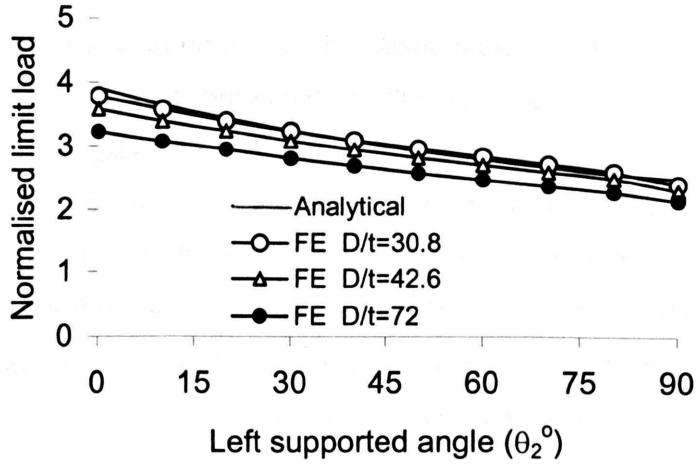

Fig.5.25 A comparison of the FE and analytical normalised limit loads for different left support angular positions, with $\theta_1=0^o$ and $\theta_5=45^o$, for X65 SAW steel material

5.6 Conclusions

The reasonably close correlation between the FE predictions of indenter force versus depth and the corresponding experimental test data indicates that the FE meshes, boundary conditions and large deformation FE analysis methods are capable of producing accurate results.

An upper bound limit load analytical approach for predicting the peak (or limit) loads gives good (i.e. close to the FE results) upper bounds for rings with elastic perfectly plastic material behaviour models. The correlation is generally good but is poorest for the larger D/t ratios because the analytical approach does not model the significant effect of the geometric nonlinearity caused by large deformations which occur with large D/t ratios.

Using a representative flow stress, which is the average of the yield stress and ultimate tensile stress, a reasonably good correlation between the analytical and FE predictions, for rings made from 6082-T6 aluminium alloy and X65 SAW steel, are obtained. For higher D/t ratios, better correlation would be obtained if the yield stress is used to predict the limit loads using the analytical approach.

The initial slope and peak values of the force versus dent depth curves can be accurately predicted using simple analytical approaches. Use of the simple analytical approaches could significantly reduce the time and effort required in assessing the likely effects on the structural integrity of dents created in pipelines due to accidents.

5.7 Summary

The results of investigations to determine the elastic-plastic response of unpressurised pipes with long offset indentations are presented in this chapter. They include the results of experimental tests, FE analyses and analytical methods. Three different materials and five different geometries were used to investigate their effects on the behaviour. A comparison of the experimental results, the FE and the analytical solutions indicates that the general analytical formulations developed in this chapter, for predicting the peak indenter loads in offset indented pipes, are reasonably accurate. Also the analyses presented in this chapter indicate that using a representative flow stress, which is the average of yield and ultimate tensile stresses, in the analytical method, is appropriate for predicting the peak indenter loads.

Chapter 6

Force-Deflection Behaviour of Pressurised Pipes Subjected to Loading by Axially Long Offset Indenters

6.1 Introduction

If an indentation is axially long, then the indenter force versus deflection behaviour can be accurately assessed using a ring model for the pipe; this greatly simplifies the analysis. The possible modes of failure which must be taken into account as a result of indentation are the immediate failure by puncturing or by low cycle fatigue due to fluctuating pressure and the significant residual stresses resulting from the indentation. Therefore, to ensure that failure does not occur, it is important to be able to predict the force versus deflection behaviour of indented pipes under a wide range of conditions as discussed in [chapters 3-5].

This chapter contains an investigation of the limit load and force versus deflection behaviours of dented rings with non-symmetrical support and offset loading, using analytical methods and FE analyses. The effects of asymmetry of supports, offset of loading, internal pressure, types of material and geometry are investigated. The loading and support conditions are the same as the shown in Fig. 5.1. The FE meshes, boundary conditions and large deformation FE analysis methods used have been validated by comparing predictions for unpressurised rings with the results of experimental tests.

6.2 FE Analysis

6.2.1 Materials

Two materials were used in the FE analyses. Fig. 3.1 shows the stress-strain curve for a practical gas pipeline material, X65 SAW steel and a 6082-T6 aluminium alloy, for which experimental test data (with zero internal pressure) is available [chapter 5]. Young's modulus, Poisson's ratio, yield stress and ultimate tensile stress for both materials are given in Table 3.2. In the FE analyses, all materials were assumed to obey an isotropic hardening rule.

6.2.2 FE Meshes, Boundary Conditions and Loading

The ABAQUS [26] FE software was used for the analyses. All models consisted of 3600 8-noded, plane-strain, reduced integration elements, as shown in Fig. 5.4. The rings were fully restrained at the outer diameter at positions C and D (Fig. 5.4 (a)). The indentation load was applied in the vertically downward direction at the outer diameter position at point A. In total 19 analyses were performed, as defined in Tables 6.1.

Table 6.1: The geometries, pressures, supporting and loading positions used in the FE analyses.

FE No.	D/t	t (mm)	θ_1	θ_2	θ_5	Pressure (MPa)	Gradient (MPa)
FE1 *6	80.0	1.5	0°	35°	55°	0	1.85
FE2 *6	42.6	3.	0°	35°	55°	0	13.15
FE3 *6	24.0	5.	0°	35°	55°	0	71.05
FE4 *X	42.6	3.	0°	45°	45°	5	58.30
FE5 *X	42.6	3.	10°	45°	45°	5	62.30
FE6 *X	42.6	3.	20°	45°	45°	5	62.60
FE7 *X	42.6	3.	30°	45°	45°	5	69.00
FE8 *X	42.6	3.	0°	55°	35°	5	60.00
FE9 *X	42.6	3.	0°	65°	25°	5	63.50
FE10 *X	42.6	3.	0°	75°	15°	5	70.40
FE11 *X	42.6	3.	0°	55°	35°	0	42.20
FE12 *X	42.6	3.	0°	55°	35°	0.5	44.20
FE13 *X	42.6	3.	0°	55°	35°	2.5	51.60
FE14 *X	42.6	3.	0°	55°	35°	8	70.82
FE15 *X	42.6	3.	0°	10°	-10°	5	203.3
FE16 *X	42.6	3.	0°	35°	15°	5	98.20
FE17 *X	72.0	1.2	10°	45°	45°	2.91	17.60
FE18 *X	72.0	1.2	0°	55°	35°	2.91	17.40
FE19 *X	30.8	3.	10°	45°	45°	7	136.60
FE20 *X	30.8	3.	0°	55°	35°	7	131.80

Note: *6 and *X refer to 6082-T6 aluminium alloy and X65 SAW steel, respectively.

The loads were applied using a rigid indenter with a 2mm radius, to match the conditions for existing experimental test data [chapter 5], and rigid surface contact elements, with no slipping between the indenter and the rings. Large deformation, elastic-plastic analyses were performed, using the standard RIKS algorithm facility within the ABAQUS [26] programs.

6.3 FE Results

6.3.1 6082-T6 Aluminium Alloy

Typical indenter force versus depth results, for an unpressurised ring, obtained from the FE1 to FE3 FE analyses, performed with the aluminium alloy material models, are shown in Fig.6.1. Also shown in Fig. 6.1 are the corresponding experimental test results. It can be seen that the agreement between the FE and experimental results is generally very good, indicating that the meshes, boundary conditions and large deformation analysis are suitable for the present application.

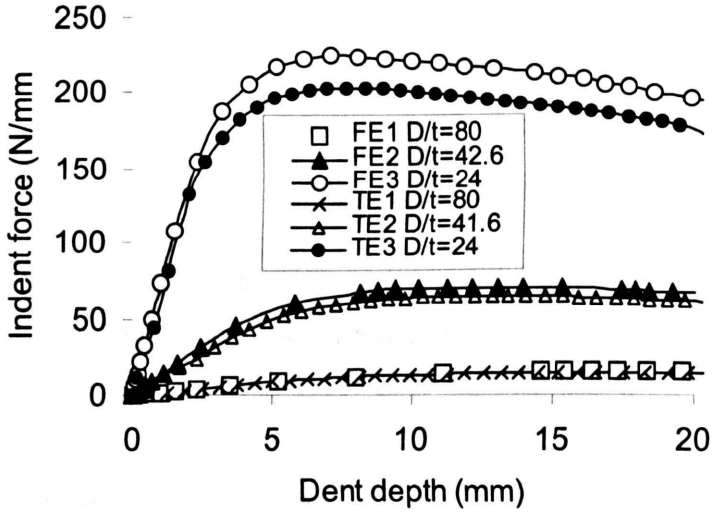

Fig.6.1 Indenter force versus dent depth obtained from experimental and FE analyses of 6082-T6 alloy rings, with $\theta_1=0°$, $\theta_2=55°$ and $\theta_5=35°$.

6.3.2 X65 SAW steel

The X65 SAW steel material has been used to investigate the effects of the loading position, the pressure, the supporting positions and the ring dimensions on the indenter force versus deflection curves.

6.3.2.1 Effect of Loading Positions

The effect of loading position has been investigated using the results of the FE4 to FE7 analyses in which the indenter offset angle, θ_1, was varied from 0° to 30°. The D/t ratio used is 42.6, the internal pressure is 5MPa and the left and right supporting angular positions are both

45°. The indenter force-deflection curves are shown in Fig 6.2. It can be seen that the differences in the curves are relatively small, but the higher curves are related to the lower offset angles.

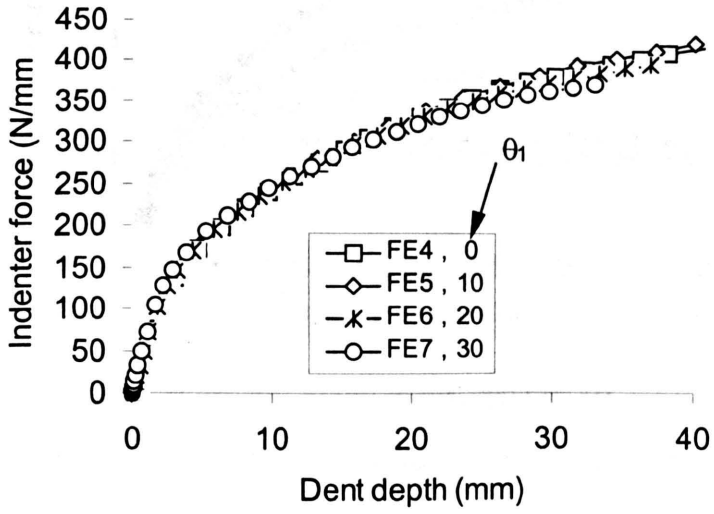

Fig. 6.2 Indenter force versus deflection curves obtained from FE analyses for the X65 SAW materials with D/t=42.6, t=3mm, a pressure of 5MPa, both support angular positions are at 45° and indenter offset angles of 0°, 10°, 20° and 30°.

6.3.2.2 Effect of Internal Pressure

The effect of internal pressure was investigated using the results of the FE8 and FE11 to FE14 analyses for D/t=42.6, θ_1=0°, θ_2=55° and θ_5=35°. The indenter force versus deflection curves are shown in Fig 6.3. It can be seen that at low pressures, there is a peak in the force versus deflection curve. However, at the higher pressures, the curves continue to increase even at high dent depths (i.e. dent depths > 10 × wall thickness).

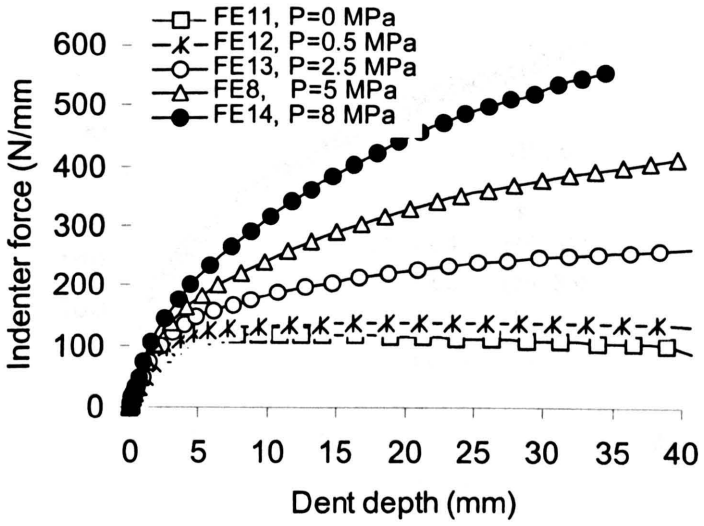

Fig. 6.3 Indenter force versus deflection curves for the X65 SAW material with D/t=42.6, t=3mm, $\theta_1=0^\circ$, $\theta_2=55^\circ$, $\theta_5=35^\circ$ and pressures of 0, 0.5, 2.5, 5 and 8MPa.

6.3.2.3 Effects of Support Position

The effect of the support position was investigated for rings with D/t=42.6, using the results of the FE4 and FE8 to FE10, FE15 and FE16 analyses. For the case where the total support span (i.e. $\theta_2 + \theta_5=90^\circ$) is constant and with a zero offset angle, i.e. $\theta_1=0^\circ$; the (θ_2, θ_5) pairs used were (45°, 45°), (55°, 35°), (65°, 25°), and (75°, 15°). The indenter force versus deflection curves are shown in Fig 6.4. It can be seen that as the support position deviates from the symmetric position, the force required to produce a given deflection decreases. However, the reduction is relatively small.

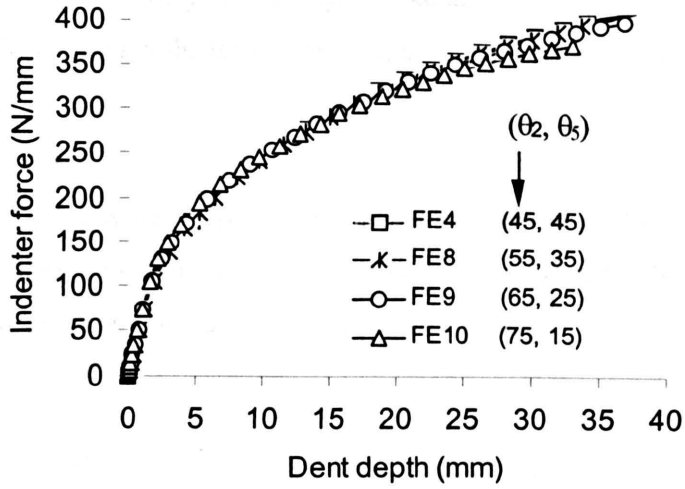

Fig.6.4 Indenter force versus deflection curves obtained from FE analyses with the X65 SAW material with a pressure of 5MPa, D/t=42.6, t=3mm and θ_1=0°, for (θ_2, θ_5) pairs of (45°, 45°), (55°, 35°), (65°, 25°) and (75°, 15°).

The results for various angular support positions of (θ_2, θ_5)=(10°, -10°), (35°, 15°) and (55°, 35°), from the FE15, FE16 and FE8 analyses, for the D/t ratio of 42.6, internal pressure of 5MPa and a zero indenter offset angle, are shown in Fig 6.5.

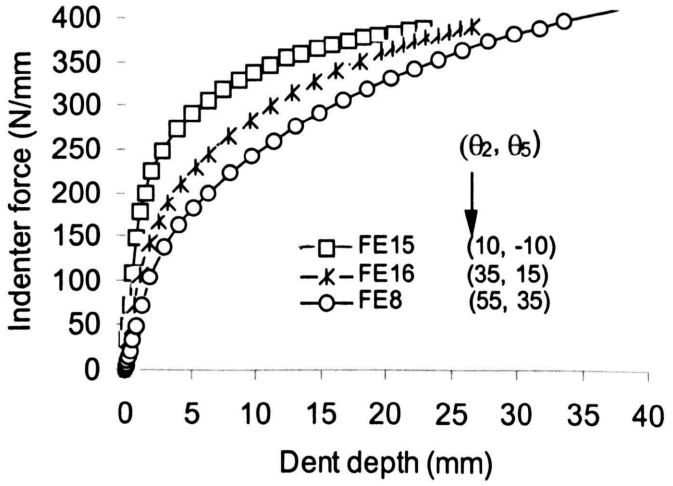

Fig. 6.5 Indenter force versus deflection curves obtained from FE analyses with the X65 SAW material with D/t=42.6, t=3mm, a zero indenter offset indentation angle, a pressure of 5MPa and support angle pairs, (θ_2, θ_5) of (10°, -10°), (35°, 15°) and (55°, 35°).

It can be seen that curves converge at the higher load and deformation levels but at lower load levels, the curves are higher when the total support span (i.e. $\theta_2 + \theta_5$) approaches zero.

6.3.2.4 Effect of D/t

The effects of the D/t ratio were investigated using the results of the FE5, FE8 and FE17 to FE20 analyses with a pressure which produces a mean hoop stress of 0.234 times the yield stress. The indenter force versus deflection curves are shown in Fig 6.6.

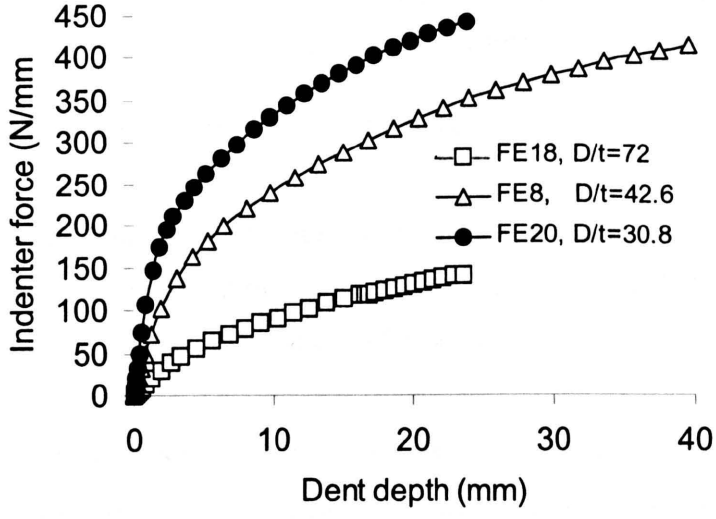

(a) Indentation with θ_1=0°, θ_2=55° and θ_5=35°, t=1.2, 3 and 3mm.

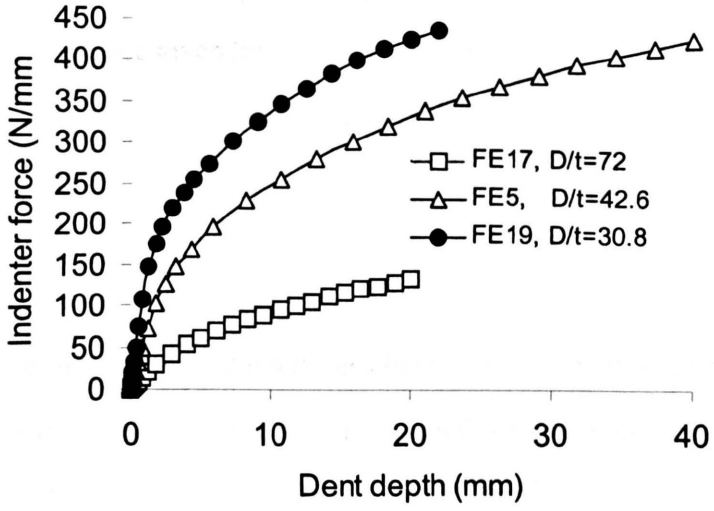

(b) Indentation with θ_1=10°, θ_2=45° and θ_5=45°, t=1.2, 3 and 3mm.

Fig. 6.6 Indenter force versus deflection curves obtained from FE analyses for the X65 SAW models with an internal pressure which produce a mean hoop stress of 0.234 times the yield stress and with D/t ratios of 72, 42.6 and 30.8.

From Fig. 6.6 (a), which presents results with θ_1=0°, θ_2=55° and θ_5=35°, it can be seen that the curves are higher when the D/t ratio reduces. Similarly, Fig. 6.6 (b) shows the same effect with θ_1=10°, θ_2=45° and θ_5=45°.

6.4 Analytical Methods

6.4. 1 Elastic Behaviour

In chapter 5, an analytical solution for the elastic indenter force versus deflection behaviour, for an unpresssurised ring, was obtained using Castiglano's theorem, see equations 5.1 and 5.2.

For the small elastic deformation range, as is the case of that with symmetric support and radial loading conditions [see chapter 4], the indenter force, for a pressurised ring with asymmetric supports and offset loading conditions, is given by

$$F = K_{ep}\delta = (K_e + K_p)\delta \tag{6.1}$$

where K_e is initial stiffness term and K_p is the stiffness associated with the stress caused by the internal pressure; K_e and K_p are given by

$$K_e = \frac{Et^3}{12R^3}\left(\frac{D}{AD+B+C}\right) \tag{6.2}$$

$$K_p = p \lim_{\delta_0 \to 0} \frac{F^P}{\delta_0} \tag{6.3}$$

where δ_0 is δ/R

The stiffness, K_p, exists due to the coupling effect of the internal pressure and the indenter force on the indenter force versus depth curve in the small deformation range, see chapter 4. δ_0, defined as δ/R, is dimensionless and F^P is given by equation (a27) in Appendix 3.A.3. For small deformation the indenter force, F, can be approximately given by [chapter 4]

$$F = \frac{Et^3}{12R^3}\left(\frac{D}{AD+B+C}\right)\delta + pR\,F^P \tag{6.4}$$

The initial gradients of the indenter force versus depth curves, obtained from the analytical approach, described by equations (6.1) to (6.3), the FE analyses in Table 6.1 and the experimental tests (TE1 to TE3), are shown in Fig.6.7. It can be seen that there is a very good correlation between the results.

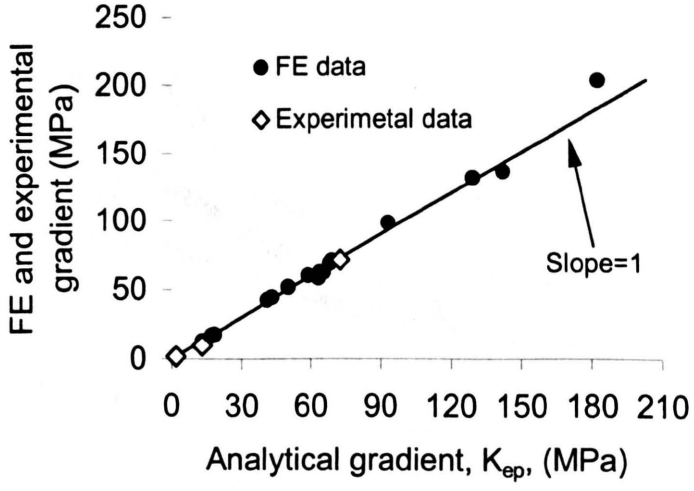

Fig.6.7 The initial gradients of the indenter force versus depth curves obtained from the analytical approach, the FE analyses and the experimental tests.

6.4.2 Non-linear Elastic-Plastic Behaviour

For long indentation of pipes, it has been shown [chapters 3, 5] that a limit method can accurately predict peak loads by assuming that plastic hinges exist at five positions A, B, C, D and E (see Fig.(3.a1)). The kinematic relationship between the vertical displacement or dent depth and angles of rotation of the hinges can be determined. From these kinematic relationships, the work done, W_p, by the internal pressure, and the work done, W_E, by the indenter force, can be obtained using an incremental method. The energy dissipated, W_I, during deformation can also be obtained using the incremental method. The indenter force, F, for a pressurised indented ring with asymmetric supports and an offset indenter loading condition, can be obtained using the same method as that used for a symmetric support and loading conditions (i.e. $\theta_1=0^o$, $\theta_2=\theta_5$) [chapter 4]. The approach is outlined in Appendix 3.A.3. Hence the indenter force, F, can be expressed as

$$F = \frac{4M_0}{R} F^M + pR F^P \qquad (6.5).$$

where F^M and F^P are both dimensionless functions related to the effects of the deformation and the internal pressure.

F^M and F^P are plotted against the non-dimensional vertical displacement (dent depth, δ_o) in Fig.6.8 for $\theta_1=0^o$, $\theta_2=\theta_5=0^o$, 25° and 45°.

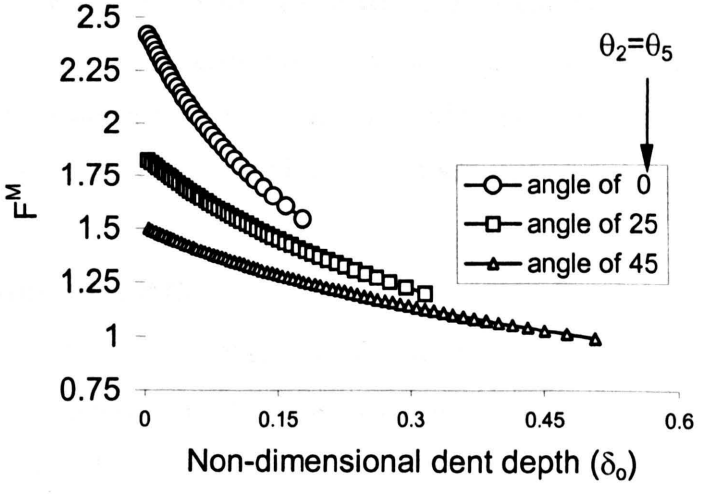

(a) Non-dimensional coefficient, F^M

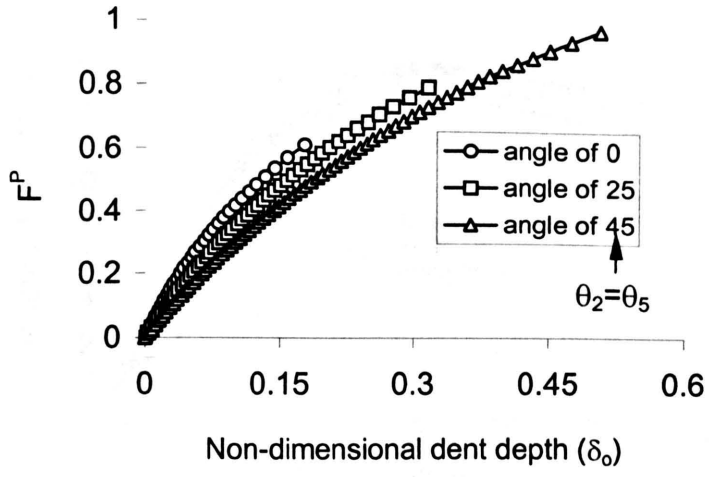

(b) Non-dimensional coefficient, F^P

Fig. 6.8 Non-dimensional coefficients for $\theta_1=0°$, $\theta_2=\theta_5=0°$, 25° and 45°.

Fig. 6.8 (a) and equation (6.5) cannot be used to predict the indenter force for the small deformation in the elastic range. Therefore, as with symmetric loading and symmetric support [chapter 4], the indenter force can be determined using the two indenter force versus depth curve predictions provided by equations (6.4) and (6.5).

6.5 Comparisons of Experimental, FE and Analytical Solutions

The results obtained from the experimental tests, the FE analyses and the analytical approach were compared in order to validate the FE modelling method (see section 6.3.1) and to assess the accuracy of the analytical approach described in this chapter.

6.5.1 6082-T6 Aluminium Alloy

The force versus deflection curves obtained from the experimental tests, FE analyses FE1 to FE3 and the analytical approach, for the 6082-T6 aluminium alloy, with $\theta_1=0°$, $\theta_2=55°$ and $\theta_5=35°$, are shown in Fig. 6.9. These curves indicate that the analytical, FE and experimental results are in broad agreement for both small and large deformations of the rings. Also, the analytical approach produces particularly good predictions in the early (small indentation depth) and large deformation stages of the deformation process.

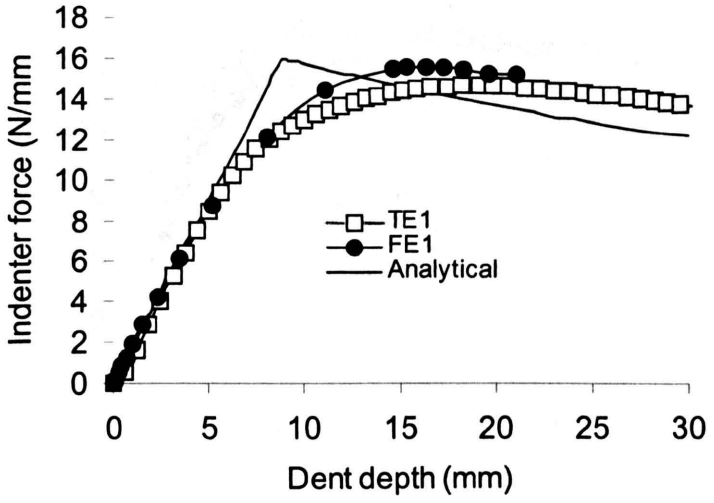

(a) D/t =80, t=1.5mm

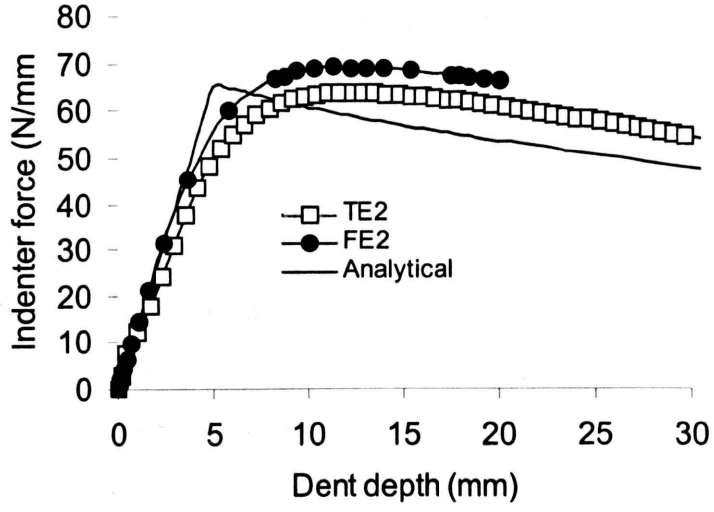

(b) D/t =41.6, t=3mm

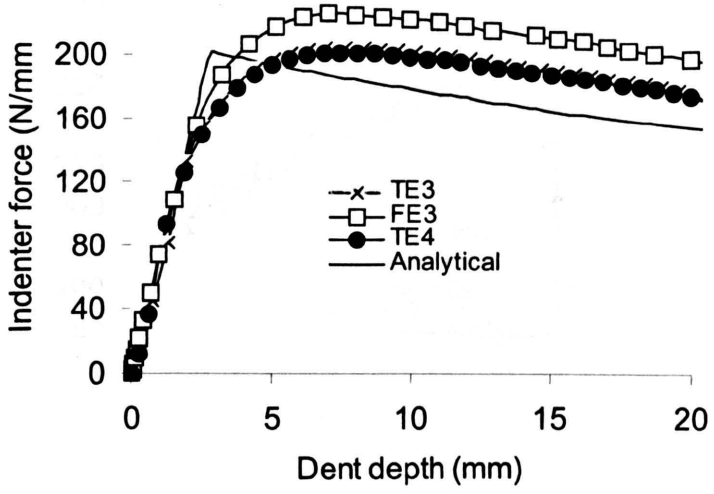

(c) D/t=30.8, t=5mm

Fig. 6.9 Indenter force versus depth curves obtained from the experimental tests, the FE analyses and the analytical approach for a ring with p=0 MPa, θ_1=0°, θ_2=55° and θ_5=35°, using 6082-T6 aluminium alloy.

6.5.2. X65 SAW Steel

6.5.2.1 Effect of Indentation Offset

The force versus deflection curves obtained from the FE analyses FE4 to FE7 and the analytical solutions for the X65 SAW steel models with θ_1=0°, 10°, 20°, and 30°, θ_2=θ_5=45° and p=5 MPa, are shown in Fig. 6.10. These curves indicate that the analytical and FE results are reasonably consistent and that the effects of the indenter offset angle on the indenter force versus deflection curves is negligible in this case.

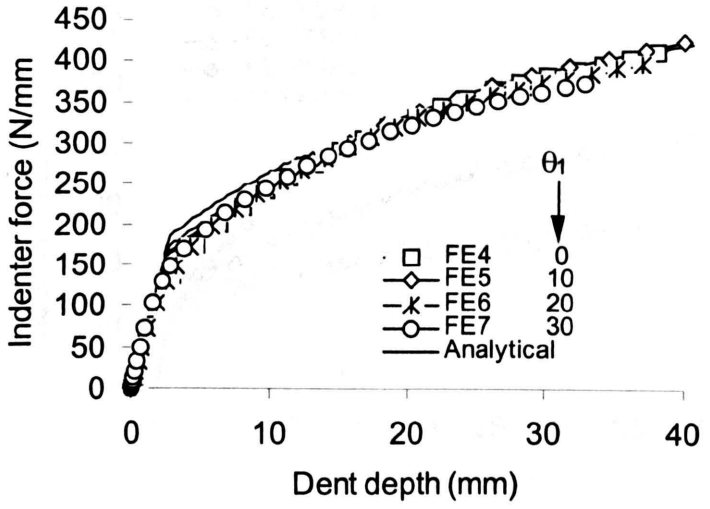

Fig. 6.10 Indenter force versus depth curves obtained from the FE and analytical solutions for θ_1=0°, 10°, 20° and 30° and for X65 SAW in rings with a D/t=42.6, t=3mm, θ_2=θ_5=45° and p=5MPa.

6.5.2.2 Effect of Internal Pressure

The indenter force versus deflection curves obtained from the FE analyses FE8 and FE11 to FE14 and the corresponding analytical solutions, for the X65 SAW steel, with different internal pressure levels, are shown in Fig. 6.11. These curves indicate that the analytical and FE results are in excellent agreement.

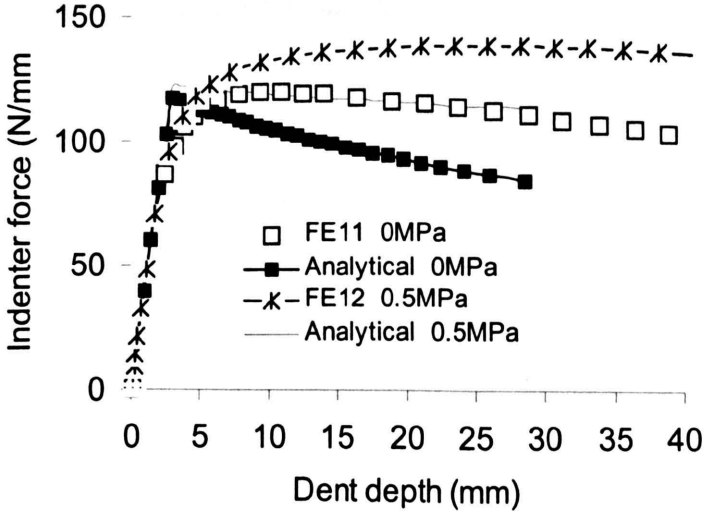

(a) p=0 and 0.5MPa

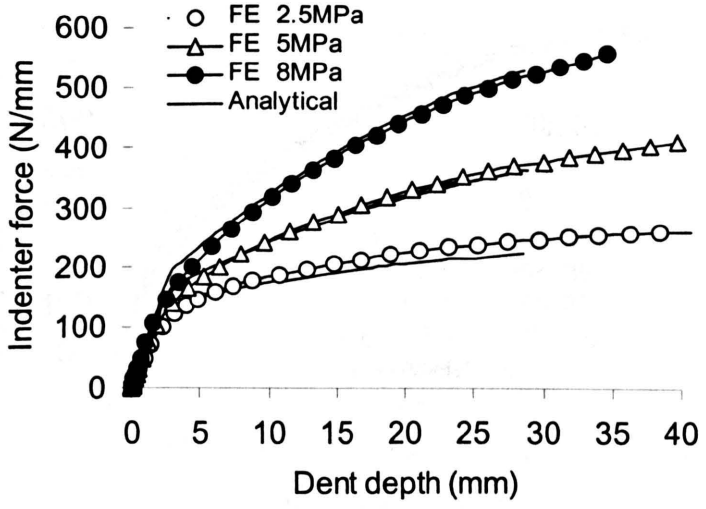

(b) p=2.5, 5 and 8MPa

Fig. 6.11 Indenter force versus depth curves obtained from the FE and analytical solutions for X65 SAW rings with D/t=42.6, t=3mm, $\theta_1=0^\circ$ and $(\theta_2, \theta_5)= (55^\circ, 35^\circ)$.

6.5.2.3 Effect of Angular support Positions

The force versus deflection curves obtained from the FE analyses FE4, FE8 to FE10 and the corresponding analytical solutions, for the X65 SAW steel, with $\theta_1=0^\circ$, $(\theta_2, \theta_5)= (10^\circ, -10^\circ)$, $(35^\circ, 15^\circ)$ and $(55^\circ, 35^\circ)$ and p=5MPa, are shown in Fig. 6.12. These curves indicate that the analytical and FE results are in good agreement and that the effect of the radial offset angles on the indenter force versus deflection curves is negligible in this case.

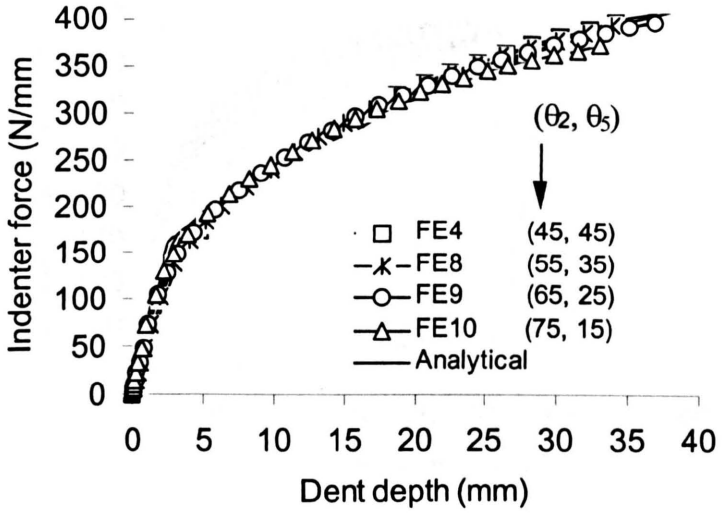

Fig. 6.12 Indenter force versus depth curves obtained from the FE and analytical solutions for $\theta_1=0^\circ$, $(\theta_2, \theta_5)=(10^\circ, -10^\circ)$, $(35^\circ, 15^\circ)$ and $(55^\circ, 35^\circ)$, for X65 SAW, with p=5MPa.

The indenter force versus deflection curves obtained from FE analyses (FE8, FE15, and FE16) and the corresponding analytical solutions, performed on the X65 SAW models, with D/t=42.6, for p=5MPa and $\theta_1=0^\circ$, are shown in Fig. 6.13. The close correlation of the curves obtained from the analytical and FE results indicates that the analytical method can accurately describe the effects of the angular support positions.

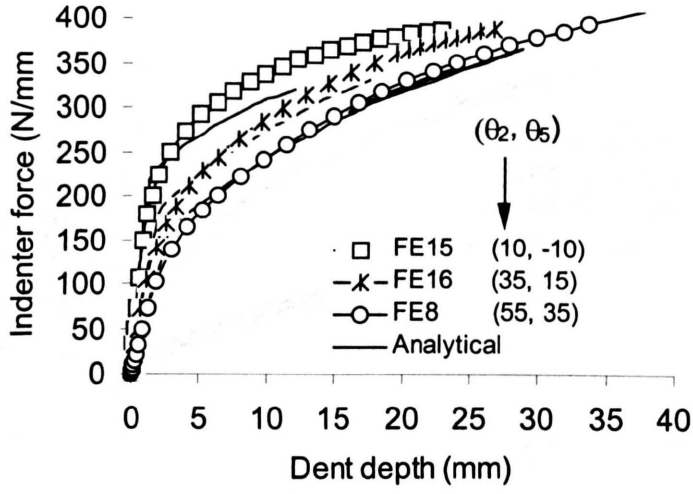

Fig. 6.13 Indenter force versus depth curves obtained from the FE and analytical solutions for X65 SAW, with D/t=42.6, t=3mm, θ_1=0°, p=5MPa and supported angle pair, (θ_2, θ_5)= (10°, -10°), (35°, 15°) and (55°, 35°).

6.5.2.4 Effect of D/t

The indenter force versus deflection curves obtained from the FE analyses FE5, FE8, FE17 and F20 and the corresponding analytical solutions, for X65 SAW steel, with D/t=72, 42.6 and 30.8, for θ_1= 10° and θ_2=θ_5= 45°, are shown in Figs. 6.14. The pressure used in the FE analyses produces a mean hoop stress of 0.234 times the material yield stress (see Table 3.1). The representative flow stress, which is the average of the yield stress and the ultimate tensile stress, was used in the analytical predictions. These curves indicate that the analytical and FE results are in good agreement for the D/t ratios used. However, there seems to be a small systematic effect of the D/t ratio on the indenter force predictions. It can be seen from Fig. 6.14 (a) that as the D/t ratio reduces, there is a tendency for the analytical predictions to be slightly lower than the corresponding FE results for large dent depths.

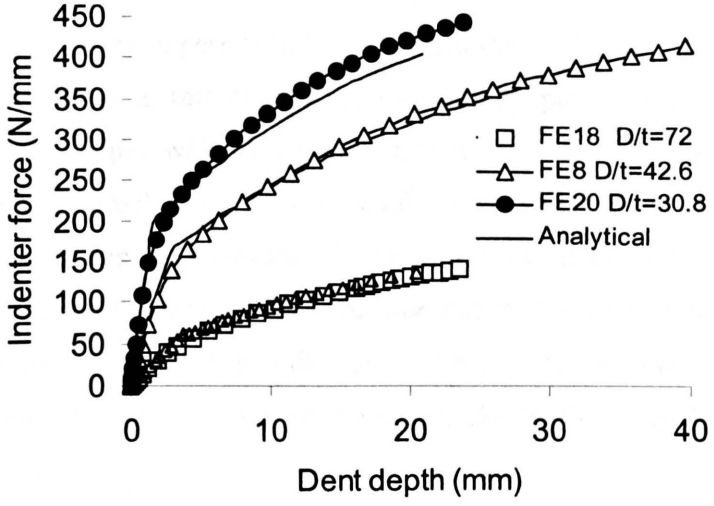

(a) $\theta_1=0^o$

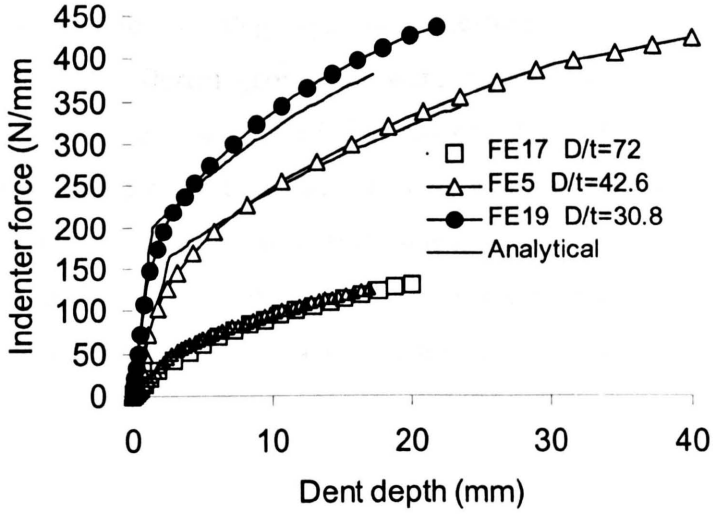

(b) $\theta_1=10^o$

Fig. 6.14 Indenter force versus deflection curves obtained from the FE and analytical solutions for D/t=72, 42.6and 30.8 for X65 SAW steel, with a pressure which produces a mean hoop stress of 0.234 times σ_y and $(\theta_2, \theta_5)= (55^o, 35^o)$.

6.6 Conclusions

The good correlation of the experimental, the FE and the analytical solutions shows that the analytical methods described in this chapter, can accurately predict the indenter force versus deflection curves for the pipes with or without internal pressures, when indented by a long indenter. The analytical formulations include the effects of the pressure, material properties, the indenter offset and angular support positions. The solutions of the FE and the analytical analyses also illustrate that the indenter force versus deflection curves are very close for all cases of the indenter offset angles investigated, i.e. less than 30°. Therefore, it is concluded that the indenter force versus deflection behaviour of rings can be accurately predicted by the analytical methods described in this chapter.

6.7 Summary

The indenter force versus deflection characteristics of pressurised pipes with long offset indentations have been investigated using experimental testing, FE and analytical methods. Two different materials and five different geometries were used to investigate their effects on the elastic-plastic behaviour. A comparison of the experimental, FE and the analytical results indicates that the analytical formulation developed in this chapter, for predicting the force-deflection curves, for pressurised pipes with offset indenters, is reasonably accurate. Also, all of the analyses presented in this chapter indicate that by using a representative flow stress, which is the average of the yield and ultimate tensile stresses, the analytical methods can accurately predict the force-deflection curves.

Chapter 7

Force-Deflection Behaviour of Pipes with Spring Type Supports due to Axially Long Indentations

7.1 Introduction

The limit load and force-deflection behaviours of dented rings with symmetry and non-symmetrical supports with symmetric and offset loading, using analytical methods and FE analyses have been reported in previous chapters [3-6]. The effects of asymmetry of supports, offset of loading, internal pressure, types of material and pipe geometry were investigated. The FE meshes, boundary conditions and large deformation FE analysis methods used have been validated by comparing predictions for unpressurised rings with the results of experimental tests.

Since the soil support around pipes is more likely to be spring-like rather than rigid, this chapter is concerned with the prediction of the indenter force-deflection behaviour when the pipes have spring type supports.

7.2 FE Analysis

7.2.1 Material

The material used in the FE analyses (see Fig.7.1) is elastic, perfectly plastic with a Poisson's ratio of 0.3, a Young's modulus, of 70GPa and a yield stress of 300MPa. In the FE analyses, the material is assumed to obey an isotropic hardening rule.

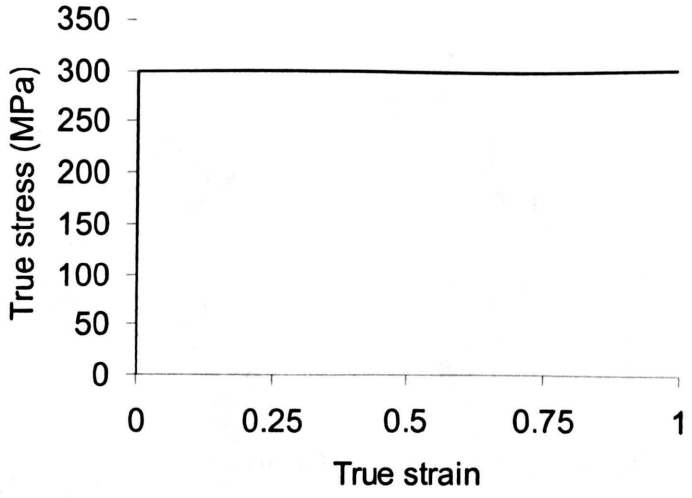

Fig. 7.1 The elastic, perfectly plastic material used in FE analyses

7.2.2 FE Meshes, Boundary Conditions and Loading

The ABAQUS [26] FE software was used for the analyses of the rings; the dimensions, support and loading conditions are shown in Fig. 7.2. Due to symmetry, only one half of the rings are modelled (see Fig. 3.4). All models consist of 3600 8-noded, plane-strain, reduced integration elements. The nodes on the rings at sections A and C (Fig. 3.4(a)) are restrained in the circumferential direction (i.e. $u_{xA}=u_{xC}=0$) for all of the analyses. Also, the rings, shown in Fig. 3.4 (a), are connected to three vertical springs with stiffnesses of K_1, K_2 and K_3, at the outer diameter at positions B, C and D, respectively, in which points B and D are at an angle θ to the x-direction. The total equivalent spring stiffness, K, caused by these three springs is $K_1+K_2+K_3$. For the rings shown in Fig. 7.2 (b), the arc BCD is connected to a uniformly distributed spring support with vertical stiffness, K_0, which results in the corresponding total equivalent stiffness, K, defined as $K = K_0(\pi - 2\theta)R$. The load was applied in the radially inwards direction at the outer diameter position at point A. In total, 12 analyses were performed, these are defined in Table 7.1.

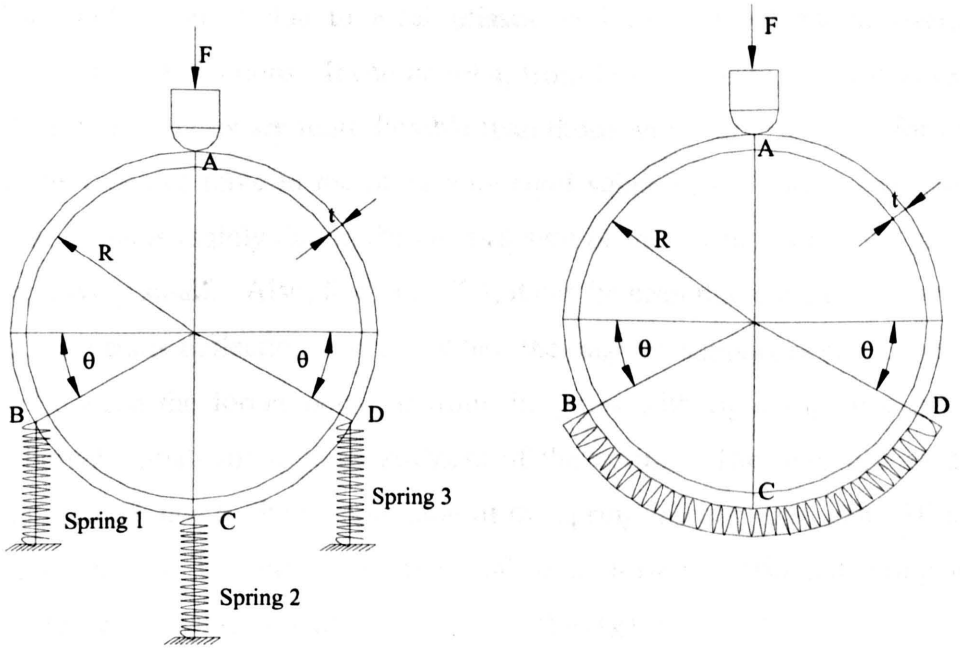

(a) (b)

Fig.7.2 Ring dimension, loading and boundary conditions

Table 7.1: The stiffness, angular support position, pressure levels (D/t=30.8, t=3mm) and initial gradients of indenter force versus displacement curves obtained from the FE analyses and the analytical method.

FE No	K_0 (MPa)	K_1 (*) (N/mm)	K_2 (*) (N/mm)	K_3 (*) (N/mm)	θ (°)	p (MPa)	FE Gradient	Analytical Gradient
FE1		10	20	10	45	0	13.11	20.26
FE2		∞	∞	∞	45	0	33.3	41.6
FE3		100	200	100	45	0	33.34	37.2
FE4		10	20	10	45	4	17.50	23.1
FE5		∞	∞	∞	45	4	44.42	53.77
FE6		0	20	0	90	0	7.73	7.93
FE7		0	∞	0	90	0	12.73	13.1
FE8		0	20	0	90	4	10.10	10.59
FE9		0	∞	0	90	4	20.40	22.33
FE10	0.5				45	4	19.20	27.33
FE11	1.0				45	4	23.29	36.4
FE12	2.0				45	4	26.50	43.75

(*) ∞ indicates that a rigid support (very stiff spring) was used.

7.2.3 FE Results

The FE analyses FE1 to FE12 are used to investigate the effects of the spring-support on the indenter force versus deflection curves, which are shown in Fig.7.3. It should be noted

that part of the deflection is due to local (elastic and plastic) behaviour, overall tube deformation and spring deflections. It can be seen, from Fig. 7.3 (a) to (g), that as expected, the pipes with spring-supports are more flexible than those with rigid supports; for the same displacement, the indenter force in the pipes with rigid supports are higher than those with spring-supports. This is mainly due to the compression of the springs, when the stiffness of the spring is relatively small. Also, from Fig. 7.3, it can be seen that the support types affect the indenter force versus deflection curves. When the angular support position is at $\theta=90^{\circ}$, the difference between the forces obtained from the pipes with rigid supports and spring-supports is relatively small for a given stiffness of the spring. The only difference is an additional displacement due to the compression of the spring in each case. The FE analyses FE10 to FE12 are used to investigate the effects of the uniformly distributed spring supports on the indenter force versus depth curves. Figs. 7.3 (e) to (g) show that as the stiffness of the springs is increased, the behaviour of the pipes with spring-supports approaches that obtained from the pipes with rigid supports. However, all of the indenter force versus depth curves exhibit the same pattern of behaviour. In particular, the peak loads obtained in all cases except for the most flexible support case (Fig.7.3 (a)), are the same with the rigid and flexible supports.

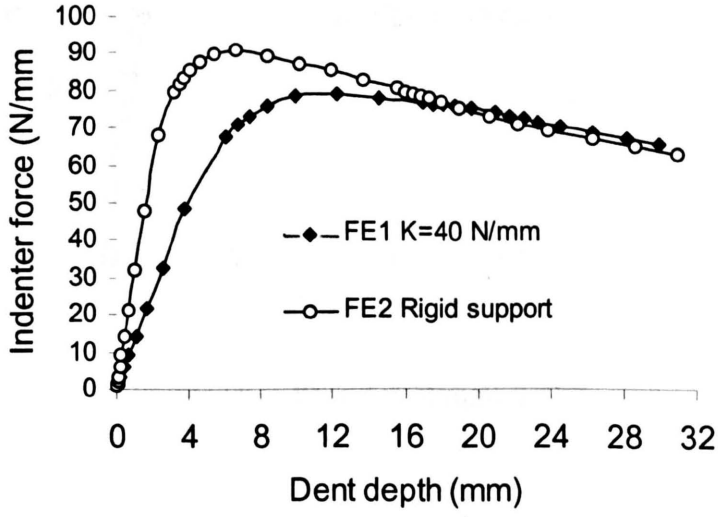

(a) $K=K_1+K_2+K_3=40$ and ∞ N/mm, $\theta=45^{\circ}$, p=0.

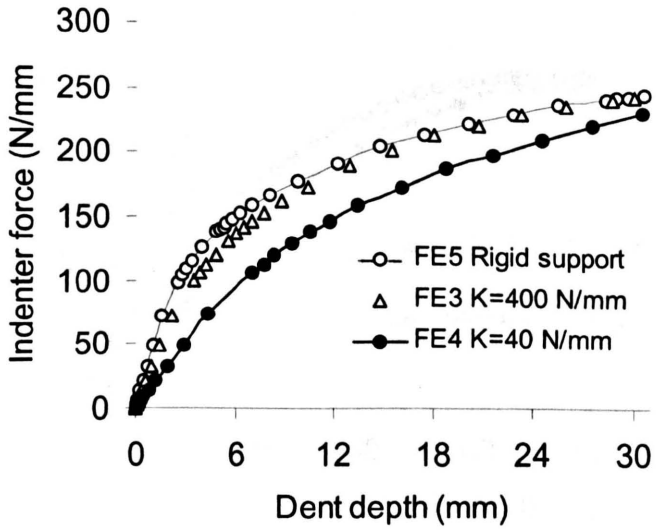

(b) $K=K_1+K_2+K_3=40$, 400 and ∞ N/mm, $\theta=45^{\circ}$, p=4MPa.

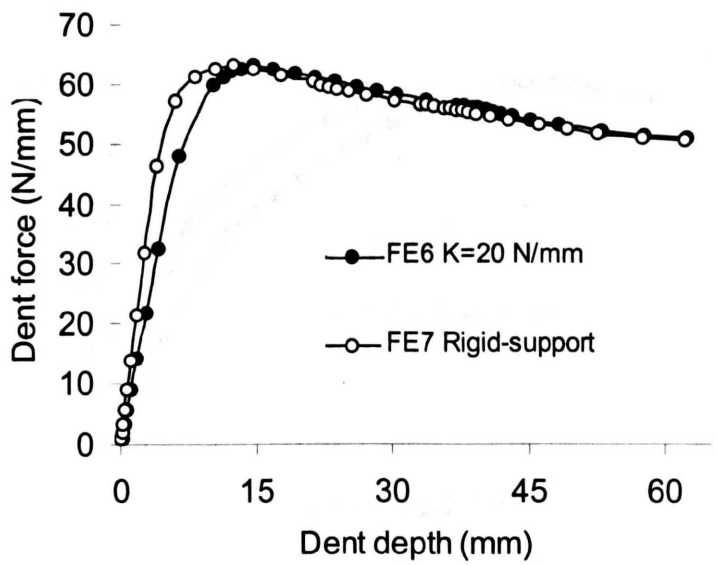

(c) $K=K_1+K_2+K_3=20$ and ∞ N/mm, $\theta=90^{\circ}$, p=0.

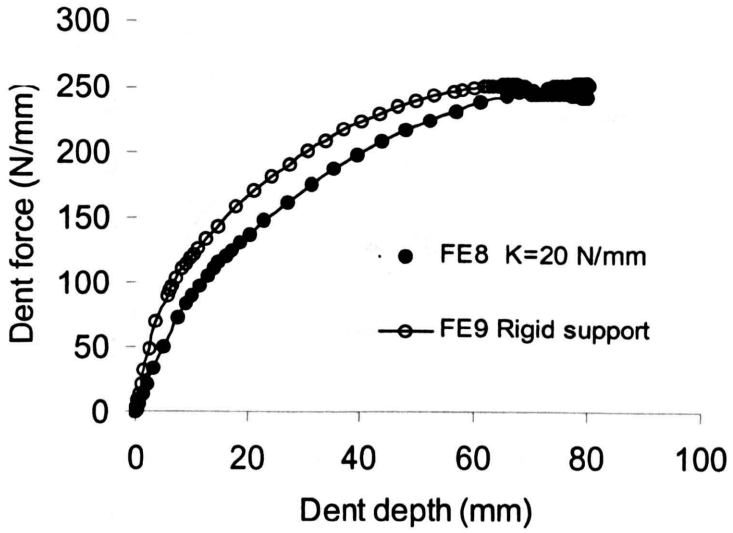

(d) $K=K_1+K_2+K_3=20$ and ∞ N/mm, $\theta=90^{\circ}$, p=4MPa.

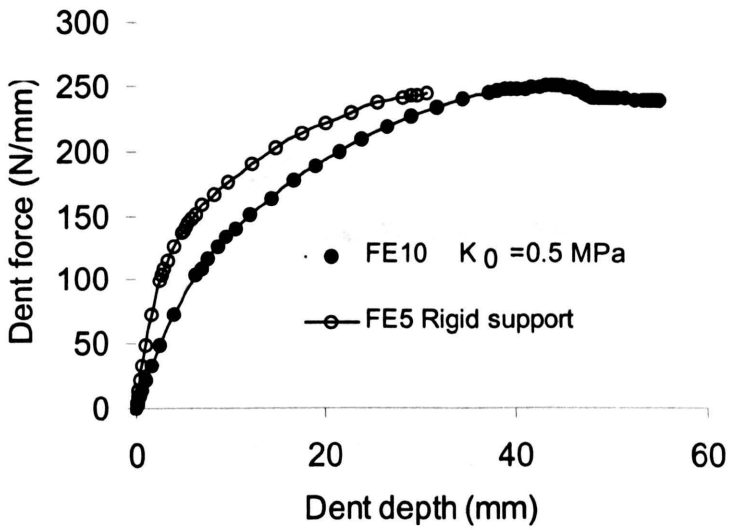

(e) $K_0=0.5$ MPa, $\theta=45^{\circ}$, p=4MPa.

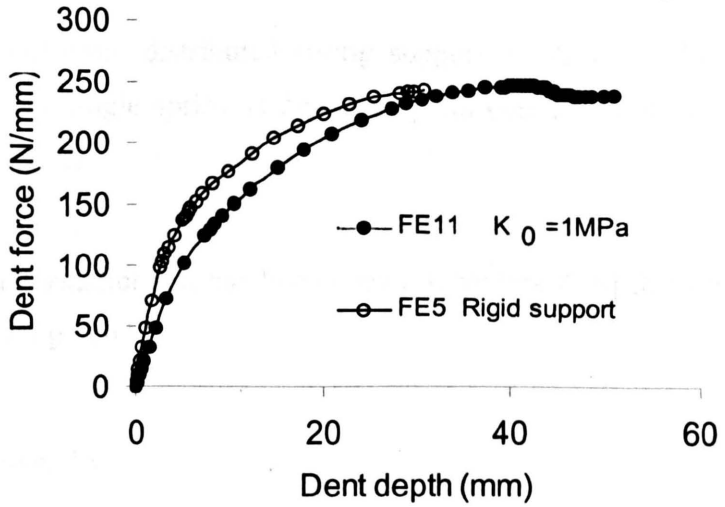

(f) K_0=1.0 MPa, θ=45°, p=4MPa.

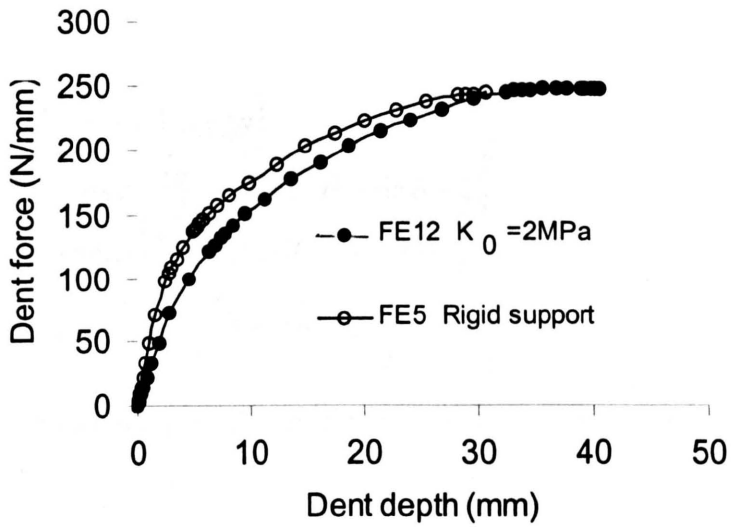

(g) K_0=2.0 MPa, θ=45°, p=4MPa.

Fig. 7.3 Indenter force versus displacement curves obtained from the FE analyses for the pipes with uniformly distributed spring supports with D/t=30.8, t=3mm.

7.3 Analytical Method

7.3.1 Elastic Behaviour

For the case of a pipe with a three-spring support condition, as shown in Fig. 7.2 (a), if the vertical stiffnesses of those springs are denoted by K_1, K_2 and K_3 (N/mm) and the pipe has a rigid vertical movement, the equivalent stiffness of these three springs, K, is given by

$$K = K_1 + K_2 + K_3 \tag{7.1}$$

For a pipe with uniformly distributed spring support as shown in Fig. 7.2 (b), if the vertical stiffness of each single spring is denoted by K_0 (MPa), the equivalent stiffness of these springs, K, is given by

$$K = (\pi - 2\theta)RK_0 \tag{7.2}$$

Assuming small deformations, it has been shown [chapters 4, 6] that the stiffness of the pressurised pipes, K_{ep}, is given by

$$K_{ep} = (K_e + K_p) \tag{7.3}.$$

where K_p and K_e are given by

$$K_p = 2p\frac{-(1-\sin\theta_0)^2\sin\frac{\theta-\theta_0}{2}+\cos\theta_0\cos\frac{\theta-\theta_0}{2}(\sin\theta+\sin\theta_0)+(1-\sin\theta_0)(1+\sin\theta)\left[\cos\frac{\theta+\theta_0}{2}+\sin\frac{\theta-\theta_0}{2}\right]}{\cos\theta_0-\cos\theta+\sin(\theta+\theta_0)\left[\cos\frac{\theta+\theta_0}{2}+\sin\frac{\theta-\theta_0}{2}\right]} \tag{7.4a}$$

$$K_e = \frac{Et^3}{12R^3}\left(\frac{D}{AD+B+C}\right) \tag{7.4b}$$

and

$$\left.\begin{aligned} A &= \frac{1}{4}\left(\frac{\pi}{2}+\theta+\frac{1}{2}\sin 2\theta\right) \\ B &= (1+\sin\theta)\left[\frac{3}{2}\sin 2\theta + 3\cos\theta - \left(\frac{\pi}{2}+\theta\right)(\cos^2\theta+\sin\theta+1)\right] \\ C &= \cos\theta\left(\frac{1}{2}+\frac{1}{2}\sin^2\theta+\sin\theta\right)\left[\left(\frac{\pi}{2}+\theta\right)\cos\theta - 2\sin\theta - 2\right] \\ D &= 2\left(\left(\frac{\pi}{2}+\theta\right)^2 - 2\cos^2\theta - \frac{1}{2}\left(\frac{\pi}{2}+\theta\right)\sin 2\theta\right) \end{aligned}\right\} \tag{7.4c}$$

Hence, the total stiffness, K_{total}, of the indented pipe with spring-support, is given by (see details in Appendix 4.A.)

$$K_{total} = \frac{K_{ep}K}{K_{ep}+K} \tag{7.5}$$

Equation (7.5) indicates that the relationship between the indenter force, F, and the deflection, δ, in the elastic range, is given by

$$F = K_{total}\delta \tag{7.6}$$

The initial gradients of the indenter force versus deflection curves obtained from the FE analyses (FE1 to FE12) and the analytical method are shown in Fig. 7.4. It can be seen that the results obtained from the analytical method are higher than those obtained from the FE analyses, because the analytical solutions do not include the deformation of positions B and D relative to point C, and the associated deformation of the material in the arc BCD, see Fig.7.2. However, the predictions obtained from the analytical method are reasonably accurate,

especially for the relatively stiff supports, which result in relatively small spring deformations in the elastic stage.

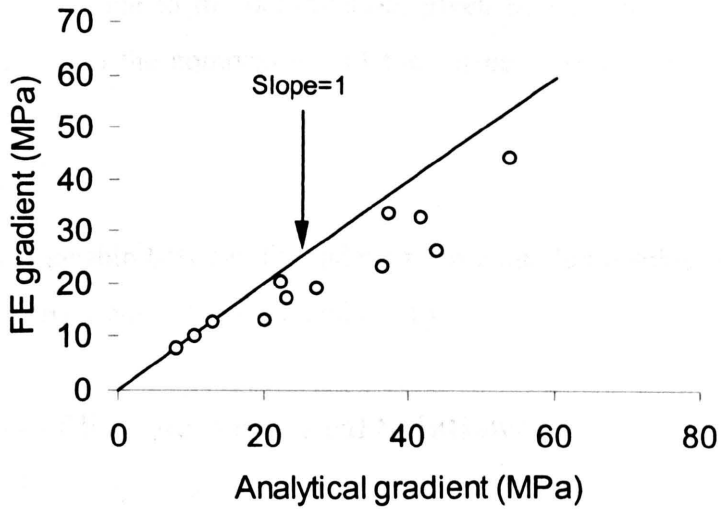

Fig. 7.4 Comparison of the initial gradients obtained from the FE analyses and from the analytical method.

7.3.2 Inelastic Behaviour

A technique for predicting the indenter force, F, of a pipe with rigid supports, in the inelastic range using limit load analysis [chapters 4, 6], has shown that

$$F = \frac{4M_0}{R} F^M + pR F^P \tag{7.7}$$

where

$$F^M = \frac{\cos(\alpha_2-\alpha_1)-\sin(\theta_0+\alpha_2-\alpha_1)+\sin(\theta+\alpha_1)+\sin(\theta_0-\alpha_1)}{\cos(\theta_0-\alpha_2)+\sin(\theta+\theta_0+\alpha_2)-\cos(\theta+\alpha_2)-\sin\alpha_2} \tag{7.8a}$$

$$F^P = 2pR\frac{(1-\sin\theta_0)\cos\left(\frac{\theta-\theta_0}{2}+\alpha_1\right)+2\sin\left(\frac{\pi}{4}-\frac{\theta_0}{2}-(\alpha_2-\alpha_1)\right)\cos\left(\frac{\pi}{4}+\frac{\theta_0}{2}\right)\left[2\cos\left(\frac{\theta+\theta_0}{2}+\frac{\alpha_2}{2}\right)\sin\frac{\alpha_2}{2}-\cos\left(\frac{\theta-\theta_0}{2}+\alpha_2\right)\right]}{\cos\left(\frac{\theta+\theta_0}{2}+\alpha_2\right)+\sin\left(\frac{\theta-\theta_0}{2}+\alpha_2\right)} \tag{7.8b}$$

$$\theta_0 = \frac{\pi}{4}-\frac{1}{2}\theta \tag{7.8c}$$

$$\alpha_2 = \frac{\pi}{4}-\frac{\theta_0}{2}+\alpha_1-\cos^{-1}\left[\frac{\cos(\theta_0-\alpha_1)-\cos(\theta+\alpha_1)+\cos\theta}{2\sin\left(\frac{\pi}{4}-\frac{\theta_0}{2}\right)}\right] \tag{7.8d}.$$

In equation (7.8), α_1 is the angular position of the plastic hinges at positions B and D, relative to point A, see Fig. 7.2. The displacement at position A, δ_p, due to the pipe elastic-plastic deformation, is given by

$$\delta_p = R[1+\sin(\theta_0+\alpha_2-\alpha_1)-\cos(\alpha_2-\alpha_1)-\sin(\theta+\alpha_1)-\sin(\theta_0-\alpha_1)+\sin\theta] \quad (7.9)$$

For the pipe with a spring-support, the displacement at the position A in Fig. 7.2, δ, is the sum of the displacement, due to the deformation, given by equation (7.9), and the vertical rigid movement, δ_s, due to the compression of the springs. Hence, the displacement, δ, is given by

$$\delta = \delta_p + \delta_s = \delta_p + \frac{F}{K} \quad (7.10)$$

Therefore, the relationship between the indenter force and the displacement of a pipe with spring-supports is given by equations (7.7) and (7.10).

7.4 Comparisons of FE and Analytical Solutions

The result of the FE analyses presented in section 7.2.3 show that the inclusion of spring-supports affects the indenter force versus displacement curves, compared with the solutions obtained for rigidly supported pipes. The indenter force versus depth curves, obtained from the FE analyses (FE1 to FE12), and the corresponding analytical solutions, are shown in Fig. 7.5. These curves indicate that the behaviour predicted by the analytical and FE results are generally consistent and that good correlation of the two sets of results is obtained when the indentation depth is high. In particular, when the support angle, θ, is 90°, the differences between the analytical and the FE results, in both the elastic and inelastic ranges, are very small, see Fig. 7.5 (d). An important conclusion from the comparisons is that the analytical methods are capable of describing the basic phenomena observed for all of the types of spring-supports investigated.

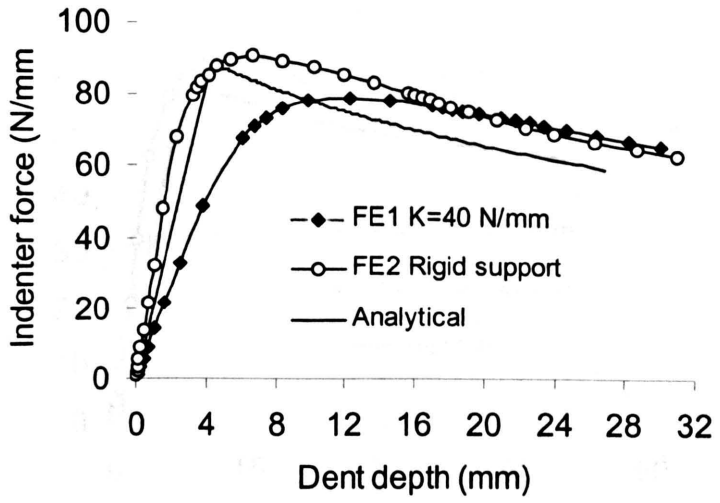

(a) $K=K_1+K_2+K_3=40$ and ∞ N/mm, $\theta=45^{\circ}$, p=0.

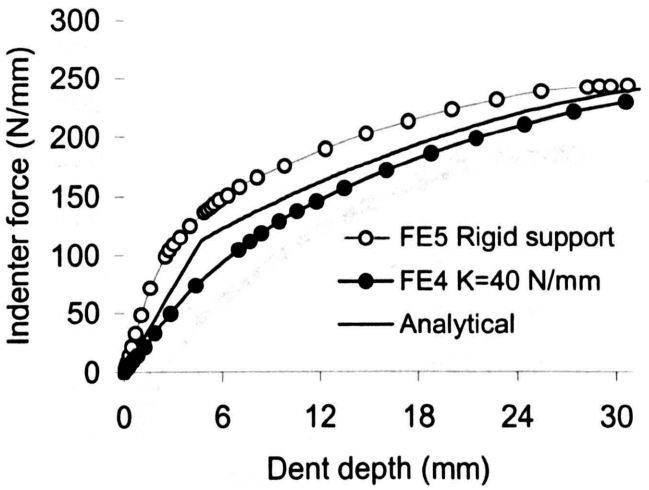

(b) $K=K_1+K_2+K_3=40$ and ∞ N/mm, $\theta=45^{\circ}$, p=4MPa.

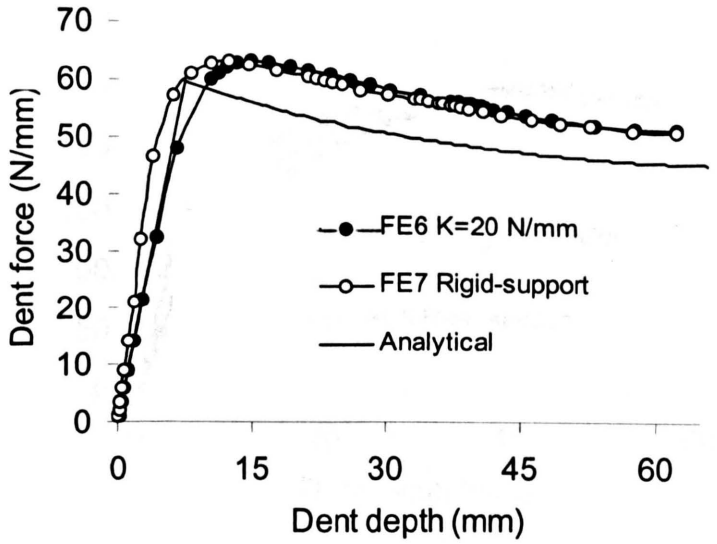

(c) $K=K_1+K_2+K_3=20$ and ∞ N/mm, $\theta=90^{\circ}$, p=0MPa.

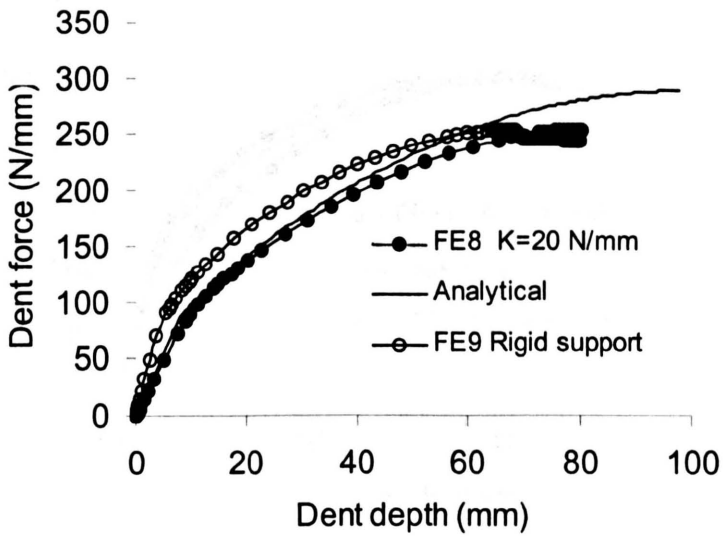

(d) $K=K_1+K_2+K_3=20$ and ∞ N/mm, $\theta=90^{\circ}$, p=4MPa.

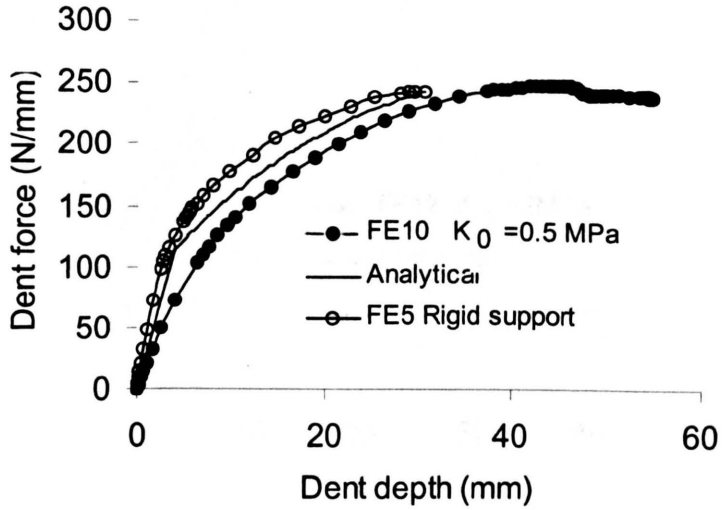

(e) K_0=0.5 MPa, θ=45°, p=4MPa.

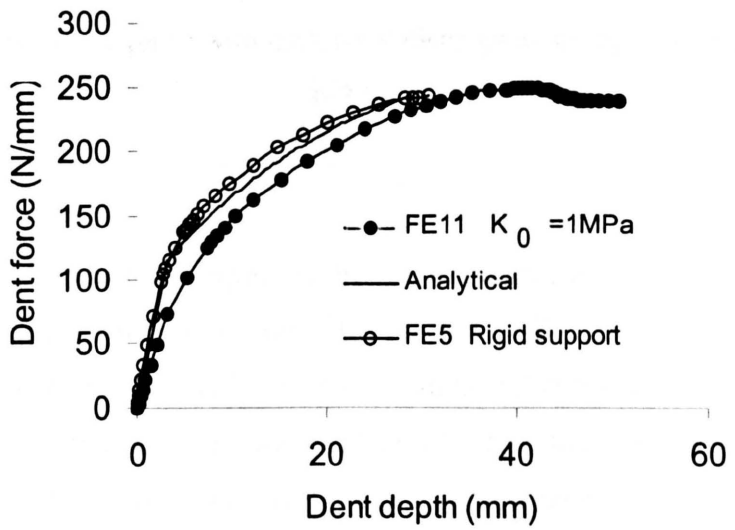

(f) K_0=1.0 MPa and ∞ N/mm, θ=45°, p=4MPa.

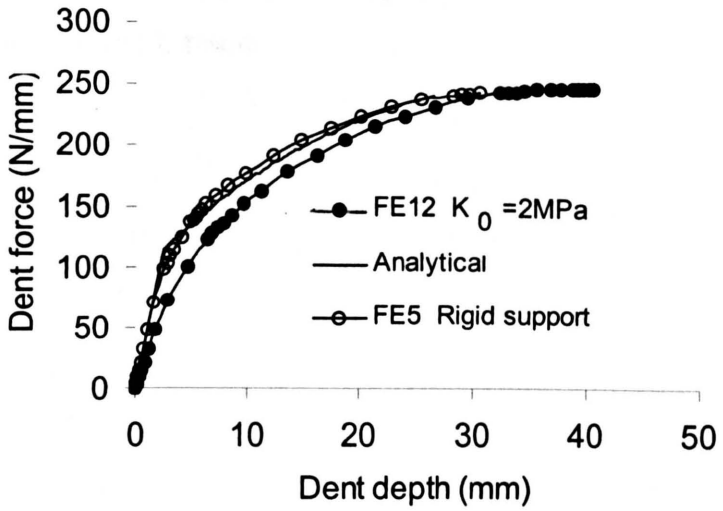

(g) K_0=2.0 MPa and ∞ N/mm, θ=45°, p=4MPa.

Fig.7.5 Indenter force versus displacement curves obtained from the FE analyses and analytical methods for the pipes with uniformly distributed spring supports with D/t=30.8, t=3mm.

7.5 Conclusions

In many practical situations, pipes are buried underground and the use of the spring-supports is a more accurate representation of the practical soil support conditions that exist for pipes. Compressions of the FE analyses and analytical solutions indicate that the analytical methods described in this chapter are capable of predicting the indenter force versus deflection curves with reasonable accuracy. Generally the analytical solutions are higher than the corresponding FE results. In previous chapters [3-6], it has been shown that the analytical methods used are able to predict the indenter force versus displacement behaviour of the pipes made from strain hardening materials. Hence, it is expected that the analytical methods described in this chapter would also be valid for strain hardening materials, although only elastic, perfectly plastic material models are used in the investigation.

7.6 Summary

The indenter force-deflection behaviour of pipes, with spring type supports, due to axially long indentations, was investigated using FE (FE) analyses and analytical methods. It is

found that the analytical methods are capable of giving reasonably accurate predictions of the behaviour by comparing with FE results.

Chapter 8

Residual Stresses due to Long External Indentation and Subsequent Stress Variations due to Pressure Fluctuations in Pipes with Long Indentations

8.1 Introduction

Limit load and indenter force-deflection results have been obtained [chapters 3-7] using experimental tests, FE analyses and analytical methods. This chapter investigates the residual hoop stresses, due to long external indentations, and the subsequent stress variations due to pressure fluctuations, in the vicinity of the indentations, using the FE method. The effects of the residual dent depth, internal pressure at the time of indentation, indenter and pipe geometry and support conditions on the residual hoop stress and stress fluctuations due to internal pressure variations are investigated.

8.2 Materials

Three materials were chosen for the FE analyses. The tensile stress-strain curves for the materials are shown in Fig. 8.1 and some of the material properties are given in Table 8.1. X65 SAW is a typical pipe steel, grade B is a 24 inch thin wall line pipe material, and grade X52 is an 18 inch thin wall seamless line pipe material.

Table 8.1: Material properties

Material	E	σ_y	σ_{UTS}	Poisson's ratio
X65 SAW	223 GPa	448 MPa	675 MPa	0.3
Grade B	144 GPa	287.7 MPa	588 MPa	0.3
X52	180 GPa	360 MPa	616 MPa	0.3

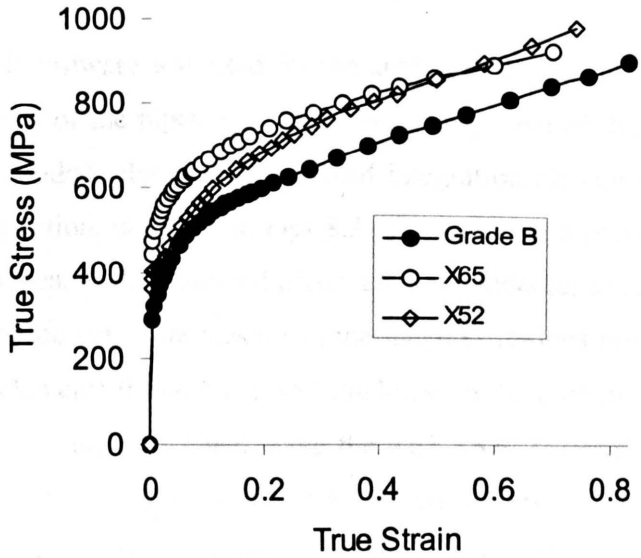

Fig. 8.1 True stress-strain curves for X65 SAW, grade B and X52 pipe steels.

The ultimate tensile stresses shown in Table 8.1 and the stresses on Fig. 8.1 all are true stresses. In the FE analyses, all of the three materials are assumed to obey an isotropic hardening rule.

8.3 Geometry, Loading and Boundary Conditions

The two-dimensional pipe indealisations have an outer diameter (D) of 914.4 mm and D/t ratios of 72, 50.8, 41.56, 35.17 and 30.48 where t is the wall thickness. The pipes are indented by a radial load, as shown in Fig.4.1. A rigid indenter which has a radius in the range of 6 to 100mm, is used to cause the indentation. The angular support positions are defined by θ, as shown in Fig. 4.1; θ was varied from 5° to 90°.

To determine the residual stresses and subsequent stress variations due to pressure fluctuations in the pipes, the loading was applied in four steps. First, internal pressure is applied, then the indenter load is applied to cause a predetermined dent depth, δ; following this, the indenter is removed to obtain the residual hoop stress, σ_r, and residual dent depth, δ_r, finally the internal pressure is changed from p to one of two predetermined levels, p_1 and p_2, to determine the resulting stress variations.

8.4 FE Modelling

The ABAQUS [26] FE software was used for the analyses. For all of the cases, it was only necessary to model one half of the pipes, due to the symmetry. All of these symmetric models consisted of 4240, 8 or 6 noded, plane-strain, reduced integration elements; part of a model, in the vicinity of a loading position, is shown in Figs 8.2. As shown in a previous publication [45], the predicted residual stresses, in the indented pipes, after the indenter is removed, are sensitive to mesh refinement and hence very fine meshes in the indenter regions are required. All of the FE models used have 32 elements through the wall thickness in the indenter regions of the pipes. Most of the FE calculations were performed using the X65 SAW material properties. Two FE calculations were carried out with grade B and X52 material properties to assess the effect of material properties on the behaviour. In total 39 analyses were performed, as defined in Table 8.2.

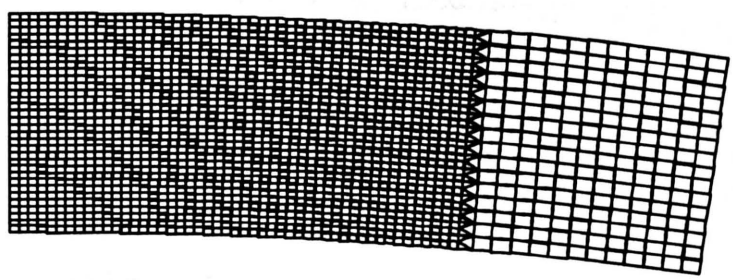

Fig. 8.2 Localised meshes used in the FE analyses for the indented ring analyses

Table 8.2: Dimensions, boundary conditions, loading conditions and some FE results.

FE(*) No.	D/t	δ mm	r mm	θ	θ_1	p MPa	Δp_1 MPa	Δp_2 MPa	δ_r mm	σ_r MPa	$\Delta\sigma_1$ /Δp_1	$\Delta\sigma_2$ /Δp_2
FE1S	72	20	12.7	45°	0°	0	**	**	0	0	**	**
FE2S	72	40	12.7	45°	0°	0	**	**	7.72	385	**	**
FE3S	72	60	12.7	45°	0°	0	**	**	21.5	591	**	**
FE4S	72	80	12.7	45°	0°	0	**	**	37.6	670	**	**
FE5S	72	100	12.7	45°	0°	0	**	**	54.6	713	**	**
FE6S	72	120	12.7	45°	0°	0	**	**	72.1	720	**	**
FE7S	72	140	12.7	45°	0°	0	**	**	89.9	727	**	**
FE8S	72	20	12.7	45°	0°	7.68	1.28	2.56	0.801	338.5	52.5	53.6
FE9S	72	40	12.7	45°	0°	7.68	1.28	2.56	4.42	621.2	92.0	94.9
FE10S	72	60	12.7	45°	0°	7.68	1.28	2.56	6.77	763.6	116	120
FE11S	72	80	12.7	45°	0°	7.68	1.28	2.56	8.55	829.3	134	139
FE12S	72	100	12.7	45°	0°	7.68	1.28	2.56	9.77	886	141	147
FE13S	72	120	12.7	45°	0°	7.68	1.28	2.56	12.3	937.5	161	169

FE14S	72	100	12.7	45°	0°	1.28	1.28	**	35.4	760	519	**
FE15S	72	100	12.7	45°	0°	2.56	1.28	2.56	25.3	778	377	375
FE16S	72	100	12.7	45°	0°	3.84	1.28	2.56	19	800	235	246
FE17S	72	100	12.7	45°	0°	5.12	1.28	2.56	15	824	186	201
FE18S	72	100	12.7	45°	0°	6.4	1.28	2.56	12	854	158	168
FE19S	72	100	12.7	45°	0°	9.0	1.28	2.56	7.89	946	151	153
FE20S	72	100	6.	45°	0°	7.68	1.28	2.56	9.83	905	166	174
FE21S	72	100	20	45°	0°	7.68	1.28	2.56	9.72	872	133	138
FE22S	72	100	30	45°	0°	7.68	1.28	2.56	9.65	860	125	130
FE23S	72	100	50	45°	0°	7.68	1.28	2.56	9.6	839	119	125
FE24S	72	100	70	45°	0°	7.68	1.28	2.56	9.5	824	115	120
FE25S	72	100	100	45°	0°	7.68	1.28	2.56	9.3	802	109	114
FE26S	50.8	100	12.7	45°	0°	7.68	1.28	2.56	22.9	841	148	155
FE27S	41.6	100	12.7	45°	0°	7.68	1.28	2.56	34	822	153	160
FE28S	35.2	100	12.7	45°	0°	7.68	1.28	2.56	46	804	152	157
FE29S	30.5	100	12.7	45°	0°	7.68	1.28	2.56	56	799	145	148
FE30S	50.8	100	12.7	45°	0°	11	1.28	2.56	15.7	900	118	123
FE31S	41.6	100	12.7	45°	0°	13.6	1.28	2.56	19.8	910	107	111
FE32S	35.2	100	12.7	45°	0°	16.2	1.28	2.56	23.5	918	97	101
FE33S	30.5	100	12.7	45°	0°	18.9	1.28	2.56	27.4	928	91	94.3
FE34S	72	100	12.7	5°	0°	7.68	1.28	2.56	10.5	1018	188	197
FE35S	72	100	12.7	25°	0°	7.68	1.28	2.56	10.6	954	165	172
FE36S	72	100	12.7	65°	0°	7.68	1.28	2.56	9.52	815	123	127
FE37S	72	100	12.7	90°	0°	7.68	1.28	2.56	10	722	103	106
FE38S	72	60	12.7	45°	0°	4.92	1.28	2.56	7.02	497	115	123
FE39S	72	60	12.7	45°	0°	6.17	1.28	2.56	6.68	608	114	120
FE40S	72	60	12.7	45°	0°	4.92	1.28	2.56	7.02	497	115	123
FE41S	72	60	12.7	45°	0°	6.17	1.28	2.56	6.68	608	114	120

(*) The cases of FE1S to FE39S were obtained for X65 SAW material, FE40S for grade B material and FE41S for X52 material.

Some of the symbols used in Table 2 are defined in the notation; r represents the radius of the indenter, the pressure ranges Δp_1 and Δp_2 are p-p_l and p-p_2, respectively, δ_r and σ_r are the residual dent depth and residual hoop stress and $\Delta\sigma_1/\Delta p_1$ and $\Delta\sigma_2/\Delta p_2$ are the first and second normalised stress variations, caused by Δp_1 and Δp_2, respectively.

8.5 FE Results

The results presented in this chapter mainly relate to the central contact point between the indenter and the pipe on the outer surface. At this position, the maximum tensile residual hoop stress values were found to occur. Since the residual stresses and stress variations associated with the internal pressure fluctuations are affected by the residual dent depth, the pipe geometry,

the angular support positions and the indenter radius, all of these parameters have been investigated separately.

8.5.1 Typical Residual Hoop Stress Distribution

The results of FE analysis FE12S, shown in Fig. 8.3 provides typical residual hoop stress distributions on the outer and inner circumferential surfaces of the pipe. In this case, the internal pressure, p=7.68 MPa, was reduced in two stages to achieve pressure decreases, Δp of 1.28 and 2.56MPa. It can be seen, from Fig. 8.3, that the residual hoop stresses in the indentation region (e.g. $|\alpha|<15^{\circ}$) are positive on the outer surface and negative on the inner surface. Also it can be seen that even when the pressure deceased by 1.28 or 2.56MPa, the residual hoop stress distribution changes are relatively small and so they remain positive on the outer surface and negative on the inner surface. Therefore, since fatigue damage is most likely to occur in regions where variations of the tensile residual stresses occur, the results presented in this chapter are mainly associated with the residual hoop stresses on the outer surfaces of the indented pipes, at the $\alpha=0^{\circ}$ position. Fig. 8.3 also indicates that the peak value of 886MPa of the residual hoop stress is much higher than the ultimate tensile stress (675MPa) of X65 Saw material. This is because the maximum stress value of the true stress versus strain curve shown in Fig.8.1 is much higher than that of the corresponding ultimate tensile stress. Also since the von Mises yield criterion was used in the FE analyses, some stress components, e.g. the hoop stress, may be in some cases higher than the corresponding von Mises stress whose maximum value is the same as that of true stresses on Fig.8.1. This can be seen from Figs. 8.4 to 8.8 in the following section.

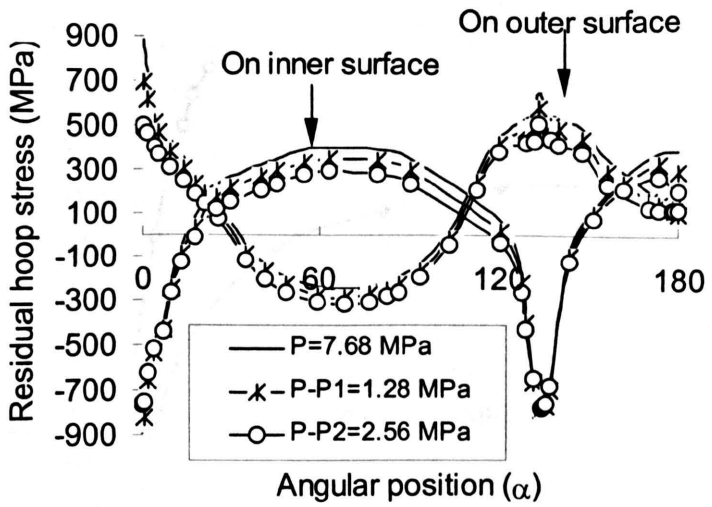

Fig.8.3 Typical residual hoop stress distributions on the inner and outer surfaces of the pipe, for X65 SAW material, with r=12.7mm, D/t=72, θ=45° and p=7.68MPa.

8.5.2 Residual Hoop Stresses

8.5.2.1 Effect of Dent depth

The magnitude of the indentation depth has a significant effect on the magnitude of the residual hoop stresses created in the pipes. The variations of the residual hoop stresses with residual dent depth, for pressurised and unpressurised pipes, are shown in Fig. 8.4. For the unpressurised pipe, it can be seen that the residual hoop stresses increase rapidly as the residual dent depth increases, for the small δ_r/D ratios, i.e. less than 0.022. However, the residual hoop stresses increase more slowly with an increase of the residual dent depths for large δ_r/D ratios. This is because the plastic deformation zone and contact area both increase as δ_r/D increased, thus limiting the magnitude of the residual stress that occurs. For the pressurised pipe, the residual hoop stresses are much higher than the corresponding values for the unpressurised pipe, at the same residual dent depth. Therefore, the pressurised pipe would be likely to be punctured at a relatively small dent depth, particularly in high-pressure circumstances.

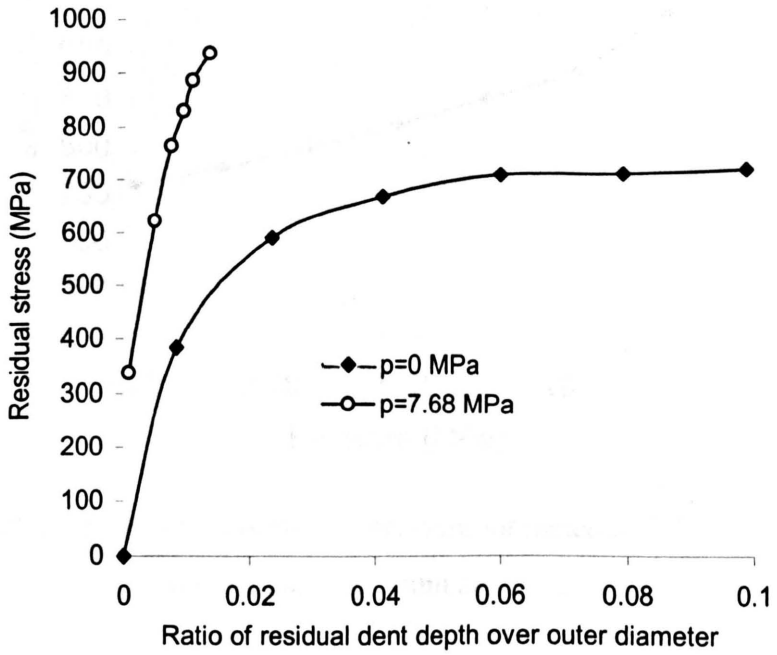

Fig.8.4 Residual hoop stress versus residual dent depth curve for material X65 SAW, D/t=72, t=12.7mm, p=0 and 7.68MPa, r=12.7 mm and θ=45°.

8.5.2.2 Effect of Pressure

The effects of the internal pressure on the residual hoop stresses, for D/t=72, t=12.7mm, r=12.7mm and θ=45°, for δ=100mm, are shown in Fig.8.5. It can be seen that the residual hoop stresses increase as the internal pressure is increased.

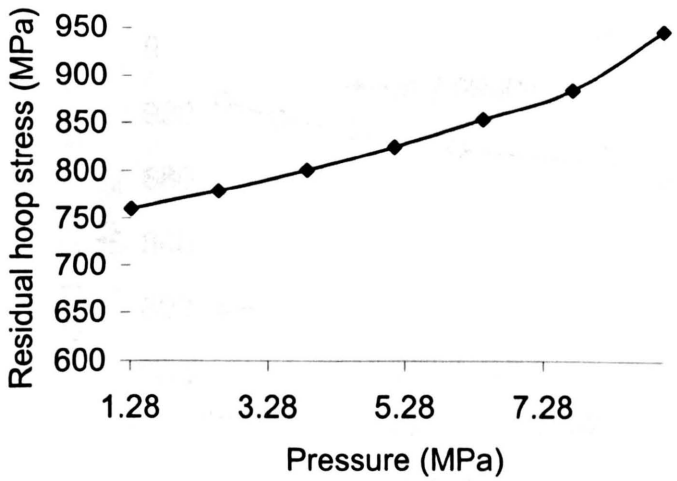

Fig.8.5 Residual hoop stress versus internal pressure for material X65, D/t=72, t=12.7mm, δ=100mm, r=12.7 mm and θ=45°.

8.5.2.3 Effect of D/t Ratio

Typical plots showing the effect of wall thickness on the residual hoop stresses, are given in Fig. 8.6. The results presented represent either constant internal pressure (p=7.68MPa) or a pressure p which causes a mean hoop stress of $0.6\sigma_y$ in the pipe. The curve presented in Fig. 8.6 for the constant internal pressure case, i.e. p=7.68 MPa, relates to a situation in which the pressure induced hoop stress (in a plain pipe) increases in proportion to D/t as D/t increases (i.e. σ=pD/2t). The curve presented in Fig. 8.6 for which the hoop stress is kept constant at $0.6\sigma_y$ represents a case in which the pressure reduces as D/t increases. In the case in which the mean hoop stress is held constant at $0.6\sigma_y$, the residual dent depths, for the larger D/t ratios (e.g. 72) are larger than those for small D/t ratios, for an applied indenter depth of 100mm. From the results in Fig.8.6 and those in Table 8.2, it can be seen that for the same dent depth, the variations in the residual stresses with D/t ratio are relatively constant, for an equivalent pressure level (i.e. a pressure level which produces the same mean hoop stress in the plain pipe with different D/t ratios).

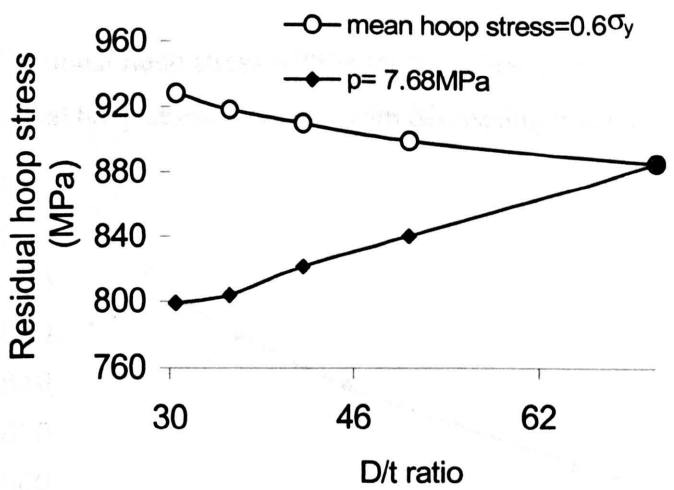

Fig.8.6 Residual hoop stress versus D/t ratio curves for material X65, with p=7.68MPa or with a mean hoop stress of 0.6 times σ_y, δ=100mm, D=914.4mm, r=12.7 mm and θ=45°.

8.5.2.4 Effect of Angular Support Position

Typical residual hoop stress versus angular support position, θ, results are shown in Fig. 8.7. This indicates that as the support angle increases, the residual hoop stresses reduce. Also the relationship between the support position and the residual hoop stress is approximately linear.

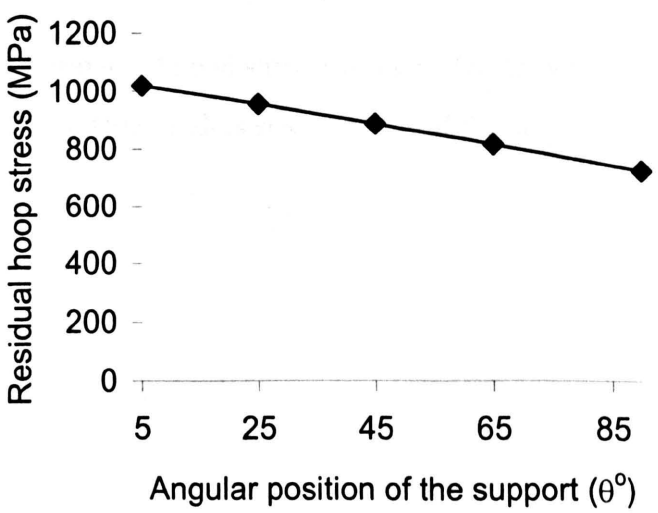

Fig.8.7 Residual hoop stress versus angular support position curve for material X65 SAW, D/t=72, t=12.7mm, p=7.68MPa, δ=100mm and r=12.7 mm.

8.5.2.5 Effect of Indenter Radius

A typical variation of residual hoop stress with indenter radius size is shown in Fig.8.8 where it can be seen that the residual hoop stress increases with decreasing indenter radius size.

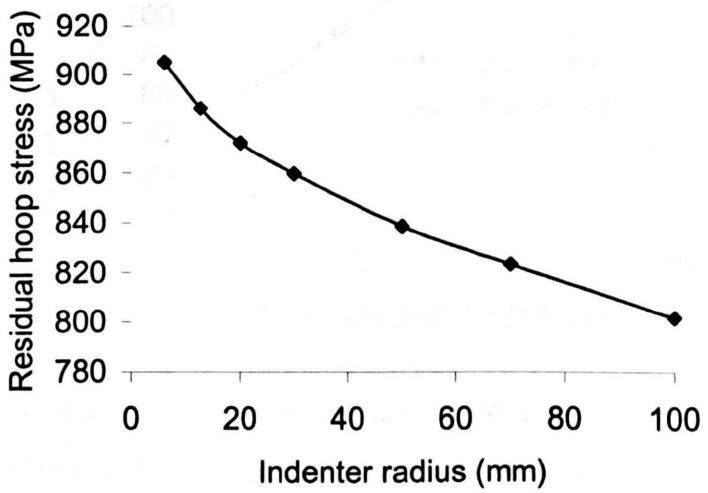

Fig.8.8 Residual hoop stress versus indenter radius curve for material X65, with D/t=72, t=12.7mm, p=7.68MPa, δ=100mm and θ=45°.

8.5.3 Stress Variations in Indented Pipes due to Pressure Fluctuations

8.5.3.1 X65 SAW

Typical variations of normalised hoop stress variation, $\Delta\sigma/\Delta p$, versus residual dent depth, δ_r, angular support position,θ, indenter radius size, r, and wall thickness, t, are shown in Fig.8.9 (a) to (d), respectively.

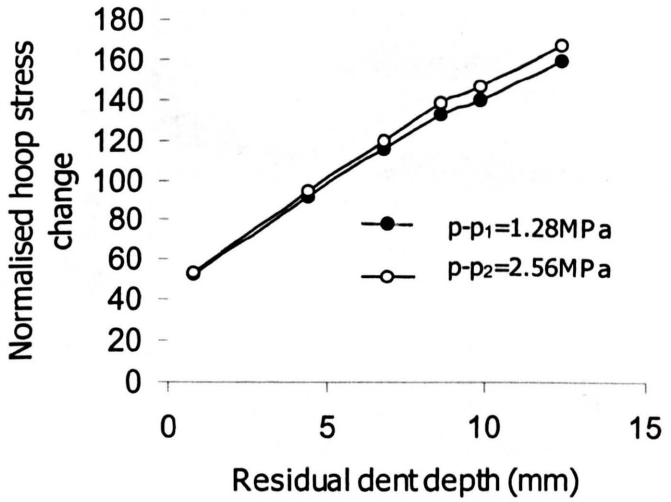

Fig.8.9 (a) Variations of normalised stress change ($\Delta\sigma/\Delta p$) with residual dent depth, δ_r, for X65 SAW, D/t=72, t=12.7mm, r=12.7mm, p=7.68MPa, θ=45°, Δp= 1.28 ($p-p_1$) and 2.56 ($p-p_2$) MPa.

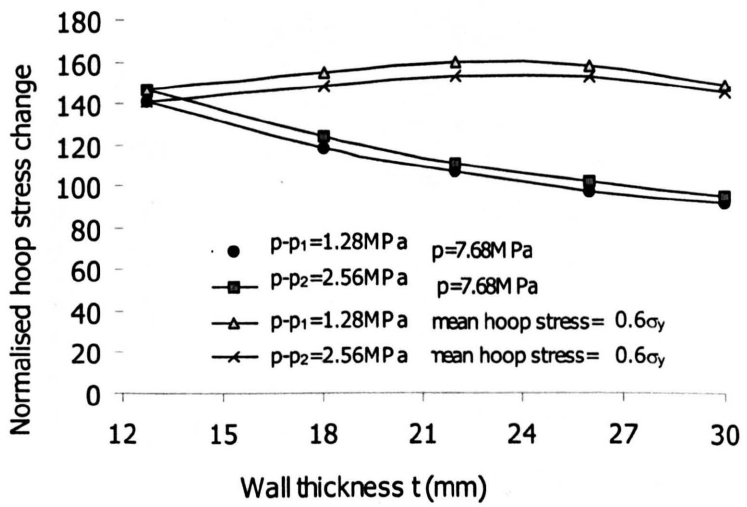

Fig.8.9 (b) Variations of normalised stress change ($\Delta\sigma/\Delta p$) with wall thickness, t, for X65 SAW, D/t=72, D=914.4mm, r=12.7mm, p=7.68MPa, θ=45°, Δp= 1.28 and 2.56MPa and applied dent depth, δ=100mm.

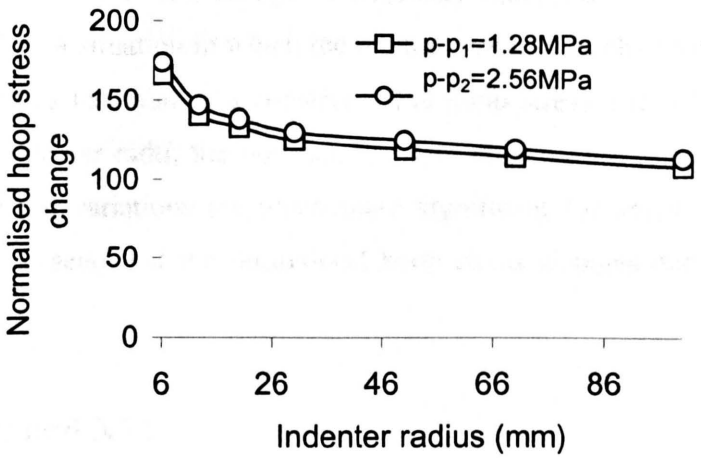

Fig.8.9 (c) Variations of normalised stress change ($\Delta\sigma/\Delta p$) with indenter radius, r, for X65 SAW, D/t=72, t=12.7mm, r=12.7mm, p=7.68MPa, θ=45°, Δp= 1.28 and 2.56MPa and applied dent depth, δ=100mm.

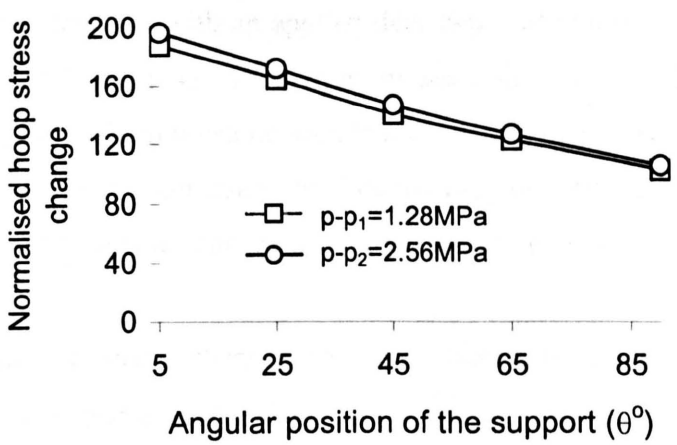

Fig.8.9 (d) Variation of normalised stress change ($\Delta\sigma/\Delta p$) with angular support position, θ, for X65 SAW, D/t=72, t=12.7mm, r=12.7mm, p=7.68MPa, Δp= 1.28 and 2.56MPa and applied dent depth, δ=100mm.

Figs.8.9 (a) and (b) indicate that the normalised hoop stress change increases with increasing residual dent depth, but decreases with the wall thickness in the same conditions (see

FE26S to FE33S). However, this change is relatively independent of wall thickness if the comparison is based on a situation in which the internal pressure is changed at the same time as the wall thickness so as to maintain a constant mean hoop stress. From Fig.8.9 (c), it can be seen that for large indenter radii, the normalised stress changes are relatively independent of indenter radius, but the variations are much more significant for small indenter radii. From Figs.8.9 (d), it can be seen that the normalised hoop stress changes decrease as the support angle,θ, is increased.

8.5.3.2 Grade B and X52

A comparison of the results from the analyses for grade B and X52 pipe materials with those for X65 SAW material, under the same conditions, allow the effects of material properties, on the normalised hoop stress changes to be assessed. All three materials are of practical importance, but the yield stresses for grade B (287 MPa) and for X52 (360 MPa) are significantly different from that of X65 SAW material (i.e. 448 MPa). For these analyses, internal pressures of 7.68, 4.92 and 6.17MPa, which produce hoop stresses in the plain pipe of 0.617 times the respective yield stresses, were used together with an applied dent depth of 60mm. The normalised stress changes for D/t=72, t=12.7mm, θ=45°, r=12.7mm, pressure ranges, Δp=1.28 and Δp=2.56MPa, are given in Table 8.3, from which it can be seen that the material properties do not significantly affect the stress changes which occur due to the internal pressure changes. This indicates that it may be possible to use the results for one material to predict the stresses for other materials.

Table 8.3 The normalised stress changes for three materials, D/t=72, t=12.7mm, θ=45°, r=12.7mm and the mean hoop stress is $0.617\sigma_y$

Material	δ_{dent} (mm)	δ_r (mm)	ΔP_1=1.28 MPa	ΔP_2=2.56 MPa
X65 SAW	60	6.77	116	120
Grade B	60	7.02	115	123
X52	60	6.68	114	120

8.6 Semi-empirical Formulation for Stress Variation

As internal pressure fluctuates, the stress changes which occur in indented pipes are elastic for the unloading and loading processes. This behaviour can be approximated to that of an

imperfect pipe undergoing elastic stress changes when internal pressure is applied. The imperfect pipe model shown in Fig. 8.10 has been used to investigate stress concentration in imperfect pipes [2-4]. The same imperfect pipe model has been used in this chapter, as the basis for the development of a semi-empirical formulation to provide an approximate relationship for the stress variation with respect to the ring geometry and residual dent depth.

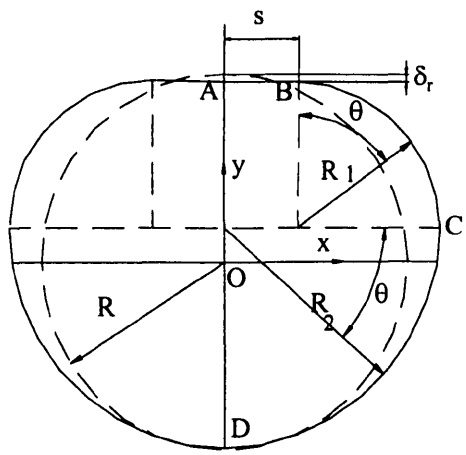

Fig.8.10 Imperfect pipe model used in elastic stress response analysis

Assuming the axial tensile force and moment at section A are denoted by N and M_0, it can be shown using force-moment relationships that the moment distribution is given by

$$\left.\begin{aligned} M_1(x) &= -\frac{1}{2}px^2 - M_0 \\ M_2(\theta) &= -Ps\left(\frac{s}{2} + R_1\sin\theta\right) - PR_1^2(1-\cos\theta) + NR_1(1-\cos\theta) - M_0 \\ M_3(\theta) &= -\frac{\pi}{2}PR_1\left(R_2\sin\left(\frac{\pi}{4}+\theta\right) - s\sin\left(\frac{\pi}{4}\right)\right) - Ps\left(R_2\cos\theta - \frac{s}{2}\right) - PR_2^2(1-\cos\theta) + \\ & N(R_1 + R_2\sin\theta) - M_0 \end{aligned}\right\} \quad (8.1)$$

where M_1, M_2 and M_3 are moments on straight segment AB, arc BC and arc CD and R_1, R_2 and s are given by

$$\left.\begin{aligned} R_1 &= R - \frac{\pi+2}{4}\delta_r \\ R_2 &= R + \frac{\pi-2}{4}\delta_r \\ s &= \frac{\pi}{2}\delta_r \end{aligned}\right\} \tag{8.2}$$

Assuming that the contributions of the axial and shear forces, to the strain energy in the ring beam, are negligible, the strain energy is given by:

$$U = \frac{12}{Et^3}\left[\int_0^s (M_1(x))^2 dx + \int_0^{\frac{\pi}{2}} (M_2(\theta))^2 R_1 d\theta + \int_0^{\frac{\pi}{2}} (M_3(\theta))^2 R_2 d\theta\right] \tag{8.3}$$

Applying Castigliano's theorem and ignoring small, high order terms, it can be shown that the form of the equation for the stress at section A is

$$\sigma = \frac{P\left(c_1\delta_r^2 + c_2 R\delta_r\right)}{t^2} + \frac{P(c_3\delta_r + R)}{t} \tag{8.4}$$

where c_1, c_2 and c_3 are constants. However, since the actual shapes of the dents in the rings are more complex than the assumed shape, shown in Fig.8.10, then predictions based on equation (8.4) will only provide an approximate solution for the stresses. In an attempt to improve the accuracy of the prediction of stress variations, it is assumed that the form of the equation will be the same for "real" indentation shapes, but that the constants (c_1, c_2, c_3 and c_4) in Eq.(8.4) are replaced by constants c_1', c_2', c_3' and c_4', so that the stress change $\Delta\sigma$ due to the pressure fluctuation ΔP, becomes

$$\Delta\sigma = \Delta P\left[\frac{\left(c_1'\delta_r^2 + c_2' R\delta_r\right)}{t^2} + \frac{\left(c_3'\delta_r + c_4' R\right)}{t}\right] \tag{8.5}$$

The constants c_1' to c_4' have been obtained by optimising the c_1' to c_4' values, to fit the results of the FE analyses, given in Table 8.2. The resulting semi-empirical formulation is

$$\frac{\Delta\sigma}{\Delta P} = \left(\frac{r}{R}\right)^{-0.1413}(-0.253\theta + 0.840)\left(\frac{1.334R + 55.11\delta_r}{t} + \frac{2.12R\delta_r - 11.074\delta_r^2}{t^2}\right) \tag{8.6}.$$

where θ is in radians.

The stress variations obtained from the FE data and equation (8.6) are shown in Fig. 8.11.

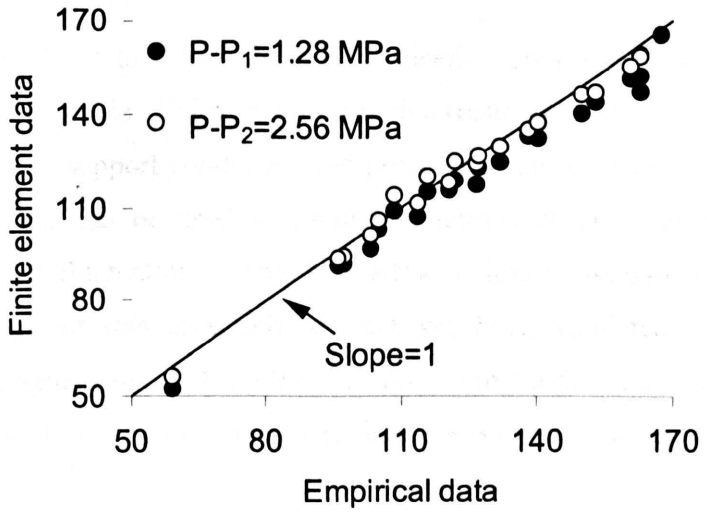

Fig. 8.11 The stress variation obtained from the FE and empirical data

It can be seen from Fig.8.11 that the semi-empirical formulation is capable of accurately predicting the effects of the indenter size, angular support position, ring geometry and residual dent depth on the normalised hoop stress variations.

8.7 Conclusions

Since the residual hoop stress is very sensitive to element sizes in an indented pipe [6], the FE mesh used in this chapter consists of 32 elements through the wall thickness in the local indentation region. In remote regions, the number of elements through the wall thickness was either 16 or 8. Therefore, it can be concluded that the residual hoop stress and normalised stress variation presented are reasonably accurate for the support and loading conditions and the material models used.

It was found that the residual hoop stresses and the normalised stress variations are related to the pipe and indenter dimensions, the pressure magnitude and the angular support position.

It should be noted that if a dent is found in a pipe, the residual dent depth, the pipe and indenter dimensions and the pipe material properties will be known or can be accurately measured. However, the actual angular support position are not well defined in most situations. Also, the angular support position is associated with the soil quality around the pipe. The determination of this angular position can only be completed through a series of tests. In

previous chapters [3-7], the relationships between the angular support position and the force-deflection curve or the limit load have been determined. Hence, an estimation of the likely support conditions can be made. Using this information (residual dent depth, material properties, pipe geometry, estimated support conditions and pressure at the time of indentation) the result, presented in this chapter can be used to obtain predictions of the residual stress and stress changes due to pressure fluctuations. This will allow a fatigue assessment to be carried out. However, the accuracy of this approach has not yet been validated by comparison with experimental pipe fatigue tests. Therefore, it is recommended for the future work that experimental tests should be performed to assess the accuracy of the method.

8.8 Summary

The residual hoop stresses in pressurised pipes caused by long external indentations and the subsequent stress variations caused by internal pressure fluctuations have been investigated for a range of residual dent depths, support positions, pressure magnitudes and indenter radii, using the FE method, including initial stress and geometrical non-linearity effects. Three materials were used in the investigation to assess the effects of material properties on the stress variations. A semi-empirical formulation has been developed, based on an imperfect, indented pipe model and the results of the FE analyses, to predict the variations of the residual stresses in the pipes.

Chapter 9

Finite Element Analysis of Indented Pipes Using Three-Dimensional Solid and Shell Elements

9.1 Introduction

This chapter presents FE analysis of indented pipe using 2D, 3D and shell elements. Two types of indenters are used; a long cylindrical indenter which can be analysed using a relatively simple 2-D plane strain model, and a tooth-type indenter (a short cylinder with rounded ends) which requires a 3-D model. Results are presented for the contact stresses and the residual stresses left within the pipe wall, due to the application of the indenter.

Three FE models using 2-D plane strain, shell and 3-D solid elements are used. A mesh sensitivity analysis is performed to determine the optimum number of elements needed across the thickness of the pipe. The FE solutions indicate that the stresses at the contact point of the indenter with the pipe are very sensitive to element sizes, particularly for large indentations. The pipe models are expected to require 20 or more elements across the pipe thickness in order to produce accurate results. Therefore, a 3-D model of the pipe using brick elements is not considered practical. However, since the plastic zone is localised around the indented region, it is possible to use sub-modelling to overcome this problem.

The shell model uses considerably less computer storage than the 3-D solid model, and is capable of producing acceptable solutions for the residual stresses, see for example [9, 12]. Based on comparison of 3-D solid and shell elements, it is shown that the shell model is valid for the analysis of the indented pipe.

In this chapter, details of the distribution of the residual stresses around the circumference of the pipe and along the axis of the pipe are presented for a number of indentation depths. Results based on using different FE models are compared.

9.2 Problem Definition

The geometry, boundary conditions and loading for the indented pipe are defined in Figure 4.1. The results presented in this chapter are based on a thin-walled pipe geometry of outer diameter, D, of 914.4 mm and wall thickness, t, of 12.7 mm (i.e. a ratio of D/t = 72). Two types of indenters are used in this work; a long cylindrical bar indenter to model a 2-D plane-

strain indentation, and a 3-D tooth-shaped indenter consisting of a rigid cylinder with two half-spheres at either end of the same radius as the cylinder.

The material, X65 SAW steel, of the pipe is elastic-plastic with isotropic work-hardening with first yield at a yield stress σ_y = 448 MPa. Figure 3.1 shows the stress-strain curve of the pipe material.

The pipe is supported over an arc from θ=135° to θ=225° along its entire axial length, where θ is measured clockwise from the point of contact with the indenter.

Two load steps are used to simulate an indented un-pressurised pipe. In the first load step, the indenter is brought into contact with the pipe wall by prescribing a vertical downward displacement with indentation depths ranging from 0.01 to 0.1 D. Following each indentation depth, the indenter is removed from the pipe leaving residual stresses within the pipe wall.

9.3 Finite Element Analyses

The ABAQUS FE package [26] is used in the analysis of the indented pipes. In all the cases, the indenter is modelled as a rigid circular surface, and is moved into the pipe by applying a prescribed displacement to the centre of the rigid surface (reference node). The FE analysis is performed with geometric non-linearity due to the large deformation of the pipe wall caused by the indenter.

9.3.1 Stress sensitivity to element sizes

For a dented pipe, stress distributions at the contact point between the pipe and the indenter are complicated and sensitive to element size [5, 20]. The contact penetrating stress between the two structures can only be accurately modelled using very fine meshes. To investigate this, a quarter of 2-D plane-strain dented pipe structure is analysed, as shown in Figure 9.1.

Three different indentations of 0.05, 0.075 and 0.1 Do are applied to the un-pressurised pipe. All movements at the bottom end of the pipe are fully restrained, and the top end is constrained to move vertically due to geometrical symmetry. A number of different meshes are used where 5, 8, 15, 20, 30 and 40 quadratic 8-node plane strain elements with 2x2 integration points are placed through the wall thickness at the contact region (x=0 plane), reducing along the circumference to 5, 8, 15, 10, 15 and 20 elements, respectively, at the remote region (y=0 plane).

Figure 9.2 shows the variation of the residual hoop stress at the contact point on the outer surface with the number of elements across the wall thickness. The FE solutions indicate that

the residual hoop stresses are very sensitive to the element sizes, particularly at large indentation depths. For an indentation depth of 0.075 D, the differences between the residual hoop stresses at the contact point vary by up to 10%, while for an indentation of 0.05 D, they vary by up to 5%. For the larger indentation depth of 0.1 D, the difference is about 11%.

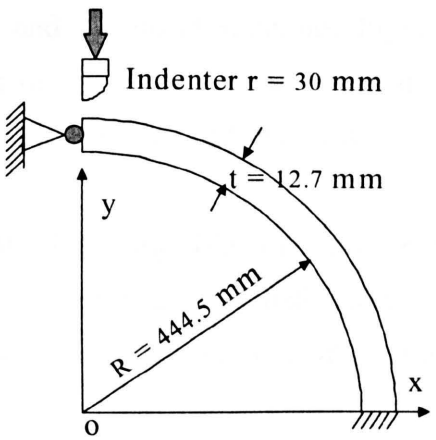

Figure 9.1 2-D plane strain problem used for mesh refinement analysis

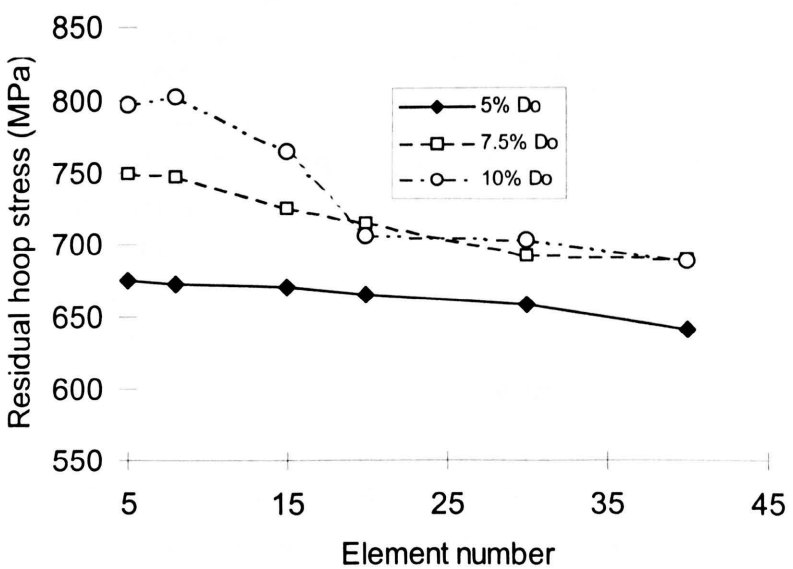

Figure 9.2 Residual hoop stress at the contact point against the number of 2-D quadratic elements through the wall thickness for different indentation depths.

To investigate the effect on the residual stresses of changing the 2-D elements from quadratic 8-node to linear 4-node elements, a pipe indented to 0.1 Do is analysed with 6 different models with 5, 10, 15, 20, 30 and 60 linear, 4-node plane strain elements with reduced integration (1 integration point) through the wall thickness at the contact region. The

FE solution for the contact and residual hoop stresses using the 4-node elements on both the inner and outer surfaces are shown in Figure 9.3 where it can be seen that contact stresses are not very sensitive to element sizes, while the residual stresses are more sensitive to mesh refinement.

To compare the 4-node and 8-element solutions, Figure 9.4 shows the residual hoop stresses at the contact point on the outer surface obtained using both element types. This shows that FE solutions using linear and quadratic elements converge when 30 elements are placed across the thickness.

The above results indicate that using 3-D solid elements would require a prohibitively large mesh which may be impractical. A shell model, however, would require less computation time than a 3-D solid model, and may offer an acceptable compromise between accuracy and computational demand.

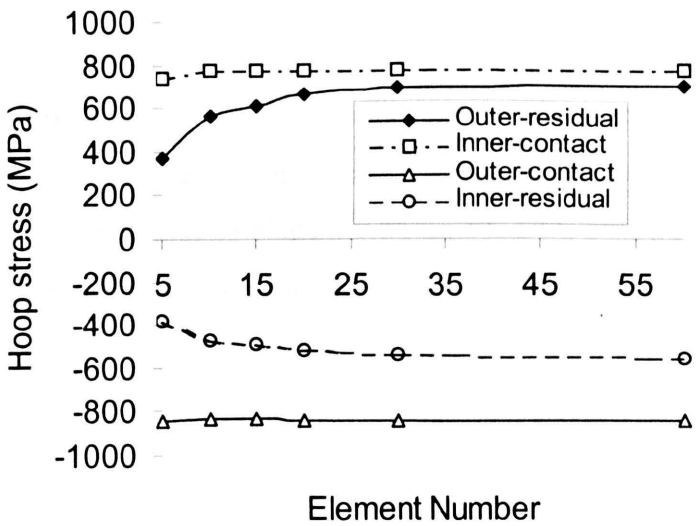

Figure 9.3 Contact and residual stress at the contact plane for the inner and outer surfaces against the number of 2-D linear elements through the wall thickness for an indentation depth of 0.1 D.

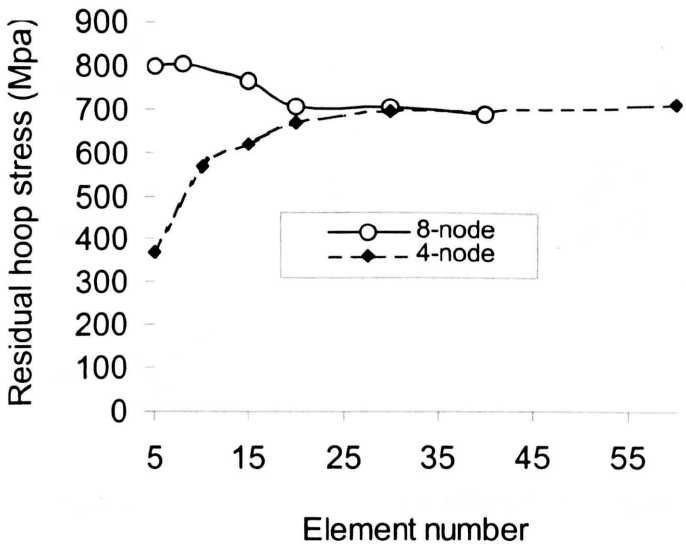

Figure 9.4 Residual hoop stress at the contact point against element numbers through the wall thickness using 2-D linear and quadratic elements for an indentation depth of 0.1 D.

9.3.2 FE Shell model

In order to validate the shell model, an eighth of a pipe model (see Figure 9.5a) in which meridional movements and rotations in plane x-y on both sides CD and EF are prevented and the axial movement on side CD is restricted. All nodes on side EF are restrained to move by an equal axial distance. Displacements in the x-direction and rotations in y-z plane on side CE are prevented. On side DF, displacements in the x and y directions and all rotations are prevented.

FE analyses are performed for different indenter radii ranging from 12.7 to 40 mm, internal pressures ranging from 0 to 5.12 MPa, indentation depths ranging from 0.02 D to 0.05 D, and wall thicknesses ranging from 12.7 to 27 mm.

The FE shell model consists of 10845 linear, 3-node and 4-node reduced integration (with 1 integration point) finite-strain elements. Two 2-D models are used for comparison purposes, one consisting of 9525 linear 3-node and 4-node elements with 1 integration point, and the other consisting of 3656 quadratic 6-node and 8-node plane strain elements with 3 and 4 integration points, respectively. The 2-D linear and quadratic element models contain 30 and 32 elements, respectively, across the wall thickness at the contact point (see Fig. 8.2). Part of the shell mesh is shown in Figure 9.5b.

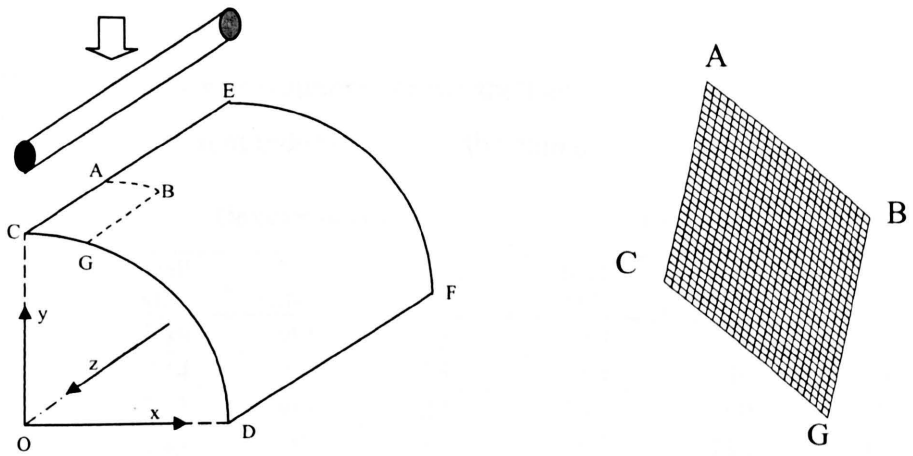

(a) Geometry (b) FE shell element mesh of region ABGC

Figure 9.5 Shell model and FE shell element mesh used to model plane strain conditions

9.3.2.1 Different indenter sizes

In order to compare the 2-D and shell models for different indenter sizes, different indenter radii of 12.7, 20, 30 and 40 mm are used. An internal pressure of 3.84 MPa is applied before indentation. The indentation depth is 0.035 D and the pipe wall thickness is 12.7 mm. The contact and residual hoop stresses at the contact position on the outer and inner surfaces, calculated by using shell elements and linear 3-node and 4-node 2-D elements, are shown in Table 9.1. The results indicate that differences in the contact stresses between shell and 2-D models are very large, up to 25 %, whereas the differences between the residual hoop stresses are much smaller at less than 5.2 %. This can be explained by the fact that the shell model cannot accurately simulate the variation of the penetrating pressure across the wall thickness caused by the indenter. A comparison of the residual stresses obtained by using shell and quadratic 2-D elements is shown in Table 9.2, where it can seen that the differences are less than 5%.

Table 9.1 Contact hoop stress solutions for the shell and 2-D linear element models for different indenter radii at the contact position

Indenter radius (mm)	On outer surface			On inner surface		
	Shell (MPa)	2-D (MPa)	Error (%)	Shell (MPa)	2-D (MPa)	Error (%)
12.7	-749	-999	25	789	740	6.6
20	-744	-993	25	784	740	5.9
30	-743	-969	23	783	740	5.8
40	-743	-895	17	783	738	6

Table 9.2 Residual hoop stress solutions for the shell and 2-D models for different indenter radii at the contact position

Indenter radius (mm)	On outer surface					On inner surface				
	Shell (MPa)	2-D linear (MPa)	Difference (%)	2-D quadratic	Difference (%)	Shell (MPa)	2-D linear (MPa)	Difference (%)	2-D quadratic	Difference (%)
12.7	741	704	5.2	737	0.4	-773	-736	5	-744	3.9
20	734	702	4.5	690	6.4	-766	-736	4.1	-743	3.1
30	729	701	3.9	697	4.6	-768	-735	4.5	-741	3.6
40	733	702	4.4	700	4.7	-764	-734	4.1	-741	3.1

9.3.2.2 Different internal pressures

To investigate the influence of the internal pressure on the shell and 2-D solutions, the FE simulations are performed by applying different internal pressures of 0, 2.56, 3.84 and 5.12 MPa before indentation. An indenter of radius 30mm is used with an indentation depth of 0.035 D and pipe wall thickness of 12.7 mm. The residual stresses are listed in Table 9.3, which show that changing the internal pressure causes differences of up to 5.9% between the shell and 2-D models.

Table 9.3 Residual hoop stress solutions for the shell and 2-D models for different pressures at the contact position

Pressure (MPa)	On outer surface					On inner surface				
	Shell (MPa)	2-D linear (MPa)	Difference (%)	2-D quadratic	Difference (%)	Shell (MPa)	2-D linear (MPa)	Difference (%)	2-D quadratic	Difference (%)
0	560	544	2.9	553	1.2	-532	-502	5.9	-539	1.3
2.56	716	682	4.9	688	4.1	-734	-708	3.7	-715	2.6
3.84	729	701	4	697	4.6	-768	-735	4.5	-741	3.6
5.12	741	711	4.2	710	4.3	-789	-752	4.9	-758	4.1

9.3.2.3 Different indentation depths

Indentation depth is the main factor that causes a dented pipe to fail either during indentation or afterwards due to fatigue failure caused by pressure fluctuations. Indentation depths of 0.02, 0.035 and 0.05 D are applied in order to investigate the solution differences between the shell and 2-D models. An internal pressure of 3.84 MPa is applied before indentation. An indenter of radius 30 mm is used with a wall thickness of 12.7 mm. The residual hoop stress solutions are shown in Table 9.4, where it can be seen that changing the indentation depth can produce differences of up to 8.6% between the shell and 2-D solutions for the range of conditions investigated.

Table 9.4 Residual hoop stress solutions for the shell and 2-D models for different indentation depths at the contact position

Indenter depth	On outer surface					On inner surface				
	Shell (MPa)	2-D linear (MPa)	Difference (%)	2-D quadratic	Difference (%)	Shell (MPa)	2-D linear (MPa)	Difference (%)	2-D quadratic	Difference (%)
0.2 Do	629	579	8.6	648	2.9	-652	-626	4.2	-637	2.3
0.35 Do	729	701	4	697	4.6	-768	-735	4.5	-741	3.6
0.05 Do	795	760	4.6	783	1.5	-826	-784	5.3	-791	4.4

9.3.2.4 Different wall thicknesses

Increasing the pipe wall-thickness can improve resistance to external impact loading and thus improve the safety of the pipe. In this section, different wall thicknesses of 12.7, 17, 22

and 27 mm are used to compare the shell and 2-D solutions without changing the number of elements across the wall thickness. An indenter of radius 30mm is used with an indentation depth of 0.035 D and an internal pressure of 3.84 MPa. Comparisons of the residual stress solutions between the shell solutions and the 2-D linear and quadratic elements are listed in Table 9.5. The results show that at the contact point on the outer surface, residual stress differences between the shell and 2-D models increase as the wall-thickness increases.

Table 9.5 Residual stress solutions for the shell and 2-D models for different wall thicknesses at the contact position

Wall-thickness (mm)	On outer surface					On inner surface				
	Shell (MPa)	2-D linear (MPa)	Difference (%)	2-D quadratic	Difference (%)	Shell (MPa)	2-D linear (MPa)	Difference (%)	2-D quadratic	Difference (%)
12.7	729	701	4	697	4.6	-768	-735	4.5	-741	3.6
17	743	703	5.6	718	3.5	-760	-733	3.6	-737	3.1
22	750	703	6.7	703	6.7	-757	-726	4.3	-730	3.7
27	757	700	8.1	705	7.4	-758	-712	6.5	-725	4.5

The above results show that stress solutions are very sensitive to mesh refinement across the pipe wall, and can only be obtained using 30 or more elements across the wall thickness for a D/t ratio of 72. This implies that in a 3-D dented pipe FE model, the number of elements needed to obtain accurate stress solutions will be very large. The above results also show that the shell FE models may not be capable of accurately calculating the contact stresses but are capable of calculating residual stresses to a reasonable degree of accuracy.

Although 2-D quadratic elements are considered to be more capable than linear elements of accurately calculating stress values, the solutions listed in the above tables indicate that for most cases using 2-D linear elements can give residual stresses on both surfaces very close to those of the quadratic elements.

In the analyses of the effects of the indenter radius, the indentation depth, the internal pressure and the wall thickness, on the differences in the solutions between the shell and 2-D models, the FE solutions show that these factors do not significantly change the residual hoop stress between the shell and 2-D models.

9.3.3 3-D solid models

To model a tooth-like indenter, rather than a long cylindrical indenter, a shell or 3-D solid model is needed. In this section, a short rigid cylindrical indenter is applied with a radius of 12.7 mm and an axial length of 20 mm with two half-spheres at either end with the same radius as the cylinder. An un-pressurised pipe in indented to a depth of 0.01 D and is then released.

A 3-D solid FE model of the dent region is created as a sub-model rather than a full model in order to increase the mesh refinement at the contact region. The sub-model is generated with 9 elements through the wall thickness in the dent region and 3 elements across the thickness elsewhere, as shown in Figure 9.6. Three types of quadratic solid elements are used; 20-node, 27-node brick elements and 15-node triangular prism elements with reduced integration. The shell FE model, shown in Figure 9.7, is generated with 4-node doubly-curved quadrilateral elements and 3-node triangular elements with reduced integration, where fine meshes are created in the dent region and coarse meshes elsewhere.

The FE solutions for the variation of hoop, axial and von Mises stresses obtained using 3-D solid and shell models are shown in Figures 9.8 and 9.9 along the circumference at the axial plane $z = 0$, and Figure 9.10 along the axial distance from the point of contact at the $\theta = 0^{o}$ plane. From these figures, it can be seen that the residual stress distributions on the pipe outer surface obtained using the 3-D solid model are not smooth but oscillatory in the dent region especially for the hoop and axial stress distributions. This phenomenon occurs because the meshes used for the 3-D solid analysis are not refined enough, even when 9 elements are placed across the wall thickness.

Comparing the residual stress distributions obtained using the shell and 3-D solid models, it is clear that they are quite consistent on the pipe inner surface, except at the dent region on the pipe outer surface where oscillations of hoop and axial stress occur in the 3-D solid model. However, von Mises equivalent stress distributions in the 3-D solid model are not oscillatory and are close to those in the shell model. Hence, the comparisons of the solutions obtained employing the shell and 3-D solid models show that the shell model can adequately simulate the residual stresses resulting from pipe indentation.

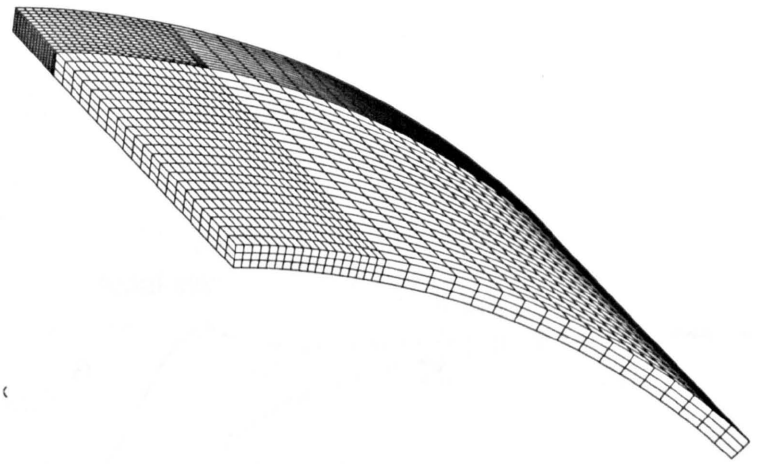

Figure 9.6 Sub-model of the 3-D solid element model.

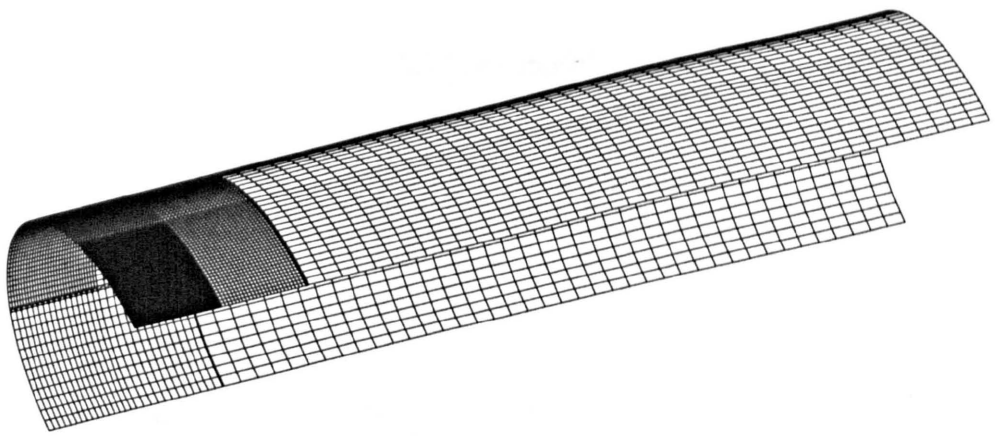

Figure 9.7 Shell mesh used to model 3-D conditions.

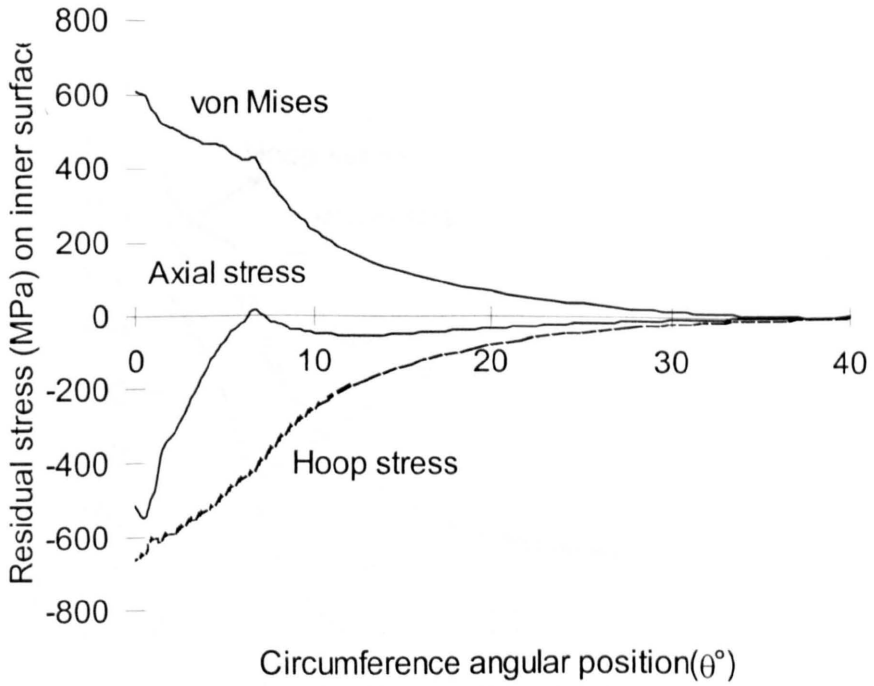

(a) Shell model

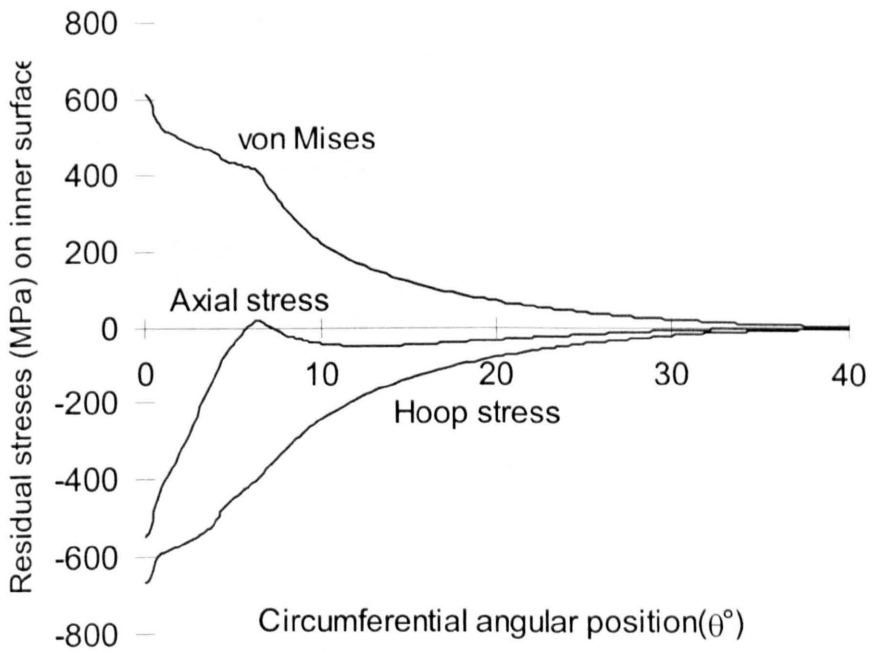

(b) 3-D solid model

Figure 9.8 Residual stress along the inner circumference of the pipe for an indentation depth of 0.01 Do at the z = 0 plane

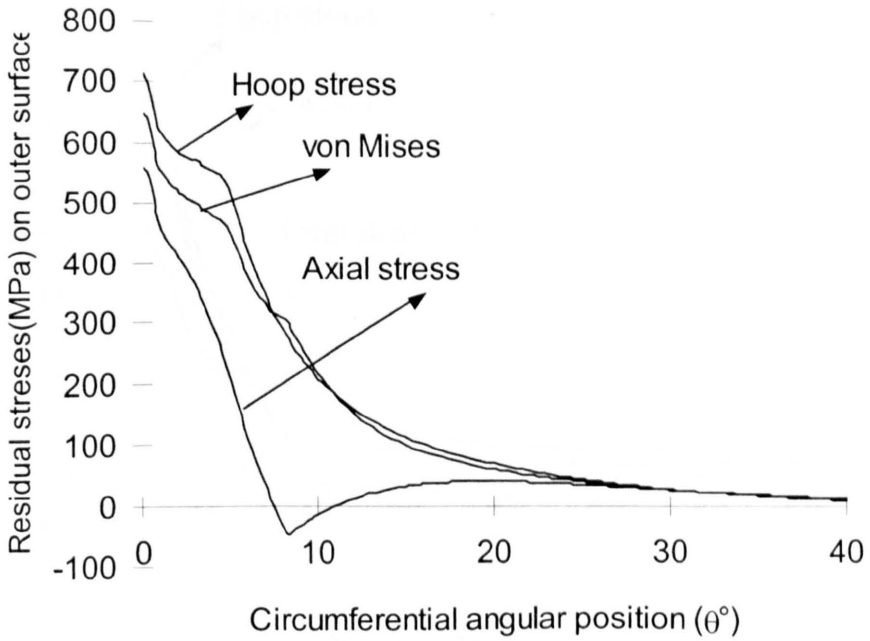

(a) Shell model

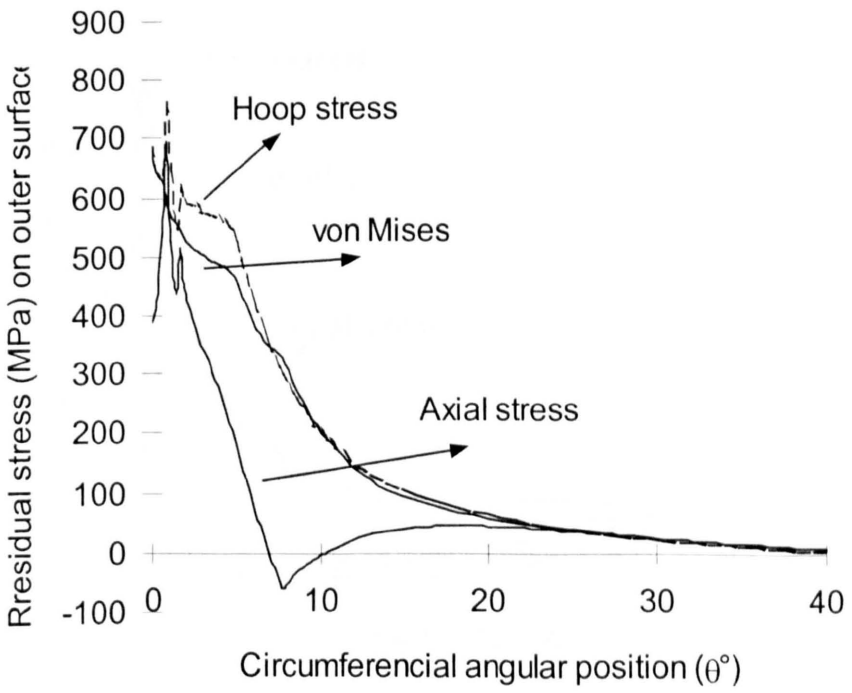

(b) 3-D solid model

Figure 9.9 Residual hoop stress along the outer circumference of the pipe for an indentation depth of 0.01 Do at the z = 0 plane

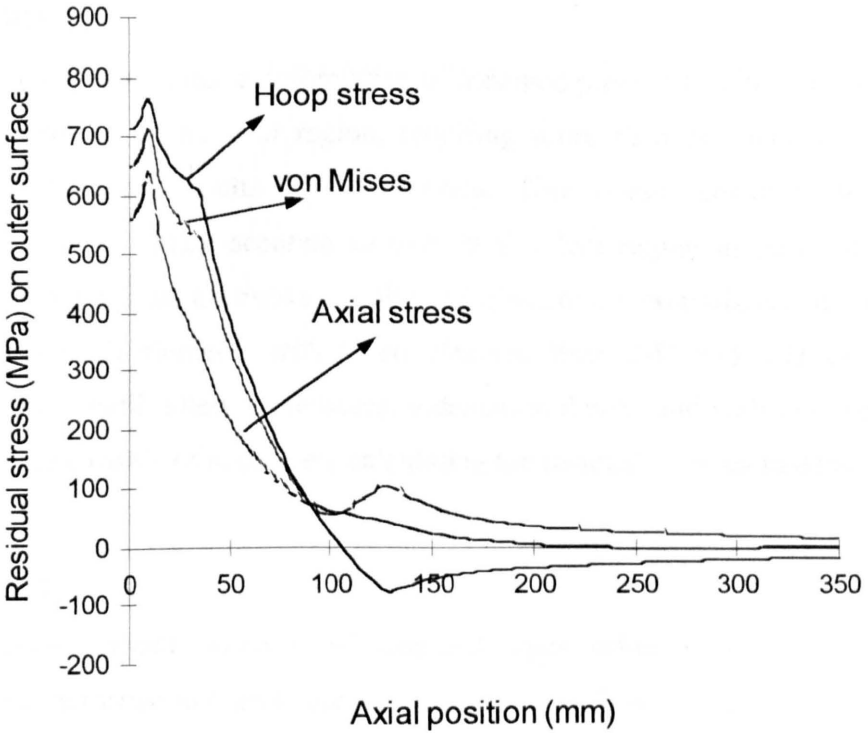

(a) Shell model

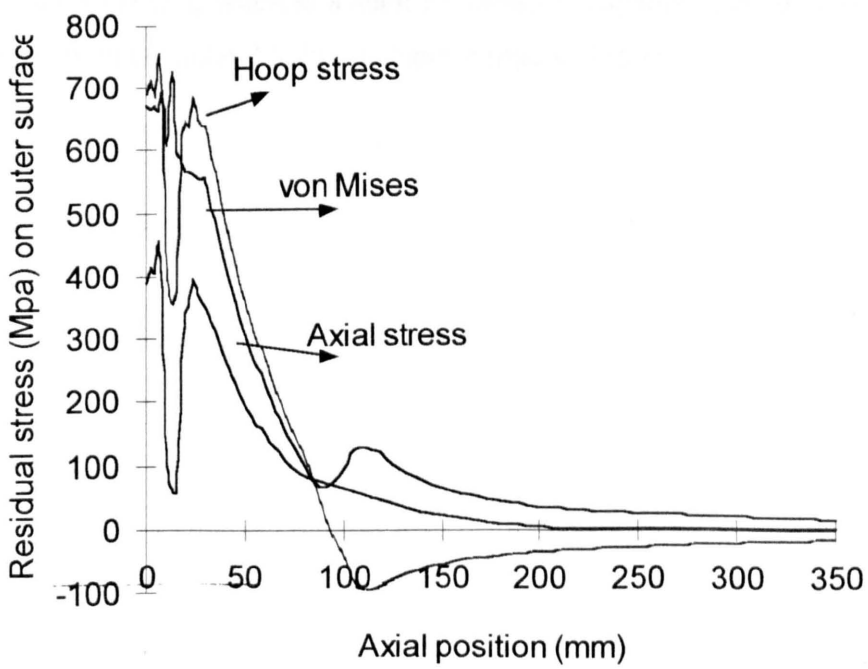

(b) 3-D solid model

Figure 9.10 Residual hoop stress along the outer axial position the pipe for an indentation depth of 0.01 Do at the $\theta = 0^{o}$ plane

9.4 Conclusions

Due to the localised plastic deformation of indented pipes, FE solutions are quite sensitive to mesh refinement in the dent region, requiring more than 30 elements across the wall thickness for accurate results to be obtained. This stress sensitivity to element sizes demonstrates that to obtain accurate stresses in the dent region using a 3-D solid element model would require an excessive number of elements. Comparisons of the FE solutions obtained using shell elements with those obtained from 2-D and 3-D solid elements for different indenter radii, internal pressures, indentation depths and wall thicknesses, show that shell models are capable of accurately calculating the residual stresses in dented pipes.

9.5 Summary

This chapter presents analysis of indented pipes using a number of FE models to determine the deformations and stresses arising in typical cylindrical pipes damaged by indenters. A number of FE models using 2-D plane strain, shell and 3-D solid elements are used. A mesh sensitivity analysis and a comparison of the stresses obtained from shell and 3-D solid elements show that a 3-D solid model may be impractical because it requires a high degree of mesh refinement, whereas a shell FE model is capable of accurately calculating the residual stresses with considerably less computer time and storage.

Chapter 10

Experimental Validation of FE Approach to Predicting the Elastic-Plastic Response of Pipes Subjected to Localised Indentations

10.1 Introduction

In previous chapters 3-7, analytical and FE solutions to the indentation of pressurised and unpressurised rings have been compared with experimental data. These results indicate that the FE method is capable of predicting the large deformation response of rings. Also, it has been shown (chapter 9) that shell elements can give similar accuracy to that obtained using three dimensional brick elements, provided that care is taken in the design of the meshes used for the shell elements.

In this chapter, comparisons of experimental test results with FE predictions are used to validate the use of shell elements for predicting the indenter force versus deflection behaviour of pipes subjected to localised three dimensional indentations, as opposed to the ring results used to simulate the long two dimensional indentation case previously investigated in chapters 3-7.

10.2 Experimental Work

10.2.1 Material

An aluminium alloy (6082-T6) was chosen for the experimental tests because of the relative ease with which small diameter pipes, with large D/t ratios, can be accurately manufactured from it. The uniaxial tensile stress versus strain curve for the material is shown in Fig.3.1. The 6082-T6 aluminium alloy material has Young's Modulus, Poisson's ratio, yield stress, and ultimate tensile stress of 70GPa, 0.3, 300MPa, and 351 MPa, respectively. From Fig. 3.1, it can be seen that 6082-T6 aluminium alloy stress-strain curve closely approximates to that of an ideal elastic perfectly plastic material behaviour.

A 6082-T6 aluminium alloy tube was supplied with a nominal outer diameter (D) of 101.6 mm and nominal wall thickness (t) of 19.05 mm. The tubes were cut into lengths of approximately 500 mm. These tubes were then line-bored and honed to produce accurately

circular inner diameters. The outer surface of the tubes was then machined to the required dimensions using the bore as datum (see Fig 10.1).

10.2.2 Geometry, Loading and Boundary Condition

The final outer diameters and wall thicknesses of the pipes were 86.4 mm and 1.2 mm, respectively, giving a D/t ratio of 72. The pipes were machined with flanged ends with a radial thickness of 22 mm and an axial length of 25 mm. To reduce the stress concentration at the junctions between the two flanged ends and the straight pipe segment, the junctions were machined with circular arc fillets with a radius of 8 mm, see Fig. 10.1. The plain section length of the pipes was 334mm.

End caps, with a thickness of 10 mm, were attached to the pipes using four bolts. Holes in the end caps allowed the oil to circulate around a loop consisting of the test pipe, the connecting pipes and the pump.

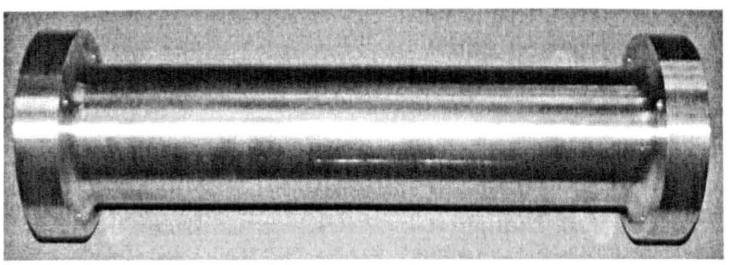

Fig.10. 1 Experimental pipe

The indenter was made of bright drawn mild steel with a shape similar to that of an excavator's tooth. The end of the indenter consists of half a cylinder and two quarter spheres with 2mm radii (r) and the axial length of the indenter (L_i) was 6mm, as shown in Fig. 10.2. The bright drawn mild steel has significantly higher Young's modulus and yield stress than the 6082-T6 aluminium alloy. Therefore, the indenter can reasonably be assumed, for the purpose of the analysis, to be a rigid body.

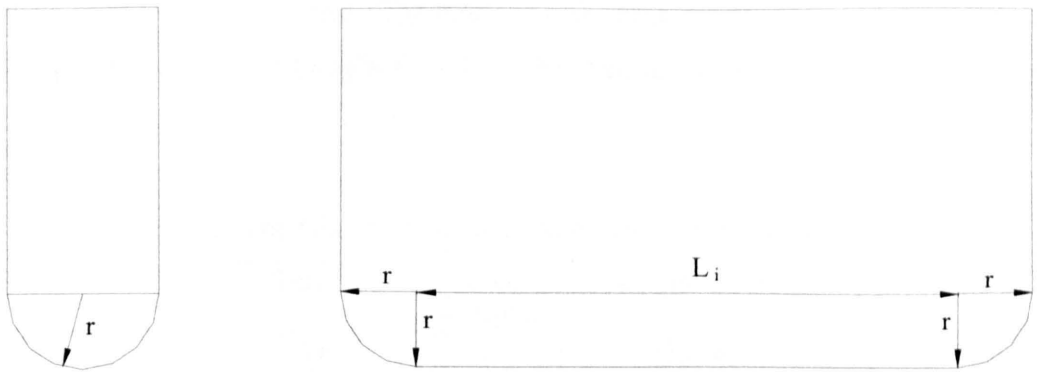

(a) Side view (b) Elevation view

Fig. 10.2 Indenter used in experimental tests

To simulate three-line constraint conditions, a flat-bottomed 90° v-groove support, as shown in Fig. 10.3, was used.

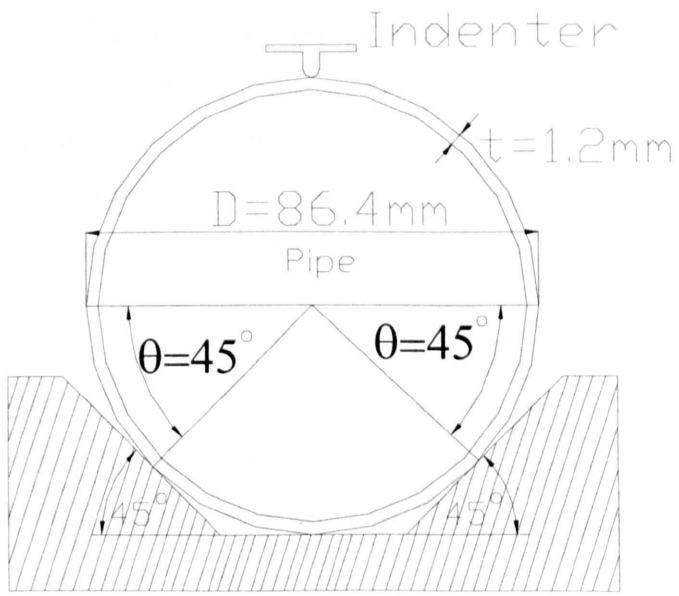

Fig.10. 3 Pipe on support

The internal pressure was kept constant during the deformation process. The indenter, shown in Fig. 10.2, was positioned in the testing machine at the centre of the pipe's length and was moved radially inwards to a predetermined dent depth, then it was released. A total of six

experimental tests were performed. The tube has a D/t ratio of 72 and a wall thickness of 1.2mm and the corresponding support angle, θ, is 45°. The loading conditions for each test are shown in Table 10.1.

Table 10.1: The tube loading conditions used in the experimental tests

Test No.	Pressure p (MPa)	Loading condition
TE1	0	on-off
TE2	2	on-off
TE3	3	on-off
TE4	4	on-off
TE5	5	on-off
TE6	2.8	Cyclic

10.2.3 Experimental Method

A Hydraulic Power Pack was used to apply a constant internal pressure during the deformation of the indented pipes. The Hydraulic Power Pack with its pressure gauge was calibrated before performing the tests.

The indenter, shown in Fig. 10.2, was fixed to the load cell of an Instron 1195 Automated Servo Electric Material Testing Machine. The cross head was moved down at a speed of 0.5 mm/second, which was slow enough to simulate a static contact process between the indenter and the pipe.

The loading and data acquisition for the experiments were attained using the standard facilities of the Instron 1195 Automated Material Testing System, which produces a force/displacement plot on a PC and also saves the test results in a data file on the PC.

To ensure that the Instron system was properly calibrated, a Dial Indicator with a range of 0 to 15mm × 0.01 mm was set up on a magnetic base to monitor the displacements of the indenter during the tests.

The FE analyses were not used to simulate the initiation and growth of a crack. Hence, good correlation between experimental and FE results would not be expected once a crack had initiated. Therefore, to monitor the development of cracks on the inside surface of the pipes, a Sony KTV-22 Video inspection system was used. This system has a camera with a long-handle

lens, which can be placed inside the pipe and can be positioned to take pictures and to record the crack development.

Schematic diagrams showing the experimental set-up used for the tests are given in Figs. 10.4 and 10.5.

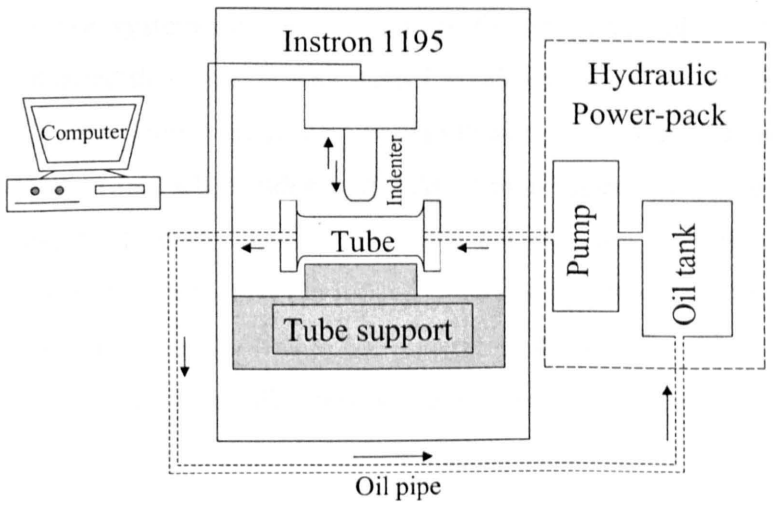

Fig. 10.4 Experimental test configuration for pressurised pipes

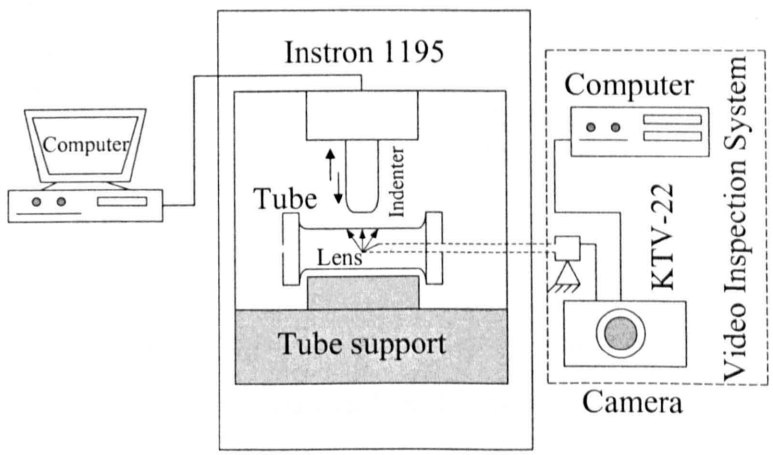

Fig 10.5 Experimental test configuration for observing internal crack initiation

10.3 Experimental Results

The experimental tests of specimens TE1 to TE5 (see Table 1) were performed with different constant pressure levels, i.e. p=0, 2, 3, 4 and 5 MPa. The results of the indenter force versus dent

depth curves are shown in Figs. 10.6 (a) to (e). The variation of the initial gradients with internal pressure, obtained from Figs. 10.6 (a) to (e), is shown in Fig.10.7. The indentation load for each test was increased to about 2.5kN and then reduced to zero. From Fig. 10.7, it can be seen that the initial slopes of the indenter force versus indentation depth curves increase as the internal pressure is increased. In the case of test TE1, which was performed with p=0 MPa, the Sony KTV-22 Video inspection system was used to monitor the initiation and growth of cracks on the inner surface. This showed that small cracks started to initiate when the indenter reached a depth of between 6 and 6.5 mm. However, as Fig. 10.6(a) indicates, the pipe was still able to carry a higher indenter force than this when indenter depths of more than 6.5mm were applied. Failure occurred at a dent depth of about 10mm. Fig. 10.6 (d) indicates that the pipe, with internal pressure of 4MPa, was punctured when the indenter reached a depth of about 4.5mm. However, in tests, TE2, TE3 and TE5, the pipes were not punctured, but small cracks with different sizes were observed on the inner surfaces after testing. It was not clear when those cracks started to initiate.

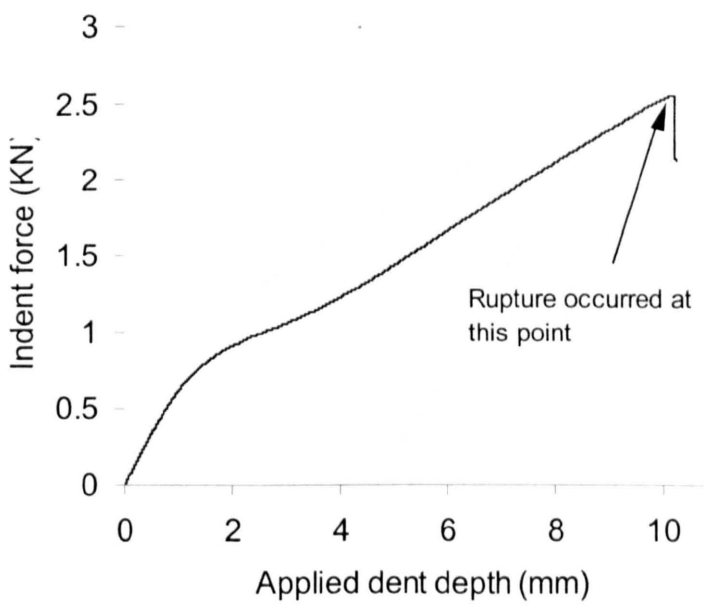

Fig. 10.6 (a) p=0 MPa

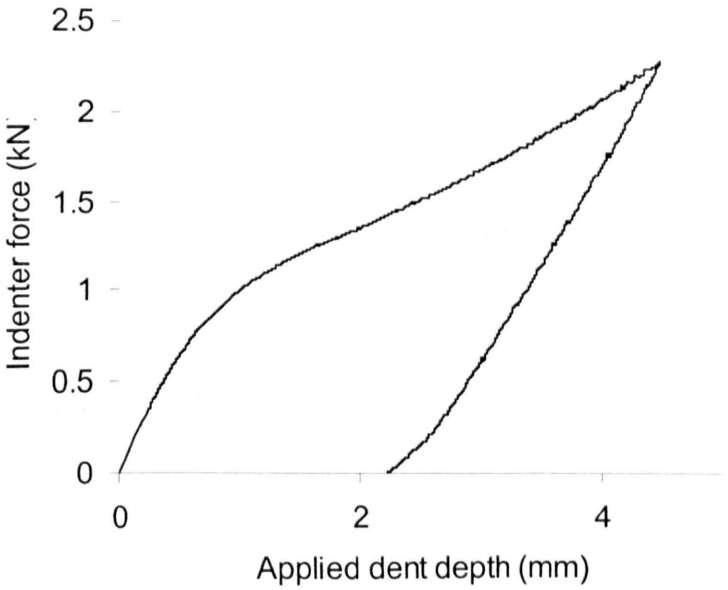

Fig. 10.6 (b) p=2 MPa

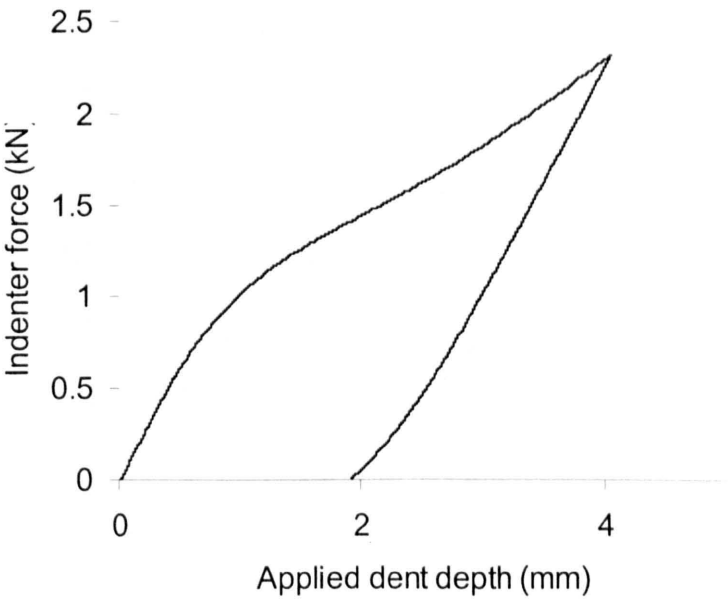

Fig. 10.6 (c) p=3 MPa

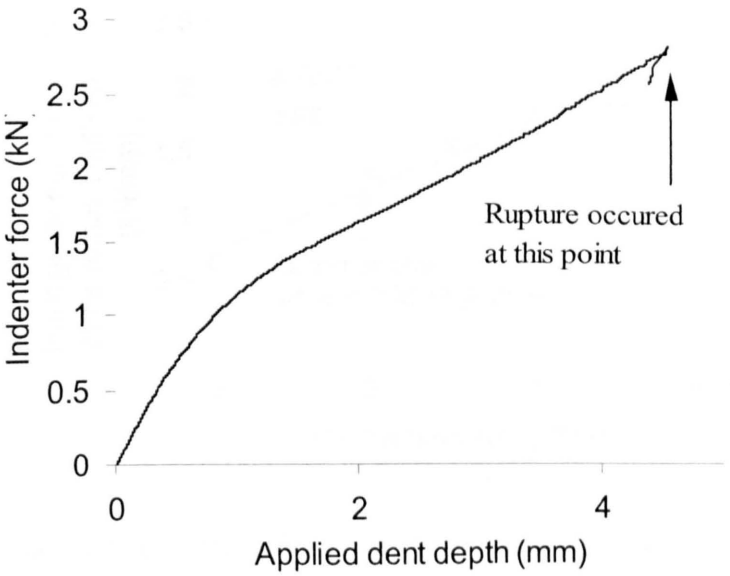

Fig. 10.6 (d) p=4 MPa

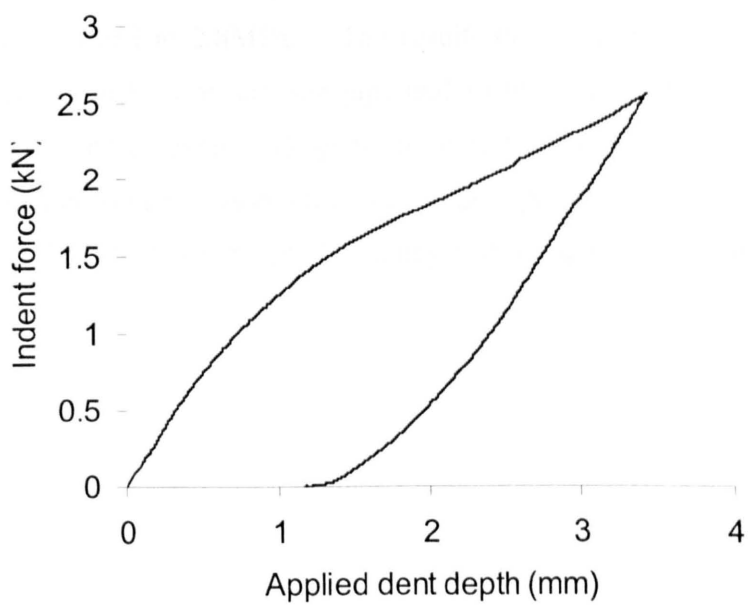

Fig. 10.6 (e) p=5 MPa

Fig. 10.6 The indenter force versus depth curves obtained from experimental tests for on-off indentation, on 6082-T6 aluminium alloy tubes with $\theta=45^{o}$, D/t=72, t=1.2mm and different internal pressure levels, i.e. p=0, 2, 3, 4 and 5 MPa.

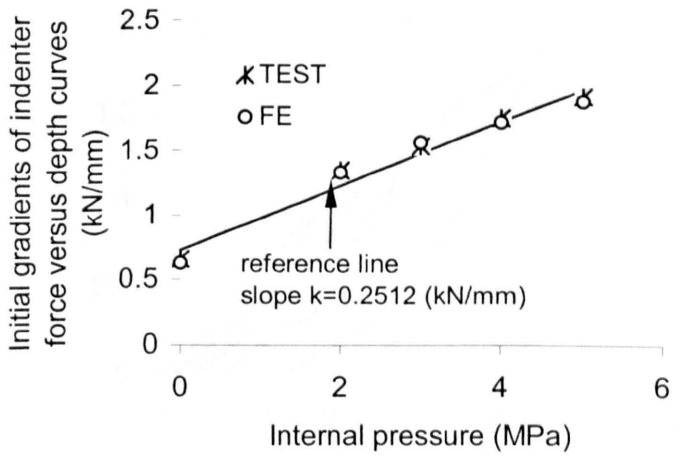

Fig. 10.7 The initial gradients obtained from the experimental tests and the FE analyses for various magnitudes of internal pressure

Specimen TE6 was used to investigate the behaviour under cyclic indenter loading conditions, with the pressure maintained at 2.8MPa. The results obtained from this test are shown in Fig.10.8, from which it can be seen that the pipe underwent both elastic-plastic and non-linear elastic deformations, during indenter load applications and releases. Also, it can be seen from Fig. 10.8 that the indenter force versus depth curves, under cyclic indentation conditions, are very similar to the curves obtained from the single loading and unloading indentation tests, shown in Fig. 10.6 (a) to (e).

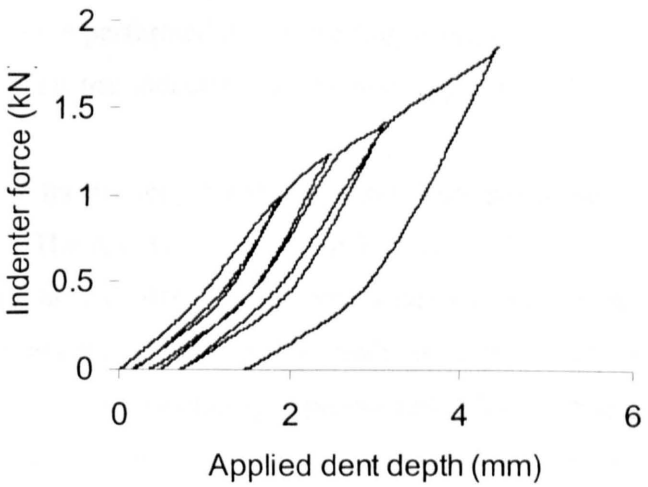

Fig. 10.8 The cyclic indenter force versus depth curves obtained from experimental test TE6 performed on the 6082-T6 aluminium alloy tube with θ=45°, D/t=72, t=1.2mm and p=2.8 MPa.

10.4 Finite Element Model

As the contact between the pipe and the indenter causes high localised stresses in the indenter region, the accurate determination of the residual stresses in the pipe, after indentation, requires very careful mesh design. Shell elements were used in order to reduce the computational time and because shell models are able to predict residual stresses with reasonably accuracy [45]. Shell element models have been widely used in pipe integrity investigations, e.g. [12]. Due to the geometric and loading symmetry, a quarter of pipe model, shown in Fig. 9.7, was generated with 4-node, doubly-curved, quadrilateral, shell elements, and 3-node, triangular shell elements, with reduced integration. Suitably fine meshes were created in the dent region and coarser meshes were used elsewhere. Details of the meshes and FE analyses procedures have been reported in chapter 9.

10.5 FE Results

In order to accurately model the force versus deflection behaviour of the indented, pressurised pipes, with elastic-plastic, large deformation response, using the ABAQUS FE software [26], all of the FE analyses included geometric non-linearity. In practice, the pipelines are long and the localised deformation of the pipe does not have a significant effect on the total internal volume of

the pipe. The internal pressure during the deformation was, therefore, kept constant in the FE analyses. These analyses were performed in two loading steps, i.e. the pipe was first subjected to an internal pressure and then the indenter loading was applied while maintaining the internal pressure constant.

Five FE analyses, using the arc-length RIKS method, were performed with internal pressures of 0, 2, 3, 4 and 5 MPa. The results are shown in Fig. 10.9 where it can be seen that at early stages of the deformation, the indenter force increases rapidly, with increase of the dent depth, when the pipes are in the elastic range. The FE predictions of the initial slopes of the curves show good agreement with the corresponding experimental values in Fig. 10.7. After the initial loading stage, it can be seen that the slopes of the curves reduce as the dent depth increases further. This occurs when the pipes start to experience significant plastic deformation. The static approach, as opposed to the use of RIKS method, was also used to obtain the indenter force versus dent depth curves for 6082-T6 aluminium alloy pipes with D/t=72, t=1.2mm and θ=45°, for p=0 and 4 MPa. The results are compared with those obtained using the RIKS approach, for the same conditions, in Fig. 10.10. It can be seen, from Fig. 10.10, that the RIKS and static approaches produce almost identical results for this type of geometry and loading.

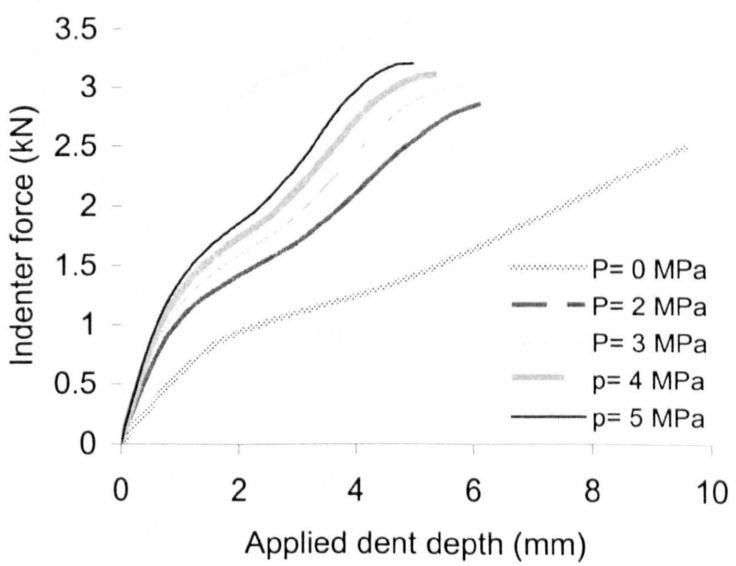

Fig. 10.9 The indenter force versus depth curves obtained from the FE analyses using the RIKS approach for on-off indentation, for 6082-T6 aluminium alloy tubes with support angle, θ=45°, D/t=72, t=1.2mm and different internal pressure levels, i.e. p=0, 2, 3, 4 and 5 MPa.

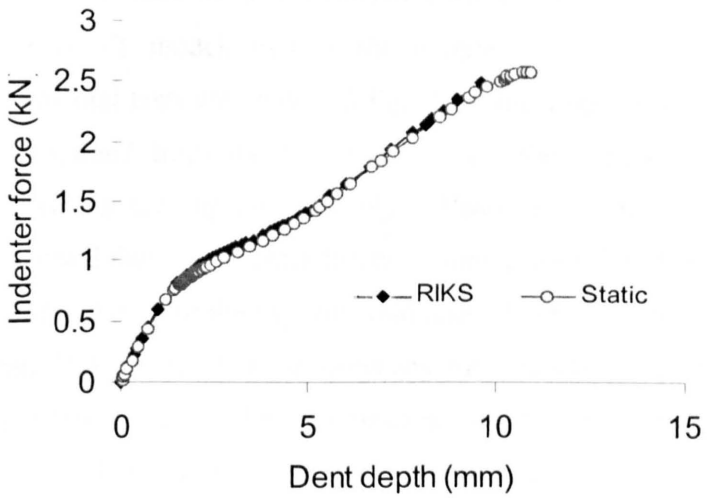

(a p=0 MPa.

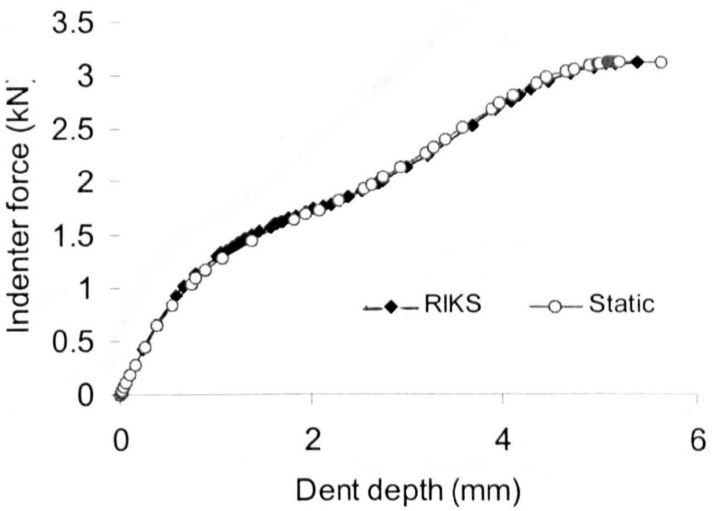

(b) p=4 MPa

Fig. 10.10 The indenter force versus depth curves obtained from the FE analyses using the RIKS and static approaches, for 6082-T6 aluminium alloy tubes, with $\theta=45^{\circ}$, D/t=72, t=1.2mm.

10.6 Comparison of FE and Experimental Test Data

In order to validate the FE models used in the analyses, the results obtained from the FE analyses and the experimental tests are shown in Fig. 10.7 and Figs. 10.11 (a) to (e). It can be seen that the results obtained from the FE analyses and the experimental test data are in extremely good agreement for the unpressurised pipe. However, for the pressurised pipes, Figs. 10.11 (b) to (e), it was found that the indenter forces obtained from the FE analyses were slightly higher than the results obtained from the experimental tests. However, the agreement is still very good (errors are within 2%). Some of the discrepancy may be due to the fact that cracks may have initiated and developed during the experiments and this was not included in the FE modelling. Therefore, predictions using the FE models, may be expected to indicate slightly stronger behaviour than the corresponding experimental tests.

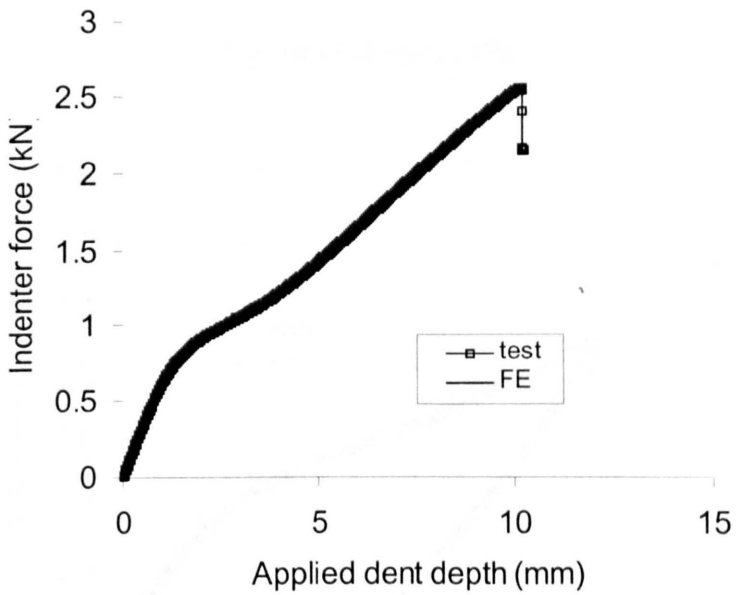

Fig. 10.11 (a) p=0 MPa

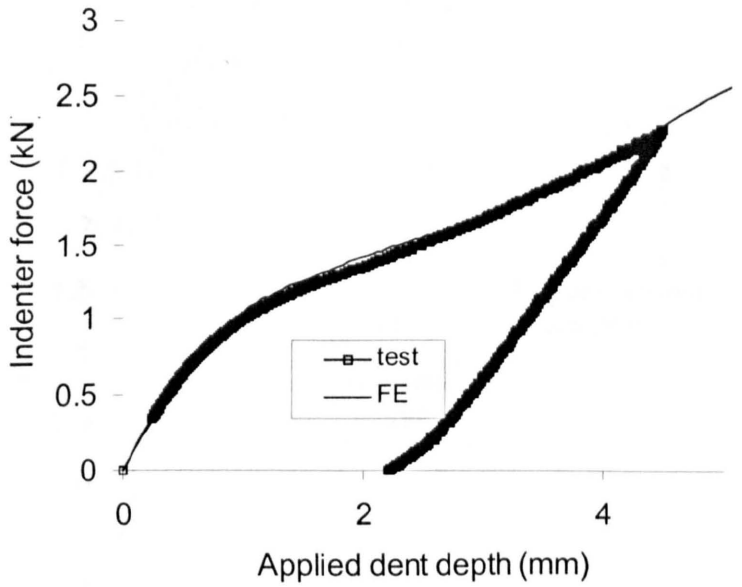

Fig. 10.11 (b) p=2 MPa

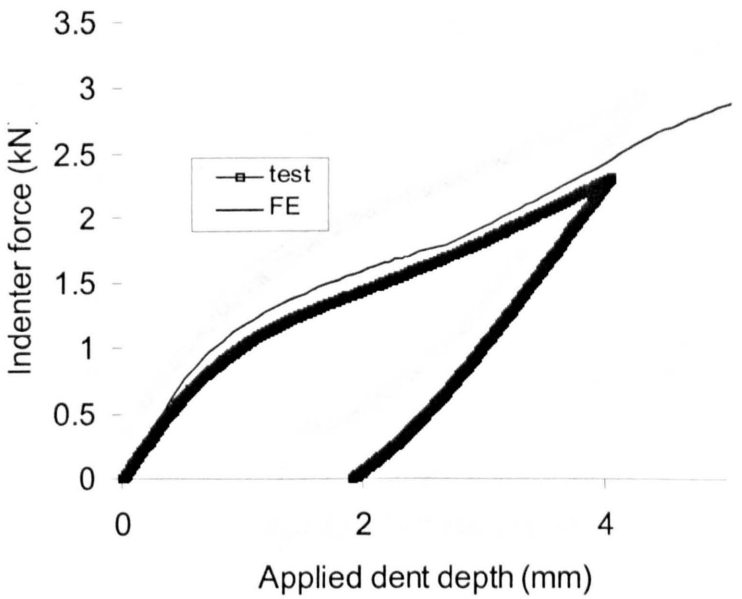

Fig. 10.11 (c) p=3 MPa

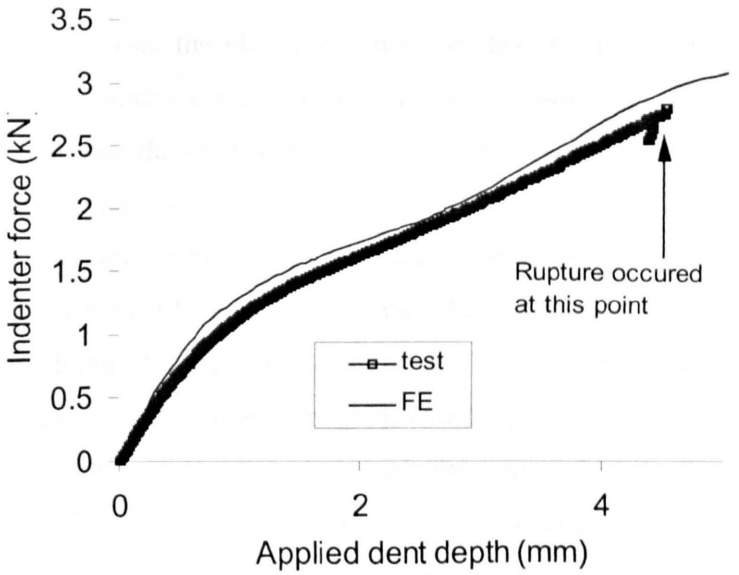

Fig. 10.11 (d) p=4 MPa

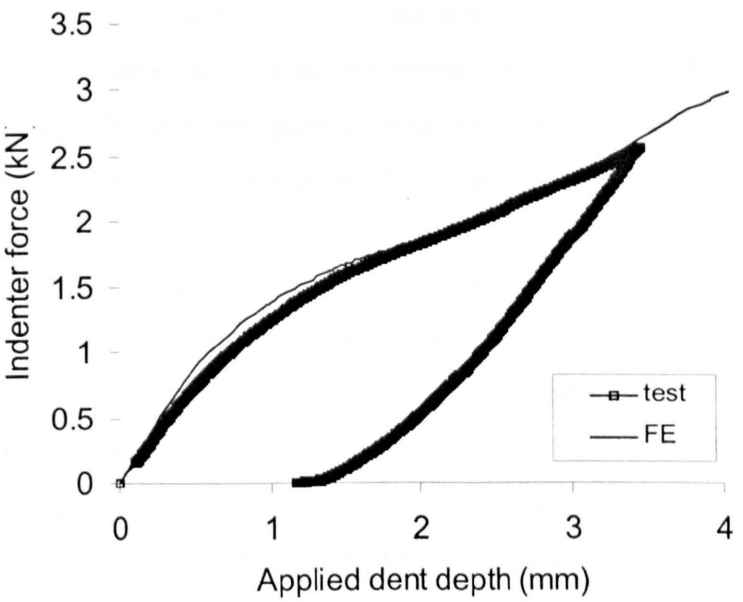

Fig. 10.11 (e) p=5 MPa

Fig. 10.11 Comparison of the indenter force versus depth curves obtained from experimental tests and the FE analyses using the RIKS approach for on-off indentation, for 6082-T6 aluminium alloy tubes with support angle, $\theta=45^{\circ}$, D/t=72, t=1.2mm and different internal pressure levels.

10.7 Discussion and Conclusions

Fig. 10.7 shows that during the elastic deformation, the initial slopes of the indenter force versus depth curves vary almost linearly with internal pressure. This close linear relationship between the initial slope and the internal pressure was also found in the FE analyses performed on the indented rings [chapters 3-7].

For the unpressurised pipe, using a video inspection system, it was found that a crack initiated at a dent depth of about 6 to 6.5 mm (i.e. at about 8% of the pipe outer diameter). The pipe finally failed at a dent depth of around 9mm (i.e. at about 11% of the pipe outer diameter). This experimental observation illustrates that, in unpressurised pipes, the FE results presented can only be expected to model the behaviour of the indented pipes up to dent depths of about 66% of the final failure dent depth, because the crack initiation process was not included in the modelling. However, it is interesting to note that the agreement between the FE and experimental force/displacement curves did not reduce when a crack was seen to have initiated.

For the pressurised pipes, crack initiation was not monitored using the video camera, but the test data show, like the unpressurised pipes, that pressurised pipes are able to experience dent forces which produce significant elastic plastic radial deformations before failure occurs due to the initial formation and growth of through-cracks. Fig. 10.6(d) shows that with an applied internal pressure of 4 MPa, which induces a hoop stress of 46.7% of the yield stress, the pipe completely failed at a dent depth of 4.4 mm (i.e. at about 5% of the pipe outer diameter). Therefore, it may be assumed that cracks start to initiate before the dent depth reaches 5% of the pipe outer diameter when an internal pressure of 4 MPa is applied.

All of the tests were performed for pipes with D/t = 72 and indenters with r/t =1.67 and axial lengths of L_i/t = 5. If the axial length were to be reduced, a higher localised stress would be produced. Hence, it is likely that the pipes would fail at dent depths of less than 5% of the pipe outer diameter when an internal pressure of 4 MPa is applied.

Generally, the FE results are in very good agreement with those obtained from the experimental tests. However, the FE models predict that the pipes are slightly stronger than that which is observed during the experimental tests, particularly when the internal pressure is increased. In this chapter, the FE models use shell elements rather than 3D brick elements. The close correlation of the results obtained indicates that the shell element models are generally good enough to allow accurate predictions of the indenter force versus deflection behaviour, for pipes

undergoing localised indentations. Also, if an indentation should be found in a pipe for which the internal pressure at the time of the indentation is known, then the force applied during the indentation can be determined. This would be the first step in an assessment of the likely effect of the indentation on the integrity of the pipeline.

10.8 Summary

The elastic-plastic response of pressurised and unpressurised pipes, subjected to localised indentations, has been investigated using FE analyses and experimental testing. A visual inspection system was used to monitor the initiation and the development of cracks during the indentation of an unpressurised pipe. The experiments show that the pipe can continue to carry significant increases of external force, after a crack has initiated, until a through-crack is formed. The close correlation of the results obtained from the experimental tests and the FE analyses indicates that the shell element models used in this chapter are capable of giving accurate results.

Chapter 11

Prediction of Residual Stresses at Localised Indentations in Pipes

11.1 Introduction

In previous chapters 3 to 7, analytical methods were successfully applied to obtain the limit loads and indenter force versus dent depth curves of indented rings. However, although analytical methods are relatively easy to use and can provide accurate predictions, the applicability of these methods is generally limited to relatively simple geometries, material models and loading conditions. For more complicated geometries and loading conditions, the FE method is widely used for performing elastic-plastic analyses [12, 20] and can be used in this case.

In this chapter, the FE method is used to predict the residual stresses in pipes which are indented by rigid 3D indenters. The localised deformations and the residual stresses were obtained and used to develop empirical formulations to predict the residual stresses as functions of the residual dent depth, internal pressure, indenter size and material properties.

11.2 Materials

Three typical pipe materials, X65 SAW, X52 and grade B steel, as shown in Fig. 8.1, were used in the FE study. The relevant material properties for these three materials are shown in Table 11.1. In the FE analyses, all materials were assumed to obey an isotropic hardening rule.

Table 11.1. The material properties for X52, X65 and grade B pipe materials.

Material	σ_y (MPa)	σ_{UTS}^{eng} (MPa)	σ_{UTS}^{true} (MPa)	ε_{UTS}^{true}	E (GPa)	Poisson's ratio ν	Hardening power exponent n
X52	360	545	616	0.123	180	0.3	4.
X65	448	598	675	0.121	223	0.3	7.56
Grade B	287	496	588	0.170	144	0.3	4.5

σ_{UTS}^{eng} is the engineering ultimate tensile stress and is given by

$$\sigma_{uts}^{eng} = \sigma_{UTS}^{true}\left(e^{-\varepsilon_{uts}^{true}}\right) \tag{11.1}$$

The work hardening exponents, n, were obtained using the empirical stress-strain formulations developed in the Appendix 5.A.

11.3 Geometry, Loading and Boundary Conditions

The pipes investigated have an outer diameter of 914.4mm and a wall thickness varying from 12.7 to 26mm. All pipes were indented by blunt, rigid indenters at the axial middle point of the pipe. A side elevation showing the contact between the indenter and the pipe is given in Fig.4.1. An idealised shape of the tooth of an excavator or tractor was used for the indenter in the FE analyses. The idealised tooth (or indenter) consists of a half cylindrical body with an axial length, L, which has two ends which are spherical with the same radius, r, as the cylindrical body. The side and front elevations of a quarter of the indenter are shown in Fig. 11.1. For most of the FE analyses, the axial length and radius of the indenter are 20mm and 12.7mm, respectively. The indenters are constrained to move radially inwards or outwards.

Because of the geometrical symmetry, only a quarter of the pipe, was modelled, see Fig.11.1. Predicted residual stresses are very sensitive to mesh sizes and very fine meshes are required in the dent region in order to obtain accurate results with solid brick elements [45]. Hence, in order to save computation time a study was conducted to establish the conditions under which accurate results can be obtained using the shell element models [45]. The pipe is fixed on lines CD and EF with an angular support position of 45°. On the symmetric plane AEC, all displacements in the z-direction and rotations about x and y axes were constrained to be zero. On the symmetrical plane ABDC, all displacements in the x- direction and rotations about the y and z axes were constrained to be zero. Also, on the plane BFD, the displacement were constrained to be zero in z- direction and on lines CD and EF the displacements in the x- and y- directions were constrained to be zero.

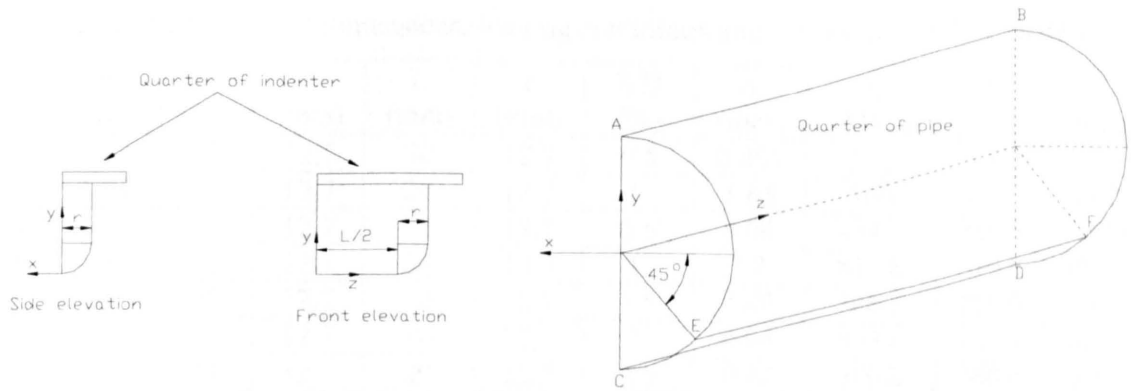

Fig.11.1 A quarter of the pipe (isometric view) and the indenter (side and front elevations).

11.4 FE Meshes

Due to the symmetry of the geometry and loading, it is only necessary to model a quarter of a pipe in the FE analyses. The FE mesh, shown in Fig. 9.7, was generated with 4-node, doubly-curved, quadrilateral shell elements and 3-node, triangular shell elements with reduced integration. Fine meshes were used for the dent region and much coarser meshes were used elsewhere. Eighty nine FE analyses were performed. The maximum residual stresses occurred at the edge of contact of the indenter. As a pipe most likely fails at the maximum residual stress position due to fatigue damage, all of the residual stresses were obtained at this critical position in this chapter. The associated geometry and loading and some of results obtained from the FE analyses are shown in Tables.11.2 to 11.4.

Table 11.2: The geometrical dimensions, loading conditions and FE results for X52 material

FE No	p (MPa)	D/t	t (mm)	L (mm)	r (mm)	δ/D (%)	δ_r (mm)	σ_h (MPa)	σ_a (MPa)	σ_e (MPa)
FE1	3.84	72	12.7	20	12.7	0.5	0.407	552	459	505
FE2	3.84	72	12.7	20	12.7	1.	1.65	709	612	660
FE3	0	72	12.7	20	12.7	0.5	0.08	454.1	380.5	422.2
FE4	0	72	12.7	20	12.7	1.	1.2	677.8	570.6	631.1
FE5	0	72	12.7	20	12.7	1.5	3.28	795.7	705.9	754.8
FE6	0	72	12.7	20	12.7	2.	6.04	889.2	752.4	829.5
FE7	0	72	12.7	20	12.7	2.5	9.22	976.2	786.4	896.5
FE8	0	72	12.7	20	12.7	3.	12.61	938.2	635	830.8
FE9	0	72	12.7	20	12.7	3.5	15.97	791.7	414	689.1
FE10	0	72	12.7	20	12.7	4.	19.31	609	381.1	532.9
FE11	5.12	72	12.7	20	12.7	0.5	0.6	570.3	459.1	523.7
FE12	5.12	72	12.7	20	12.7	0.75	1.55	692.3	586.9	646
FE13	5.12	72	12.7	20	12.7	1.0	2.74	786.1	668.9	734.8
FE14	5.12	72	12.7	20	12.7	1.25	4.1	860.7	746.9	810.3
FE15	5.12	72	12.7	20	12.7	1.5	5.54	929.1	810	876.1
FE16	5.12	72	12.7	20	12.7	1.75	7.1	989.3	866.7	934.4
FE17	5.12	72	12.7	20	12.7	2.0	8.73	1017	895.4	962
FE18	0	72	12.7	20	5	2.0	5	921.8	741.6	846.4
FE19	0	72	12.7	20	30	2.0	30	869.5	683.5	793.1
FE20	0	72	12.7	20	50	2.0	50	826.8	622	745.9
FE21	0	72	12.7	20	70	2.0	70	790.3	578.8	708.6
FE22	0	72	12.7	20	90	2.0	90	763.2	545.2	680.9
FE23	0	72	12.7	20	110	2.0	110	739.3	525	658.9
FE24	0	72	12.7	20	130	2.0	130	719.9	507.9	640.8
FE25	0	72	12.7	0	12.7	2.0	6.71	1043	900.6	980
FE26	0	72	12.7	40	12.7	2.0	5.16	901	702.3	819.9
FE27	0	72	12.7	60	12.7	2.0	4.7	883.4	673	799.3
FE28	0	72	12.7	80	12.7	2.0	4.37	866.2	661.3	784.2
FE29	0	72	12.7	100	12.7	2.0	4.14	855.9	625.3	769.1
FE30	0	72	12.7	140	12.7	2.0	4.14	855.9	625.3	769.1
FE31	0	72	12.7	180	12.7	2.0	4.14	855.9	625.3	769.1
FE32	3.84	65.3	14	20	12.7	1.0	14	828.9	715.6	778.4
FE33	3.84	50.8	18	20	12.7	1.0	18	818.1	719	773.3
FE34	3.84	41.6	22	20	12.7	1.0	22	819.2	728.3	777.8
FE35	3.84	35.2	26	20	12.7	1.0	26	826	736.4	785

Table 11.3 The geometrical dimensions, loading conditions and FE results for grade B material

FE No	p (MPa)	D/t	t (mm)	L_i (mm)	r (mm)	δ/D (%)	d (mm)	σ_h (MPa)	σ_a (MPa)	σ_e (MPa)
FE36	0	72	12.7	20	12.7	0.5	0.11	318.9	244.9	289.2
FE37	0	72	12.7	20	12.7	1.0	1.13	541.9	417.4	491.7
FE38	0	72	12.7	20	12.7	1.5	3.06	640.6	509.4	586.1
FE39	0	72	12.7	20	12.7	2.0	5.7	721.4	561	656.2
FE40	0	72	12.7	20	12.7	2.5	8.79	803.3	592.9	721.8
FE41	0	72	12.7	20	12.7	3.	12.17	817.6	547.9	722.6
FE42	0	72	12.7	20	12.7	3.5	15.6	645.7	414.8	568.1
FE43	0	72	12.7	20	12.7	4.0	18.99	515.6	275.2	447.2
FE44	5.12	72	12.7	20	12.7	0.5	0.68	517.1	412	473.4
FE45	5.12	72	12.7	20	12.7	0.75	1.65	613.9	508.2	568.5
FE46	5.12	72	12.7	20	12.7	1.0	2.85	682.7	571.2	634.5
FE47	5.12	72	12.7	20	12.7	1.25	4.2	751.2	635.8	701
FE48	5.12	72	12.7	20	12.7	1.5	5.64	808.6	705.6	762.6
FE49	5.12	72	12.7	20	12.7	1.75	7.15	860.2	759.3	814.6
FE50	5.12	72	12.7	20	12.7	2.0	8.73	904.5	796.4	855.7
FE51	0	72	12.7	20	12.7	0.25	0.001	24.85	16.45	21.89

Table 11.4 The geometrical dimensions, loading conditions and FE results for X65 material

FE No	p (MPa)	D/t	t (mm)	L_i (mm)	r (mm)	δ/D (%)	d (mm)	σ_h (MPa)	σ_a (MPa)	σ_e (MPa)
FE52	0	72	12.7	20	12.7	0.5	0.09	471.8	365.2	428.8
FE53	0	72	12.7	20	12.7	1.0	1.18	717.8	567.6	655.8
FE54	0	72	12.7	20	12.7	1.5	3.25	816	664.6	751.9
FE55	0	72	12.7	20	12.7	2.0	6.03	895.6	737.2	828.2
FE56	0	72	12.7	20	12.7	2.5	9.26	953.6	783.3	881.2
FE57	0	72	12.7	20	12.7	3.0	12.72	970.6	818.7	893.9
FE58	0	72	12.7	20	12.7	3.5	16.28	966.8	797.9	894.7
FE59	0	72	12.7	20	12.7	4.0	19.68	787.6	669.9	737.8
FE60	1.28	72	12.7	20	12.7	1	1.77	767.8	624.6	707.2
FE61	2.56	72	12.7	20	12.7	1	2.17	799.5	660.3	739.8
FE62	3.84	72	12.7	20	12.7	1	2.47	816.6	684.7	759.5
FE63	5.12	72	12.7	20	12.7	1	2.68	830.1	711.6	778
FE64	6.4	72	12.7	20	12.7	1	2.84	837.2	735.4	791.7
FE65	7.68	72	12.7	20	12.7	1	2.96	841.7	752.5	801.4
FE66	9.80	72	12.7	20	12.7	1	3.05	845.1	766.7	809.4
FE67	1.28	72	12.7	20	12.7	2	7.44	947.5	789.8	879.7
FE68	2.56	72	12.7	20	12.7	2	8.15	956.8	814.5	894.4
FE69	3.84	72	12.7	20	12.7	2	8.56	947.3	830	894.5
FE70	5.12	72	12.7	20	12.7	2	8.79	933.3	850.1	894.6
FE71	6.4	72	12.7	20	12.7	2	8.93	915.8	872.6	895.2
FE72	7.68	72	12.7	20	12.7	2	8.97	896.6	892.1	895.1
FE73	9.80	72	12.7	20	12.7	2	8.91	879.6	908.5	895.4
FE74	3.84	72	12.7	20	12.7	0.25	0.02	370.5	267.4	331.3
FE75	3.84	72	12.7	20	12.7	0.5	0.44	657.2	521.8	601.1
FE76	3.84	72	12.7	20	12.7	0.75	2.47	816.6	684.7	759.5
FE77	3.84	72	12.7	20	12.7	1.0	3.84	874.5	751.4	820.4
FE78	3.84	72	12.7	20	12.7	1.25	5.32	928.7	794.9	870
FE79	3.84	72	12.7	20	12.7	1.5	6.91	953	815.4	892.5
FE80	3.84	72	12.7	20	12.7	1.75	10.31	934.5	850.3	895.6
FE81	3.84	72	12.7	20	12.7	2.0	12.12	912.3	867.4	892.1
FE82	5.12	72	12.7	20	12.7	0.25	0.06	496.8	378.1	449.7
FE83	5.12	72	12.7	20	12.7	0.5	0.62	681.3	549.3	625.8
FE84	5.12	72	12.7	20	12.7	0.75	2.84	837.2	735.4	791.7
FE85	5.12	72	12.7	20	12.7	1.0	4.22	900.4	800.6	855.4
FE86	5.12	72	12.7	20	12.7	1.25	5.69	927.4	832.1	884
FE87	5.12	72	12.7	20	12.7	1.5	7.26	932.5	849.1	893.7
FE88	5.12	72	12.7	20	12.7	1.75	10.67	877.7	907	894.2
FE89	5.12	72	12.7	20	12.7	2.0	12.42	825.3	825.1	827.9

11.5 FE Results

11.5.1 Residual Stress Distribution on Pipe Surfaces

In chapter 9, it is shown that tensile residual stresses occur on the outer surfaces of pipes in the vicinity of the dents and that compressive residual stresses occur on the inner surfaces. From FE analyses FE1 and FE2, the residual hoop and axial stress distributions on the outer surfaces of the pipes made from material X52 were obtained and these are shown in Figs 11.2 (a) to (d).

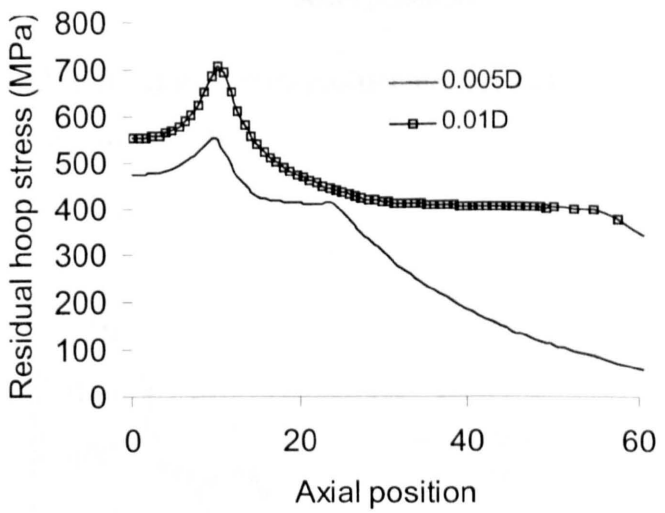

Fig.11.2 (a) Residual hoop stress against axial position on the plane of symmetry AB (Fig.11.1), for two dent depths (δ=0.005 and 0.01D).

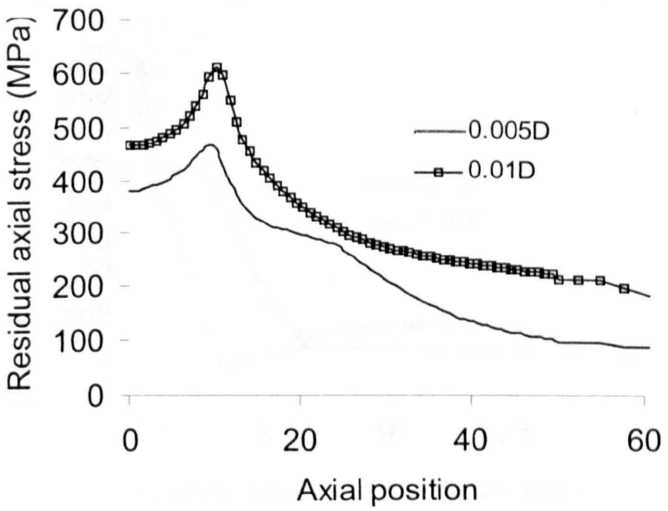

Fig.11.2 (b) Residual axial stress against axial position on the plane of symmetry AB (Fig.11.1), for two dent depths (δ=0.005 and 0.01D).

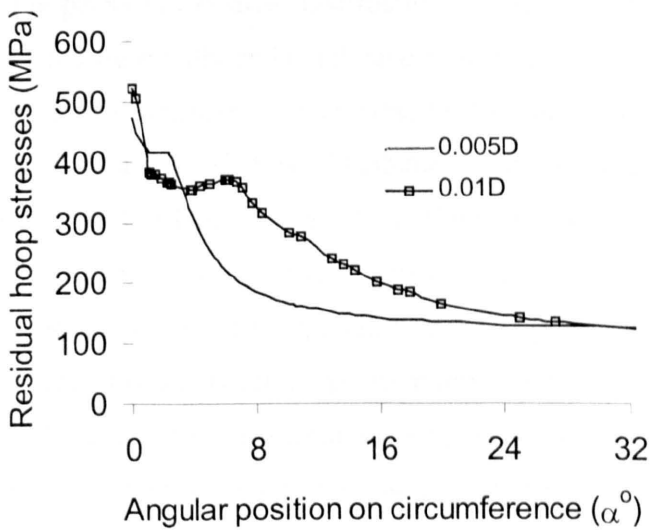

Fig. 11.2 (c) Residual hoop stress against angular position on the plane of symmetry AEC (Fig.11.1), for two dent depths (δ=0.005 and 0.01D).

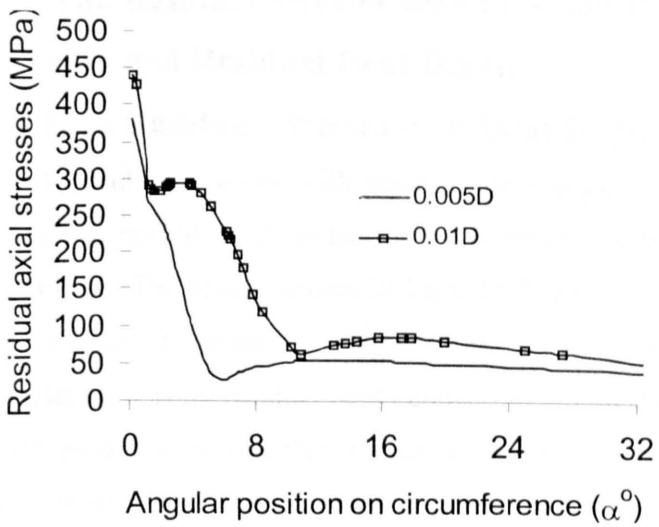

Fig.11.2 (e) Residual axial stress against angular position on the plane of symmetry AEC (Fig.11.1), for two dent depths (δ=0.005 and 0.01D).

From Figs. 11.2(a) and (b), it can be seen that the residual stresses are generally very high in the dent region and that the peaks in the stress distribution are very sharp. Away from the dent region the residual stresses reduce rapidly and reach levels close to those which appear in perfect pipes, associated with the internal pressure. From Figs. 11.2 (c) and (d), it can be seen that the peak values of the residual hoop and axial stress distributions, on the circumference, occur at the centre of the dent region (i.e. on the plane of symmetry). Careful investigation of all of the stress distributions indicates that the maximum residual stresses (i.e. axial, hoop and von Mises stresses) in the pipe occur at the position corresponding to the edge of contact of the indenter in the axial direction. This is the most likely failure position due to fatigue of the indented pipe and therefore it has been the subject of an experimental investigation [16, 17]. The evidence in [16, 17] also shows that in the contact between a punch and a foundation, the contact stresses reach the maximum values at the end of contact of the indenter with the foundation. Hence, in this chapter, all of the residual stress results were obtained from these critical positions on the indented pipes using the FE analyses.

11.5.2 Variations of Peak Residual Stresses with Pipe and Indenter Geometry, Pressure and Residual Dent Depth

11.5.2.1 Variation of Peak Residual Stresses with Dent Depth

The variations of peak residual stresses with residual dent depth, obtained from the FE analyses, at a position near the end of axial contact of the indenter, for the three materials, are shown in Figs. 11.3 (a) to (g). The results shown in Figs. 11.3 (a) to (c) were obtained for an unpressurised pipe. In this case, it can be seen that the residual stresses (hoop, axial and von Mises) initially increase with increasing residual dent depths, but at a dent depth of about 10mm the residual stresses reach peak values and then reduce with further increase in residual dent depth. This is because the plastic deformation zone and contact area both increase. The residual stresses in the pipes redistribute in response to the increase in plastic and contact areas resulting in lower peak residual stresses for the high residual dent depths.

From Figs. 11.3 (d) to (g), it can be seen that for pressurised pipes, the relationship between the residual stresses and the residual dent depths are similar to those obtained for unpressurised pipes, but the residual stresses for pressurised pipes are higher. Figs. 11.3 (d) to (g) also indicate that variation of residual stress with residual dent depth is not highly sensitive to the material properties but that it is sensitive to the internal pressure and to the residual dent depth.

From Table 11.1 and Figs. 11.3 (a) to (g), it can be seen that the peak values of either the residual hoop stresses or the residual von Mises stresses, obtained from the FE analyses, for the pipes made from the three materials, X52, X65 and grade B, are much higher than the ultimate engineering tensile stresses. This is because the maximum stress value of the true stress versus strain curves shown in Fig.8.1 is much higher than that of the corresponding ultimate tensile stress. Also since the von Mises yield criterion was used in the FE analyses, some stress components, e.g. the hoop stress, may be higher than the corresponding von Mises stress whose maximum value is the same as that of true stresses on Fig.8.1 when the residual dent depth reaches a certain level. This is why sometimes the hoop stress is higher than 1000MPa. However, the relationship of the von Mises and equivalent strain obtained from the FE analyses must be consistent with that of the true stress and the plastic strain obtained from tensile tests.

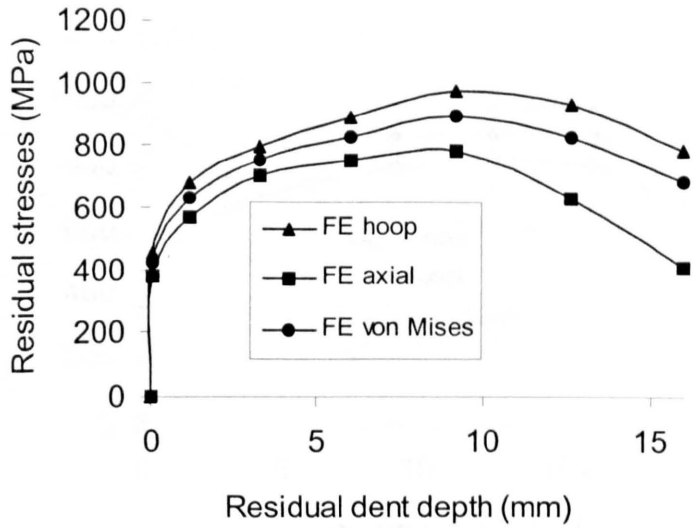

Fig. 11.3 (a) Residual stresses with residual dent depth for the pipe with X52 material and internal pressure p=0 MPa obtained from FE analyses FE3 to FE10.

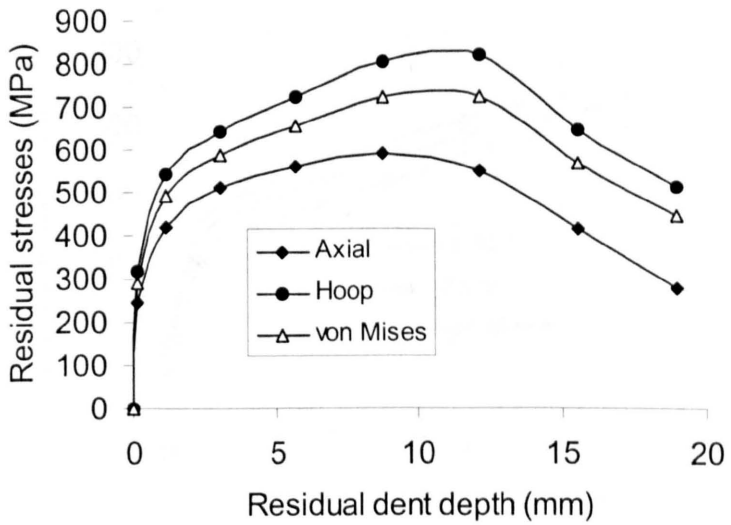

Fig. 11.3 (b) Residual stresses with residual dent depth for the pipe with grade B line pipe material and internal pressure p=0 MPa obtained from FE analyses FE36 to FE43.

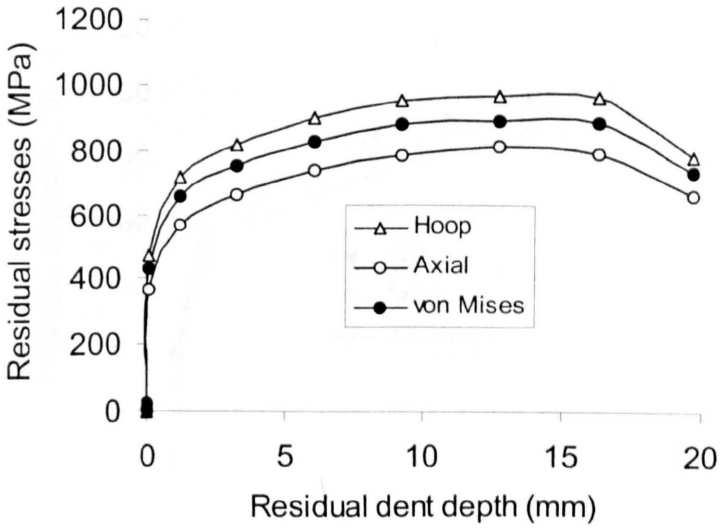

Fig. 11.3 (c) Residual stresses with residual dent depth for the pipe with X65 SAW steel material and internal pressure p=0 MPa obtained from FE analyses FE51 to FE63

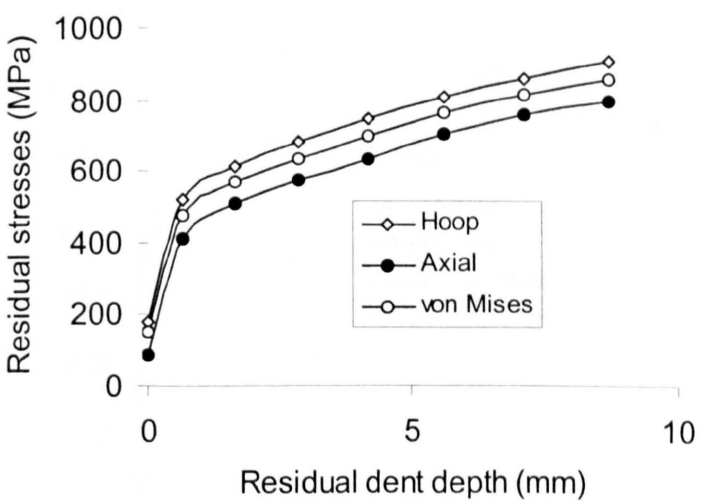

Fig. 11.3 (d) Residual stresses with residual dent depth for the pipe with X52 material and internal pressure p=5.12 MPa obtained from FE analyses FE11 to FE16.

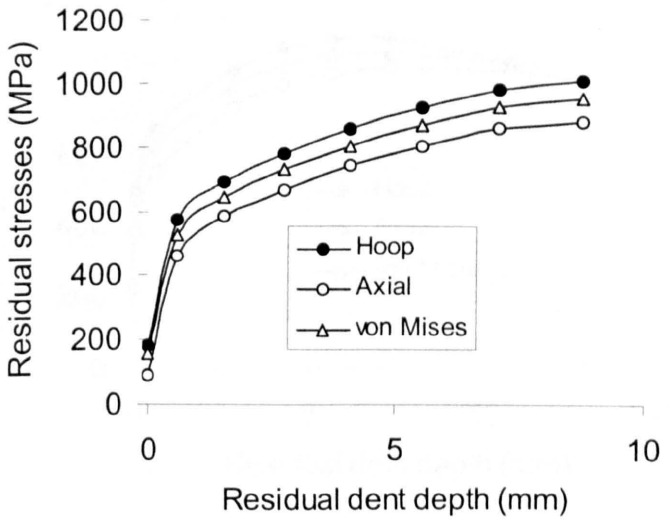

Fig. 11.3 (e) Residual stresses with residual dent depth for the pipe with grade B line pipe material and internal pressure p=5.12 MPa obtained from FE analyses FE44 to FE50.

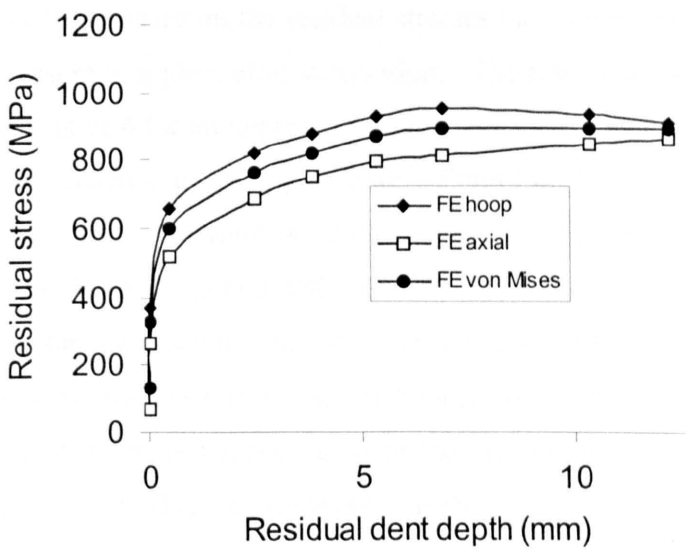

Fig. 11.3 (f) Residual stresses with residual dent depth for the pipe with X65 material and internal pressure p=3.84 MPa obtained from FE analyses FE74 to FE81.

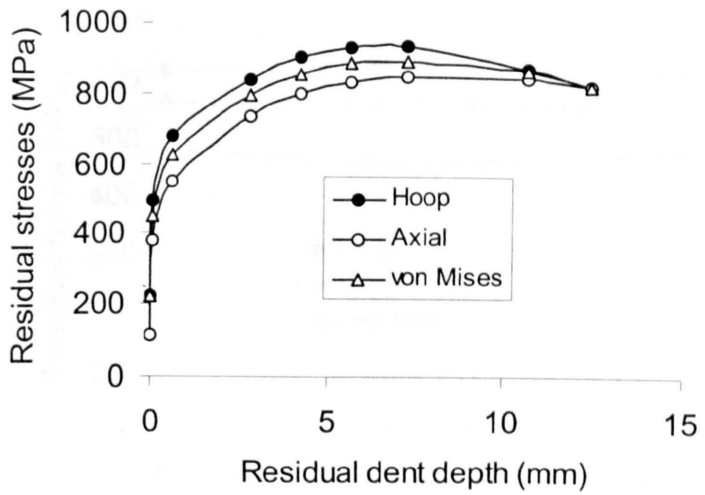

Fig. 11.3 (g) Residual stresses with residual dent depth for the pipe with X65 material and internal pressure p=6.4 MPa obtained from FE analyses FE82 to FE89.

11.5.2.2 Variation of Peak Residual Stresses with Internal Pressure

The effects of internal pressure on the residual stresses have been investigated in two ways. Firstly, the internal pressure is applied after indentation. The results shown in Fig. 11.4 (a) were obtained from FE analysis FE4 for an unpressurised pipe with X52 material, which was indented and then subjected to an increasing internal pressure. From Fig. 11.4 (a), it can be seen that the effect of the increasing internal pressure is almost negligible. In the second case, pressurised pipes made from X65 SAW material and with different internal pressure levels (FE59 to FE73) were indented by a constant dent depth of 9.144mm (1% of D) or 18.288 (mm). From Figs. 11.4 (b) and (c), it can be seen that the residual stresses increase as the internal pressure increases. This is due to the fact that the pipes become stiffer as the internal pressure is increased and hence greater forces are required to produce the same dent depth.

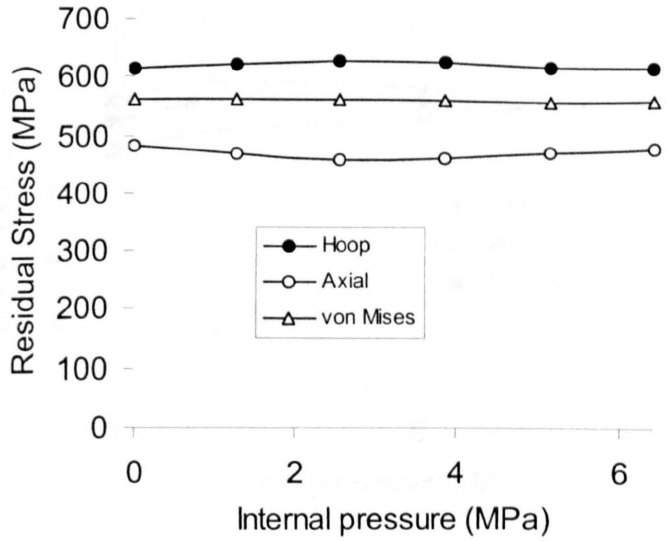

Fig. 11.4 (a) Residual stress with internal pressure for an unpressurised pipe with X52 material in which the internal pressure increases after indentation.

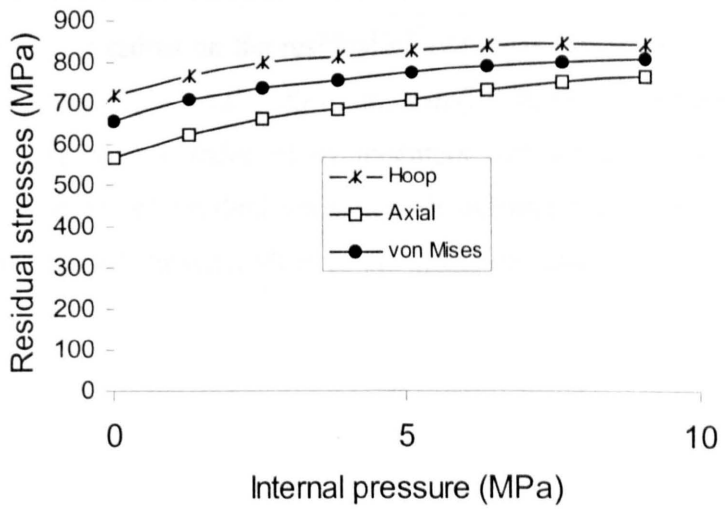

Fig. 11.4 (b) Residual stress with internal pressure for pressurised pipes with X65 material for δ=0.01 D.

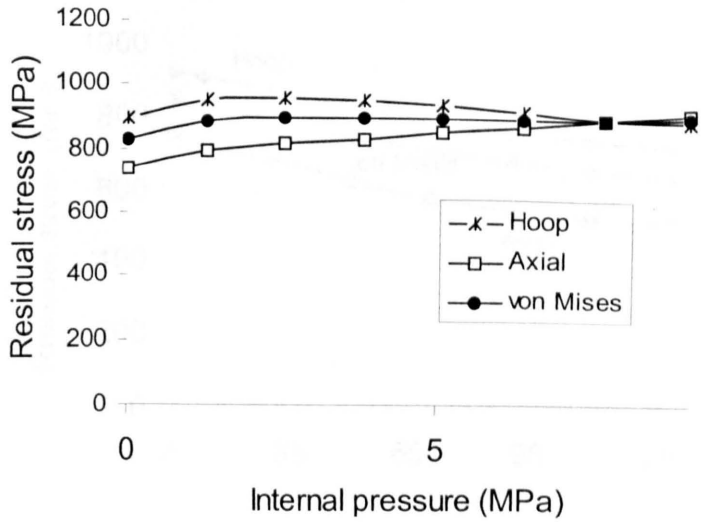

Fig. 11.4 (c) Residual stress with internal pressure for pressurised pipes with X65 material for δ=0.02 D.

11.5.2.3 Variation of Peak Residual Stresses with Indenter Radius

The effect of the indenter radius on the residual stresses was investigated using FE analyses FE17 to FE24 for which the applied dent depth is 18.3mm (2% of D) for unpressurised pipes with material X52. These pipes were indented by indenters with an axial length of 20mm and different radii. The variations of residual stresses with indenter radius are shown in Fig.11.5 which indicates that the residual stresses reduce as the radius increases.

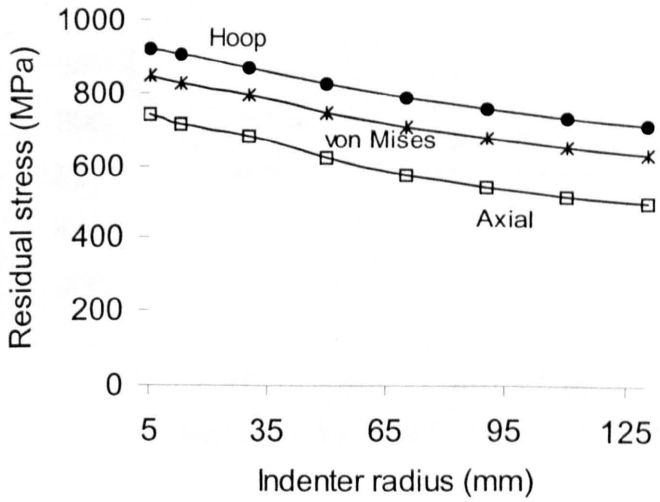

Fig. 11.5Residual stress with indenter's radius for an ressurised pipe with X52 material, obtained from the FE analyses (FE17 to FE24).

11.5.2.4 Variation of Peak Residual Stresses with Indenter Axial Length

The effects of the axial length of the indenter were investigated using FE analyses FE25 to FE31 for unpressurised X52 pipes; indentations of depths of 18.3mm (2%D) were used and the indenter axial length was varied from 0 to 180mm. The results obtained from these FE analyses are shown in Fig. 11.6. It can be seen from Fig. 11.6 that the highest residual stresses occur as the axial length approaches zero and that the residual stresses reduce with increasing axial length until the half axial length reaches 50mm after which the residual stresses have constant values. Hence, if the indenter's axial length is larger than 100mm the effect of the axial length on the residual stresses is negligible.

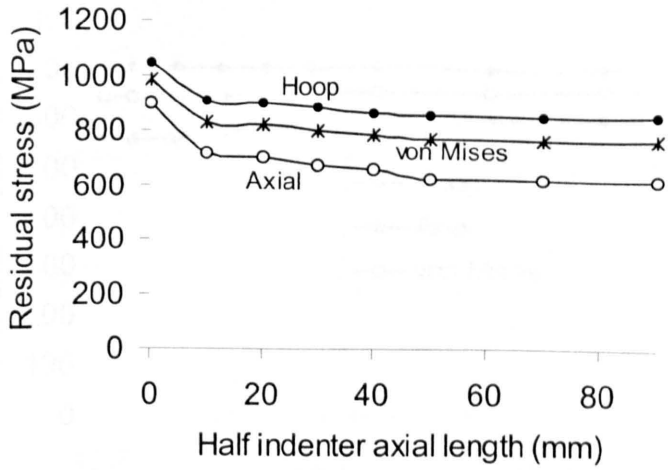

Fig. 11.6 Residual stress with indenter's axial length for an ressurised pipe with X52 material, obtained from the FE analyses (FE25 to FE31).

11.5.2.5 Variation of Peak Residual Stresses with Wall Thickness

The effect of the pipe wall thickness on the residual stresses was investigated using the FE analyses FE32 to FE35, obtained from the X52 pipe materials with an internal pressure of 3.84 MPa. The wall thickness of these pipes varies from 12.7 to 26mm. The residual stresses, shown in Fig. 11.7, indicate that the pipe wall thickness has a negligible effect on the residual stresses. However, previously shown results in Fig.8.6 in chapter 8, have shown that the wall thickness has an affect on the stress ranges caused by internal pressure fluctuations. The stress ranges reduce with increasing wall thickness for a given pressure fluctuation.

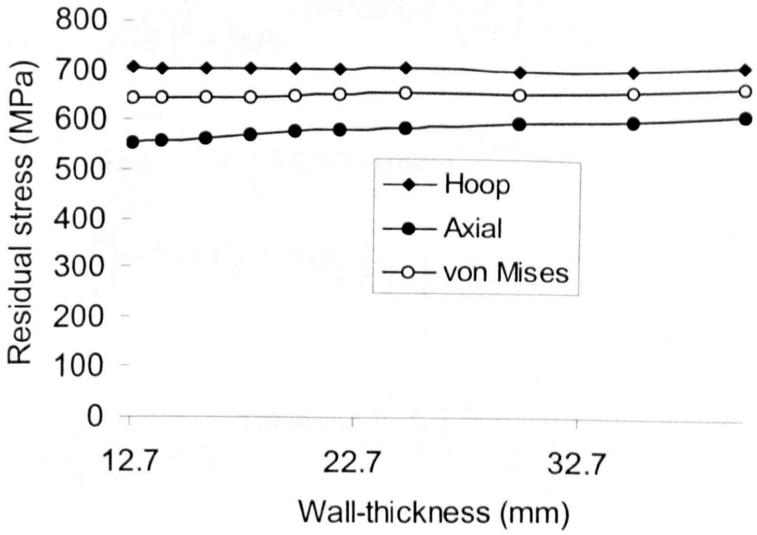

Fig. 11.7 Residual stress with wall thickness for pressurised pipes with X52 material and p=3.84MPa, obtained from the FE analyses (FE32 to FE35).

11.6 Empirical Formulations for Residual Stress Predictions

Using the results of the FE analyses and curve fitting techniques, it has been possible to derive empirical formulations for predicting the residual hoop, von Mises and axial stresses at the maximum stress concentration positions on the outer pipe surface. These include the effects of the residual dent depth, internal pressure, indenter radius and axial length and the material properties. The equations are as follows:

$$\left.\begin{aligned} \sigma_h &= g_h\left(\left(1.5\sigma_f\right)^{\frac{n-1}{n}}\left(E\frac{\delta_r}{R}\right)^{\frac{1}{n}} + 36Pe^{-561.161(n)^{1.5}\left(\frac{P}{\sigma_f}\right)\left(\frac{\delta_r}{R}\right)} f_h\right) \\ g_h &= 0.7943 + 0.2324e^{-4.3155\frac{r}{R}} \\ f_h &= \left(1. - 118.726\frac{\delta_r}{R} + 1059\left(\frac{\delta_r}{R}\right)^2\right) \end{aligned}\right\} \quad (11.2)$$

$$\left.\begin{aligned}\sigma_{axial} &= g_{axial}\left(\left(1.1\sigma_f\right)^{\frac{n-1}{n}}\left(E\frac{\delta_r}{R}\right)^{\frac{1}{n}} + 36Pe^{-109.5297(n)^{1.5}\left(\frac{P}{\sigma_f}\right)\left(\frac{\delta_r}{R}\right)}\right) f_{axial}\\ g_{axial} &= \left(0.903 + 0.1427e^{-8.52\frac{L}{R}}\right)\left(0.6397 + 0.445e^{-7.482\frac{r}{R}}\right)\\ f_{axial} &= \left(\frac{1}{2} - 20.49\frac{\delta_r}{R} + 2608\left(\frac{\delta_r}{R}\right)^2\right)\end{aligned}\right\} \quad (11.3)$$

$$\left.\begin{aligned}\sigma_e &= g_e\left(\left(1.33\sigma_f\right)^{\frac{n-1}{n}}\left(E\frac{\delta_r}{R}\right)^{\frac{1}{n}} + 36Pe^{-318.403(n)^{1.5}\left(\frac{P}{\sigma_f}\right)\left(\frac{\delta_r}{R}\right)}\right) f_e\\ g_e &= 0.7631 + 0.2732e^{-5.05\frac{r}{R}}\\ f_e &= \left(\frac{\sqrt{3}}{2} - 96.9\frac{\delta_r}{R} + 7251\left(\frac{\delta_r}{R}\right)^2\right)\end{aligned}\right\} \quad (11.4)$$

where the flow stress, σ_f, is defined as the average of the yield stress and engineering ultimate tensile stress.

The results obtained from the FE analyses FE3 to FE89 and from the empirical formulae (11.2) to (11.4) are shown and compared in Figs.11.8 (a) to (q).

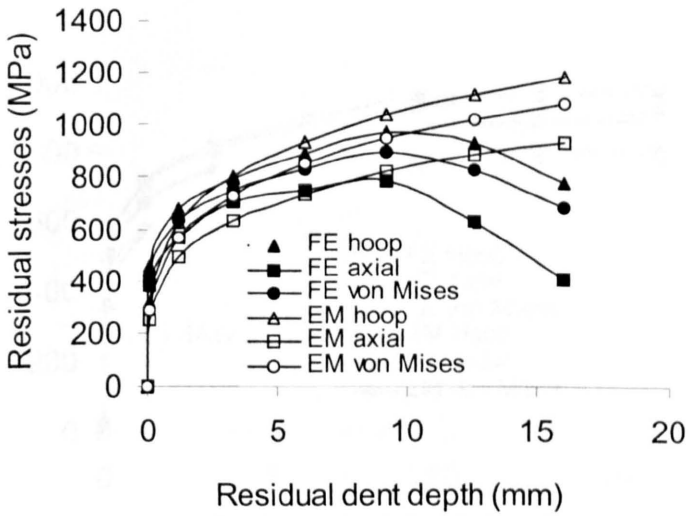

Fig.11.8 (a) Variations of the residual stress with residual dent depth obtained from the FE analyses (FE3 to FE10) and from the empirical formulations, for the pipes with material X52 and p=0 MPa.

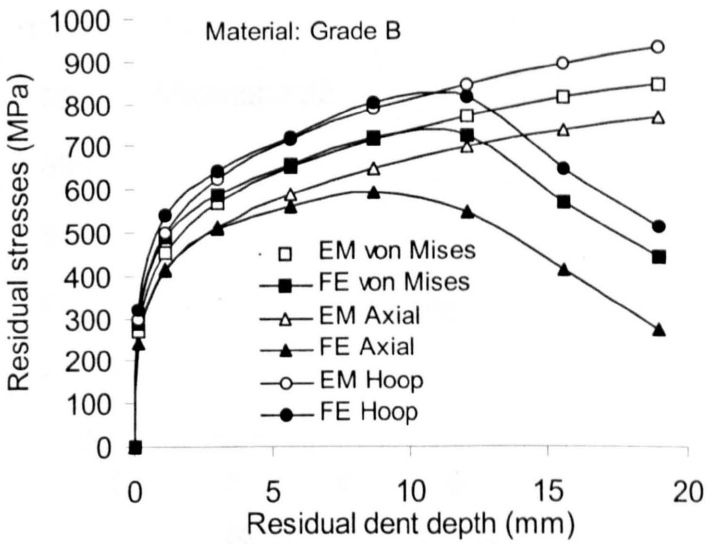

Fig.11.8 (b) Variations of the residual hoop stress with residual dent depth obtained from the FE analyses (FE36 to FE43) and from the empirical formulations, for the pipes with material grade B and p=0 MPa.

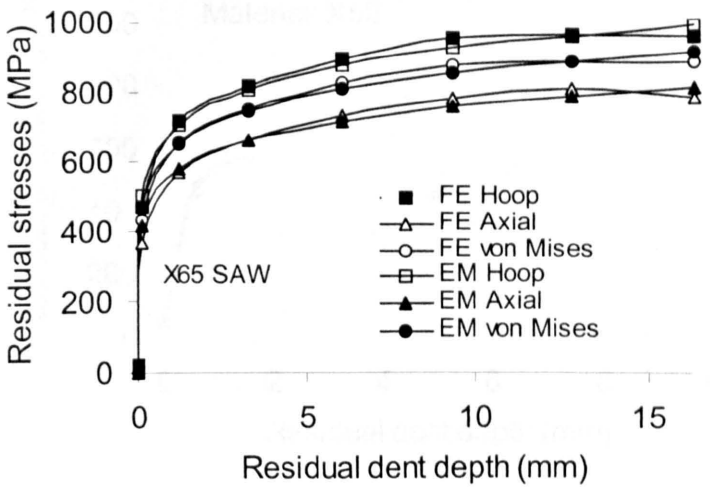

Fig.11.8 (c) Variations of the residual hoop stress with residual dent depth obtained from the FE analyses (FE51 to FE59) and from the empirical formulations, for the pipes with material X65 and p=0 MPa.

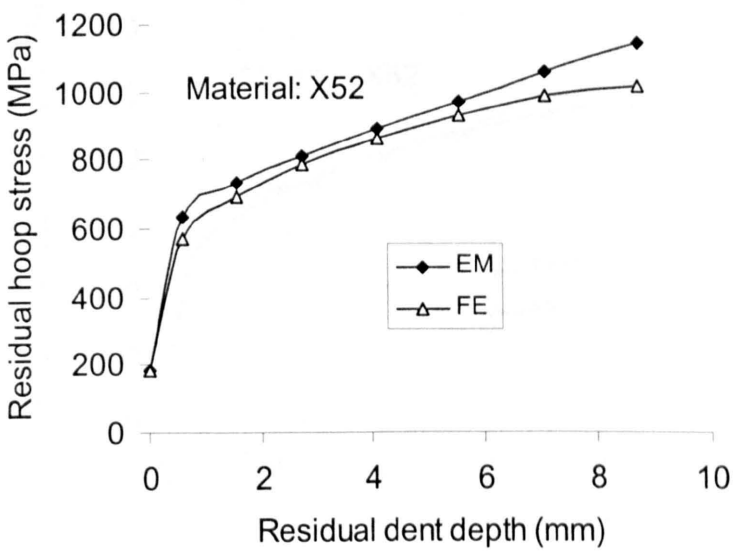

Fig.11.8 (d) Variations of the residual hoop stress with residual dent depth obtained from the FE analyses (FE11 to FE16) and from the empirical formulations, for the pipes with material X52 and p=5.12 MPa.

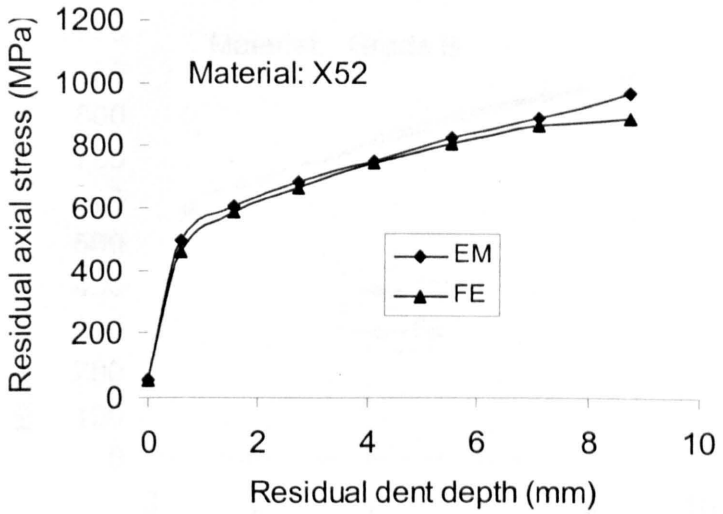

Fig.11.8 (e) Variations of the residual axial stress with residual dent depth obtained from the FE analyses (FE11 to FE16) and from the empirical formulations, for the pipes with material X52 and p=5.12 MPa.

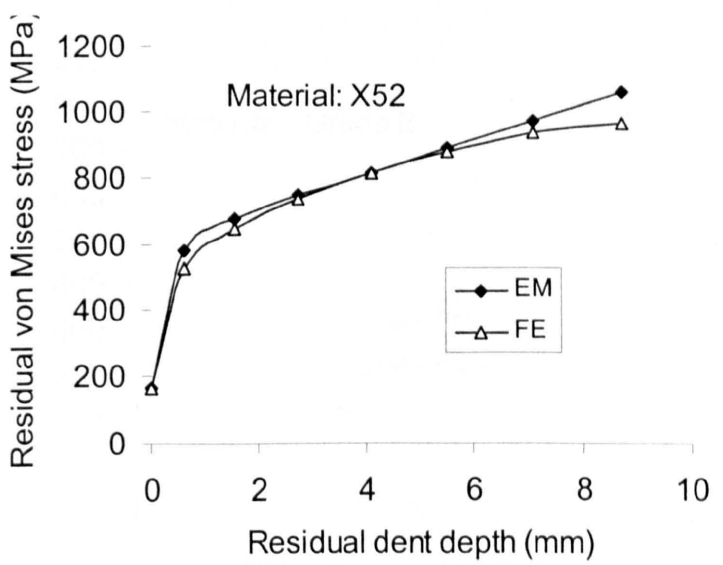

Fig.11.8 (f) Variations of the residual von Mises stress with residual dent depth obtained from the FE analyses (FE11 to FE16) and from the empirical formulations, for the pipes with material X52 and p=5.12 MPa.

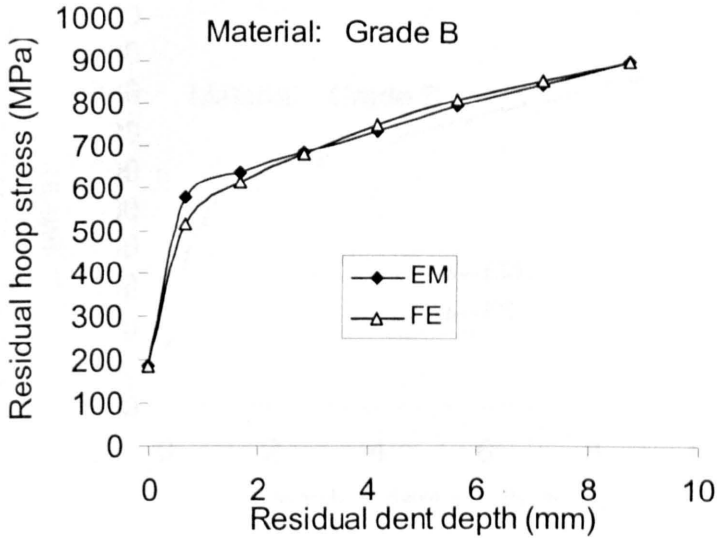

Fig.11.8 (g) Variations of the residual hoop stress with residual dent depth obtained from the FE analyses (FE44 to FE50) and from the empirical formulations, for the pipes with material grade B and p=5.12 MPa.

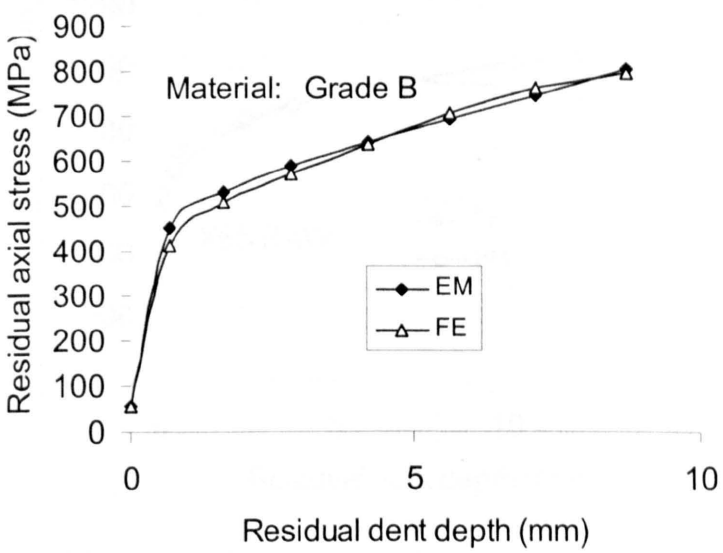

Fig.11.8 (h) Variations of the residual axial stress with residual dent depth obtained from the FE analyses (FE44 to FE50) and from the empirical formulations, for the pipes with material grade B and p=5.12 MPa.

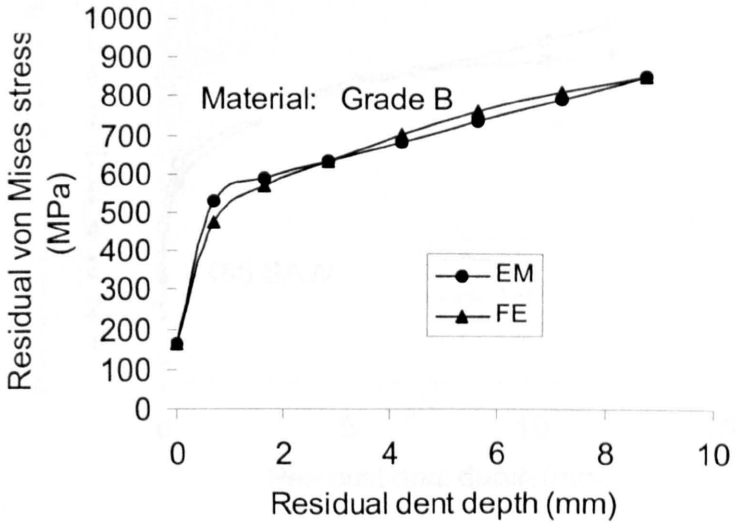

Fig.11.8 (i) Variations of the residual von Mises stress with residual dent depth obtained from the FE analyses (FE44 to FE50) and from the empirical formulations, for the pipes with material grade B and p=5.12 MPa.

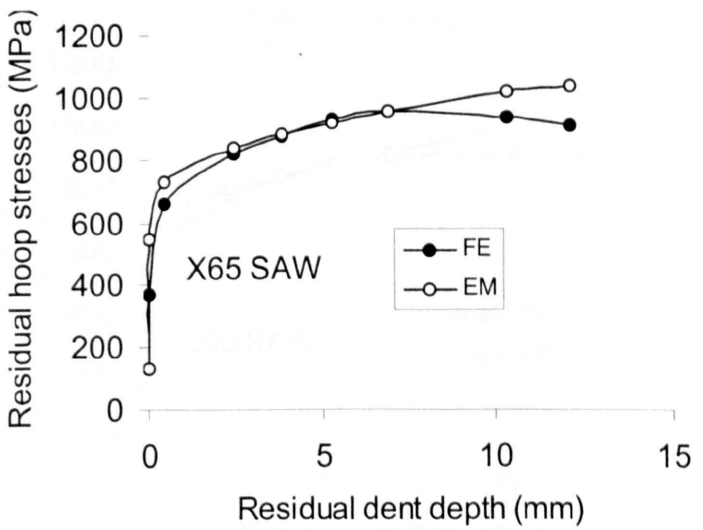

Fig.11.8 (j) Variations of the residual hoop stress with residual dent depth obtained from the FE analyses (FE74 to FE81) and from the empirical formulations, for the pipes with material X65 and p=3.84 MPa.

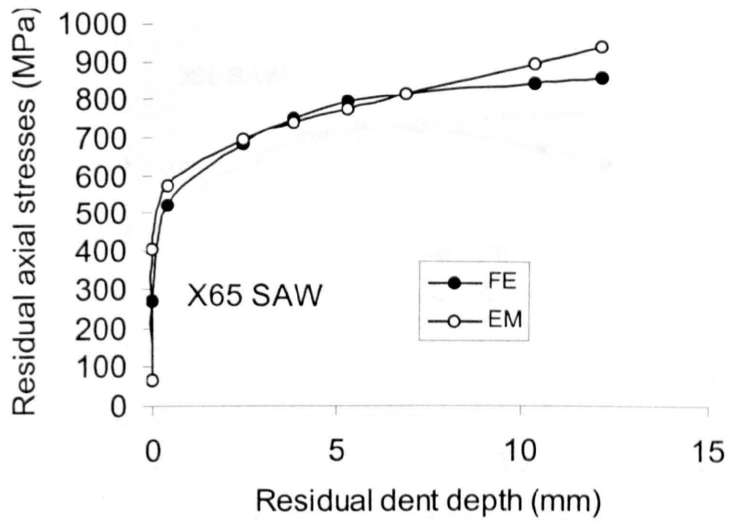

Fig.11.8 (k) Variations of the residual axial stress with residual dent depth obtained from the FE analyses (FE74 to FE81) and from the empirical formulations, for the pipes with material X65 and p=3.84 MPa.

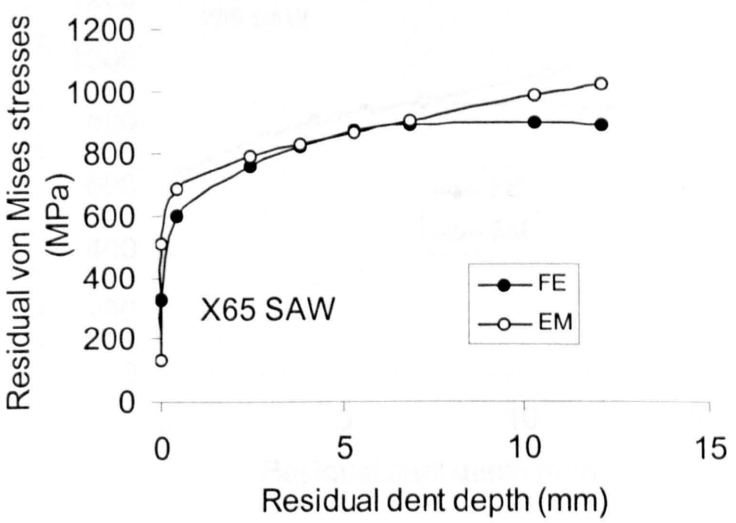

Fig.11.8 (l) Variations of the residual von Mises stress with residual dent depth obtained from the FE analyses (FE74 to FE81) and from the empirical formulations, for the pipes with material X65 and p=3.84 MPa.

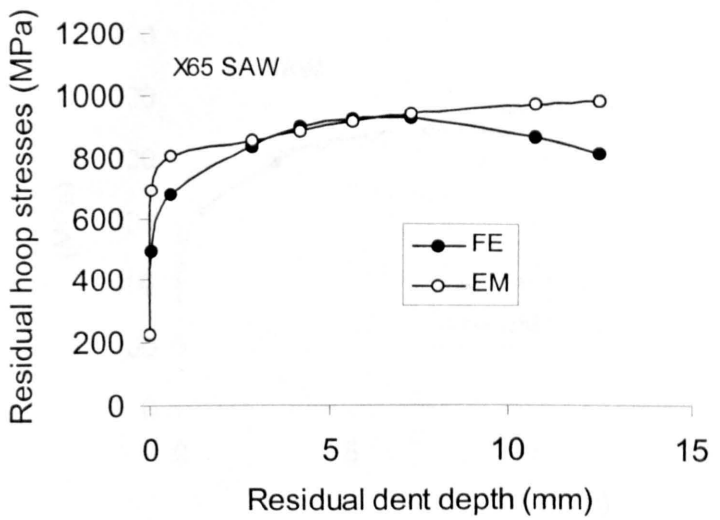

Fig.11.8 (m) Variations of the residual hoop stress with residual dent depth obtained from the FE analyses (FE82 to FE89) and from the empirical formulations, for the pipes with material X65 and p=6.4 MPa.

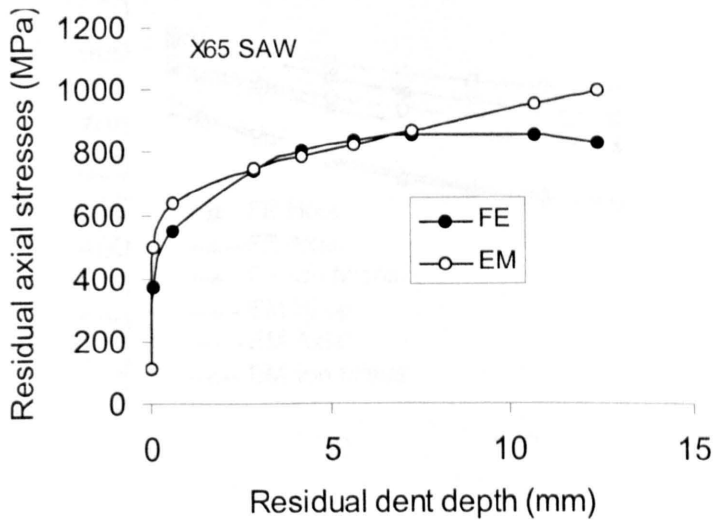

Fig.11.8 (n) Variations of the residual axial stress with residual dent depth obtained from the FE analyses (FE82 to FE89) and from the empirical formulations, for the pipes with material X65 and p=6.4 MPa.

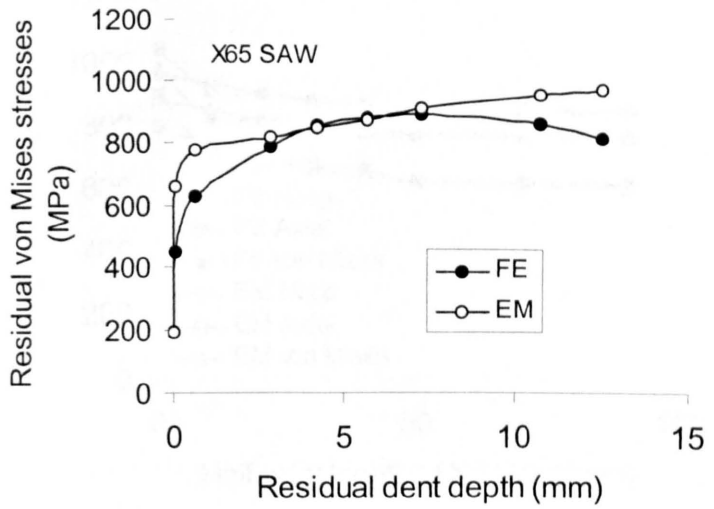

Fig.11.8 (o) Variations of the residual von Mises stress with residual dent depth obtained from the FE analyses (FE82 to FE89) and from the empirical formulations, for the pipes with material X65 and p=6.4 MPa.

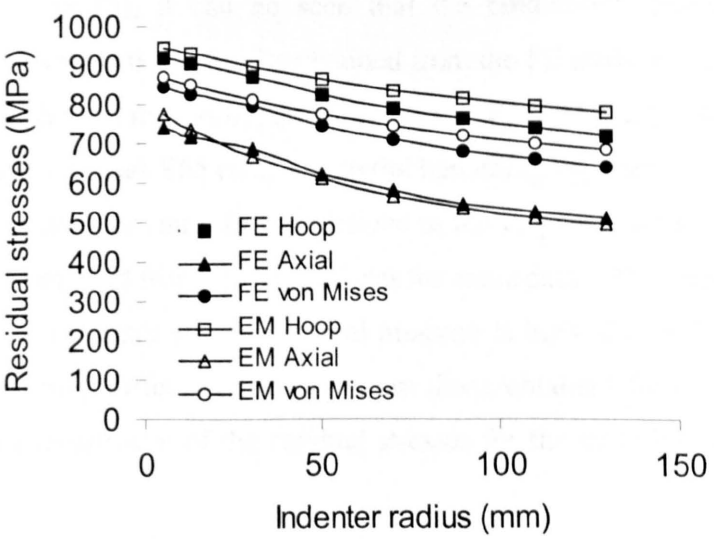

Fig.11.8 (p) Variations of the residual stress with indenter's radius obtained from the FE analyses (FE18 to FE24) and from the empirical formulations, for the pipes with material X52 and p=0 MPa.

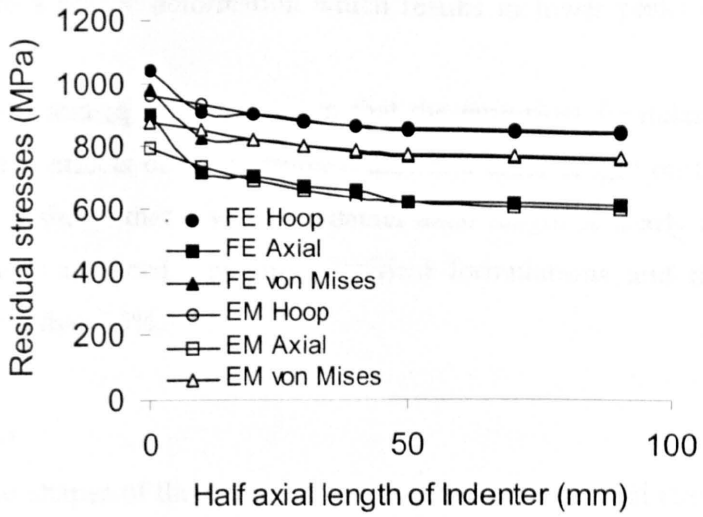

Fig.11.8 (q) Variations of the residual stress with indenter's half axial length obtained from the FE analyses (FE25 to FE31) and from the empirical formulations, for the pipes with material X52 and p=0 MPa.

From Figs.11.8 (a) to (q), it can be seen that the predictions, based on the empirical formulations, correlate well with the results obtained from the FE analyses over the vast range of the parameters for which the data was obtained. However, Figs. 11.8(m) to (o) show for internal pressure of 6.4MPa and material X65 (with a material hardening exponent of 7.56), that when the residual dent depth is less than 1mm, the predictions of the empirical formulations may be 40% higher than the results obtained from the FE analyses for some data. This indicates that when the residual dent depth is very small and the internal pressure is high, the predictions based on the empirical formulations may differ significantly from those obtained from the FE analyses and that there may be an overestimate of the residual stresses for the materials with high hardening exponents (i.e. 7.56).

From Figs. 11.8 (a) to (c), it can be seen that accurate residual stress predictions can be obtained for large residual dent depths, i.e. more than 10mm (≈1%D), but these predictions are less accurate for pipes deformed by small indenters, i.e. D/r ratio = 72 as in the present investigation. At high pressure and with small indenters, pipes may be punctured before a residual dent depth of 1% of D is achieved. However, for large indenters, i.e. D/r=10, the pipe may be indented to a relatively large depth without being punctured, because a very large area of

the pipe may undergo a plastic deformation which results in lower peaks in the values of the residual stresses.

From Figs. 11.8 (p) and (q), it can be seen that the empirical formulations can reasonably accurately represent the effects of the indenter radius and axial length on the residual stresses. However, Fig. 11.8 (q) shows that when the indenter axial length is nearly zero, the differences between the predictions obtained from the empirical formulations and the FE analyses are relatively large, but less than 15%.

11.7 Discussion

From the deformed shapes of the pipes and the outer surface residual stress distributions (see Figs. 11.2(a) to (e)) it can be seen that the maximum residual tensile stresses occur at very localised positions on the plane of symmetry when the residual dent depth is small, i.e. $\delta/D < 0.01$. Hence, the residual stresses at this position on the indented pipe are the most important in relation to the determination of remaining life, which could be relatively short if the pressure fluctuation ranges are large. However, when the residual dent depth is large, the zone of plasticity in the pipe is larger and the peak values of the residual stresses reduce as a result of stress redistribution associated with the large deformation.

The FE analyses performed on the unpressurised and pressurised pipes all show that the residual stresses are particularly sensitive to the residual dent depth, especially when the indenter radius is small. The effects of the internal pressure on the residual stresses are of concern under two conditions. The first condition is that of an indentation caused with zero internal pressure and the internal pressure increases to the operating condition after the indentation has occurred. In this case, the residual stresses remain almost constant during the application of the internal pressure. The second condition is that of the internal pressure being applied before an indentation is created. In this case, the effect of the internal pressure levels when the indentation occurs, on the residual stresses is non-linear and is dependent on the residual dent depth. In this case, the effects of the internal pressure on the residual stresses are significant.

The effects of the indenter size (radius and axial length) on the residual stresses were also investigated here. The results show that the indenter radius has an effect on the residual stresses and that the residual stresses increase as the indenter radius reduces, for the same residual dent depth. The indenter axial length is found to affect the residual stresses at the same applied dent

depth but not to affect the residual hoop and von Mises stresses at the same residual dent depth; see the empirical formulations (11.2) to (11.4).

The effects of the material properties on the residual stresses were investigated. For three typical pipe materials used, the residual stress distribution patterns are similar to one another.

All of the FE analyses were performed with an angular support position of 45°. For localised indentations, with small residual dent depths, it is not expected that the angular support position will have a significant effect on the residual stresses. However, if the residual dent depth is large, then the deformations may be more widespread and hence the angular support positions are likely to have a larger effect on the residual stresses. This is in contrast to previous results in chapter 8 for long two dimensional indentations in pipes, for which it was found that the angular support position does have an effect on the residual stresses and on the indenter force versus dent depth behaviour.

The empirical formulations (11.2) to (11.4) were developed in order to be able to predict the residual stresses for other materials and for other loading conditions, without the need for performing further FE analyses. From Figs. 11.8 (a) to (q), it can be seen that the empirical formulations are able to accurately predict the residual stresses. For pipes made from material grade B, an internal pressure of 5.12 MPa, which produces mean hoop stresses of 0.624 times yield stress, the residual stresses obtained from the empirical formulations (11.2) to (11.4) are in very good agreement with those obtained from the FE analyses. For unpressurised pipes made from X52 or X65 SAW material, the residual stresses obtained from the empirical formulations are also very close to those obtained from the FE analyses. For the pipes made from material X52, with an internal pressure of 5.12 MPa, which produces mean hoop stresses of 0.50 times yield stress, close correlation of the residual stresses obtained from the FE analyses and the empirical formulations were also obtained. These results show that even when the internal pressure is high (e.g. producing a mean hoop stress of 0.624 times yield stress), the empirical formulations are capable of accurately predicting the residual stresses, for the pipes with materials having relatively low hardening exponents, i.e. $n \approx 4.5$.

For the pipes made from material X65 SAW, with an internal pressure of 3.84 MPa, which produces a mean hoop stress of 0.3 times yield stress, the residual stresses obtained from the empirical formulations are in good agreement with those obtained from the FE analyses. However, at an internal pressure of 6.4 MPa, which produces a mean hoop stress of over 0.5

times yield stress, the residual stresses obtained from the empirical formulations for d/D<0.1 are about 40% higher than those obtained from the FE analyses. This indicates that the empirical formulations are not capable of giving good predictions of the residual stresses for pipes with high pressure (producing a mean hoop stress of 0.5 times yield stress) and with a relatively high hardening exponent, i.e. n=7.56.

The investigations of the effects of the indenter size, including radius and axial length, on the residual stresses indicate that the empirical formulations are able to predict, with reasonable accuracy, the effects of the indenter size.

For all three materials, and the pressure levels investigated here, it was found that the empirical formulations were not able to predict the residual stress decrease which occurs due to the large scale plastic deformation resulting from the large applied dent depths. All of the results shown in Figs.11.8 (a) to (o) indicate that as the δ/D ratios exceed 0.01, the residual stresses begin to reduce with increase of the residual dent depth and that the empirical formulations fail to predict the phenomenon. Therefore, the empirical formulations should only be used for δ/D<0.01, for pipes with low hardening exponent, i.e. n<5, and for pipes with high hardening exponents, i.e. n>7.56 and low pressure, which may produce a mean hoop stress in a perfect pipe of less than 0.4 σ_y.

11.8 Summary

A comprehensive elastic-plastic FE analyses of residual stresses caused by localised pipe indentations is presented. The effects of residual dent depth, internal pressure, indenter size and material properties have been studied. Empirical formulae are developed to predict the residual stresses for other pipe materials and parameters. It has been shown that empirical formulations can accurately predict the residual stresses for pipe materials with a low hardening exponent and for pipe materials with a high hardening exponent and low pressures.

Chapter 12

Predictions of Stress Variations in Indented Pipes due to Internal Pressure Fluctuations

12.1 Introduction

In chapter 11 it has been shown that the residual stress is dependent upon the residual dent depth and the internal pressure in the pipe at the time at which the dent was created; the indenter geometry, pipe geometry and material properties are also important factors. By inspection of a dent found during inspection, the shape of the indenter which caused the dent can be determined and also the material and pipe geometry will be known. The dent depth can be measured with whatever pressure exists within the pipe at the time of measuring. Therefore, if the current pressure is different from the pressure at the time at which the dent was created, a correction to the measured dent depth to obtain the dent depth for the pressure at which it was created is required. Therefore, if a relationship between the change of dent depth, $\Delta\delta$, and change of pressure, Δp, can be established, then the residual stress at the time of the indentation can be obtained. If the change of stresses, $\Delta\sigma$, due to the change of pressure, Δp, can also be obtained, then this data (residual stresses and stress changes) can be used to perform a fatigue assessment. The variations of stresses and dent depths due to internal pressure fluctuation are investigated in this chapter.

12.2 Material Properties

Two typical pipe materials were used in the FE study. They are grade X52, seamless line pipe material, and a 32 inch thick wall, grade X65 SAW, line pipe material. The uniaxial true stress versus true strain curves are shown in Fig.8.1. The relevant material properties for these two materials are given in Table 8.1. Some analyses were also performed using an elastic material behaviour model with a Young's modulus of 180GPa.

In the FE analyses, all materials were assumed to obey an isotropic hardening rule. Since engineering stresses are generally defined as F/S, whereas F is the initial force applied to a uniaxial tensile specimen and S is the initial cross-section area of the specimen, then the peak value of the engineering stress (commonly referred to as the ultimate tensile stress) is lower

than the stress obtained from a true stress versus strain curve. Hence, the true stresses in Fig.8.1 are significantly higher than the true tensile stresses.

12.3 Geometry, Loading and Boundary Conditions

All of geometry, loading and boundary conditions used in this chapter are the same as used in chapter 11, see Figs. 4.1 and 11.1.

12.4 FE Meshes

Due to the symmetry of the geometry and loading, it is only necessary to model a quarter of a pipe in the FE analyses, a typical mesh is shown in Fig. 9.7, generated with 4-node, doubly-curved, quadrilateral shell elements and 3-node, triangular shell elements, with reduced integration. Fine meshes were used for the dent region and coarser meshes were used elsewhere. Seventy four FE analyses were performed, the details of the analyses are given in Tables 12.1 to 12.6 and all of the results were taken at the edge of contact of the indenter, where the maximum residual stresses occurred [chapter 11]. For all of the non-linear, elastic-plastic analyses, large deformation and large strain effects were incorporated in order to obtain the stress variations within the indented pipes. In addition, some linearly elastic analyses were also performed on the imperfect pipes.

Table 12.1: The Geometry and loading conditions used in the FE analyses, and the residual dent depth and normalised stress variation results obtained for the pipes with X52 material, with an indenter radius of 12.7mm and length 20mm.

FE No	D/t	t (mm)	δ (% of D)	P (MPa)	Δp (MPa)	δ_r (mm)	$\Delta\sigma_h$ /Δp	$\Delta\sigma_a$ /Δp	$\Delta\sigma_e$ /Δp
FE1	72	12.7	1.	0	0	1.2	0	0	0
FE2	72	12.7	1.5	0	0	3.28	0	0	0
FE3	72	12.7	2.	0	0	6.04	0	0	0
FE4	72	12.7	2.5	0	0	9.22	0	0	0
FE5	72	12.7	0.5	3.84	1.28	0.6	39.53	11.72	29.38
FE6	72	12.7	0.75	3.84	1.28	1.55	49.84	17.66	37.03
FE7	72	12.7	1.0	3.84	1.28	2.74	61.41	24.38	46.56
FE8	72	12.7	1.25	3.84	1.28	4.1	73.75	29.06	55.31
FE9	72	12.7	1.5	3.84	1.28	5.54	80.78	34.69	61.56
FE10	72	12.7	1.75	3.84	1.28	7.1	87.03	38.59	66.72
FE11	72	12.7	2.0	3.84	1.28	8.73	92.34	41.72	70.94
FE12	65.3	14	1.0	5.12	1.28	2.71	53.13	20.78	40
FE13	57.2	16	1.0	5.12	1.28	2.67	43.91	16.72	33.13
FE14	50.8	18	1.0	5.12	1.28	2.67	37.66	14.06	28.13

FE15	45.7	20	1.0	5.12	1.28	2.7	32.97	12.03	24.53
FE16	41.5	22	1.0	5.12	1.28	2.75	29.37	10.62	21.72
FE17	36.6	25	1.0	5.12	1.28	2.87	25.63	9.06	18.75
FE18	30.5	30	1.0	5.12	1.28	3.09	20.78	7.66	15.31
FE19	26.1	35	1.0	5.12	1.28	3.31	17.81	6.56	12.81
FE20	22.8	40	1.0	5.12	1.28	3.51	15.16	5.62	11.25

Table 12.2: The Geometry and loading conditions used in the FE analyses, and the residual dent depth and normalised stress variation results obtained for the pipes with X65 material, with an indenter radius of 12.7mm and length 20mm.

FE No	D/t	T (mm)	δ (% of D)	P (MPa)	Δp (MPa)	δ_r (mm)	$\Delta\sigma_h$ /Δp	$\Delta\sigma_a$ /Δp	$\Delta\sigma_e$ /Δp
FE21	72	12.7	0.25	6.4	0.64	0.06	36.52	12.94	27.93
FE22	72	12.7	0.5	6.4	0.64	0.62	39.84	13.91	29.49
FE23	72	12.7	0.75	6.4	0.64	1.6	50.78	17.77	37.5
FE24	72	12.7	1.0	6.4	0.64	2.84	62.11	21.88	45.31
FE25	72	12.7	1.25	6.4	0.64	4.22	74.02	27.69	55.08
FE26	72	12.7	1.5	6.4	0.64	5.69	82.03	34.16	61.72
FE27	72	12.7	1.75	6.4	0.64	7.26	89.45	38.87	66.99
FE28	72	12.7	2.0	6.4	0.64	8.93	95.31	42.38	70.12
FE29	72	12.7	2.25	6.4	0.64	10.67	104.3	47.85	73.44
FE30	72	12.7	2.50	6.4	0.64	12.42	113.87	55.27	83.4
FE31	69.3	13.2	2.0	6.4	0.64	8.92	91.02	40.62	67.19
FE32	66.7	13.7	2.0	6.4	0.64	8.93	86.33	37.89	64.06
FE33	64.4	14.2	2.0	6.4	0.64	8.94	82.03	35.74	60.94
FE34	62.2	14.7	2.0	6.4	0.64	8.96	77.93	33.98	58.01
FE35	57.2	16	2.0	6.4	0.64	9.1	69.92	28.52	51.17
FE36	50.8	18	2.0	6.4	0.64	9.23	58.98	24.22	43.36
FE37	41.5	22	2.0	6.4	0.64	9.48	44.92	18.36	32.81

Table 12.3: The Geometry and loading conditions used in the FE analyses, and the residual dent depth and normalised stress variation results obtained for the pipes with X65 material, with a pressure of 6.4MPa and a pressure range of 0.64MPa.

FE No	D/t	t (mm)	δ (% of D)	r (mm)	L (mm)	δ_r (mm)	$\Delta\sigma_h$ /Δp	$\Delta\sigma_a$ /Δp	$\Delta\sigma_e$ /Δp
FE38	72	12.7	2.0	16	20.0	8.9	94.7	44.5	73.0
FE39	72	12.7	2.0	20	20.0	8.8	93.2	43.0	74.8
FE40	72	12.7	2.0	24	20.0	8.7	93.0	42.4	76.8
FE41	72	12.7	2.0	28	20.0	8.6	92.8	42.0	77.3
FE42	72	12.7	2.0	36	20.0	8.5	92.8	41.6	78.3
FE43	72	12.7	2.0	40	20.0	8.4	93.0	41.4	78.5
FE44	72	12.7	2.0	50	20.0	8.3	93.0	41.4	78.7

FE45	72	12.7	2.0	60	20.0	8.1	93.2	41.2	78.9
FE46	72	12.7	2.0	70	20.0	8.0	93.2	41.4	78.7
FE47	72	12.7	2.0	80	20.0	7.9	93.4	41.4	78.7
FE48	72	12.7	2.0	90	20.0	7.7	93.4	41.4	78.7
FE49	72	12.7	2.0	100	20.0	7.6	93.4	41.4	78.5
FE50	72	12.7	2.0	110	20.0	7.5	93.4	41.6	78.3
FE51	72	12.7	2.0	12.7	0	10.4	81.5	42.0	70.5
FE52	72	12.7	2.0	12.7	8	10.1	87.5	44.3	75.8
FE53	72	12.7	2.0	12.7	20	8.9	95.3	42.4	82.7
FE54	72	12.7	2.0	12.7	30	8.4	97.5	42.6	84.6
FE55	72	12.7	2.0	12.7	40	7.9	98.4	42.2	85.5
FE56	72	12.7	2.0	12.7	50	7.4	97.3	41.2	84.6
FE57	72	12.7	2.0	12.7	80	6.4	96.7	39.5	84.2
FE58	72	12.7	2.0	12.7	100	5.8	94.5	37.5	82.4
FE59	72	12.7	2.0	12.7	140	5.8	94.5	37.7	82.4

Table 12.4: The Geometry and loading conditions used in the FE analyses for the situations with a pressure increase after indentation occurred and for the pipes with X52 material, with an indenter radius of 12.7mm and length 20mm.

FE No	D/t	t (mm)	δ (% of D)	p_0 (MPa)	P_1 (MPa)	p_2 (MPa)	p_3 (MPa)	p_4 (MPa)	p_5 (MPa)
FE60	72	12.7	1	0	1.28	2.56	3.84	5.12	6.4
FE61	72	12.7	1.5	0	1.28	2.56	3.84	5.12	6.4
FE62	72	12.7	2	0	1.28	2.56	3.84	5.12	6.4
FE63	72	12.7	3	0	1.28	2.56	3.84	5.12	6.4
FE64	72	12.7	1	5.12	5.76	6.4	7.04	7.68	
FE65	72	12.7	2	5.12	5.76	6.4	7.04	7.68	
FE66	72	12.7	3	5.12	5.76	6.4	7.04	7.68	
FE67	41.5	22	2	0	1.28	2.56	3.84	5.12	
FE68	22.86	40	2	0	1.28	2.56	3.84	5.12	

Table 12.5: The Geometry and loading conditions used in FE analyses for the case of a pressure increase after indentation has occurred and for the pipes with X65 SAW material, with an indenter radius of 12.7mm and length 20mm.

FE No	D/t	t (mm)	δ (% of D)	p_0 (MPa)	p_1 (MPa)	p_2 (MPa)	p_3 (MPa)	p_4 (MPa)	p_5 (MPa)
FE69	72	12.7	1	0	1.28	2.56	3.84	5.12	6.4
FE70	72	12.7	1.5	0	1.28	2.56	3.84	5.12	6.4
FE71	72	12.7	2	0	1.28	2.56	3.84	5.12	6.4
FE72	72	12.7	3	0	1.28	2.56	3.84	5.12	6.4

Table 12.6: The Geometry and loading conditions used in FE analyses for the case of a pressure increase after indentation has occurred and for the pipes with X52 material, D/t=72 and t=12.7mm.

FE No	R (mm)	L (mm)	δ (% of D)	p_0 (MPa)	p_1 (MPa)	p_2 (MPa)	p_3 (MPa)	p_4 (MPa)
FE73	50	20	2	0	1.28	2.56	3.84	5.12
FE74	12.7	80	2.	0	1.28	2.56	3.84	5.12

12.5 FE Results

12.5.1 The effect of Residual Dent Depth on the Stress Variations due to pressure variations

The variations of stress in the indented pipes, due to internal pressure fluctuations, were investigated using the result of FE analyses FE5 to FE11 and FE21 to FE30. For the pressurised pipes made from the X52 material, with an initial pressure, p, of 3.84MPa and an internal pressure range, Δp, of 1.28MPa, i.e. the internal pressure was reduced to 2.56MPa after indentation, the stress variations were normalised by dividing them by the internal pressure range, Δp. The dependence of the normalised stress variations versus the residual dent depth can be seen from Fig. 12.1 (a). Similarly, for the pressurised pipes made from X65 material and an initial internal pressure, p, of 6.4MPa and a pressure range, Δp, of 0.64MPa, the normalised stress variations on residual dent depth curves are shown in Fig. 12.1 (b). From Figs. 12.1 (a) and (b) it can be seen that the normalised stress (hoop, axial and von Mises) variations increase as the residual dent depth increases. It can also be seen that the normalised stress variations obtained are related to the residual dent depth but appear to be only weakly dependent upon the material properties and on the internal pressure amplitude and range. This is because the pipe undergoes an elastic springback process as the internal pressure is reduced.

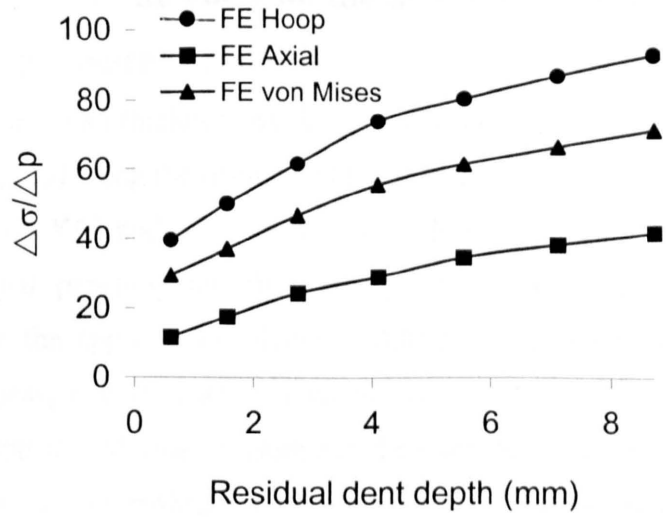

Fig. 12.1 (a) Variation of normalised stress changes versus residual dent depth curves obtained from the pipes with X52 material for D/t=72, t=12.7mm, r=12.7mm, L=20mm, p=3.84MPa and Δp=1.28MPa.

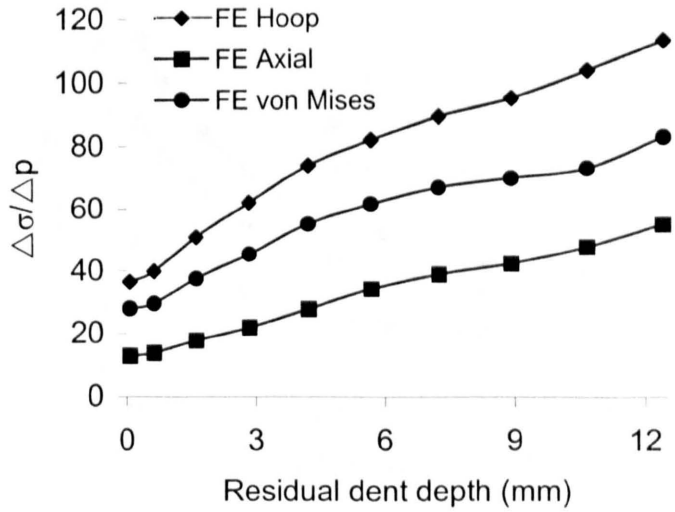

Fig. 12.1 (b) Variation of normalised stress changes versus residual dent depth curves obtained from the pipes with X65 material for D/t=72, t=12.7mm, r=12.7mm, L=20mm, p=6.4MPa and Δp=0.64MPa.

12.5.2 The effect of Wall Thickness on the Stress Variations which occur due to pressure variations

The effects of the pipe wall thickness on the stress variations which occur due to pressure variations were investigated using the results of FE analyses FE12 to FE20 and FE31 to FE37, performed on pipes with X52 and X65 SAW steels. For the pipes with X52 material, the initially applied internal pressure and the subsequent pressure range are 5.12MPa and 1.28MPa, respectively; the applied dent depth is 0.01D. The normalised stress variation versus the wall thickness, t, curves are shown in Fig. 12.2 (a). For the pipes with X65 material, the initially applied internal pressure and the subsequent pressure range are 6.4MPa and 0.64MPa, respectively; the applied dent depth is 0.02D. The normalised stress variation versus the wall thickness, t, curves, obtained from the X65 material pipes, are shown in Fig. 12.2 (b). From the Figs. 12.2 (a) and (b), it can be seen that the stress variations reduce as the wall thickness increases.

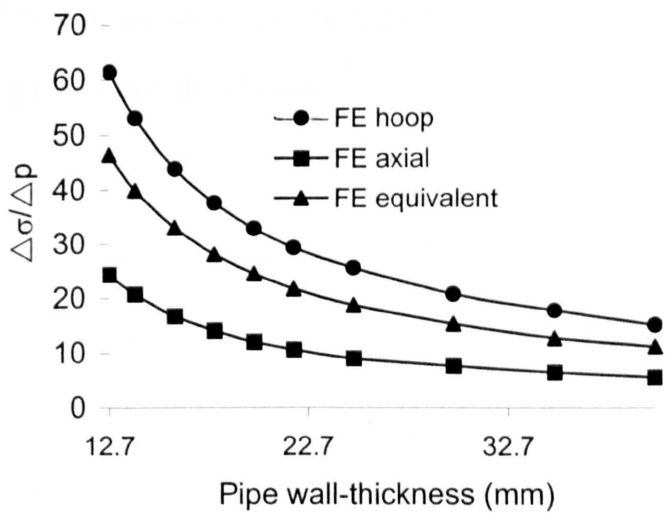

Fig. 12.2 (a) Variation of normalised stress changes versus wall thickness curves obtained from the pipes with X52 material for r=12.7mm, L=20mm, δ=0.01D, p=3.84MPa and Δp=1.28MPa.

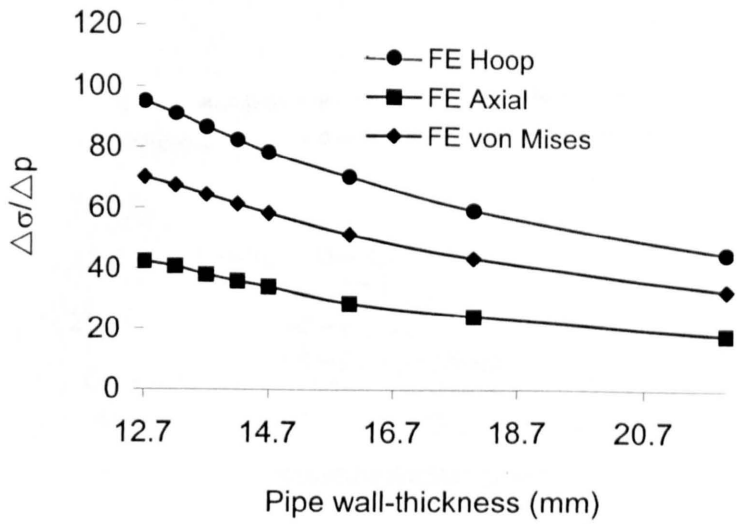

Fig. 12.2 (b) Variations of normalised stress changes versus wall thickness curves obtained from the pipes with X65 material for r=12.7mm, L=20mm, δ=0.02D, p=6.4MPa and Δp=0.64MPa.

12.5.3 The effect of Indenter Size on the Stress Variations which occur due to pressure variations

The effects of the indenter size (including the radius and the axial length) on the stress variations were investigated using the results of the FE analyses FE38 to FE59, performed on the X65 pipes with an initially applied internal pressure, p, of 6.4MPa, a pressure range, Δp, of 0.64MPa, and an applied dent depth, δ, of 0.02D. The stress variation versus indenter radius curves, obtained for an indenter with an axial length of 20mm, are shown in Fig. 12.3 (a). The stress variation versus the indenter axial length, obtained for an indenter with a radius of 12.7mm, are shown in Fig. 12.3 (b). From Fig. 12.3 (a), it can be seen that the indenter radius has a relatively small effect on the stress variations. Fig. 12.3 (b) shows that the indenter axial length may have a significant effect on the hoop and von Mises stress variations when the length is small. However, both Figs. 12.3 (a) and (b) show that the axial stress variation is not sensitive to the indenter size.

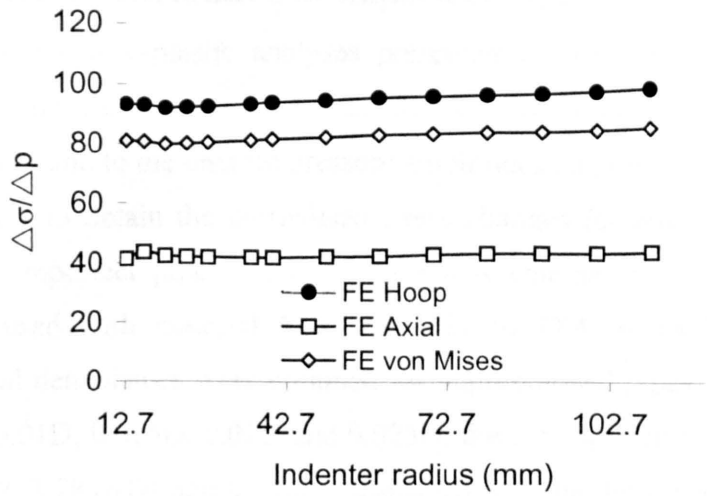

Fig. 12.3 (a) Variation of normalised stress changes versus indenter radius, obtained from the pipes with X65 material for D/t=72, t=12.7mm, L=20mm, δ=0.02D, p=6.4MPa and Δp=0.64MPa.

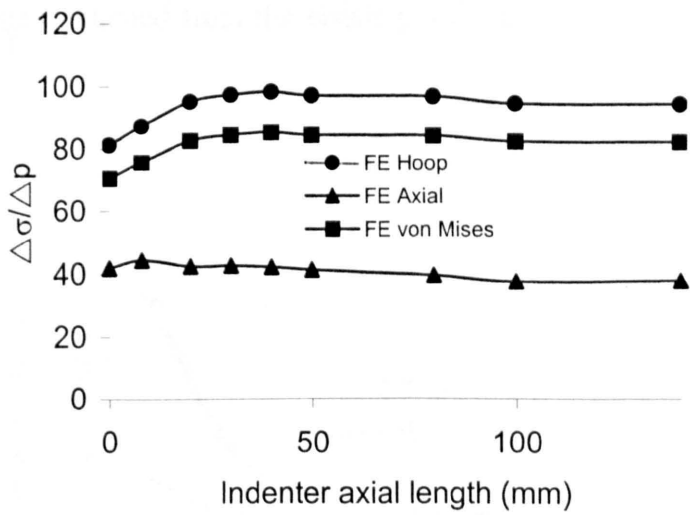

Fig. 12.3 (b) Variation of normalised stress changes versus indenter axial length, obtained from the pipes with X65 material for D/t=72, t=12.7mm, r=12.7mm, δ=0.02D, p=6.4MPa and Δp=0.64MPa.

12.5.4 Elastic Stress Distribution in Imperfect Pipes

As seen from the elastic-plastic analyses presented in sections 12.5.1 to 12.5.3, the normalised stress changes due to pressure fluctuations do not seem to be strongly related to the material properties and to the internal pressure amplitudes and ranges. Therefore, it would appear to be possible to obtain the normalised stress changes for any material from elastic analyses, using an imperfect pipe. In order to assess whether this is accurate, four FE calculations were used with material X52 (see FE1 to FE4 in Table 12.1). In these calculations, residual dent shapes were obtained for unpressurised pipes subjected to applied indenter depths of 0.01D, 0.015D, 0.02D and 0.025D; the corresponding residual dent depths were found to be1.2, 3.28, 6.04 and 9.22mm, respectively. The deformed shapes from these analyses were used as the shapes of imperfect pipes in the subsequent elastic analyses, i.e. all of residual stresses were set to zero and the deformed shapes were taken to be the initial geometry of the imperfect pipes. A pressure of 5.12MPa was applied in the elastic analyses. Typical elastic stress distributions for the imperfect pipes, which were obtained using applied dent depths of 0.01D and 0.02D, are shown in Figs. 12.4 (a) to (d). From Figs. 12.4 (a) to (d), it can be seen that the elastic stress distributions, for these imperfect pipes, are different from the residual stresses obtained from the elastic-plastic analyses previously discussed in chapter 11 (Fig.11.2).

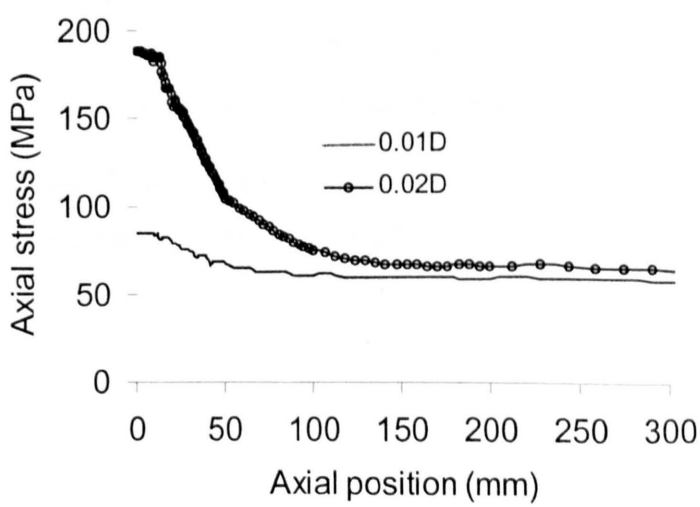

Fig. 12.4 (a) Variation of axial stress with axial position for imperfect pipes obtained using linear elastic analyses, for applied dent depths of 0.01D and 0.02D.

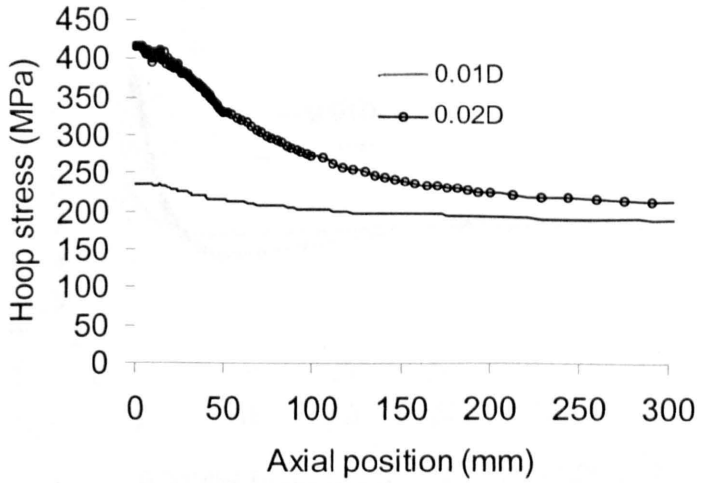

Fig. 12.4 (b) Variation of hoop stress with axial position for imperfect pipes obtained using linear elastic analyses, for applied dent depths of 0.01D and 0.02D.

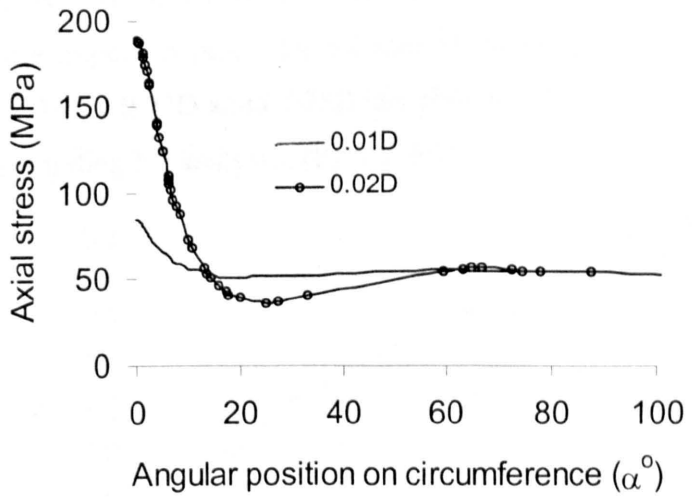

Fig. 12.4 (c) Variation of axial stress with circumferential position for imperfect pipes obtained using linear elastic analyses, for applied dent depths of 0.01D and 0.02D.

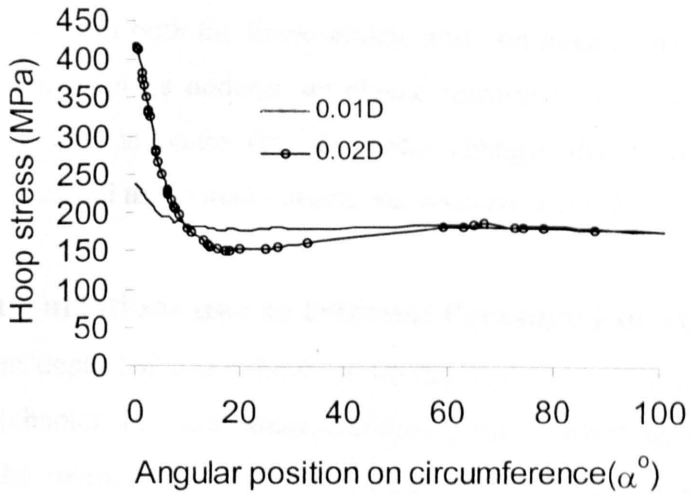

Fig. 12.4 (d) Variation of hoop stress with circumferential position for imperfect pipes obtained using linear elastic analyses, for applied dent depths of 0.01D and 0.02D.

The normalised stresses, obtained by dividing the stresses by the internal pressure (i.e. 5.12MPa) applied to the imperfect pipes, for all four imperfect pipes, obtained for applied dent depths of 0.01D, 0.015D, 0.02D and 0.025D, are shown in Fig. 12.5, which also presents the results of the corresponding FE analyses, (FE5 to FE11).

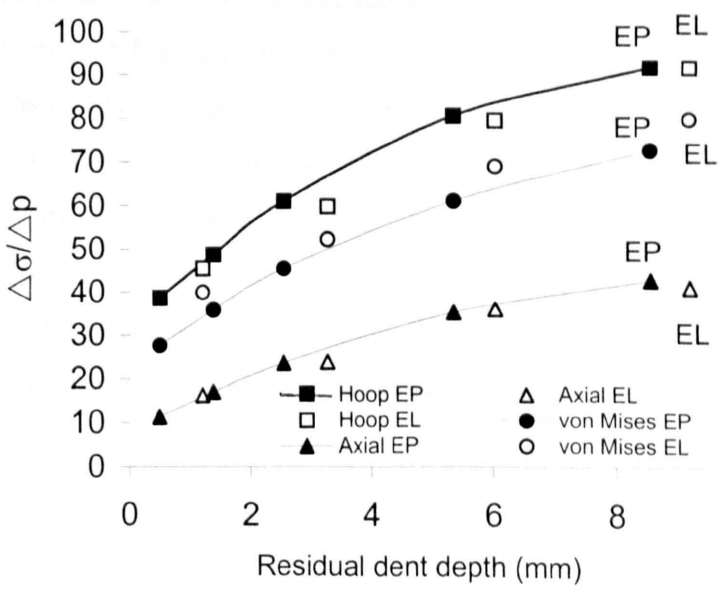

Fig. 12.5 Variation of normalised stress and stress changes versus residual dent depth obtained from linear elastic and non-linear, elastic-plastic analyses (FE5 to FE11) for the pipes with X52 material (EP and EL refer to elastic plastic and elastic analyses, respectively).

From Fig. 12.5, it can be seen that for the normalised stresses, there is good correlation between results obtained from both the linear elastic and non-linear, elastic plastic analyses. This confirms that indented pipes undergo an elastic restoration process when the internal pressure is reduced. It also indicates that the stress changes due to pressure changes in indented pipes can be obtained using linear elastic analyses performed on imperfect pipes [3].

12.5.5 Dent Depth Variations due to Internal Pressure Fluctuations

As the residual dent depth has been shown to be the most important parameter affecting the residual stresses [chapter 11] and stress variations, the residual dent depth variations which occur due to the internal pressure fluctuations has been investigated using the FE analyses FE56 to FE70. For the pipes with material X52, the geometry and loading conditions are shown in Tables 12.4 to 12.6. The residual dent depth versus internal pressure curves, obtained from the FE analyses (FE56 to FE64), are shown in Figs. 12.6 (a) to (c). For the pipes with material X65 SAW, the geometry and loading conditions are shown in Table 12.4. The residual dent depth versus internal pressure curves, obtained from the FE analyses (FE65 to FE68), are shown in Fig. 12.6 (d). From Figs. 12.6 (a) to (d), it can be seen that the residual dent depth after indentation reduces as the internal pressure increases and that the relationship between the residual dent depth and the internal pressure is almost linear. The negative residual dent depths in Fig.12.6 (d) indicate that the overall expansion of the pipes after internal pressure was increased is greater than the previous residual dent depth.

The relationship between the residual dent depth and the internal pressure for large indenter sizes, i.e. (r=50mm and L=20mm) and (r=12.7mm and L=80mm), were investigated using the FE analyses (FE69 and FE70) performed on the initially unpressurised pipes with material X52 and the results are shown in Fig.12.6 (e). It can be seen, from Fig. 12.6 (e), that indenter size does not significantly affect the gradient of the residual dent depth versus internal pressure curves.

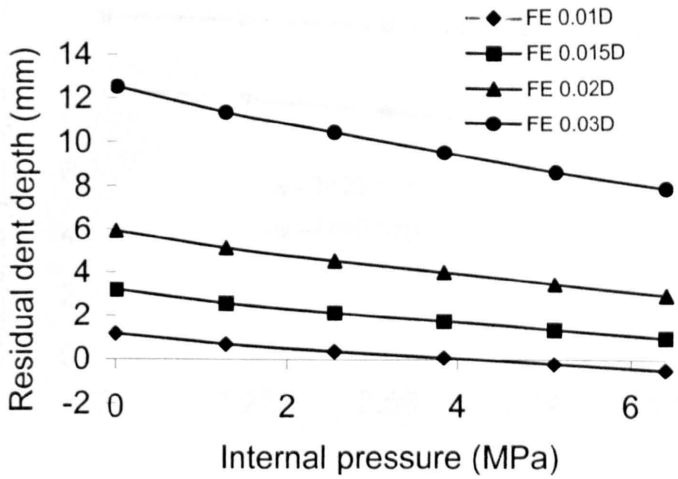

Fig.12.6 (a) The residual dent depth versus internal pressure curves obtained from the initially unpressurised pipes with material X52 for δ=0.01D, D/t=72, t=12.7mm, r=12.7mm and L=20mm.

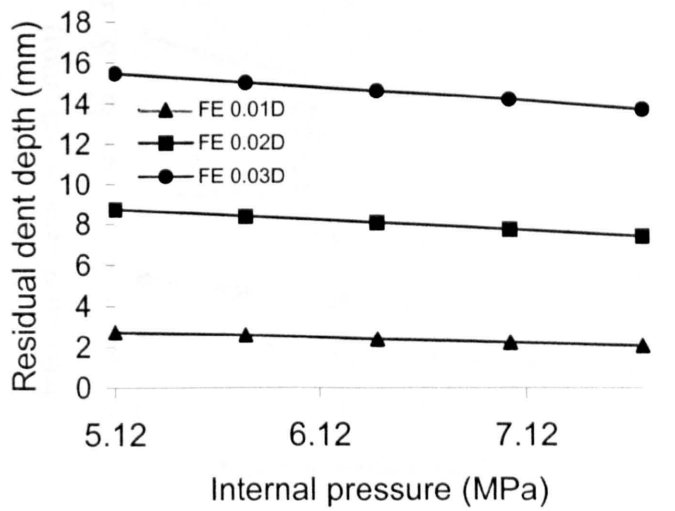

Fig.12.6 (b) The residual dent depth versus internal pressure curves obtained from the initially pressurised pipes with material X52 and with initial pressure p_0=5.12MPa, for δ=0.01D, D/t=72, t=12.7mm, r=12.7mm and L=20mm.

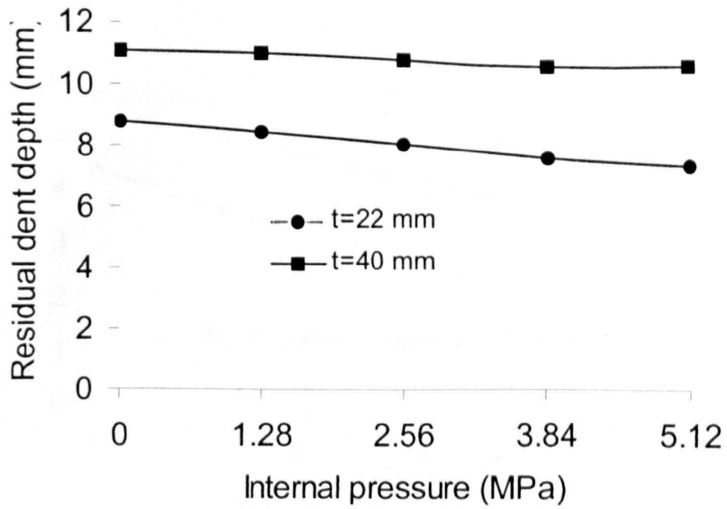

Fig.12.6 (c) The residual dent depth versus internal pressure curves obtained from the initially unpressurised pipes with material X52 for δ=0.02D, D=914.4mm and for t=20 and 40mm, r=12.7mm and L=20mm.

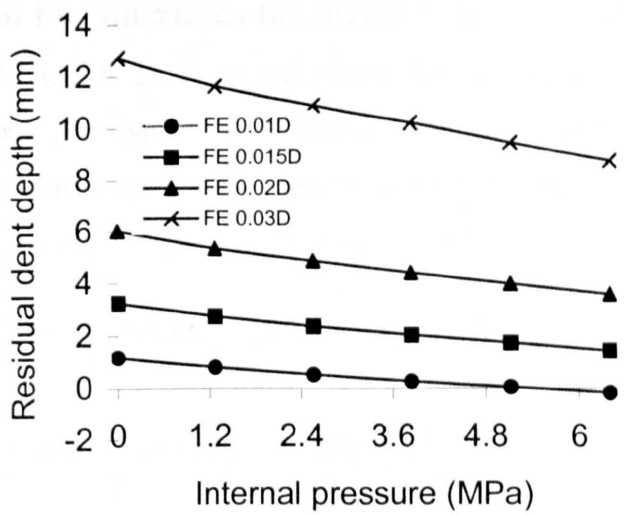

Fig.12.6 (d) The residual dent depth versus internal pressure curves obtained from the initially unpressurised pipes with material X65 for δ=0.01D, D/t=72, t=12.7mm, r=12.7mm and L=20mm

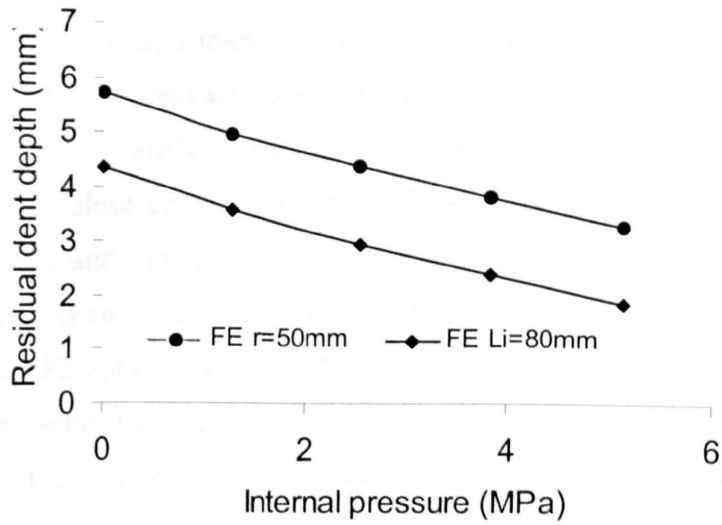

Fig.12.6 (e) The residual dent depth versus internal pressure curves obtained from the FE analyses for the initially unpressurised pipes with material X52 for δ=0.02D, D/t=72, t=12.7mm, for large indenters, i.e., (r=50mm, L=20mm) and (r=12.7mm and L=80mm).

12.6 Semi-empirical Formulations for Stress Variation Predictions

Using the results of the FE analyses and curve fitting techniques, a semi-empirical formulation for predicting the changes in stress and the dent depth, due to the internal pressure fluctuations, were developed. The basic form of the equations was taken from the analysis of imperfect rings [chapter 8]. The resulting formulations are as follows:

$$\left.\begin{aligned}
\frac{\Delta\sigma_h}{\Delta p} &= \left(1.15-0.38e^{-15.46\frac{L}{R}}\right)\left(\frac{-45.92\delta_r^2+3.0926R\delta_r}{t^2}+\frac{13.615\delta_r+R}{t}\right)\\
\frac{\Delta\sigma_{axial}}{\Delta p} &= \frac{10.186\delta_r^2+1.009R\delta_r}{t^2}+\frac{-6.49\delta_r+\frac{1}{2}R}{t}\\
\frac{\Delta\sigma_e}{\Delta p} &= \left(1.4-0.45e^{-15.46\frac{L}{R}}\right)\left(\frac{-24.606\delta_r^2+1.9636R\delta_r}{t^2}+\frac{7.134\delta_r+\frac{\sqrt{3}}{2}R}{t}\right)
\end{aligned}\right\} \qquad (12.1)$$

and

$$\frac{\Delta\delta}{\Delta p}=\frac{R^3}{Et^3}\left(0.00257R+0.23\delta_m\right) \qquad (12.2)$$

Equation (12.1) includes the effects of the residual dent depth, the pipe radius, the wall thickness and the axial length of the indenter on the normalised stress variations. Equation (12.2) enables the effect of the change of internal pressure to the residual dent depth, to be

predicted. For the given sets of the dimensions and residual dent depths, obtained from FE analyses FE5 to FE59, given in Tables 12.1 to 12.3, the normalised stress variations were predicted using equation (12.1) and are shown in Figs. 12.7 (a) to (e). The normalised stress changes obtained from the FE analyses are also shown in Figs. 12.7 (a) to (e) for comparison. It can be seen that very close correlation between the normalised stress changes, obtained using the equation (12.1), and from the FE analyses, was obtained.

In cases where there is an increase in the internal pressure, the dent depths obtained from equation (12.2) and the FE analyses FE12 to FE20 and FE31 to FE37, are shown in Figs. 12.8 (a) to (d). It can be seen from Figs. 12.8 (a) to (d) that equation (12.2) gives reasonably accurate predictions of the changes in dent depth as the internal pressure increases, after indentation. For large indenter sizes, the dent depth versus internal pressure curves obtained from the FE analyses FE73 and FE74 and the semi-empirical formulation, equation (12.2), are shown in Fig.12.8 (e) which indicates that the semi-empirical formulation also accurately predicts the dent depth changes for large indenter sizes.

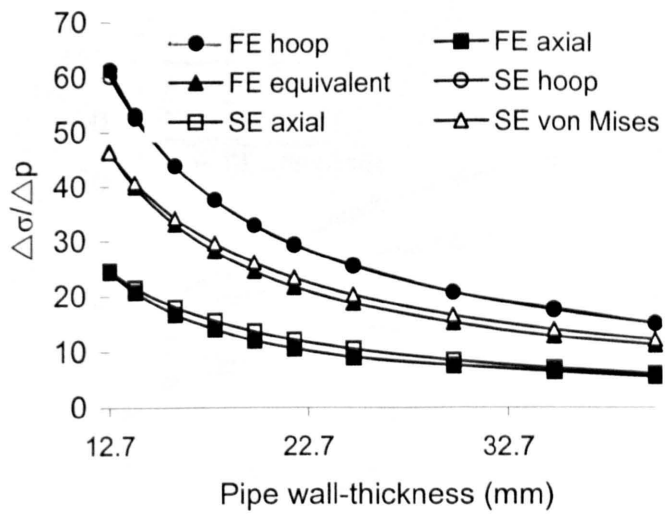

Fig. 12.7 (a) Normalised stress changes versus wall thickness curves obtained from the semi-empirical formulation and the FE analyses for the pipes with material X52 for r=12.7mm, L_i=20mm, δ=0.01D, p=5.12MPa and Δp=1.28MPa.

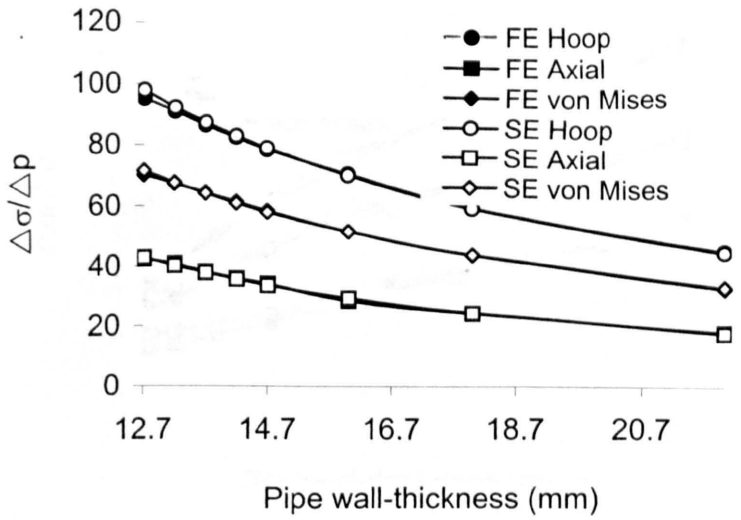

Fig. 12.7 (b) Normalised stress variation versus wall thickness curves obtained from the semi-empirical formulation and the FE analyses for the pipes with material X65 for r=12.7mm, L_i=20mm, δ=0.02D, p=6.4MPa and Δp=0.64MPa.

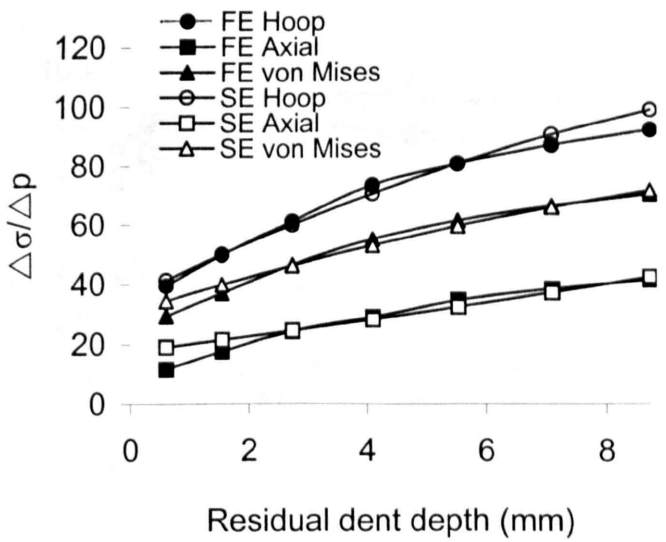

Fig. 12.7 (c) Normalised stress variation versus residual dent depth curves obtained from the semi-empirical formulation and the FE analyses for the pipes with material X52 for D/t=72, t=12.7mm, r=12.7mm, L_i=20mm, δ=0.01D, p=5.12MPa and Δp=1.28MPa.

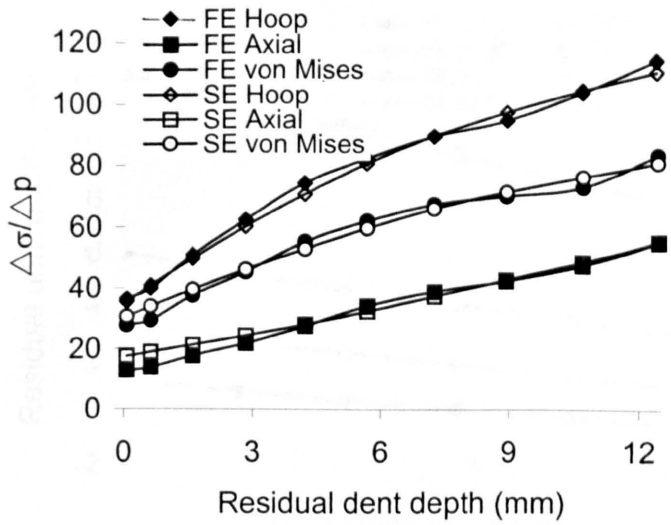

Fig. 12.7 (d) Normalised stress variation versus residual dent depth curves obtained from the semi-empirical formulation and the FE analyses for the pipes with material X65 for D/t=72, t=12.7mm, r=12.7mm, L_i=20mm, δ=0.02D, p=6.4MPa and Δp=0.64MPa.

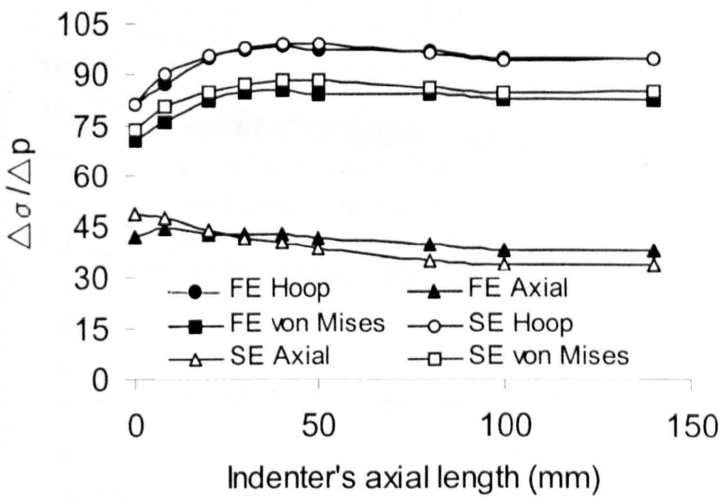

Fig. 12.7 (e) Normalised stress variation versus indenter's axial length curves obtained from the semi-empirical formulation and the FE analyses for the pipes with material X65 for D/t=72, t=12.7mm, r=12.7mm, δ=0.02D, p=6.4MPa and Δp=0.64MPa.

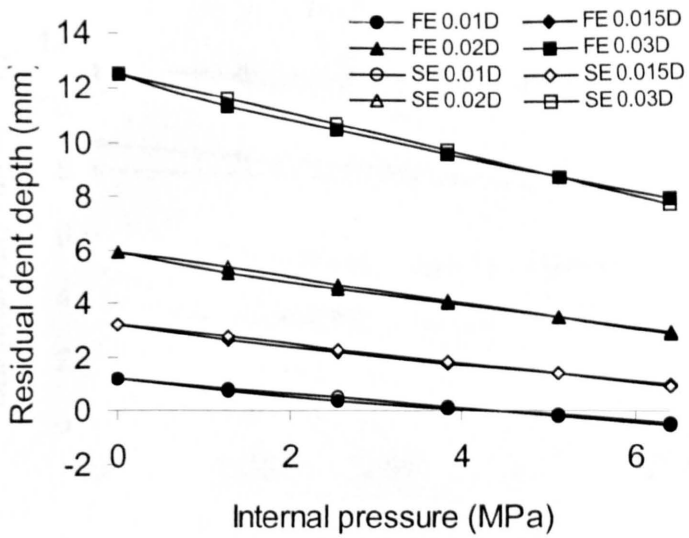

Fig.12.8 (a) The dent depth versus internal pressure curves obtained from the semi-empirical formulation and the FE analyses for the initially unpressurised pipes with material X52 for δ=0.01, 0.015, 0.02 and 0.03D, D/t=72, t=12.7mm, r=12.7mm and L_i=20mm

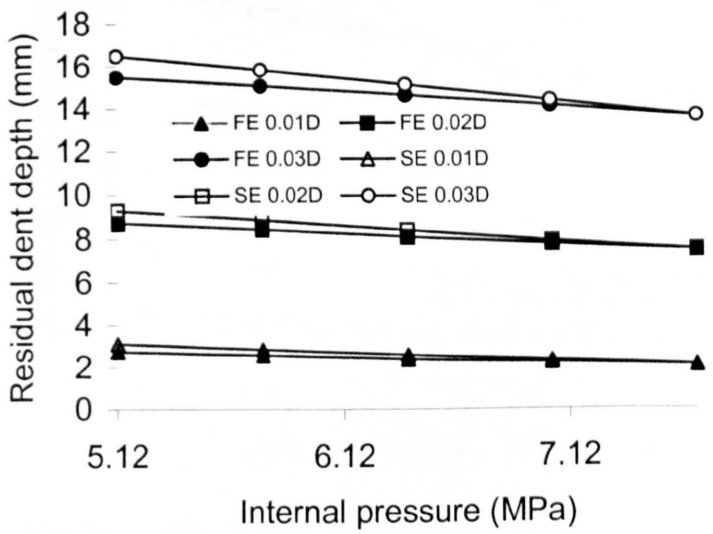

Fig.12.8 (b) The dent depth versus internal pressure curves obtained from the semi-empirical formulation and the FE analyses for the initially pressurised pipes with material X52 and with initial pressure, p=5.12MPa for δ=0.01, 0.02 and 0.03D, D/t=72, t=12.7mm, r=12.7mm and L_i=20mm

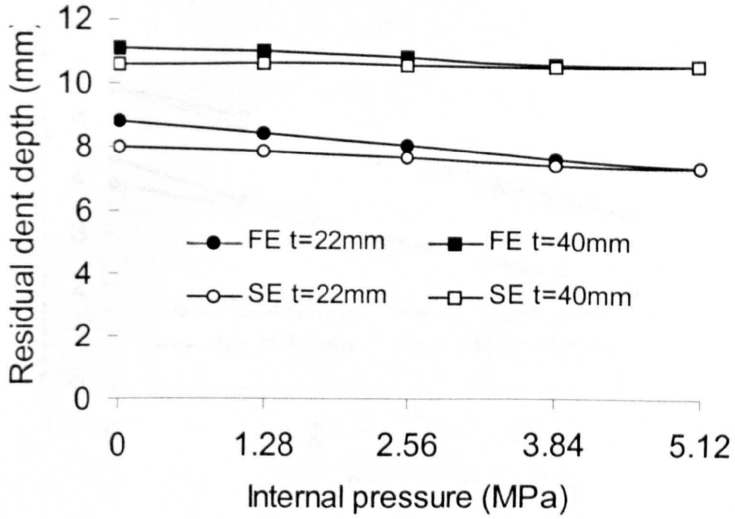

Fig.12.8 (c) The dent depth versus internal pressure curves obtained from the semi-empirical formulation and the FE analyses for the initially unpressurised pipes with material X52 for δ=0.02D, D=914.4mm, t=20 and 40mm, r=12.7mm and L_i=20mm

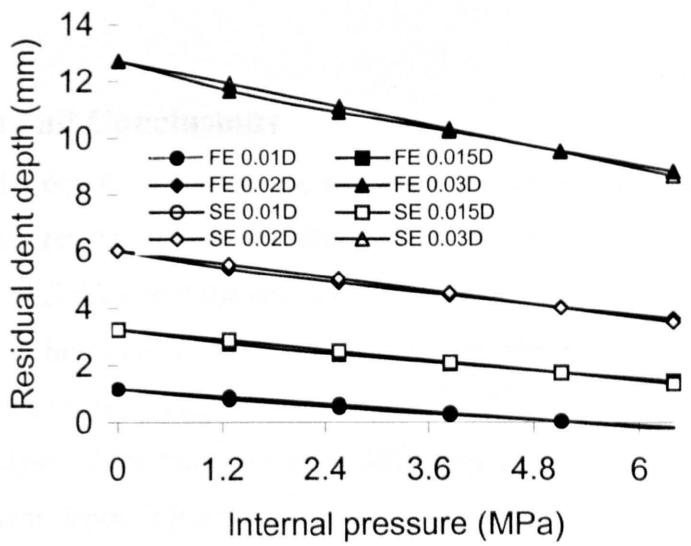

Fig.12.8 (d) The dent depth versus internal pressure curves obtained from the semi-empirical formulation and the FE analyses for the initially unpressurised pipes with material X65 for δ=0.01, 0.015, 0.02 and 0.03D, D/t=72, t=12.7mm, r=12.7mm and L_i=20mm.

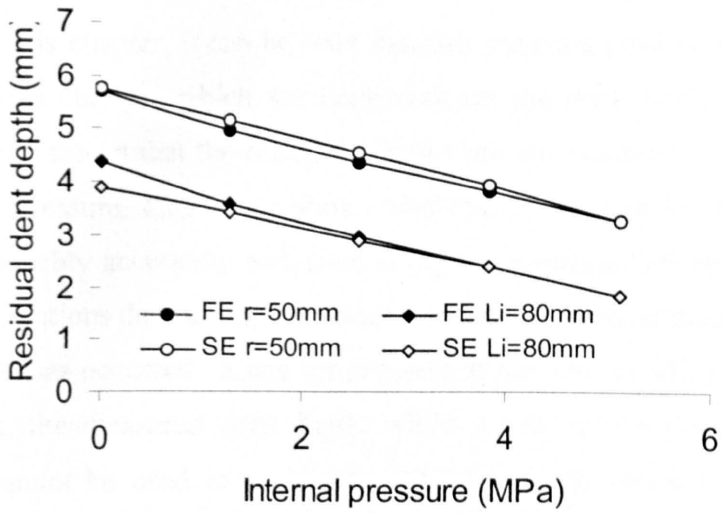

Fig.12.8 (e) The dent depth versus internal pressure curves obtained from the FE analyses and the semi-empirical formulation (2) for the initially unpressurised pipes with material X52 for δ=0.02D, D/t=72, t=12.7mm, for large indenters, i.e., (r=50mm, L_i=20mm) and (r=12.7mm and L_i=80mm).

12.7 Discussion and Conclusions

Results obtained from the FE analyses and semi-empirical formulations show that the normalised stress changes due to pressure fluctuations are strongly dependent on the residual dent depth and pipe wall thickness (or D/t ratio). For deep dent depths, the normalised stress changes are large, and therefore, the fatigue life of the indented pipe would be relatively short. Increasing the wall thickness of a pipe can greatly reduce the normalised stress changes.

Although FE analyses show that the normalised stress changes are related to the D/t ratios and to the residual dent depth, it has been shown that the indenter axial length also affects the normalised stress changes. The close correlation of the results obtained from the linear elastic analyses using imperfect pipe models and the non-linear, elastic-plastic analyses indicates that the normalised stress changes are not strongly related to the material properties and to the intenal pressure fluctuations. The semi-empirical formulation, equation (12.1), reflects the effects of the R/t ratio, the wall thickness t, the residual dent depth and the indenter axial length on the normalised stress changes. In most of the cases investigated in this chapter, the differences between the results obtained from the semi-empirical formulation and the FE analyses are negligible.

If the internal pressure is increased after indentation, the dent depth is reduced. From the results presented in this chapter, it can be seen that this makes a positive contribution to the reduction in the stress changes which are dependent on the dent depth. In the previous chapter 11 it has been shown that the residual stresses remain practically constant during the increase of internal pressure, after indentation. However, as shown in chapter 11, residual stresses can be reasonably accurately estimated using the results of FE analyses or from the semi-empirical formulations developed; these require measurements of the residual dent depth when the indentation has occurred. Since the pressure at the time at which the dent occurred may not be known, the measured dent depth, which could reduce due to an increase of internal pressure, cannot be used to accurately predict residual stresses. Therefore, it is necessary to estimate the residual dent depth based on dent depth measurement made at a different pressure. The semi-empirical formulation, equation (12.2), in this chapter was developed for this purpose. Figs. 12.8 (a) to (d) show that the formulation can predict reasonably accurate dent depths as the indentation occurred. All of the differences between the results obtained above from the semi-empirical formulation, equation (12.2), and the FE analyses are within 14%. Fig. 12.8 (e) indicates that the relationship between the dent depth and the internal pressure is not strongly influenced by the indenter size.

12.8 Summary

The stress variations which occur in indented pipes, due to internal pressure fluctuations are investigated using the results of FE analyses for two typical pipe steel materials. It is found that the stress variations in indented pipes due to the internal pressure variations are in the elastic range for practical pressures. Semi-empirical formulations for predicting the stress variations and the dent depth changes due to internal pressure fluctuations were developed. A very close correlation was obtained between the results obtained from the FE analyses and the predictions based on semi-empirical formulations.

Chapter 13
Conclusions & Future Work

13.1 Conclusions

Experimental tests, analytical solutions and FE analyses were performed on pressurised and unpressurised pipes subjected to external indentations in order to investigate the fatigue damage induced. With applications of Castiglano's theorem and the elastic-plastic energy-based method to indented rings with or without pressure, the limit loads and the relationship between the indenter force and dent depth were investigated and predicted analytically. Analytical solutions of the limit loads and the indenter force versus dent depth curves were obtained and validated for a variety of geometrical dimensions, material properties, boundary conditions and external loads by comparing with both the experimental results and the FE solutions.

Residual stresses and stress variations due to the internal pressure fluctuations in the indented rings were investigated using the FE analysis where 8-node, plane strain, reduced integration elements were used. The maximum residual hoop stresses are found to occur at a position beneath the indenter on the outer surface of rings. An internal pressure and a residual dent depth were found to have a significant impact on the magnitude of the residual hoop stresses, and increasing the indenter pressure and residual dent depth results in the large residual stresses. Decreasing the indenter radius was also found to have positive effects but not as seriously as the internal pressure or the residual dent depth. The support angular position,θ, and the D/t ratio are two further factors influencing the residual hoop stresses. Increasing the range of θ reduces the residual hoop stress value while reducing the D/t ratio results in a relatively small value of the residual hoop stresses.

Residual hoop stress variations due to the internal pressure fluctuations were investigated using the FE analyses and analytical methods. Using the FE solutions and curve fitting techniques, a semi-empirical formulation was developed to predict the hoop stress variations. It can be seen that increasing the residual dent depth increases the hoop stress variation and increasing the wall thickness reduces the hoop stress variation.

The indenter force-deflection relationship was investigated using experimental tests, performed on the 6082-T6 aluminium alloy tubes with or without pressure, and FE analyses

where both 3D brick and shell elements were used. Results obtained from these analyses show that a shell element model can give reasonably accurate predictions of the indenter force-deflection relationship, the residual stresses and the stress variations. Subsequent investigations of the sensitivity of residual stresses to element sizes indicate that using a shell element model is valid and can save a lot computer time when compared to a 3D brick element model.

For a constant internal pressure, the residual stress solutions of indented pipes were investigated using FE analyses where shell element models with reasonable fine meshes in the indented regions were used. Parametric analyses were carried out for a variety of internal pressures, D/t ratios, indenter sizes, material properties and residual dent depths. Based on the results obtained from the parametric analyses and referring to the uniaxial true stress-strain empirical formulations in appendix 5.A, empirical formulations predicting residual stresses were therefore developed. Using these empirical formulations it is possible to predict the residual stresses for other indented pipes without performing any further FE analyses in order to assess the subsequent fatigue damage.

For the internal pressure changes after an indentation, the subsequent stress variations were investigated using elastic and elastic-plastic models and FE analysis where shell element models were used. Results show that the stresses respond elastically to the internal pressure fluctuations. Semi-empirical formulations were developed based on parametrical analyses and the analytical solution obtained for indented rings, see chapter 8. These semi-empirical formulations are able to explain the effects of the pipe wall thickness, the indenter size and residual dent depth on the normalised stress variations and can give accurate predictions. The response of the residual dent depth to the internal pressure was also investigated using FE analyses and was predicted using empirical formulations. Therefore, the residual dent depth at the time at which the indenter is removed can be assessed from the measured dent depth at any time after the indentation whether the internal pressure fluctuates or remains constant. For the practical range of pipe parameter used in this work, the fatigue life of an indented pipe therefore can be assessed by calculating the residual stresses and stress variations using the empirical and semi-empirical formulations obtained in this thesis without performing any further FE analyses.

Therefore, use of the results obtained in this thesis and S-N curves can predict the fatigue life of the indented pipes.

13.2 Future Work

Future work can focus on fatigue experimental tests, residual stress analysis for asymmetrical indentations and the analysis of crack development in a dented pipe.

Fatigue experimental tests can be performed to provide enough information to develop formulations to predict the remaining life of dented pipes, based on the results of the present work.

Also based on the present work, shell element models can be used to calculate the residual stresses and stress range distributions for different indentation positions to form a database or to develop new semi-empirical formulae. The work is limited to 2D symmetrical and asymmetrical loading, and 3D symmetrical loading. Future work can include unsymmetrical (offset) 3D loading.

The residual stress and stress range distributions may be calculated also by using an inverse method. If the residual deformation of the dented pipe is measured, the strain distribution can be analytically or semi-analytically calculated based on the non-linear relationship of the strain and displacement. Therefore, the stress may be finally calculated from the uniaxial stress-strain relationship and the strain value obtained before. However, this method may not be efficient.

The crack development research can mainly focus on thick-wall pipes. A microcrack on the outer surface of the dented pipe can develop due to low cycle fatigue damage accumulations. It may develop into a through-crack under the action of section bending moments and membrane forces resulting from the internal pressure and the residual stress concentration in the indented region. In this case, the remaining life of the pipe is short and repair processes have to be performed immediately. For thick-wall pipes, especially as the indented deformation is relatively small, the residual stress concentration and bending moment are small, making the formation of a through-crack less detrimental. Due to the complex geometry, FE modelling will be the main analysis method rather than the analytical LEFM approach. However, some analytical solutions are likely to be obtained. Residual stress concentrations are the main causes of crack initiations and they still are the main causes of crack developments in the indented region after a microcrack forms because these concentrations increase the bending moments. The relationship of the stress intensity factor, crack geometry, residual dent depth and internal pressure can be established through a parametric analysis. Use of this stress intensity factor formulation and Paris or Forman relationship can predict the remaining life of the indented pipe after a crack forms.

References

1. Fatemi A. and Yang L., "Cumulative Fatigue Damage and Life Prediction Theories: A survey of the State of the Art for Homogeneous Materials", International Journal of Fatigue, Vol. 20, No. 1, 1998, pp9-34.
2. Tam C.K.W & Croll J.G.A, "Elastic Stress Concentrations in Cylindrical Shells Containing Local Damage", Applied Solid Mechanics -2, Ed.A.S. Tooth and J.Spencer, Elsevier Appl. Sci. Pub, 1988, pp.155-177.
3. Tam C.K.W & Croll J.G.A, "Stress Concentrations in Circular Tubulars Local Damage", Journal of Offshore Mech. and Arctic Eng., Trans. ASME., Vol.111, 1989, pp.278-284.
4. Tam C.K.W & Croll J.G.A., "Stresses in damaged Circular Cylinder Shells",Applied Stress Analysis, Ed. T.H.Hyde, E. Ollerton, Elsevier Science Publisher LTD, 1990, p.386-397.
5. Godoy Luis A., "A Perturbation Formulation for Sensitivity and Imperfection Analysis of Thin-Walled Structures", Latin American Applied Research 20, 1990, p.147-153.
6. Godoy Luis A., "Finite Element/Perturbation Analysis of Plates and Shells with Geometric Damage Using a Symblic Manipulator", International Journal of Pressure Vessels and Piping, Vol.73, 1997, p.249-257.
7. Flores Fernando G. & Godoy Luis A., "Linear Versus Nonlinear Analysis of Imperfect Spherical Pressure Vessels", International Journal of Pressure Vessels and Piping, Vol.33, 1988, p.95-109.
8. Ohtani Y., Koguchi H. & Yada T., ".Nonlinear Stress Analysis for Thin Spherical Vessels with Local Non-axisymmetric Imperfections", International Journal of Pressure Vessels and Piping, Vol.45, 1991, p.289-299.
9. Fowler, J. R.; Alexander, C.R.;Kovach,P.J.;Connelly,L.M., ".Fatigue Life of Pipes With Dents and Gouges Subjected to Cyclic Internal Pressure",American Society of Mechanical Engineers,Petroleum Division (Publication) PD, Vol. 69, 1995, p.17-35.
10. ZAREA Mures F., PHILIBERT Christian E. & Isabelle DEO, "Numerical models for static denting and dynamic puncture of gas transmission linepipe and their validation", International Pipe Conference--Vol. 2 ASME 1996.
11. Hart James D., Powell Graham H., Maple James A., Stevick Glen R., and Norton J. David, ".Fatigue Damage Calculations for a Dented and Ovalled section of the

Transalaska Pipe System at Thompson Pass", International Pipe Conference, Vol. 1, pp.263-278, ASME 1998.

12. Alexander C. R., "Analysis of dented pipes considering constrained and unconstrained dent configurations", Energy Sources and Technology conference & Exhibition, ASME, ETCE99-6686, 1999.
13. Corder I., British Gag & Chaptain P., Gaz de France, "EPRG recommendations for the assessment of the resistance of pipes to external damage", AGA/EPRG Seminar, England, 1995.
14. Kiefner, J. F.; Alexander, C.R.; and Fowler, J.R., 1996, "Repair of Dents Containing Minor Scratches", 9th Symposium on Pipe Research, PRC Internatioal, American Gas Association, paper 5, p.1-21.
15. Hagiara,N.; Meziere,Y.; Oguchi,N.; Zarea, M.; and Chanpavere,R., ".Study on the Fatigue of Steel Pipes Containing Idealized Flaws Under Fluctuating Pressures", Proceedings of International Gas Research Conference (IGRC 98), San diego, CA, Vol. 2, p. 13-24, 1998.
16. Lancaster,E.R.;Palmer,S.C.,"Strain Concentrations in Pressured Indented pipes", Proceedings of the Institution of Mechanical Engineers, Part E: Journal of Process Mechanical Engineering, Vol. 210, E1, 1996, p.29-38.
17. Lancaster,E.R.;Palmer,S.C.,"Burst Pressures of Pipes containing Dents and Gouges", Proceedings of the Institution of Mechanical Engineers, Part E: Journal of Process Mechanical Engineering, Vol. 210, E1, 1996, p.29-38.
18. Doglione,R.; Firrao,D., ".Structure Collapse Calculations of Old Pipes", International Journal of Fatigue, Vol.20, No.2, Feb., 1998, p. 161-168.
19. Calpham L., Mandal K., Sabet-Sharghi R., Atherton D.L. & Holden T., ".Variations in Stress Concentration factors Near Simulated Corrosion Pits as Monitored by Magnetic flux Leakage, Magnetic Barkhausen Noise and Neutron Diffraction", International Pipe Conference, Vol. 1, pp.505-512, ASME 1998.
20. Leis,B.N.;Francini,R.B.;Mohan,R.;Rudland,D.L.;Olson,R.J.,"Pressure-Displacement Behavior of Transmission Pipes Under Outside Forces-Towards a Serviceability Criterion for Mechanical Damage", Proceedings of the International Offshore and Polar Engieering Conference, Vol. 2, 1998, p.60-67.
21. Roosenfeld Michael J. & Kiefner P.E., ".Investigations of Dent Reounding Behavior", International Pipe Conference, Vol. 1, ASME, 1998.

22. Rosenfeld Michael J.,"Investigation of Dent Rerounding Behavior", Proceedings of the International Pipe Conference, IPC,Vol. 1, 1998,p.291-304.
23. King P. J., Becker A. A. and Mihsein M. J. A., "Non-Linear Finite Element Analysis of Indented Pressured Pipes", Proceedings of the NAFEMS World Congress on Effective Engineering Analysis, pp. 167-178, NAFEMS, Glasgow, 1999.
24. Ong,L.S.;Soh,A.K.;Ong,J.H., ".Experimental and Finite Element Investigation of a Local Dent On a Pressured Pipe",Journal of Strain Analysis for Engineering Design, Vol. 27, No.3, 1992, p.177-185.
25. Hagiwara N. & Oguchi N., "Fatigue Behavior of Line Pipes Subjected to Severe Mechanical Damage", Journal of Pressure Vessel Technology,Vol. 121, pp. 369-374, Transactions of ASME, Nov., 1999.
26. ABAQUS, Version 5.5, Hibbitt, Karlsson and Sorenson, Inc., 1998
27. Bai Y & Song R, "Fracture assessment of indented pipes with cracks and reliability-based calibration of safety factor", Int. J. Pres. Ves. & Piping 74 (1997) 221-229.
28. Wilmott M. J. & Sutherby R. L., ".The role of Pressure Fluctuations in the Growth of Stress Corrosion Cracks in Line Pipe Steels", International Pipe Conference, Vol. 1, pp.409-422, ASME 1998.
29. Eiber R J., Leis B N. and Battelle, "Line pipe resistance to outside force", AGA/EPRG Seminar, England, 1995.
30. Kannappan, S, "Structure Integrity of Offshore Pipe", American Society of Mechanical Engineers, Petrolelum Division (publication), PD, 1998.
31. Specification for Line Pipe, API Specification 5L, Forty-First Edition, April 1, 1995.
32. Miller A.G.,"Review of Limit Loads of Structures Containing Defects" International Journal of Pressure Vessels and Piping, Vol.32, 1988, p.197-327.
33. Newman J. C., Raju I. S., "Stress-Intensity Factors for Internal Surface Cracks in Cylindrical Pressure Vessels", Journal of Pressure Vessel Technology, 342/Vol. 102, November 1980.
34. Koh Seung-Kee & Na Eui-Gyun, "Fatigue crack growth life of thick-walled cylinders with an external radial crack", Internal journal of Fatigue , 21 (1999), 135-146.
35. Raju I.S. and Newman J.C., "Stress-Intensity Factors for Circumferential Surface Cracks in Pipes and Rods under Tension and Bending Loads", Fracture Mechanics: Vol. 17, ASTM STP 905 1986, pp 789-805.

36. Zheng X.J., Kiciack A., and Glinka G., ".Weight Functions and Stress intensity Factors for Internal Surface Semi-elliptical Crack in Thick-walled Cylinders",Engineering Fracture Mechanics, Vol.58, No. 3, 1997, p.207-211.
37. Zarrabi, K., ".Plastic Colapse Pressure For Defected Cylindrical Vessels", Internal tional Journal of Pressure Vessels and Piping, Vol. 60, No. 1, 1994, p.65.-69.
38. Suresh S., "Fatigue of Materials", Cambridge University Press, 1998.
39. Paris P. & Erdogan F., 'A Critical Analysis of Crack Propagation Laws', Transaction of the ASME, Journal of Basic Engineering, p. 528-534, Dec., 1963.
40. Forman R. G., Kearney V.E. & Engle R. M., 'Numerical Analysis of Crack Propagation in Cyclic-Load Structures', Transaction of the ASME, Journal of Basic Engineering, Sept., 1967, P. 459 - 464.
41. Hibbeler, R. C. Mechanics of Materials, 4th ed. Upper Saddle River, N.J.; London: Prentice Hall.
42. Chen W.F., Han D.J., "Plasticity for Structural Engineers", Springer-Verlag Berlin Heidelberg New York, 1988.
43. Neal, B. G. 1963, The Plastic Methods of Structure Analysis, 2nd Ed, Chapman and Hall, London.
44. Becker A. A., " Background to Finite Element Analysis of Geometric Non-linearity Benchmarks ", NAFEMS, the International Association for the Engineering Analysis Community, 1999.
45. Hyde T. H., Luo R. and Becker A. A., "Finite Element Analysis of Indented Pipes Using Three-dimensional Solid and Shell elements", IGRC-2001 proceeding, Amsterdan, Netherlands, 2001.
46. Shannon, R.W.E. The failure behaviour of line pipe defects, *Int. J. Pressure Vessels & Piping*, 2, 243-255, 1974.
47. Fearnhough, G.D. and Jones, D.G., An approach to defect tolerance in pipelines, Conference on Tolerance of Flaws in Pressurised Components, I. Mech.E., London, 1978.
48. Ainsworth, R.A. The assessment of defects in structures of strain hardening material, *Eng. Fracture Mechanics*, 19, 633-642, 1984.
49. Omidvar B., Wnuk M. P. and Choroszynski M., "Relationship between the COD and J-Integral for Stationary and Growing Cracks. Closed-Form Solutions", International Journal of Fracture 87: 1997, P. 331-334.

50. Timings R. L., "Engineering Materials", p. 290, Second Edition, Volume One, Addison Wesley Longman Limited, Edinburgh.

Appendices

Appendix 1.A. Analytical Formulations in Pressurised Rings with Symmetrical Supports

1.A.1.Kinematic Analysis

A kinematic field of an indented ring is shown in Fig. (1.a1). It is assumed that the relative angular rotations of the plastic hinges at positions D and F are α_1 and α_2, respectively, that the vertical displacement at plastic hinge A is δ and that half of the angular rotation at A is α_3. Hence, compatibility of deformations gives

$$\cos(\theta_0+\alpha_2-\alpha_1)+\sin(\alpha_2-\alpha_1)+\cos(\theta+\alpha_1)-\cos(\theta_0-\alpha_1)-\cos\theta=0 \qquad (1.a1)$$

$$\delta=R[1+\sin(\theta_0+\alpha_2-\alpha_1)-\cos(\alpha_2-\alpha_1)-\sin(\theta+\alpha_1)-\sin(\theta_0-\alpha_1)+\sin\theta]=R\delta_0 \qquad (1.a2)$$

$$\alpha_3=\alpha_2-\alpha_1 \qquad (1.a3)$$

where δ_0 is the non-dimensional displacement at position, A, obtained by dividing δ by R., i.e., $\delta_0=\delta/R$.

The position, θ_0, of the plastic hinge at F, after large deformation, is assumed to stay in the same position as its initial position when the deformation is small. The position, θ_0, is therefore given by in chapter 3

$$\theta_0=\frac{\pi}{4}-\frac{\theta}{2} \qquad (1.a4)$$

Hence, from equations (1.a1) to (1.a4), it can be seen that

$$\alpha_2=\frac{\pi}{4}-\frac{\theta_0}{2}+\alpha_1-\cos^{-1}\left[\frac{\cos(\theta_0-\alpha_1)-\cos(\theta+\alpha_1)+\cos\theta}{2\sin\left(\frac{\pi}{4}-\frac{\theta_0}{2}\right)}\right] \qquad (1.a5).$$

Therefore, δ (δ_0), α_2 and α_3 can all be related to α_1 and the support angle, θ.

Taking α_{1max} to be the value of α_1 when the hinges at F, A and E are in line (beyond this, equation (2.a5) is no longer valid) and α_{2max} is the value of the α_2 when α_{1max} occurs, then

$$\alpha_{1max}=\tfrac{1}{8}\pi-\tfrac{3}{4}\theta-\sin^{-1}\left[1-\frac{\cos\theta}{2\sin\left(\frac{\pi}{8}+\frac{\theta}{4}\right)}\right]=\tfrac{5}{8}\pi-\tfrac{3}{4}\theta-\cos^{-1}\left[1-\frac{\cos\theta}{2\sin\left(\frac{\pi}{8}+\frac{\theta}{4}\right)}\right] \qquad (1.a6)$$

and

$$\alpha_{2\max} = \frac{\pi}{8} + \frac{\theta}{4} + \alpha_{1\max} \tag{1.a7}$$

where equation (1.a6) can also be obtained by assuming the fourth term of the right side of the equation (1.a5) to be zero.

Denoting δ_{max} as the value of δ when α_{1max} and α_{2max} occur, gives

$$\delta_{\max} = R\left[1 + \sin\theta - 2\sin\left(\frac{\pi}{8} + \frac{\theta}{4}\right)\sin\left(\frac{5}{8}\pi - \frac{3}{4}\theta - \alpha_{1\max}\right)\right] \tag{1.a8}.$$

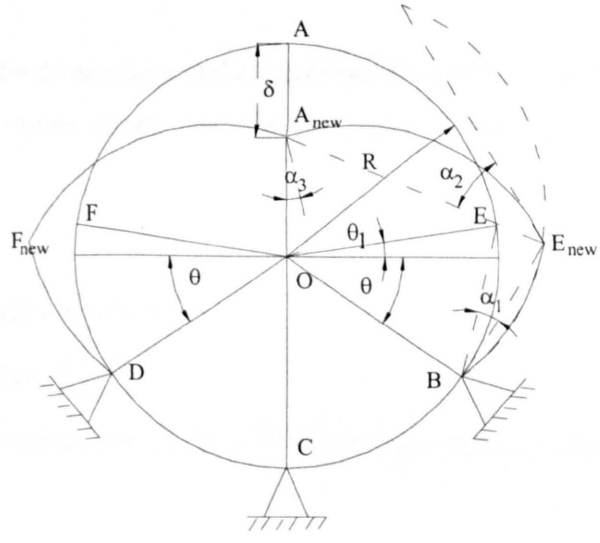

Fig. (1.a1) Kinematic field for an indented ring

1.A. 2. Elastic Energy Stored

For an unpressurised ring, five elastic hinges are assumed to exist at positions D, F, A, E and C in Fig. (1.a1) and a spring constant, K, is also assumed for each elastic hinge. Hence, the elastic energy, W_{IE}, stored by all of the five hinges is given by

$$W_{IE} = \frac{K}{2}\left[2(\alpha_1)^2 + 2(\alpha_2)^2 + (2\alpha_3)^2\right] \tag{1.a9}$$

It was shown that from in chapter 3 that if the small deformation relationship between force and deflection, for an unpresssurised ring, is obtained, using Castiglano's method, then

$$F = \frac{Et^3}{12R^3}\left(\frac{D}{AD+B+C}\right)\delta \tag{1.a10}$$

where A, B, C and D are functions of the support angle θ, defined as follows:

$$\left.\begin{aligned} A &= \frac{1}{4}\left(\frac{\pi}{2}+\theta+\frac{1}{2}\sin 2\theta\right) \\ B &= (1+\sin\theta)\left[\frac{3}{2}\sin 2\theta+3\cos\theta-\left(\frac{\pi}{2}+\theta\right)(\cos^2\theta+\sin\theta+1)\right] \\ C &= \cos\theta\left(\frac{1}{2}+\frac{1}{2}\sin^2\theta+\sin\theta\right)\left[\left(\frac{\pi}{2}+\theta\right)\cos\theta-2\sin\theta-2\right] \\ D &= 2\left(\left(\frac{\pi}{2}+\theta\right)^2-2\cos^2\theta-\frac{1}{2}\left(\frac{\pi}{2}+\theta\right)\sin 2\theta\right) \end{aligned}\right\} \quad (1.a11)$$

Hence, for the small deformations the overall "stiffness", K_e, is given by

$$K_e = \frac{Et^3}{12R^3}\left(\frac{D}{AD+B+C}\right) \quad (1.a12)$$

which is only related to the dimensions and support position of the ring and Young's modulus.

The elastic energy stored in the five elastic hinges in the ring, for small deformation, is therefore also given by

$$W_{IE} = \frac{K_e}{2}\delta^2 \quad (1.a13).$$

Equating equation (a13) to (a9) gives

$$W_{IE} = \frac{K}{2}\left[2(\alpha_1)^2+2(\alpha_2)^2+(2\alpha_3)^2\right] = \frac{K_e}{2}\delta^2 \quad (1.a14)$$

Hence, the spring constant (or 'stiffness'), K, for each elastic hinge can be determined and given by

$$K = \lim_{\alpha_1 \to 0} \frac{K_e\delta^2}{(2\alpha_1)^2+2(\alpha_2)^2+(2\alpha_3)^2} \quad (1.a15).$$

For a pressurised ring, the internal pressure does not change the spring constant, K, therefore, the elastic energy stored at the five hinges for small deformations is also given by equation (1.a9), irrespective of the existence of pressure. Hence, it can be seen that from equation (1.a14) the elastic energy stored in the ring can be expressed by equation (1.a13) for pressurised or unpressurised rings.

1.A. 3. Plastic Work Dissipated

The internal energy dissipation in the plastic hinges is the sum of work done by the fully plastic bending moment at the hinges. Based on the rigid plastic deformation assumption and equation (1.a3), the internal energy dissipation, W_I, at the five plastic hinges, per unit axial length, is given by

$$W_I = 2(M_0\alpha_1 + M_0\alpha_2 + M_0\alpha_3) = 4M_0\alpha_2 \qquad (1.a16)$$

where M_0, the plastic bending moment, is given by

$$M_0 = \frac{\sigma_y t^2}{4} \qquad (1.a17).$$

1.A. 4. Work Done by Internal Pressure

Since the dented ring undergoes non-linear large deformations, the expressions for the work done by the internal pressure are complicated because the direction of internal pressure is normal to the deformed ring and hence changes during deformation. Therefore, differential-integration techniques were used to calculate the sum of the work done by the internal pressure for each small increment of deformation.

When the rigid arcs BE and DF in Fig. (1.a1) rotate with respect to the plastic hinge B and D, respectively, by an angle α_1, the work done, W_p^1, by the internal pressure p, is given by

$$W_p^1 = 2\alpha_1 pR^2(1-\cos(\theta+\theta_0)) \qquad (1.a18).$$

However, when the rigid arcs EA and FA move to the new positions of $E_{new}A_{new}$ and $F_{new}A_{new}$, respectively, in Fig. (1.a1), which are functions of the rotational angles α_1 and α_2, for a small increment $d\alpha_1$, the work done, dW_p^2, by the internal pressure p, is given by

$$dW_p^2 = 2pR^2\left\{-(1-\sin\theta)\left(\frac{d\alpha_2}{d\alpha_1}-1\right)+[\sin(\theta-\alpha_2)+\sin(\theta_0+\alpha_2)+\cos(\theta+\theta_0+\alpha_2)-\cos\alpha_2]\right\}d\alpha_1 \qquad (1.a19).$$

Therefore, when the rigid arcs EA and FA move to the new positions of $E_{new}A_{new}$ and $F_{new}A_{new}$, respectively, the work done, W_p^2, by the internal pressure, is given by

$$W_p^2 = 2pR^2\int_0^{\alpha_1}\left\{-(1-\sin\theta)\left(\frac{d\alpha_2}{d\alpha_1}-1\right)+[\sin(\theta-\alpha_2)+\sin(\theta_0+\alpha_2)+\cos(\theta+\theta_0+\alpha_2)-\cos\alpha_2]\right\}d\alpha_1 \qquad (1.a20).$$

Hence, for the given kinematic mechanism shown in Fig. (1.a1), the total work done, W_p, by the internal pressure p during the deformation is given by

$$W_p = W_p^1 + W_p^2 \qquad (1.a21)$$

Appendix 2.A.1: Details of FE Analyses in Chapter 5

Table A1: Ring dimensions, loading and support positions, and limit load solutions obtained from the FE analyses for 6082-T6 aluminium alloy

FE No.	D/t	θ_1	θ_2	θ_5	F_{limit} N/mm
FE1	80.0	0°	35°	55°	15.5
FE2	41.6	0°	35°	55°	69.5
FE3	24.0	0°	35°	55°	225

Table A2: Ring dimensions, loading and support positions, and limit load solutions obtained from the FE analyses for the idealised material (ideal-A) and for X65 SAW, for D/t=72.

D/t	θ_1	θ_2	θ_5	Idealised –A Results		X65 SAW Results	
				FE No.	F_{limit} N/mm	FE No	F_{limit} N/mm
72.0	0°	45°	45°	FE4	12.7	FE115	24.2
72.0	10°	45°	45°	FE5	12.7	FE116	24.4
72.0	20°	45°	45°	FE6	12.9	FE117	25.0
72.0	30°	45°	45°	FE7	13.9	FE118	26.2
72.0	40°	45°	45°	FE8	15.1	FE119	28.6
72.0	50°	45°	45°	FE9	17.3	FE120	32.7
72.0	60°	45°	45°	FE10	20	FE121	38.2
72.0	20°	45°	0°	FE11	20.8	FE122	39.5
72.0	20°	45°	10°	FE12	18.3	FE123	34.5
72.0	20°	45°	20°	FE13	16.4	FE124	30.9
72.0	20°	45°	30°	FE14	14.8	FE125	28.2
72.0	20°	45°	40°	FE15	13.5	FE126	26.0
72.0	20°	45°	50°	FE16	12.8	FE127	24.1
72.0	20°	45°	60°	FE17	11.7	FE128	22.5
72.0	20°	45°	70°	FE18	11	FE129	21.2
72.0	20°	45°	80°	FE19	10.3	FE130	19.8
72.0	20°	45°	90°	FE20	9.35	FE131	17.9
72.0	20°	0°	45°	FE21	13.8	FE132	26.8
72.0	20°	10°	45°	FE22	13.6	FE133	26.5
72.0	20°	20°	45°	FE23	13.4	FE134	26.1
72.0	20°	30°	45°	FE24	13.2	FE135	25.5
72.0	20°	40°	45°	FE25	13.0	FE136	25.3
72.0	20°	50°	45°	FE26	12.8	FE137	24.8
72.0	20°	60°	45°	FE27	12.6	FE138	24.3
72.0	20°	70°	45°	FE28	12.4	FE139	23.9
72.0	20°	80°	45°	FE29	12.2	FE140	23.4
72.0	20°	90°	45°	FE30	11.7	FE141	22.4
72.0	0°	0°	45°	FE31	15.0	FE142	29.8
72.0	0°	10°	45°	FE32	14.5	FE143	28.3
72.0	0°	20°	45°	FE33	13.9	FE144	27.0
72.0	0°	30°	45°	FE34	13.5	FE145	25.8
72.0	0°	40°	45°	FE35	13	FE146	24.7

72.0	0°	50°	45°	FE36	12.4	FE147	23.7
72.0	0°	60°	45°	FE37	12.0	FE148	22.8
72.0	0°	70°	45°	FE38	11.7	FE149	22.0
72.0	0°	80°	45°	FE39	11.2	FE150	21.2
72.0	0°	90°	45°	FE40	10.4	FE151	19.9

Table A3: Ring dimensions, loading and support positions, and limit load solutions obtained from the FE analyses for the idealised material (ideal-A) and for X65 SAW, for D/t=42.6.

D/t	θ_1	θ_2	θ_5	Ideal –A Results		X65 SAW Results	
				FE No.	F_{limit} N/mm	FE No	F_{limit} N/mm
42.6	0°	45°	45°	FE41	63	FE152	119
42.6	10°	45°	45°	FE42	63.5	FE153	120.
42.6	20°	45°	45°	FE43	65	FE154	125
42.6	30°	45°	45°	FE44	69	FE155	133.
42.6	40°	45°	45°	FE45	76.5	FE156	145.
42.6	50°	45°	45°	FE46	89	FE157	166
42.6	60°	45°	45°	FE47	107	FE158	199.
42.6	20°	45°	0°	FE48	106	FE159	202
42.6	20°	45°	10°	FE49	92	FE160	176
42.6	20°	45°	20°	FE50	81.5	FE161	157
42.6	20°	45°	30°	FE51	73.5	FE162	142
42.6	20°	45°	40°	FE52	67.5	FE163	130
42.6	20°	45°	50°	FE53	63	FE164	120.
42.6	20°	45°	60°	FE54	59	FE165	112.
42.6	20°	45°	70°	FE55	55.5	FE166	105
42.6	20°	45°	80°	FE56	52	FE167	98
42.6	20°	45°	90°	FE57	46.8	FE168	88
42.6	20°	0°	45°	FE58	71	FE169	134.
42.6	20°	10°	45°	FE59	70	FE170	133
42.6	20°	20°	45°	FE60	68.5	FE171	130.
42.6	20°	30°	45°	FE61	67.5	FE172	128.
42.6	20°	40°	45°	FE62	66	FE173	126
42.6	20°	50°	45°	FE63	64.5	FE174	124
42.6	20°	60°	45°	FE64	63	FE175	121.
42.6	20°	70°	45°	FE65	62	FE176	119.
42.6	20°	80°	45°	FE66	61	FE177	117
42.6	20°	90°	45°	FE67	56.5	FE178	110.
42.6	0°	0°	45°	FE68	75.5	FE179	148.
42.6	0°	10°	45°	FE69	72.5	FE180	140.
42.6	0°	20°	45°	FE70	69.5	FE181	133.
42.6	0°	30°	45°	FE71	67	FE182	127
42.6	0°	40°	45°	FE72	64	FE183	121.
42.6	0°	50°	45°	FE73	62.5	FE184	116.
42.6	0°	60°	45°	FE74	59.5	FE185	112
42.6	0°	70°	45°	FE75	57.5	FE186	108
42.6	0°	80°	45°	FE76	55	FE187	104
42.6	0°	90°	45°	FE77	50.5	FE188	96

Table A4: Ring dimensions, loading and support positions and limit load solutions obtained from the FE analyses for the idealised material (ideal-A) and for X65 SAW, for D/t=30.8.

D/t	θ_1	θ_2	θ_5	Ideal –A Results		X65 SAW Results	
				FE No.	F_{limit} N/mm	FE No	F_{limit} N/mm
30.8	0°	45°	45°	FE78	90.5	FE189	170.
30.8	10°	45°	45°	FE79	91	FE190	177.
30.8	20°	45°	45°	FE80	92.5	FE191	179
30.8	30°	45°	45°	FE81	99	FE192	190.
30.8	40°	45°	45°	FE82	111	FE193	203.
30.8	50°	45°	45°	FE83	128.	FE194	237.
30.8	60°	45°	45°	FE84	152.	FE195	284
30.8	20°	45°	0°	FE85	153.	FE196	292
30.8	20°	45°	10°	FE86	133.	FE197	254.
30.8	20°	45°	20°	FE87	117	FE198	226
30.8	20°	45°	30°	FE88	104.	FE199	203.
30.8	20°	45°	40°	FE89	96	FE200	186
30.8	20°	45°	50°	FE90	89.5	FE201	172
30.8	20°	45°	60°	FE91	83.5	FE202	160
30.8	20°	45°	70°	FE92	78	FE203	149
30.8	20°	45°	80°	FE93	73	FE204	138.
30.8	20°	45°	90°	FE94	66.5	FE205	124.
30.8	20°	0°	45°	FE95	101	FE206	192
30.8	20°	10°	45°	FE96	99	FE207	189.
30.8	20°	20°	45°	FE97	97.5	FE208	186.
30.8	20°	30°	45°	FE98	95	FE209	183.
30.8	20°	40°	45°	FE99	93.5	FE210	180.
30.8	20°	50°	45°	FE100	91.5	FE211	177.
30.8	20°	60°	45°	FE101	90	FE212	174.
30.8	20°	70°	45°	FE102	88.5	FE213	171.
30.8	20°	80°	45°	FE103	86.5	FE214	167.
30.8	20°	90°	45°	FE104	81.5	FE215	157.
30.8	0°	0°	45°	FE105	109.	FE216	214
30.8	0°	10°	45°	FE106	104.	FE217	202
30.8	0°	20°	45°	FE107	100	FE218	191
30.8	0°	30°	45°	FE108	96	FE219	182
30.8	0°	40°	45°	FE109	92	FE220	174
30.8	0°	50°	45°	FE110	88.5	FE221	167
30.8	0°	60°	45°	FE111	85.5	FE222	160.
30.8	0°	70°	45°	FE112	82	FE223	154.
30.8	0°	80°	45°	FE113	78.5	FE224	148
30.8	0°	90°	45°	FE114	72	FE225	136.

Appendix 3.A. Analytical Formulations in Pressurised Rings with Asymmetrical Supports

3.A.1. Kinematic System

A kinematic field of an offset indented ring is shown in Fig. (3.a.1). If it is assumed that α_1, α_2, α_3, α_4 and α_5 are the angles of rotation of the plastic *hinges at positions* B, C, D, E and A, respectively, and the vertical displacement at plastic hinge A is denoted by δ, geometrical compatibility of the deformation gives

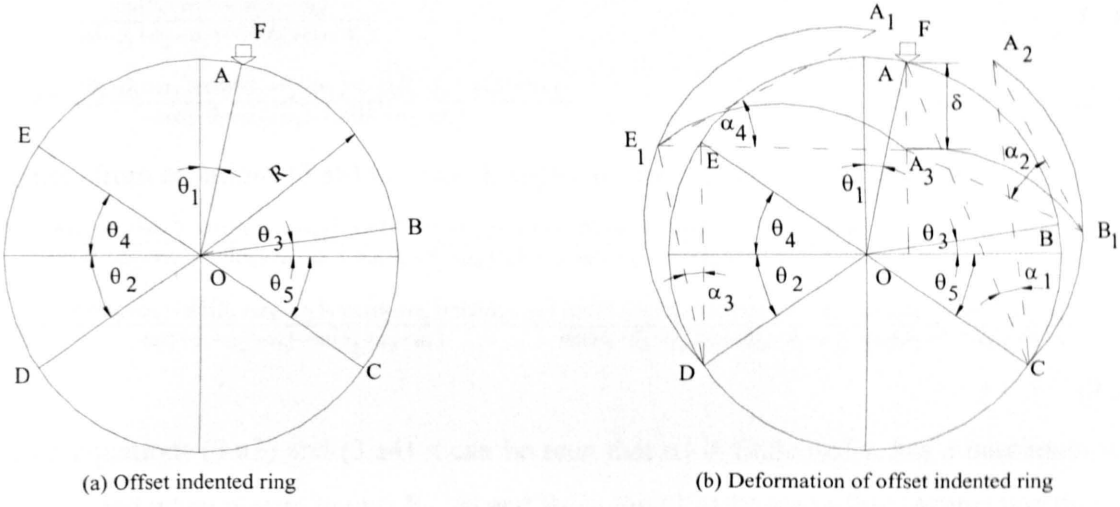

(a) Offset indented ring

(b) Deformation of offset indented ring

Fig. (3.a.1) Kinematically admissible displacements used for the force versus deflection analysis of an indented ring.

$$\cos(\theta_4+\alpha_4-\alpha_3)+\sin(\theta_1+\alpha_4-\alpha_3)+\cos(\theta_2+\alpha_3)-\cos(\theta_4-\alpha_3)-\cos\theta_2-\sin\theta_1=0 \tag{3.a1}$$

$$\delta=R[\cos\theta_1+\sin(\theta_4+\alpha_4-\alpha_3)-\cos(\theta_1+\alpha_4-\alpha_3)-\sin(\theta_2+\alpha_3)-\sin(\theta_4-\alpha_3)+\sin\theta_2] \tag{3.a2}$$

$$\cos(\theta_3+\alpha_2-\alpha_1)+\sin(-\theta_1+\alpha_2-\alpha_1)+\cos(\theta_5+\alpha_1)-\cos(\theta_3-\alpha_1)-\cos\theta_5+\sin\theta_1=0 \tag{3.a3}$$

$$\delta=R[\cos\theta_1+\sin(\theta_3+\alpha_2-\alpha_1)-\cos(-\theta_1+\alpha_2-\alpha_1)-\sin(\theta_5+\alpha_1)-\sin(\theta_3-\alpha_1)+\sin\theta_5] \tag{3.a4}$$

$$\alpha_5=\alpha_2+\alpha_4-\alpha_1-\alpha_3 \tag{3.a5}.$$

In equations (3.a1) to (3.a5), there are six unknown variables (α_1, α_2, α_3, α_4, α_5 and δ). Therefore, five of the six variables are not independent. The plastic hinge positions,θ_3 and θ_4, are given by

$$\theta_3=\frac{\pi}{4}-\frac{\theta_5+\theta_1}{2} \tag{3.a6}$$

$$\theta_4 = \frac{\pi}{4} - \frac{\theta_2 - \theta_1}{2} \tag{3.a7}$$

For large deformations, from equations (3.a1) to (3.a4), the relationships between the rotations of the plastic hinges and the vertical displacement are given by

$$\frac{d\alpha_4}{d\alpha_3} - 1 = \frac{\sin(\theta_2+\alpha_3)+\sin(\theta_4-\alpha_3)}{\cos(\theta_1+\alpha_4-\alpha_3)-\sin(\theta_4+\alpha_4-\alpha_3)} \tag{3.a8}$$

$$\frac{d\delta}{d\alpha_3} = R\frac{\sin(\theta_4+\theta_2+\alpha_4)+\cos(\theta_4-\theta_1-\alpha_4)-\cos(\theta_2+\theta_1+\alpha_4)-\sin\alpha_4}{\cos(\theta_1+\alpha_4-\alpha_3)-\sin(\theta_4+\alpha_4-\alpha_3)} \tag{3.a9}$$

and

$$\frac{d\alpha_2}{d\alpha_1} - 1 = \frac{\sin(\theta_5+\alpha_1)+\sin(\theta_3-\alpha_1)}{\cos(-\theta_1+\alpha_2-\alpha_1)-\sin(\theta_3+\alpha_2-\alpha_1)} \tag{3.a10}$$

$$\frac{d\delta}{d\alpha_1} = R\frac{\sin(\theta_3+\theta_5+\alpha_2)+\cos(\theta_3+\theta_1-\alpha_2)-\cos(\theta_5-\theta_1+\alpha_2)-\sin\alpha_2}{\cos(-\theta_1+\alpha_2-\alpha_1)-\sin(\theta_3+\alpha_2-\alpha_1)} \tag{3.a11}.$$

Hence, from equations (3.a8) to (3.a11), angles α_3 and α_4 can be expressed as

$$\frac{d\alpha_3}{d\alpha_1} = \frac{\cos(\theta_1+\alpha_4-\alpha_3)-\sin(\theta_4+\alpha_4-\alpha_3)}{\cos(-\theta_1+\alpha_2-\alpha_1)-\sin(\theta_3+\alpha_2-\alpha_1)}\frac{\sin(\theta_3+\theta_5+\alpha_2)+\cos(\theta_3+\theta_1-\alpha_2)-\cos(\theta_5-\theta_1+\alpha_2)-\sin\alpha_2}{\sin(\theta_4+\theta_2+\alpha_4)+\cos(\theta_4-\theta_1-\alpha_4)-\cos(\theta_2+\theta_1+\alpha_4)-\sin\alpha_4} \tag{3.a12}$$

$$\frac{d\alpha_4}{d\alpha_1} = \frac{\cos(\theta_1+\alpha_4-\alpha_3)-\sin(\theta_4+\alpha_4-\alpha_3)+\sin(\theta_2+\alpha_3)+\sin(\theta_4-\alpha_3)}{\cos(-\theta_1+\alpha_2-\alpha_1)-\sin(\theta_3+\alpha_2-\alpha_1)}\frac{\sin(\theta_3+\theta_5+\alpha_2)+\cos(\theta_3+\theta_1-\alpha_2)-\cos(\theta_5-\theta_1+\alpha_2)-\sin\alpha_2}{\sin(\theta_4+\theta_2+\alpha_4)+\cos(\theta_4-\theta_1-\alpha_4)-\cos(\theta_2+\theta_1+\alpha_4)-\sin\alpha_4}$$

(3.a13).

From equations (3.a3) and (3.a4) it can be seen that α_1 is finite and it has a maximum value, α_{1max}, obtained when plastic hinges E_1, A_3 and B_1 in Fig.(3.a1.b) are in line. At this position α_{1max} is given by

$$\alpha_{1\max} = \frac{5}{8}\pi - \frac{3}{4}\theta_5 - \frac{1}{4}\theta_1 - \cos^{-1}\left[1 - \frac{\cos\theta_5 - \sin\theta_1}{2\sin\left(\frac{\pi}{8}+\frac{\theta_5-\theta_1}{4}\right)}\right] \tag{3.a14}.$$

Similarly, the maximum value of α_2, i.e. α_{2max}, and the maximum vertical displacement, δ_{max}, of position A, are given by

$$\alpha_{2\max} = \frac{\pi}{8} + \frac{\theta_5+2\theta_1}{4} + \alpha_{1\max} \tag{3.a15}$$

and

$$\delta_{\max} = R\left[\cos\frac{3}{4}\theta_1 + \sin\theta_5 - 2\sin\left(\frac{\pi}{8}+\frac{\theta_5-\theta_1}{4}\right)\sin\left(\frac{5}{8}\pi - \frac{3\theta_5+\theta_1}{4} - \alpha_{1\max}\right)\right] \tag{3.a16}.$$

The differential equation set consisting of equations (3.a8) to (3.a13) does not have a valid solution beyond those maximum values defined by equations (3.a14) to (3.a16). Beyond this position, the geometrical compatibility equations are not valid. However, when δ_{max} is reached,

the deformations are generally very large and therefore predictions for higher values of δ would be of little practical interests.

3.A.2. Internal Energy Dissipation and Work Done by Pressure

Based on a rigid-plastic assumption of the deformation of the dented ring, the internal energy dissipation, W_I, is the total work done by the bending moment at the five plastic hinges and is given by

$$W_I = M_0(\alpha_1 + \alpha_2 + \alpha_3 + \alpha_4 + \alpha_5) = 2M_0(\alpha_2 + \alpha_4) \tag{3.a17}$$

where M_0 is the fully plastic bending moment per unit length and is given by

$$M_0 = \frac{\sigma_y t^2}{4} \tag{3.a18}.$$

Since the indented ring undergoes non-linear, large deformation, the analysis of the work done by the internal pressure is complicated. The internal pressure acts in a direction normal to the inner surface of the rigid arcs, DE_1, E_1A_3, A_3B_1 and B_1C (see. Fig.3.a1.b) during deformation. Hence the work done, W_P, by the internal pressure is obtained by summing all of the increments of work during deformation, using an integration technique. In this way the work done, W_P, by the internal pressure, is given by

$$W_p = \left(W_p^L + W_p^R\right) pR^2 \tag{3.a19}$$

where W_P^L and W_P^R can be determined from

$$\frac{dW_p^L}{d\alpha_3} = \left\{1 - \cos(\theta_4 + \theta_2) - (1 - \sin(\theta_4 - \theta_1))\left(\frac{d\alpha_4}{d\alpha_3} - 1\right) + \begin{bmatrix}\sin(\theta_4 - \alpha_4 - \theta_1) + \\ \sin(\theta_2 + \alpha_4 + \theta_1) + \cos(\theta_2 + \theta_4 + \alpha_4) - \cos\alpha_4\end{bmatrix}\right\} \tag{3.a20}$$

and

$$\frac{dW_p^R}{d\alpha_1} = \left\{1 - \cos(\theta_3 + \theta_5) - (1 - \sin(\theta_3 + \theta_1))\left(\frac{d\alpha_2}{d\alpha_1} - 1\right) + \begin{bmatrix}\sin(\theta_3 - \alpha_2 + \theta_1) + \\ \sin(\theta_5 + \alpha_2 - \theta_1) + \cos(\theta_5 + \theta_3 + \alpha_2) - \cos\alpha_2\end{bmatrix}\right\} \tag{3.a21}.$$

W_p^L and W_p^R are the work done by the internal pressure when the rigid arcs DE and EA, and CB and BA, in Fig. (3.a.1. b), move to the new positions of DE_1 and E_1A_3, and CB_1 and B_1A_3, respectively.

3.A.3. Indenter Force

Since the deformation is non-linear and the displacement, δ, is a function of the angle of rotation α_1 (see equation (3.a11)), then W_E can be expressed as

$$W_E = \int_0^{\alpha_1} F \frac{d\delta}{d\alpha_1} d\alpha_1 \qquad (3.a22).$$

Using the conservation of energy concept, and equations (3.a17), (3.a19) and (3.a22), gives

$$\int_0^{\alpha_1} F \frac{d\delta}{d\alpha_1} d\alpha_1 + \left(W_p^L + W_p^R\right) pR^2 = 2M_0(\alpha_2 + \alpha_4) \qquad (3.a23).$$

Differentiating both sides of equation (6.15) with respect to α_1, gives

$$F \frac{d\delta}{d\alpha_1} + \left(\frac{dW_p^L}{d\alpha_1} + \frac{dW_p^R}{d\alpha 1}\right) pR^2 = 2M_0\left(\frac{d\alpha_2}{d\alpha_1} + \frac{d\alpha_4}{d\alpha_1}\right) \qquad (3.a24).$$

Therefore, from equation (3.a24), the indenter force, F, is given by

$$F = \left[2M_0\left(\frac{d\alpha_2}{d\alpha_1} + \frac{d\alpha_4}{d\alpha_1}\right) - \left(\frac{dW_p^L}{d\alpha_3}\frac{d\alpha_3}{d\alpha_1} + \frac{dW_p^R}{d\alpha_1}\right) pR^2\right] \frac{d\alpha_1}{d\delta} \qquad (3.a25).$$

For convenience, two non-dimensional coefficients, F^M and F^P, are defined by

$$F^M = \frac{R}{2}\left(\frac{d\alpha_2}{d\alpha_1} + \frac{d\alpha_4}{d\alpha_1}\right)\frac{d\alpha_1}{d\delta} \qquad (3.a26).$$

and

$$F^P = -R\left(\frac{dW_p^L}{d\alpha_3}\frac{d\alpha_3}{d\alpha_1} + \frac{dW_p^R}{d\alpha_1}\right)\frac{d\alpha_1}{d\delta} \qquad (3.a27).$$

Therefore, the indenter force, F, can be expressed as

$$F = \frac{4M_0}{R} F^M + pR F^P \qquad (3.a28).$$

Appendix 4.A. Equivalent Stiffness of Springs

A two-spring structure is shown in Fig. (4.a1). The two springs have stiffnesses of K_1 and K_2. The displacements at positions A and B are denoted by δ_A and δ_B. Spring 1 is fixed at position C and a compressive external force, F, is applied to spring 2 at position A. Therefore,

$$F = K_1\delta_B = K_2(\delta_A - \delta_B) \qquad (4.a.1).$$

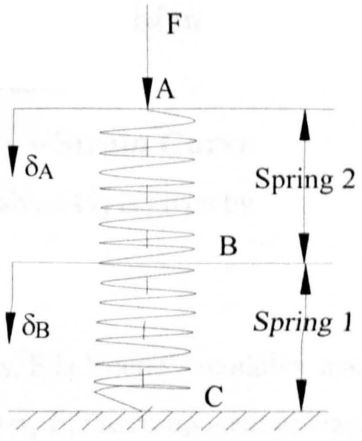

Fig. (4.a 1) A two-spring structure

Hence, the displacement at the position B is given by

$$\delta_B = \frac{K_2}{K_1+K_2}\delta_A \qquad (4.a.2).$$

Substituting equation (4.a.2) into (4.a.1), gives the external force, F, as

$$F = \frac{K_1K_2}{K_1+K_2}\delta_A \qquad (4.a.3).$$

Equation (4.a.3) indicates that the equivalent stiffness, K_{eq}, of a two-spring structure is given by

$$K_{eq} = \frac{K_1K_2}{K_1+K_2} \qquad (4.a.4).$$

Appendix 5.A. Approximate Expressions for Uniaxial Tensile Stress-Strain Curves

5.A.1 Ramberg-Osgood Stress-Strain Curve

The Ramberg-Osgood relationship [49] is given by

$$E\varepsilon = \sigma + \alpha\left(\frac{\sigma}{\sigma_y}\right)^{n-1}\sigma \tag{5.a.1}$$

where α and n is material constants, E is Young's modulus, and σ_y is the yield stress.

When ε is large compared with σ_y/E, the component of elastic strain in Eq.(5.a.1) is negligible and it is possible to rewrite Eq.(5.a.1) as

$$E\varepsilon = \alpha\left(\frac{\sigma}{\sigma_y}\right)^{n-1}\sigma \tag{5.a.2}$$

or

$$\sigma = \left(\frac{1}{\alpha}\right)^{\frac{1}{n}}\left(\sigma_y\right)^{\frac{n-1}{n}}\left(E\varepsilon\right)^{\frac{1}{n}} \tag{5.a.3}.$$

Let $\sigma_0 = \sigma_y \alpha^{\frac{1}{1-n}}$, then Eq.(5.a.3) can be re-written as

$$\sigma = \left(\sigma_0\right)^{\frac{n-1}{n}}\left(E\varepsilon\right)^{\frac{1}{n}} \tag{5.a.4}.$$

It can be seen from this stress-strain relationship that for a material undergoing large strains, equation (5.a.4) can be used whereas for small "elastic" deformation, the stress-strain relationship may be described using Hook's law, i.e.,

$$\sigma = E\varepsilon \tag{5.a.5}.$$

5.A.2 Stress-strain Expressions for Non-mild Steels

By linking Eqs.(5.a.4) and (5.a.5), a new formulation can be written as follows:

$$\sigma\left(E,n,\varepsilon,\varepsilon_0,\beta_1\right) = E\varepsilon + \frac{1}{2}\left[\left(\sigma_0\right)^{\frac{n-1}{n}}\left(E\varepsilon\right)^{\frac{1}{n}} - E\varepsilon\right]\left[th\beta_1\left(\varepsilon-\varepsilon_0\right)+1\right] \tag{5.a.6}$$

where assuming $\varepsilon_0 = \frac{\sigma_0}{E}$ and β_1 and σ_0 are constants, such that β_1 is chosen to satisfy

$$\sigma\left(E,n,\varepsilon,\varepsilon_0,\beta_1\right) \to E\varepsilon \quad for \quad \varepsilon \le \varepsilon_0 \tag{5.a.7(a))}$$

$$\sigma\left(E,n,\varepsilon,\varepsilon_0,\beta_1\right) \to \left(\sigma_0\right)^{\frac{n-1}{n}}\left(E\varepsilon\right)^{\frac{1}{n}} \quad for \quad \varepsilon > \varepsilon_0 \tag{5.a.7(b)).}$$

For a practical pipe material, eg X65 SAW pipe steel with E=230GPa and σ_y=448MPa, and for 6082-T6 aluminium alloy, with E=70GPa and σ_y=300MP, the true stress-strain curves are shown in Figs. 5.a.1 and 2, respectively. It was found that if (n, β_1, σ_0) in Eq. (5.a.7) are (7.65, 5000 and 400MPa) and (29.25, 5000 and 320 MPa) for materials X65 SAW and 6082-T6 alloy, respectively, the predicted stress-strain curves, obtained using Eq. (5.a.7), shown in Figs. 5.a.1 and 2, are obtained.

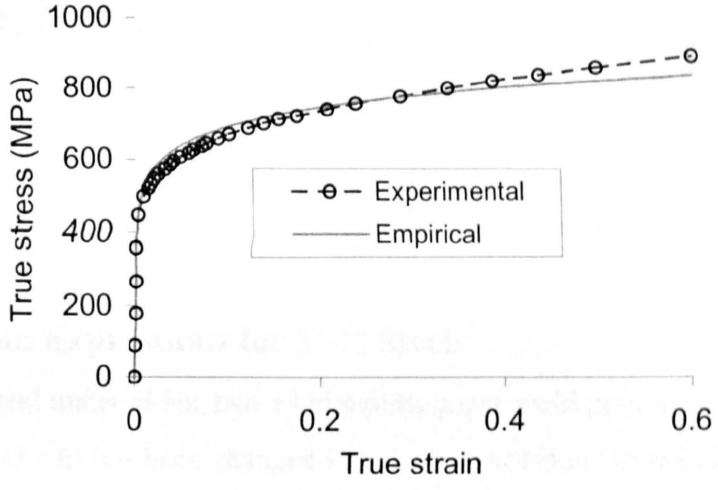

Fig. 5.a.1 True stress versus strain curves of X65 SAW obtained from experimental tests and empirical formulation with n=7.65, β_1=5000 and σ_0=400MPa

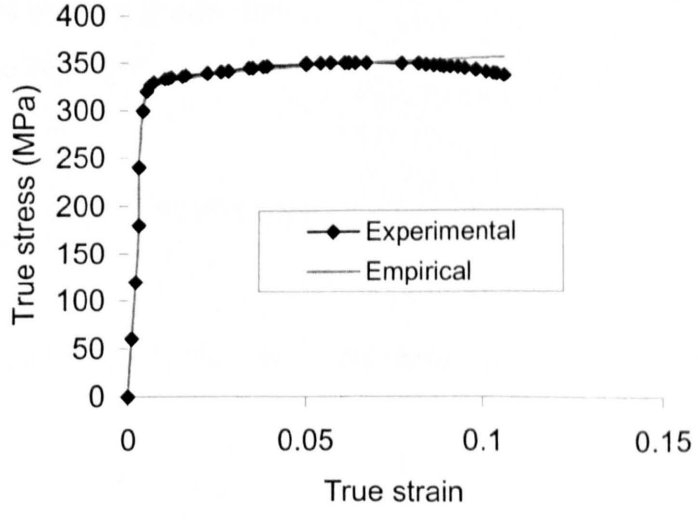

Fig. 5.a.2 True stress versus strain curves of 6082-T6 aluminium alloy obtained from experimental tests and empirical formulation with n=29.25, β_1=5000 and σ_0=320MPa

Substituting (ε_y, σ_y) into Eq.(5.a.6) gives

$$\sigma_y = E\varepsilon_y + \frac{1}{2}\left[(\sigma_0)^{\frac{n-1}{n}}(E\varepsilon_y)^{\frac{1}{n}} - E\varepsilon_y\right]\left[th\beta_1(\varepsilon_y - \varepsilon_0) + 1\right] \quad (5.a.8).$$

Assuming $\left[th\beta_1(\varepsilon_y - \varepsilon_0) + 1\right] \neq 0$, then

$$\left[(\sigma_0)^{\frac{n-1}{n}}(E\varepsilon_y)^{\frac{1}{n}} - E\varepsilon_y\right] = 0 \quad (5.a.9).$$

This gives

$$\sigma_0 = E\varepsilon_y = \sigma_y \quad (5.a.10)$$

which indicates that σ_y is a physical property which is a reasonable estimate for the constant σ_0.

5.A.3 Stress-strain Expressions for Mild Steels

Since the mild steel material has two yield points, upper yield point (σ_{up},ε_{up}) and lower yield point (σ_{low},ε_{low}), Eq.(5.a.6) has been changed in order to correspond to the experimental uniaxial tensile stress-strain curve, seen in Fig. 5.a.3. Hence, the from of equation used is

$$\sigma(E,n,\varepsilon,\varepsilon_0,\beta_1) = E\varepsilon + \frac{1}{2}\left[(\sigma_0)^{\frac{n-1}{n}}(E\varepsilon)^{\frac{1}{n}} - E\varepsilon\right]\left[th\beta_1(\varepsilon - \varepsilon_0) + 1\right] + \beta_2 E\varepsilon \sec h\left[K_\sigma(\varepsilon - \varepsilon_{up})/(\varepsilon_{low} - \varepsilon_{up})\right] \quad (5.a.11)$$

where K_σ is a constant which is greater than 3.

σ_{up} is assumed to be related to ε_{up} using the relationship

$$\sigma_{up} = E\varepsilon_{up}(1 - \beta_3) \quad (5.a.12)$$

which leads to the value of β_3 being given by:

$$\beta_3 = \frac{E\varepsilon_{up} - \sigma_{up}}{E\varepsilon_{up}} \quad (5.a.13).$$

Using Eqs.(5.a.11) and (5.a.13), the upper yield stress can be expressed as

$$\sigma_{up} = E\varepsilon_{up}(1 - \beta_3) = E\varepsilon_{up} + \frac{1}{2}\left[(\sigma_0)^{\frac{n-1}{n}}(E\varepsilon_{up})^{\frac{1}{n}} - E\varepsilon_{up}\right]\left[th\beta_1(\varepsilon_{up} - \varepsilon_0) + 1\right] + \beta_2 E\varepsilon_{up} \quad (5.a.14).$$

If the value of β_1 is such that $th\beta_1(\varepsilon_{up}-\varepsilon_0)=1$, then β_2 can be expressed as

$$\beta_2 E\varepsilon_{up} = E\varepsilon_{up}(1-\beta_3)-(\sigma_0)^{\frac{n-1}{n}}(E\varepsilon_{up})^{\frac{1}{n}} \tag{5.a.15}$$

so that β_2 is given by

$$\beta_2 = 1-\beta_3-\left(\frac{E}{\sigma_0}\varepsilon_{up}\right)^{\frac{n-1}{n}} \tag{5.a.16}.$$

At the lower yield point, Eq.(5.a.11) becomes

$$\sigma_{low} = E\varepsilon_{low}+\frac{1}{2}\left[(\sigma_0)^{\frac{n-1}{n}}(E\varepsilon_{low})^{\frac{1}{n}}-E\varepsilon_{low}\right]\left[th\beta_1(\varepsilon_{low}-\varepsilon_0)+1\right] \tag{5.a.17}$$
$$+\beta_2 E\varepsilon_{low}\sec h(K_\sigma)$$

Since K_σ>3 and β_1 is relatively large, then Eq.(5.a.17) can be simplified to

$$\sigma_{low} = (\sigma_0)^{\frac{n-1}{n}}(E\varepsilon_{low})^{\frac{1}{n}} \tag{5.a.18}$$

or

$$\sigma_0 = (\sigma_{low})^{\frac{n}{n-1}}(E\varepsilon_{low})^{-\frac{1}{n-1}} \tag{5.a.19}.$$

For a typical uniaxial tensile stress-strain curve for an annealed mild steel [50], as shown in Fig.5.a.3, Young's modulus is 20.4GPa, and the upper and lower yield points are nearly at (0.0125, 266.8 MPa) and (0.025, 250.4MPa), respectively.

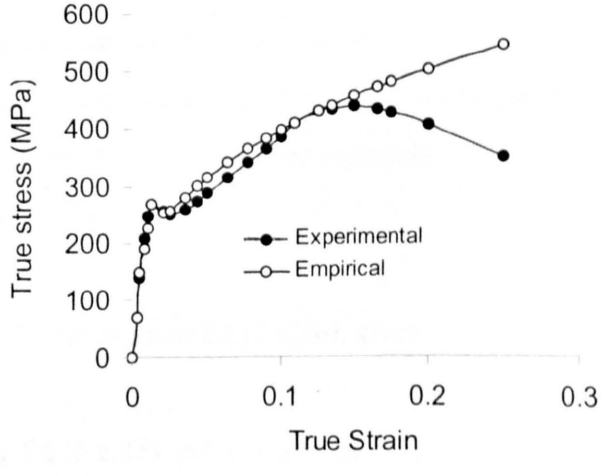

Fig. 5.a.3 True stress versus strain curves of an annealed mild steel, obtained from experimental tests and the empirical formulation, with n=2.941, β_1=5000, β_2=0.2177,β_3=0.1615, σ_0= 154.7MPa and K_σ=4.25

Therefore, from Eqs.(5.a.13), (5.a.16) and (5.a.19), it follows that:

$$\left.\begin{aligned}\beta_3 &= 0.1615\\ \beta_2 &= 0.2177\\ \sigma_0 &= 154.7\end{aligned}\right\} \qquad (5.a.20).$$

With this set of material properties, it can be seen (Fig.5.a.3) that the empirical formula produces a good approximation to the true stress-strain curve.

Although Eqs.(5.a.11) to (5.a.19) have been developed in order to represent a material which has a uniaxial tensile stress-strain curve with two yield points, such as that commonly obtained for mild steel, it can be shown that Eq.(5.a.11) is also suitable for materials with characteristics different from those of mild steel.

For such materials, it is recognised that

$$\sigma_y = E\varepsilon_y \qquad (5.a.21).$$

Therefore Eq.(5.a.13) can be expressed by

$$\beta_3 = \frac{E\varepsilon_{up} - \sigma_{up}}{E\varepsilon_{up}} = \frac{E\varepsilon_y - \sigma_y}{E\varepsilon_y} = 0 \qquad (5.a.22).$$

Also σ_0 is likely to be very close in magnitude to σ_y, so that Eq.(5.a.16) leads to

$$\beta_2 = 1 - \beta_3 - 1 = 0 \qquad (5.a.23).$$

So that in this case, Eq.(5.a.11) is the same as Eq.(5.a.6) indicating that Eq.(5.a.11) can represent other types of materials as well as mild steel.

The material work-hardening exponent (n) in Eq.(5.a.11) can be used to represent linear elastic (n=1) and perfect plasticity ($n=\infty$) types of materials.

If n=1, it is seen from Eq.(5.a.13) that

$$\beta_3 = 0 \qquad (5.a.24).$$

Substituting Eq.(5.a.24) and n=1into Eq.(5.a.16), gives

$$\beta_2 = 0 \qquad (5.a.25).$$

Therefore substituting Eq.(5.a.25) and n=1 into Eq.(5.a.11), gives

$$\sigma = E\varepsilon \qquad (5.a.26).$$

This verifies that Eq.(5.a.13) can be used to represent linear elastic material behaviour. If $n=\infty$, then at the yield point Eq.(5.a.11) can be expressed to

$$\sigma_{1} = E\varepsilon_{1} + \frac{1}{2}\left(\sigma_{y} - E\varepsilon_{y}\right) + \beta_{2}E\varepsilon_{y} \qquad (5.a.27)$$

which gives

$$\beta_{2} = 0 \qquad (5.a.28).$$

When n=∞ and ε<1, Eq.(5.a.11) can be further simplified to give

$$\sigma = E\varepsilon + \left(\sigma_{0} - E\varepsilon\right) = \sigma_{0} = \sigma_{y} \qquad (5.a.29)$$

This indicates that Eq.(5.a.11) can also be used to represent perfectly plastic materials.